Tracing subduction zone processes with magnesium isotopes

Yan Hu

A dissertation

submitted in partial fulfillment of the

requirements for the degree of

Doctor of Philosophy

University of Washington

2018

Reading Committee:

Fang-Zhen Teng, Chair

Bruce K. Nelson

Ronald S. Sletten

Program Authorized to Offer Degree:

Earth and Space Sciences

University of Washington

Abstract

Tracing subduction zone processes with magnesium isotopes

Yan Hu

Chair of the Supervisory Committee:
Professor Fang-Zhen Teng
Department of Earth and Space Sciences

Subduction and recycling of oceanic plates change the chemical composition of mantle and affect its physical properties, thereby modulating Earth's dynamics. Stable Mg isotopes (δ^{26}Mg) can trace this recycling process as crustal materials are highly fractionated compared to the average mantle composition. This dissertation focuses on Mg isotope fractionation during subduction-related processes and the consequent mantle heterogeneity.

The dissertation first compares inconsistent δ^{26}Mg values of San Carlos peridotitic olivines that are published by several laboratories. We analyzed mineral grains from two San Carlos peridotites with disparate lithologies and determined that all mineral phases have indistinguishable δ^{26}Mg values to within 0.07‰. With analytical precision and accuracy being confirmed, the significance of anomalous δ^{26}Mg values can be understood in the context of

mantle heterogeneity. The next paper investigates the Mg isotopic heterogeneity in mantle pyroxenites that have formed by multi-stage interactions between peridotites and melts with diverse origins. Pyroxenites formed by reaction with melts derived from subducted oceanic crust and carbonate sediments are shown to have variable δ^{26}Mg values (−1.51‰ to −0.10‰). In contrast, pyroxenites that are formed by reaction with silicate melts from deep mantle has δ^{26}Mg values similar to common mantle peridotites. Therefore, subducted oceanic slab can indeed produce local Mg isotopic heterogeneities. The third paper aims to characterize the Mg isotopic compositions of subducting sediments, which account for a substantial Mg input to global subduction zones. We analyzed 77 bulk sediments that were recovered from drill cores worldwide; these cores contain diverse lithologies with a wide compositional variation. The sediments display a large variation in δ^{26}Mg, ranging from −1.34‰ (carbonate-rich sediments) to +0.46‰ (clay-rich sediments), indicating that sediment recycling is a feasible process to alter the Mg isotopic composition of local mantle. The fourth paper assesses the Mg isotopic distribution in a typical mantle wedge overlying an active subduction zone, where fluids released from subducting slab acting as a transfer medium for elements between slab and mantle wedge. A suite of sub-arc peridotites from Avacha, Russia, are chosen to represent western Pacific mantle wedge. The isotopic compositions of these peridotites are similar to normal mantle peridotites, suggesting that fluids produced by slab dehydration at relatively shallow depth (pressure of 2-3 GPa) are too depleted in Mg to leave a measurable fingerprint on the Mg-rich mantle wedge. Therefore, large-scale dehydration of isotopically distinct minerals at higher pressures, such as serpentine, are likely to be required to produce mantle domains with atypical δ^{26}Mg.

Collectively, this dissertation confirms the existence of locally heterogeneous mantle domains caused by subducted slabs, highlights the potential of recycling sediments for

introducing heterogeneous δ^{26}Mg to the mantle, and emphasizes the importance of subduction zone thermal structure, which controls the dehydration path of a subducting slab, in generating atypical δ^{26}Mg in mantle wedge. The results from this dissertation contribute to the overall development of using Mg isotopic system to trace crustal recycling and associated mantle heterogeneities.

Table of Contents

List of Figures

List of Tables

Acknowledgments

On the 6-hour flight to visit the flowing lava in Hawaii, I started the first sentence in my PhD dissertation. I think it is all started from there, my passion for geology and my love for rocks.

I became involved in Mg isotope research as a visiting scholar in my PhD advisor's, Prof. Fang-Zhen Teng's, world-renowned laboratory in University of Arkansas, Fayetteville, when I was pursuing my master's degree and changed my major from Gemology to Geochemistry. Back in that time, I know nothing about a clean laboratory nor mass spectrometers. Therefore, I would like to express my deepest gratitude to my advisor, for teaching me analytical chemistry from scratch, for providing a rich environment to carry my PhD research, for trusting me in the laboratory and on the instruments, for encouraging me to interact with people from diverse disciplines, for caring about not only my academic progress but also my daily life.

My PhD work will not be possible without the help from my committees. I would like to thank Prof. Ronald Sletten, for his knowledge on surface processes and aquatic chemistry, for providing opportunities of fantastic field trips, for teaching me do not feel sorry for myself, and do not be defeated by myself. I am grateful to Prof. Bruce Nelson, for his expertise on both instrumental analysis and isotope geochemistry, for his thoughtful advice on my research and constant support during various geologic society meetings, as well as making me realize having small hands are something that I could put on my resume when applying jobs in mass spectrometry! I thank Prof. John Stone, for sharing his interests in rocks, minerals, meteorites, and stars. His passion for teaching always motivates me to be a good teaching assistant. I would also like to recognize Prof. Bo Zhang, my Graduate

School Representative, for his constructive input and for raising thoughtful questions at my General and Final Exams.

My PhD work has also been benefited greatly from interactions with all my coauthors. I would like to specially thank Prof. Terry Plank at Columbia University for her support and collaborative research on global subducting sediments, as well as her mentoring during the CIDER workshop at University of Berkeley in 2017 summer. I am also grateful to Prof. Ionov Dimitri from Université de Montpellier, France, for providing precious sub-arc peridotite samples for my research, as well as sharing with me his professional knowledge on mantle xenoliths. I also thank my friend Prof. Xiao-Ming Liu from University of North Carolina at Chapel Hill, for teaching me how to tune the Nu Plasma MC-ICPMS and to take criticism seriously, but not personally.

I would like to express my sincere thanks to our laboratory manager Dr. Scott Kuehner, for maintaining the instrument and clean laboratory with extreme care, patience, and enthusiasm, for his technical, academic, and life support. I like his saying "Let's see what we can break" whenever I ask him for help on the instrument. Profs. Antony Irvine and Bernard Evans are thanked for fruitful and fun discussions on planetary, mantle, and subduction-zone processes. Prof. Stewart McCallum is thanked for teaching me how to read (his)stories from rock thin sections and for his help when I was the teaching assistant for Igneous Petrology. In addition, I am indebted to all the people working in the main office, as well as Noéll Bernard-Kingsley, Meghan Oxley, Dave McDougall, and Nathan Briley, for helping me with various daily questions and problems. I am also grateful to my academic brothers and sisters, and my fellow graduate students for their support and help along this beautiful journey.

My additional thanks are due to the various funding sources supported my PhD endeavors, including the National Science Foundation, Graduate Student Research Grant from Geological Society of America (2014 and 2015), Robert and Nadine Bassett Fellowship (2014), Kenneth C. Robbins Fellowship (2015), George Edward Goodspeed Geology Scholarship (2015), Peter Misch Fellowship (2016), Harry Wheeler Scholarship (2017), David A. Johnston Memorial Fellowship (2018), and Inquisitive Graduate Student Support Fund (2014) from the Department of Earth and Space Sciences at the University of Washington. These awards not only provided financial support for the completion of my PhD research, but also built confidence in my scholarly abilities.

Last but not the least, I would like to express my greatest appreciation to my family in China for their consistent support, love, encouragement, and inspiration over all these years.

This will not be an end, but rather, a brand-new start, and I am feeling excited.

Chapter 1. Introduction

Subduction zones are the primary sites where oceanic plates dive into the mantle and forming juvenile continental crust. Accompanying these processes are active cycling of elements and volatiles between Earth's surface and interior. The efficiency of this cycling process varies for different chemical species, which is related to the nature of the species and the thermal structure of a given subduction zone. As a result, certain species are preferentially transferred from the subducting slab to the overlying mantle wedge, which are subsequently incorporated to arc magmas and return back to surface. Materials that are retained in the downgoing plate subduct to the deeper mantle and contribute to the development of long-term chemical heterogeneities in the mantle. Therefore, subduction zone processes play a central role in the dynamic evolution of the Earth.

Isotope systematics allow tracing subduction-related modification in the mantle since oceanic slab inherits a crustal- or seawater-like isotope signature during seawater/hydrothermal alteration and sedimentation before entering the trench. Studies of radiogenic/radioactive and cosmogenic isotopes, such as Sr, Nd, Pb, Hf, Os, $^{238}U/^{235}U$, and ^{10}Be, on oceanic basalts and mantle peridotites suggest that the mantle is compositionally heterogeneous on all spatial and temporal scales, with subducted materials being one of the essential contributors to enriched mantle domains (e.g., Tera et al., 1986; Zindler and Hart, 1986; Morris and Tera, 1989; O'Reilly and Griffin, 2013; Hofmann, 2014; Andersen et al., 2015). Stable isotopes, such as oxygen isotopes, are time-independent sensitive tracers for recycled slab materials because they fractionate significantly during low-temperature interactions with Earth's surface whereas fractionations occurring at mantle temperatures are largely negligible (e.g., Woodhead et al., 1987, 1993; Eiler, 2001). Despite the ever-

increasing evidence of subduction recycling and mantle heterogeneity, fundamental questions and controversies remain. For example, where do the enriched, crust-like signature of arc magmas originate from? How do elements transfer from downgoing plate to arc magmas? And, could subducted materials be responsible for chemical heterogeneities seen in intra-plate continental alkaline basalts as well as ocean island basalts?

Rapid growth in studies of non-traditional stable isotopes (e.g., Li, Mg, Fe, and K) have been facilitated by analytical advances in Multi-Collector Inductively Coupled Plasma Mass Spectrometry (MC-ICPMS) over the past decade. These advances allow sub-permil isotopic variations to be resolved and provide a new technique for studying subduction zone processes. The magnesium isotopic system is proving to be an effective tracer of such processes due to the sharp contrast in the values and ranges of δ^{26}Mg ratios (δ^{26}Mg (‰) = $[(^{26}Mg/^{24}Mg)_{sample}/(^{26}Mg/^{24}Mg)_{DSM3} - 1] \times 1000$) between mantle ($\delta^{26}$Mg = −0.25 ± 0.07‰, Teng et al., 2010a) and surface materials (−5.57‰ to +1.81‰, Wombacher et al., 2011; Liu et al., 2014), and negligible fractionation during metamorphic dehydration (Teng et al., 2013; Li et al., 2014; Wang et al., 2014b).

Magnesium is an abundant +2 cation in both silicate rocks and the hydrosphere, constituting ~ 15% of the Earth by mass. It has three naturally occurring stable isotopes (^{24}Mg, 78.99%; ^{25}Mg, 10.00% and ^{26}Mg, 11.01%, Rosman and Taylor, 1998). The large relative mass differences (4 to 8%) and its high solubility in fluids lead to significant mass-dependent Mg isotope fractionation during low-temperature surface processes. For example, continental weathering preferentially leaches light Mg isotopes from rock, resulting in light Mg isotopic composition in rivers (average δ^{26}Mg = −1.09‰, Tipper et

al., 2006a) and oceans (average δ^{26}Mg = −0.83 ± 0.09‰, Foster et al., 2010; Ling et al., 2011), and a complementary isotopically heavy weathering residue (e.g., Teng et al., 2010b; Liu et al., 2014). On the other hand, during carbonate precipitation, the weak Mg-O bond in carbonate minerals cause preferential incorporation of light Mg isotopes from aqueous solutions (Saenger and Wang, 2014). Therefore, carbonates have a characteristic light δ^{26}Mg signatures (typically between −5‰ and −1‰, see review in Teng, 2017), which makes the Mg isotopes an effective tracer for subducted carbonate. By contrast, similarly strong Mg-O bond strength shared by common mantle minerals, i.e., olivine, clinopyroxene, and orthopyroxene, limits the extent of equilibrium isotope fractionation during mantle partial melting and fractional crystallization, resulting in a uniform δ^{26}Mg mantle on a global scale (−0.25 ± 0.07‰, Teng et al., 2007, 2010a). Exceptions to this are spinel and garnet, which have a 4-fold and 8-fold coordination for Mg, respectively. Therefore, spinel is enriched in heavy Mg isotopes (0‰ to +0.65‰, Young et al., 2009; Liu et al., 2011; Xiao et al., 2013) whereas garnet is enriched in the light isotopes (−2.15‰ to −0.37‰, Wang et al., 2012; 2015c; Hu et al., 2016b; An et al., 2017).

The application of Mg isotopes as a tracer for crust-mantle interaction requires both clearly defined values for surface and mantle Mg reservoirs as well as the knowledge of processes and mechanisms governing these distributions. Magnesium is the most abundant cation in the mantle (MgO = 36.77 wt.%, Palme and O'Neill, 2014), and over 99% of the Mg inventory resides in the mantle. Mass-balance calculation suggests difficulty in perturbation of the homogeneous Mg isotopic distribution in the mantle; however, subduction recycling does appear to alter these values. For example, continental and arc magmas have display large δ^{26}Mg variation ranging from −0.61‰ to +0.06‰ (Yang et al.,

2012; Wang et al., 2016; Li et al., 2017; Su et al., 2017; Sun et al., 2017). However, oceanic basalts, particularly ocean island basalts, sampled on a global scale do not show similarly large variation, but are rather homogeneous (−0.26 ± 0.07‰, n = 110, Teng et al., 2010a). This paradox raises the question that whether the anomalous δ^{26}Mg values in continental and arc magmas reflect genuine mantle signature or are a crust-modified signature during magma ascent. If the former is the case, then what processes are uniquely involved in basalts formed in continental and arc settings from those produced in oceanic realm?

Basalts are derived from partial melting of the mantle and thus they are indirect mantle samples. Studies on mantle xenoliths offer a more direct view of mantle composition because they are fragments of solid mantle that are incidentally entrained in magmas and brought to the surface during volcanic eruptions. This dissertation explores the extent, distribution, and mechanism of mantle Mg isotopic heterogeneity recorded in mantle xenoliths and their linkage with subduction-related processes. The first chapter examines the nature of large inter-laboratory difference in δ^{26}Mg measured on San Carlos peridotites, while the next three chapters focus on Mg isotopic compositions of mantle pyroxenite xenoliths, modern subducting marine sediments, and sub-arc mantle peridotite xenoliths. This dissertation is presented as four independent papers that have either already been published or will be submitted for publication. They are described briefly below.

Chapter 2 examines Mg isotopic heterogeneity of San Carlos peridotite xenoliths, which display large inconsistent δ^{26}Mg values in olivine samples measured from different laboratories. Two batches of olivine grains from a lherzolite and four batches of olivine, clinopyroxene, and orthopyroxene grains from a harzburgite have been analyzed. The six different batches of olivine grains yield homogeneous δ^{26}Mg to within 0.03‰ (2SD) and

are isotopically indistinguishable to co-existing pyroxene grains. Therefore, previously documented large inter-laboratory discrepancies are likely not accurate, and our study further supports that mantle peridotites in general have a homogeneous Mg isotopic composition. This work was published as an article entitled "**Magnesium isotopic homogeneity of San Carlos olivine: a potential standard for Mg isotopic analysis by multi-collector inductively coupled plasma mass spectrometry**" in *Rapid Communications in Mass Spectrometry*.

With our analytical accuracy being confirmed by Chapter 2, the measured anomalous δ^{26}Mg values in the following chapters are attributed to genuine mantle heterogeneity. Chapter 3 examines the existence of small-scale heterogeneity in local mantle domains caused by melt-rock interaction (i.e., metasomatism). To explore this possibility, this study presents the first systematic Mg isotopic analyses on pyroxenite xenoliths, which are physical evidence for melt infiltration into the lithospheric mantle. Twenty-five pyroxenite with diverse petrological occurrences and origins were measured, which revealed a large range in whole-rock δ^{26}Mg values with large inter-mineral disequilibrium isotope fractionations that are explained to reflect the various origins of the metasomatic melts. These heterogeneous δ^{26}Mg values may be linked to the large variations seen in continental basalts as they often contain contributions from lithospheric mantle to various externs. The relatively cold lithospheric mantle and lack of convection also facilitate preservations of mantle heterogeneities. This work was published as an article entitled "**Metasomatism-induced mantle magnesium isotopic heterogeneity: Evidence from pyroxenites**" in *Geochimica et Cosmochimica Acta*.

A natural question following the findings in Chapter 3 is the origin of metasomatic

melts in the mantle. Chapter 4 presents the first systematic investigation on Mg isotopic variation in subducting marine sediments, which have been considered as an essential contributor to isotopic heterogeneity of the mantle. A total of 77 bulk sediments collected from 10 drill sites worldwide yield a wide δ^{26}Mg range from −1.34‰ to +0.46‰, the variation of which appears to be linked to sediment lithology. In addition, the flux-weighted δ^{26}Mg of −0.336‰ is estimated for Global Subducting Sediments (GLOSS-II), which is isotopically lighter than the mantle average. Therefore, this study demonstrates that subducting marine sediments are a source of heterogeneous δ^{26}Mg in the mantle. This work was published as an invited research article entitled "**Magnesium isotopic composition of subducting marine sediments**" in *Chemical Geology*.

The highly variable Mg isotopic input from subducting slab suggests that components with atypical Mg isotopic compositions may be present in the mantle wedge as fractionated crustal materials are recycled into the mantle at subduction zones. Chapter 5 presents the first systematic study on the Mg isotopic composition of a typical supra-subduction zone mantle domain by analyzing 23 large and fresh harzburgite xenoliths from the Avacha volcano in Kamchatka, Russia. Both sub-arc mantle xenoliths and arc lavas are well studied for this region (e.g., Kersting and Arculus, 1995; Kepezhinskas et al., 1996, 1997; Kepezhinskas and Defant, 1996; Yogodzinski et al., 2001; Widom et al., 2003; Ionov, 2010; Ishimaru and Arai, 2008a,b,c, 2011; Kayzar et al., 2014; Bénard et al., 2017). This study finds that melting residues in the mantle wedge in the western Pacific, where dehydration of slab crust at pressures of 2-3 GPa serves as the major water supplier for melting and metasomatism, likely have a mantle-like δ^{26}Mg due to the low Mg concentrations in fluids released at such depths. Large-scale dehydration of isotopically

distinct phases at higher pressures may be required to produce isotopically diverse arc lavas, such as those seen in lavas from Lesser Antilles and Philippines (Teng et al., 2016; Li et al., 2017). In addition, since Mg rich carbonate (magnesite) and K-rich silicate such as phlogophie and phengite do not typically dehydrate at sub-arc depth, they may preserve their distinct δ^{26}Mg to deeper mantle, which may be tapped later by (ultra)potassic magmas (e.g., Liu et al., 2015; Sun et al., 2017). This work will be submitted soon as an article entitled "**Magnesium cycling at subduction zones constrained by Mg isotopic composition of sub-arc mantle beneath southern Kamchatka**".

The perspectives for this work and future suggested research are presented in Chapter 6.

Chapter 2. Magnesium isotopic homogeneity of San Carlos olivine: a potential standard for Mg isotopic analysis by multi-collector inductively coupled plasma mass spectrometry

This chapter is published as:

Hu, Y., Teng, Harrington, M. D., Sun, Y., Konter, J. and Teng, F.-Z. (2016) Magnesium isotopic homogeneity of San Carlos olivine: a potential standard for Mg isotopic analysis by multi collector inductively coupled plasma mass spectrometry, Rapid Commun. Mass Spectrom, 30, 2123-2132.

Abstract

RATIONALE: Previous analyses on San Carlos olivine from Arizona (USA) have shown inter-laboratory δ^{26}Mg differences of up to 0.67‰, while mantle olivine samples worldwide are homogeneous at a current analytical uncertainty of ~0.1‰. The differing measurements on San Carlos olivine may be attributable to analytical artifacts or sample heterogeneity. The latter must be ruled out before using it as a standard for Mg isotopic analysis.

METHODS: To examine sample homogeneity, two different batches of San Carlos olivine from a lherzolite and four batches from a harzburgite have been analyzed together with coexisting harzburgitic pyroxene. In addition, the effect of acid purity on resin performance and the reusability of AG50W-X8 resin for Mg separation have been evaluated by processing another batch of lherzolitic San Carlos olivine and Hawaiian seawater through both new and used resins cleaned with different acids.

RESULTS: Six different batches of olivine grains from two San Carlos peridotite xenoliths show homogeneous δ^{26}Mg values to within 0.03‰, and all the mineral phases in the harzburgite are in Mg isotope equilibrium. Furthermore, there is no resolvable δ^{26}Mg shift in either lherzolitic San Carlos olivine or Hawaiian seawater by using either new or used resins that were cleaned with single-distilled or double-distilled acids.

CONCLUSIONS: The new data are consistent with the narrow δ^{26}Mg range of mantle olivine worldwide, while they stand in contrast to the wide range measured on the same San Carlos olivine powder in different laboratories. Therefore, previous inter-laboratory discrepancies reflect analytical artifacts instead of sample heterogeneity, and San Carlos olivine is a suitable standard for Mg isotopic analysis.

1. Introduction

The application of multi-collector inductively coupled plasma mass spectrometry (MC-ICP-MS) in magnesium (Mg) isotope geochemistry has made it possible to achieve a routine precision of better than 0.1‰, compared with a precision of 1-2‰ by thermal ionization or secondary ionization mass spectrometry. This tenfold improvement in analytical capability now allows small mass-dependent Mg isotope fractionation in terrestrial samples, especially in high-temperature samples, to be resolved. Studies on peridotite xenoliths and oceanic basalts have shown that the mantle, which holds > 99% of Earth's total Mg inventory, has a homogeneous Mg isotopic composition (δ^{26}Mg = −0.25 ± 0.07‰, 2SD) (Teng et al., 2010a). A compilation of olivine data from peridotite xenoliths worldwide also suggests a narrow δ^{26}Mg range (−0.25 ± 0.12‰, 2SD) despite differences in age (Phanerozoic to Archean), and degree of melt extraction and metasomatic

refertilization of the host peridotites (Fig. 2-1a) (Handler et al., 2009; Yang et al., 2009; Liu et al., 2011; Pogge von Strandmann et al., 2011; Xiao et al., 2013; Wang et al., 2015 a,b, 2016). However, olivine grains from San Carlos peridotites (Arizona, USA) seem to span an unexpectedly large range, from −0.73‰ to −0.06‰ (Fig. 2-1b) (Pearson et al., 2006; Teng et al., 2007; Wiechert and Halliday, 2007; Handler et al., 2009; Huang et al., 2009; Wimpenny et al., 2010; Pogge von Strandmann et al., 2011; Sio et al., 2013; Wang et al., 2015 a, b, 2016;). More strikingly, analyses on aliquots of the same large batch of San Carlos olivine powder by multiple laboratories have still yielded a wide range, from −0.55‰ to −0.19‰ (Fig. 2-1b) (Young et al., 2009; Chakrabarti and Jacobsen, 2010; Liu et al., 2010; Yang et al., 2012; Bouvier et al., 2013). As mass dependent isotope fractionation produced during chemical purification and instrumental analysis follows the same behavior as occurs in nature, it is still unclear whether these discrepancies are the result of analytical artifacts or sample heterogeneity.

Understanding the source of these inconsistent results is important as they indicate either that the mantle is not universally homogeneous or that there is inter-laboratory bias for Mg isotopic analysis. The peridotite xenoliths from San Carlos, as in most other studied locations, represent a range of mantle processes and sources. If sample heterogeneity is the cause, previous suggestion of the homogeneous, chondritic Mg isotopic composition of the mantle (Teng et al., 2010a) might need to be re-examined. On the contrary, if the differing measurements are caused by analytical issues, results from different laboratories cannot be compared directly. More importantly, the 0.36‰ interlaboratory difference on aliquots of the same San Carlos olivine powder (−0.55 to −0.19‰, Fig. 2-1b) (Young et al., 2009; Chakrabarti and Jacobsen, 2010; Liu et al., 2010; Yang et al., 2012; Bouvier et al., 2013)

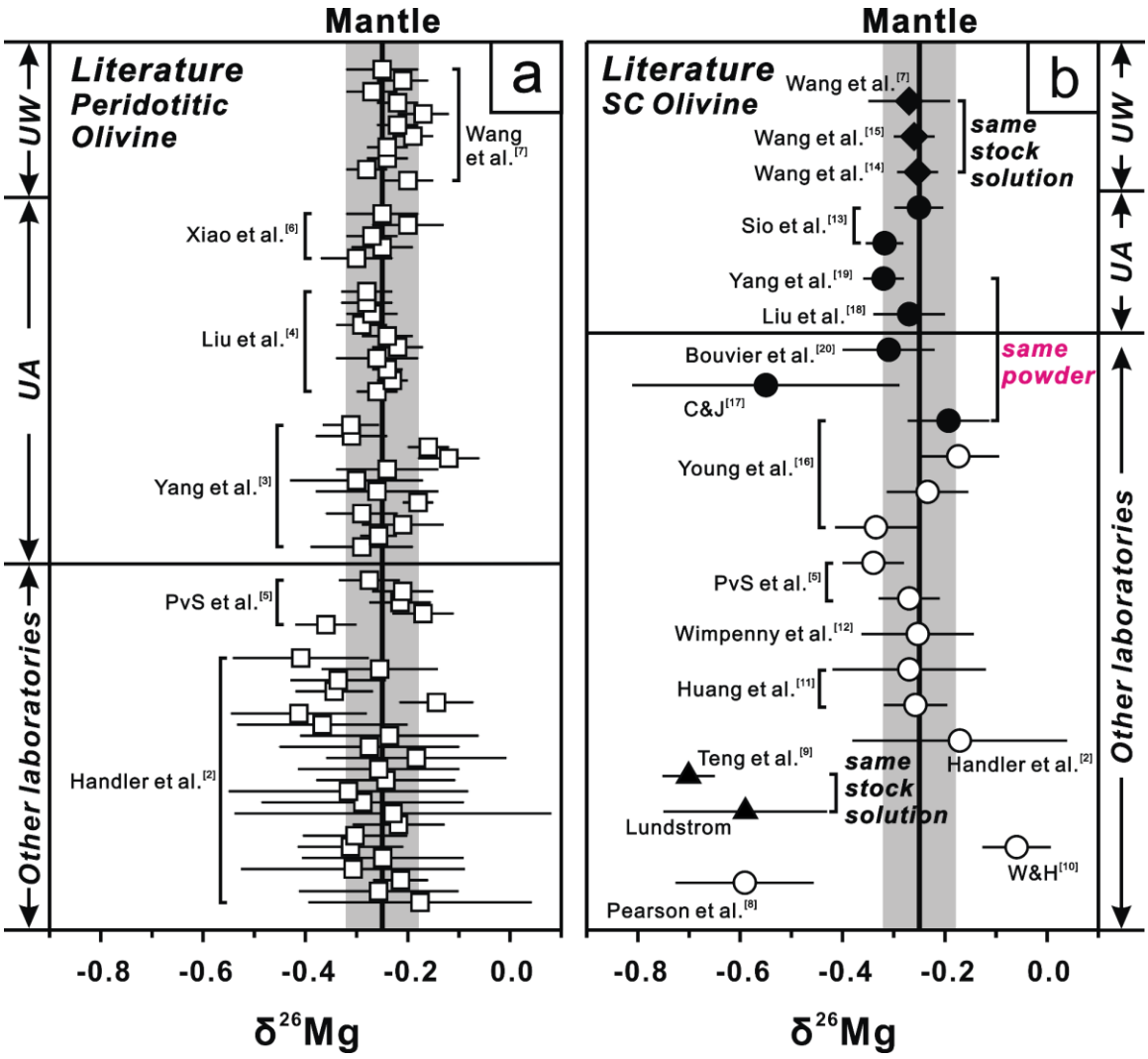

Figure 2-1. Compilations of δ^{26}Mg data for (a) mantle olivine from peridotite xenoliths and (b) San Carlos olivine. Data sources: Handler et al. (2009); Yang et al. (2009); Liu et al. (2011); Pogge von Strandmann (PvS) et al. (2011); Xiao et al. (2013) and Wang et al. (2016). Handler et al. (2009); Pogge von Strandmann (PvS) et al. (2011); Wang et al. (2015 a,b, 2016); Pearson et al. (2006); Teng et al. (2007); Wiechert and Halliday (W&H), (2007); Huang et al. (2009); Wimpenny et al. (2010); Sio et al. (2013); Young et al. (2009); Chakrabarti and Jacobsen (C&J), (2010); Liu et al. (2010); Yang et al. (2012); Bouvier et al. (2013) and Lundstrom [unpublished]. The gray bar in each panel represents two standard deviations (2SD) of the average mantle δ^{26}Mg (−0.25 ± 0.07‰) (Teng et al., 2010), which is shown as the black vertical line in the center of the gray bar. Error bars in this and the following figures represent 2SD. UW = Isotope Laboratory at the University of Washington and UA = Isotope Laboratory at the University of Arkansas, both of which use the same analytical method as in this study.

leaves the argument for a non-chondritic Earth by some laboratories questionable, as their measured differences between peridotites and chondrites are only 0.1 to 0.3‰ (Wiechert and Halliday, 2007; Young et al., 2009). These differences have not been found in other studies that reported data from simultaneously analyzed peridotites and chondrites (Teng et al., 2007; Handler et al., 2009; Yang et al., 2009; Teng et al., 2010a; Pogge von Strandmann, 2011; Chakrabarti and Jacobsen, 2010; Bouvier et al., 2013), further suggesting that previous argument for a non-chondritic Earth may be based on an analytical artifact.

Investigating the Mg isotopic homogeneity of San Carlos olivine is also important with respect to its use as a standard for data quality control and inter-laboratory comparison. Olivine has several advantages as a Mg isotopic standard if its Mg isotopic composition can be demonstrated to be homogeneous. First, olivine is a common mineral in a wide diversity of lithologies on Earth, Moon, and in some meteorites (e.g., pallasite and chassigny). Second, olivine can be used to monitor laboratory-induced Mg isotope fractionation through the whole procedure, starting with sample dissolution through chemical purification and instrumental analysis. Olivine in hence better in this respect than solution standards, such as Cambridge-1, that do not need sample preparation as solid materials. Third, only a small quantity of olivine is needed as a standard due to its high Mg content, which also prevents Mg isotopic resetting by late-stage modifications. Finally, fresh, clear, and large olivine grains are easily accessible from peridotite localities worldwide. Olivine from mantle xenoliths is also more representative of mantle Mg isotopic composition than some altered peridotite whole rock standards (e.g., USGS dunite standard DTS-1).

Here, we further examine the Mg isotopic homogeneity of San Carlos olivine and its use as a standard for Mg isotopic analysis. Independent analyses on four different batches of olivine, clinopyroxene, and orthopyroxene grains from a San Carlos harzburgite yield consistent results, suggesting homogeneity within and among all phases. The other two batches of olivine from a San Carlos lherzolite have identical δ^{26}Mg values to those from the harzburgite, suggesting inter-xenolith Mg isotopic homogeneity. The results from this study together with the narrow δ^{26}Mg range of olivine grains from global peridotite xenoliths argue for analytical issues in reported inconsistent measurements on San Carlos olivine. San Carlos olivine can therefore be used as a reliable standard for establishing analytical accuracy and long-term reproducibility for Mg isotopic measurement.

2. Experimental

2.1. Samples

The peridotite xenoliths used in this study were collected from the Peridot Mesa (33.33°N, 110.47°W), a well-known mesa-capping lava flow from one of the vents in the San Carlos volcanic field, southwestern United States. There, abundant ultramafic xenoliths with gem-quality coarse olivine grains were carried to the surface by Late Tertiary to Quaternary alkaline volcanism. Both lherzolite and harzburgite are present in the locality (~ 45 to 90% olivine), interlayered with pyroxene-rich rocks in some cases (Frey and Prinz, 1978; Galer and O'Nions, 1989). One lherzolite and one harzburgite xenolith were selected for Mg isotopic analyses based on their freshness, large mineral grains, and characteristic mineral assemblages of each peridotite type (Fig. 2-2). Both peridotites contain Mg rich olivine and Cr-rich diopside and therefore are classified as Group I xenoliths after Frey and Prinz (1978). The peridotite xenoliths were interpreted as

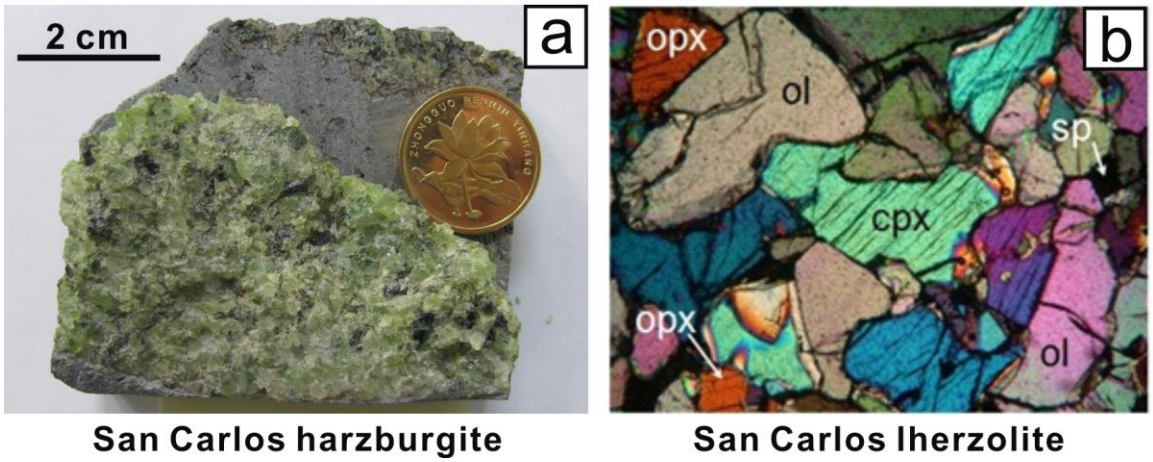

Figure 2-2. The two San Carlos peridotites analyzed in this study. (a) Hand specimen of the harzburgite. (b) Photomicrograph of the lherzolite under cross-polarized light. Ol = olivine; Cpx = clinopyroxene; Opx = orthopyroxene; Spl = spinel.

melting residues but have undergone multi-stage metasomatic modifications, which might be related to the pyroxene-rich rocks (Frey and Prinz, 1978; Galer and O'Nions, 1989). Olivine separates were hand-picked from the two coarse-grained peridotites (Fig. 2-2). Coexisting clinopyroxene and orthopyroxene were also picked from the harzburgite to evaluate inter-mineral Mg isotope equilibrium. Previous major element analyses on constituent minerals suggested a complete chemical equilibrium between coexisting minerals, and the equilibrium temperature calculated for San Carlos peridotites is around 1022°C (Galer and O'Nions, 1989). Moreover, as a major element, Mg has a restricted range of concentrations in olivine (Mg# = 87-91), clinopyroxene (Mg# = 88-93), and orthopyroxene (Mg# = 88-92), where Mg# represents the molar ratio of 100 × $Mg/(Mg+Fe^{2+})$ (Galer and O'Nions, 1989).

2.2. Analytical methods

Magnesium separation and isotopic analyses were performed at the Isotope Laboratory of the University of Washington (UW), Seattle (WA, USA). The procedures follow those detailed in previous studies conducted at the Isotope Laboratory of the University of Arkansas (UA), Fayetteville (AR, USA) (Teng et al., 2007; Yang et al., 2009; Li et al., 2010; Teng et al., 2010a; Teng and Yang., 2014) and are summarized here.

Mineral separates from the two San Carlos peridotites were selected for purity and clarity under a binocular microscope. In order to examine intra-xenolith Mg isotopic homogeneity and inter-mineral isotope equilibrium, four batches of mineral grains for each mineral phase were hand-picked from the San Carlos harzburgite. Meanwhile, two batches of olivine grains from the San Carlos lherzolite were picked to examine inter-xenolith Mg

isotopic homogeneity. Only a small number of mineral fragments were selected in each mineral batch to minimize the homogenization effect from mixing of large quantities of samples. The mineral separates were first cleaned in an ultrasonic bath using Milli-Q water (18.2 MΩ·cm resistivity, Millipore, Billerica, MA, USA), then powdered using an agate mortar and a pestle. The mineral powders were subsequently dissolved and fluxed in screw-top Teflon beakers (Savillex, Eden Prairie, MN, USA) in a series of concentrated acids: HF-HNO_3, HCl-HNO_3, and HNO_3.

The sample solutions were evaporated to dryness between each step and were finally dissolved in 1 N HNO_3 in preparation for column chemistry. Magnesium separation and purification were achieved via cation-exchange chromatography with 200–400 mesh AG50W-X8 pre-cleaned resin (Bio-Rad, Hercules, CA, USA), following the procedure first outlined by Teng et al. (2007). In brief, the resin was first conditioned in 1 N HNO_3. Matrix elements were then removed with 16 mL 1 N HNO_3. The Mg fraction was subsequently collected with 19 mL of 1 N HNO_3. Two rounds of column chemistry were performed using this same elution sequence to ensure a pure Mg solution.

The magnesium isotopic ratios were measured on a Nu Plasma (Nu Instruments, Wrexham, UK) high-resolution multi-collector inductively coupled plasma mass spectrometer using the sample-standard bracketing method with an individual beaker for each standard replicate. Pure Mg solutions in 3% double-distilled HNO_3 (~ 300 ppb) were introduced into the source region using a quartz Cinnabar spray chamber (Glass Expansion, Pocasset, MA, USA) and a MicroMist glass concentric nebulizer (100 μL/min) (Glass Expansion). The intensities of sample solutions were diluted to within 95% of the intensities of the bracketing standard solutions. The three Mg isotopes (^{24}Mg, ^{25}Mg, and

^{26}Mg) were well separated in low-resolution mode with a typical ^{24}Mg signal of ~3.5-4.5 V. The magnesium isotopic data are reported relative to the DSM-3 standard, which is a pure Mg solution made of ~10 g of pure Mg metal (Dead Sea Magnesium Ltd, Israel) dissolved in 1 L of ~0.3 N HNO_3.

3. Results and discussion

The magnesium isotopic data are reported in Table 2-1 for the reference materials, Table 2-2 for the mineral separates from San Carlos peridotites, and Table 2-3 for the results of the lherzolitic San Carlos olivine and Hawaiian seawater processed through different types of resins. The resin codes used in Table 2-3 and Fig. 2-6 are explained in Table 2-4. All the samples analyzed during the course of this study fall on a single mass-dependent fractionation line with a slope of 0.513 (R^2 = 0.994) (Fig. 2-3). Hereafter we only discuss δ^{26}Mg values.

3.1. Data accuracy and precision

An USGS peridotite standard, PCC-1, was processed and analyzed to assess data accuracy, which yielded a δ^{26}Mg value of −0.22‰, in agreement with the recommended value of −0.229 ± 0.055‰ (Teng et al., 2015). Furthermore, Hawaiian seawater, which has been used as a reliable in-house standard in the laboratory for over 5 years, was analyzed repeatedly to further monitor data accuracy and long-term reproducibility (Table 2-1). Three duplicates of the Hawaiian seawater yielded δ^{26}Mg values between –0.83‰ and −0.84‰, with an average of −0.83 ± 0.04‰, consistent with the recommended value of −0.843 ± 0.057‰ (Teng et al., 2015).

3.2. Magnesium isotopic composition of mineral separates from San Carlos peridotites

All the mineral separates from the two San Carlos peridotites analyzed in this study have a homogeneous Mg isotopic composition with limited variation (Fig. 2-4a). The harzburgitic and lherzolitic olivine grains have similar δ^{26}Mg ranges (−0.27‰ to −0.23‰) with an average of −0.24 ± 0.03‰. These values are consistent with previous measurements on different olivine grains from the same San Carlos lherzolite hand specimen (−0.27‰ to −0.23‰) (Wang et al., 2016; Wang et al., 2015 a,b). The two types of pyroxene also yield identical δ^{26}Mgvalues, from −0.25‰ to −0.21‰ (average = −0.23 ± 0.04‰) for clinopyroxene, and from −0.26‰ to −0.20‰ (average = −0.22 ± 0.05‰) for orthopyroxene. The lack of measurable fractionation between them ($\Delta^{26}Mg_{Cpx\text{-}Ol}$ = 0.01 ± 0.05‰, $\Delta^{26}Mg_{Opx\text{-}Ol}$ = 0.02 ± 0.06‰) indicates an inter-mineral Mg isotope equilibrium, as olivine and pyroxene have a similar Mg-bonding environment and hence similar Mg–O bond strength (Fig. 2-4b) (Liu et al., 2011; Shauble, 2011).

3.3. Comparisons with previous data

A compilation of δ^{26}Mg data for peridotitic olivine worldwide suggests an overall homogeneity at current analytical uncertainties (Fig. 2-1a), regardless of the different melt extraction and modification histories undergone by their host peridotites (Handler et al., 2009). Furthermore, the compiled fractionation factors between clinopyroxene and olivine and between orthopyroxene and olivine reveal a broad Mg isotope equilibrium among the major mantle minerals (Fig. 2-5). These observations suggest a general Mg isotopic

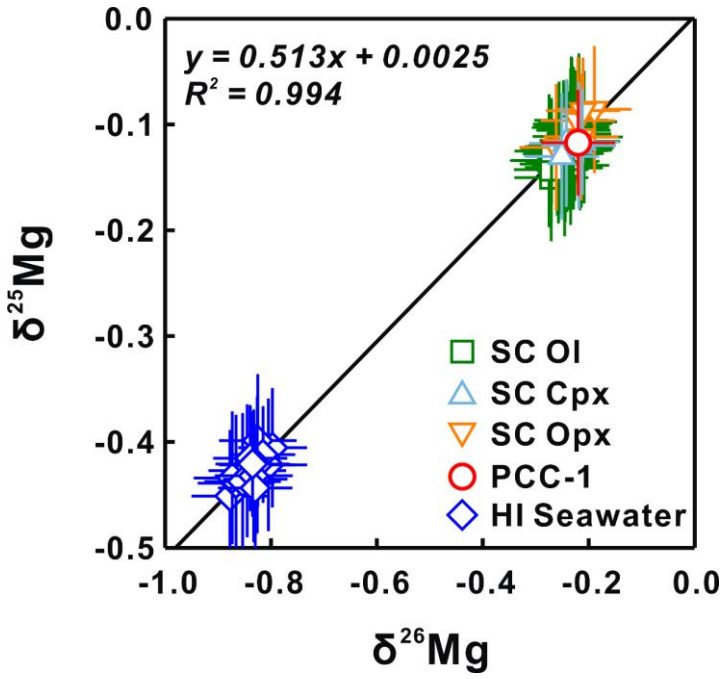

Figure 2-3. Magnesium three-isotope plot (relative to DSM-3 standard). SC = San Carlos; HI = Hawaiian; Ol = olivine; Cpx = clinopyroxene, Opx = orthopyroxene. PCC-1 is an USGS peridotite standard.

Table 2-1. Magnesium isotopic compositions of reference materials.

Reference Materials	**δ^{26}Mg (‰)**	**2SD**	**δ^{25}Mg (‰)**	**2SD**
PCC-1 (USGS, peridotite)	−0.22	0.07	−0.12	0.05
Recommended value	−0.229	0.055	-0.101	0.01
Hawaiian seawater	−0.84	0.07	−0.42	0.05
chemistry duplicate	−0.83	0.07	−0.44	0.06
chemistry duplicate	−0.83	0.07	−0.42	0.05
Hawaiian seawater average	***−0.83***	***0.04***	***−0.42***	***0.03***
Recommended value	−0.843	0.057	−0.433	0.040

2SD = two times the standard deviation of multiple analyses of bracketing standards during an analytical session.

Chemistry duplicate indicates analyses of different aliquots of the dissolved sample that were processed individually through chemical separation.

Recommended values for PCC-1 and Hawaiian seawater are from Teng et al. (2015).

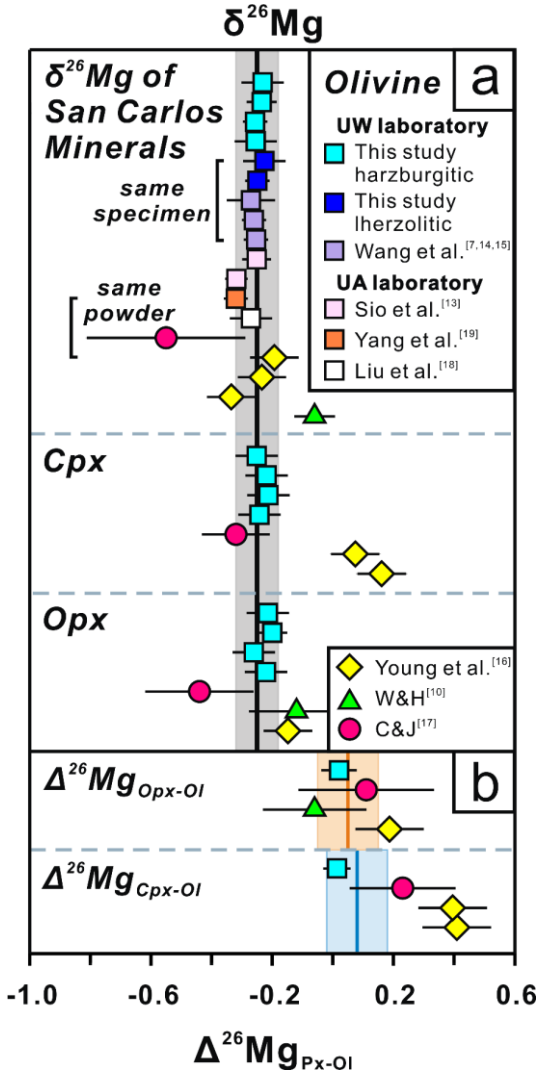

Figure 2-4. (a) Mg isotopic compositions of mineral separates from the San Carlos (SC) peridotites. (b) Inter-mineral Mg isotope fractionation of Cpx-Ol and Opx-Ol pairs from the San Carlos peridotites. The x-axis in (a) represents δ^{26}Mg values while in (b) it represents Δ^{26}Mg between pyroxene (Px) and olivine (Ol). Data from Wiechert and Halliday (W&H), (2007); Young et al. (2009) and Chakrabarti and Jacobsen (C&J), (2010), which also reported δ^{26}Mg data for Cpx-Ol and Opx-Ol pairs, are plotted for comparison. In addition, published data for San Carlos olivine analyzed in UW and UA laboratories by other authors have also been plotted for comparison, including Wang et al. (2015a,b, 2016); Sio et al. (2013); Liu et al. (2010) and Yang et al. (2012). The gray bar in (a) represents 2SD of the average mantle δ^{26}Mg (−0.25 ± 0.07‰) (Teng et al., 2010a), which is shown as the black vertical line. The orange and blue bars in (b) represent the calculated ranges of equilibrium inter-mineral fractionation of Opx-Ol and Cpx-Ol pairs, respectively, at temperatures between 800 and 1200°C. The theoretical fractionation factors used in the calculation are from Schauble (2011). The vertical orange and blue lines in the center of the bars represent the fractionation factor at 1000°C in each case, which is the average equilibrium temperature for San Carlos peridotites (Galer and O'Nions, 1989).

Table 2-2. Magnesium isotopic compositions of mineral separates from San Carlos peridotites.

Minerals	δ^{26}Mg (‰)	2SD	δ^{25}Mg (‰)	2SD
San Carlos harzburgite				
Ol-1	−0.25	0.07	−0.13	0.05
Ol-2	−0.27	0.07	−0.14	0.05
repeat	−0.27	0.07	−0.13	0.05
chemistry duplicate	−0.23	0.07	−0.11	0.06
Ol-2 average	*−0.26*	*0.04*	*−0.13*	*0.03*
Ol-3	−0.24	0.07	−0.12	0.05
chemistry duplicate	−0.23	0.07	−0.10	0.06
Ol-3 average	*−0.23*	*0.05*	*−0.11*	*0.04*
Ol-4	−0.23	0.07	−0.10	0.05
Harzburgitic Ol average	***−0.24***	***0.03***	***−0.12***	***0.03***
Cpx-1	−0.24	0.07	−0.12	0.06
Cpx-2	−0.21	0.07	−0.12	0.05
Cpx-3	−0.22	0.07	−0.12	0.06
Cpx-4	−0.25	0.07	−0.13	0.06
Harzburgitic Cpx average	***−0.23***	***0.04***	***−0.12***	***0.01***
Opx-1	−0.22	0.07	−0.10	0.06
Opx-2	−0.26	0.07	−0.12	0.06
Opx-3	−0.19	0.07	−0.09	0.06
repeat	−0.21	0.07	−0.09	0.05
Opx-3 average	*−0.20*	*0.05*	*−0.09*	*0.04*
Opx-4	−0.21	0.07	−0.11	0.06
Harzburgitic Opx average	***−0.22***	***0.05***	***−0.10***	***0.03***
Ol-1	−0.25	0.07	−0.13	0.05
repeat	−0.23	0.07	−0.12	0.05
repeat	−0.27	0.07	−0.15	0.06
average	***−0.25***	***0.04***	***−0.13***	***0.03***
Ol-2	−0.23	0.07	−0.10	0.05
Lherzolitic Ol average	***−0.24***	***0.04***	***−0.12***	***0.03***

Ol = olivine; Cpx = clinopyroxene; Opx = orthopyroxene.

Repeat indicates instrumental analyses of the same purified sample solution in different analytical session.

homogeneity in mantle olivine and are consistent with the narrow δ^{26}Mg range of global peridotite xenoliths (Teng et al., 2010a). Therefore, the Mg isotopic composition of mantle olivine seems well buffered by its high Mg concentration, while any isotopic heterogeneity is expected to be erased quickly due to the fast diffusion rate of Mg at mantle temperature (e.g., ~1×10^{-18} m^2/s at 980°C for Fo_{85-93}) (Chakraborty, 1997).

Measurements on San Carlos olivine, however, have shown noticeable inter-laboratory variation in δ^{26}Mg values, ranging from −0.73‰ to −0.06‰ (Fig. 2-1b) (Pearson et al., 2006; Teng et al., 2007; Wiechert and Halliday, 2007; Handler et al., 2009; Huang et al., 2009; Wimpenny et al., 2010). To eliminate the potential influence from sample heterogeneity, Chakrabarti and Jacobsen (2010) prepared a homogenized San Carlos olivine sample by powdering ~ 50g of hand-picked olivine grains. This sample was measured at four laboratories on three different types of instruments: Thermo Neptune (Thermo Fisher Scientific, Waltham, MA, USA), GVI IsoProbe-P (GV Instruments, Manchester, UK), and Nu Plasma (Nu Instruments). The reported δ^{26}Mg values are similar (−0.19‰ to −0.32‰) (Young et al., 2009; Liu et al., 2010; Yang et al., 2012; Bouvier et al., 2013) except for a much lower δ^{26}Mg value of −0.55‰ obtained by Chakrabarti and Jacobsen (2010). Despite the 0.67‰ total variation in published δ^{26}Mg data for the San Carlos olivine (Teng et al., 2007; Wiechert and Halliday, 2007), the results from most studies (Huang et al., 2009; Young et al., 2009; Liu et al., 2010; Wimpenny et al., 2010; Pogge von Strandmann, 2011; Yang et al., 2012; Bouvier et al., 2013; Sio et al., 2013; Wang et al., 2015 a,b, 2016), including this one, are similar and fall within the mantle range. For example, olivine grains separated from five different San Carlos peridotite specimens by five different authors using the same analytical method as used in this study gave a narrow

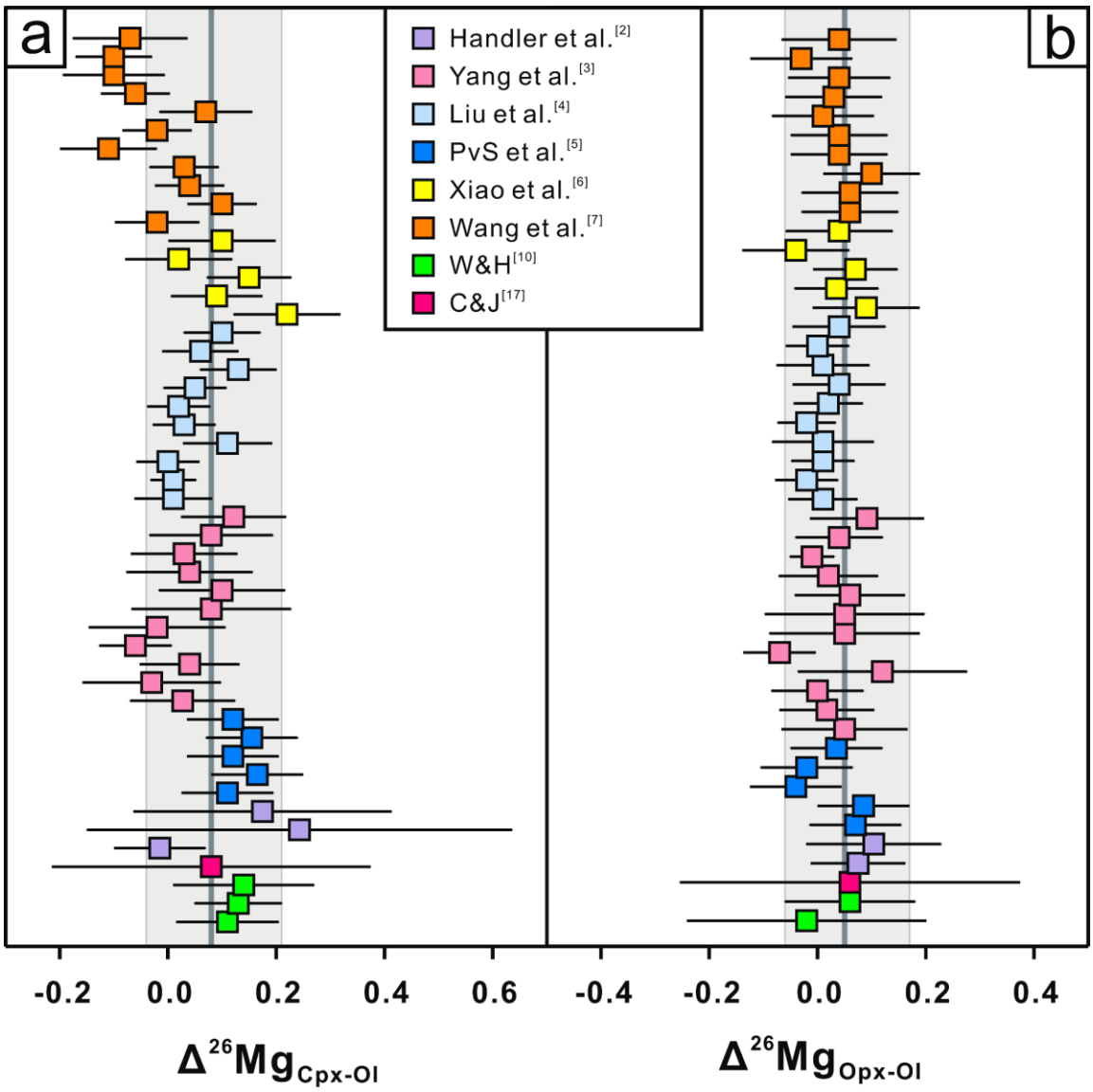

Figure 2-5. Compilation of inter-mineral Mg isotope fractionation of (a) Cpx-Ol and (b) Opx-Ol pairs in peridotite xenoliths. Data sources: Handler et al. (2009); Yang et al. (2009); Liu et al. (2011); Pogge von Strandmann (PvS) et al. (2011); Xiao et al. (2013); Wang et al. (2016); Wiechert and Halliday (W&H), (2007) and Chakrabarti and Jacobsen (C&J), (2010). The gray bars in (a) and (b) represent the calculated ranges of equilibrium inter-mineral fractionation of Cpx-Ol and Opx-Ol pairs, respectively, at temperatures between 800 and 1200°C. The theoretical fractionation factors used in the calculation are from Schauble (2011). The dark gray vertical lines in the center of the bars represent the fractionation factor at 1000°C in each case.

δ^{26}Mg range of −0.32‰ to −0.23‰ (Fig. 2-4a) (Liu et al., 2010; Yang et al., 2012; Sio et al., 2013; Wang et al., 2015, a,b, 2016), although these measurements were performed in two laboratories (UA and UW). Given the limited range of results from this study and from mantle olivine in general, the wide range of δ^{26}Mg values obtained from the same San Carlos olivine powder measured in different laboratories therefore suggests that analytical issues are responsible for the previous inconsistent measurements of San Carlos olivine.

3.4. Evaluating the influence of resin cleaning on Mg isotopic analysis

Both Teng and Yang (2014) and Chang et al. (2003) have noted that the cleaning procedure for ion-exchange resin can affect the accuracy of Mg isotopic measurements, as resin impurities may cause instability in instrumental fractionation. The acids used in the routine resin cleaning procedure in the Isotope Laboratory of University of Washington are prepared by sub-boiling distillation from single-distilled HCl (trace metal grade, matrix element concentration ≤1 ppb, Thermo Fisher Scientific) using a Savillex DST-1000 acid purification unit. We evaluated the influence of acid purity on resin performance by comparing the analytical results from resins cleaned with single-distilled HCl to those cleaned with double-distilled HCl. In addition, as ion-exchange resin may show deterioration in performance due to exposure to oxidizing HNO_3 during column chemistry, we also investigated the reusability of Bio-Rad AG50W-X8 resin for Mg isotopic analysis.

Separate batches of lherzolitic San Carlos olivine and Hawaiian seawater were processed through different types of resins – either new or used resins cleaned with either double-distilled or single-distilled HCl. The lherzolitic San Carlos olivine yielded δ^{26}Mg

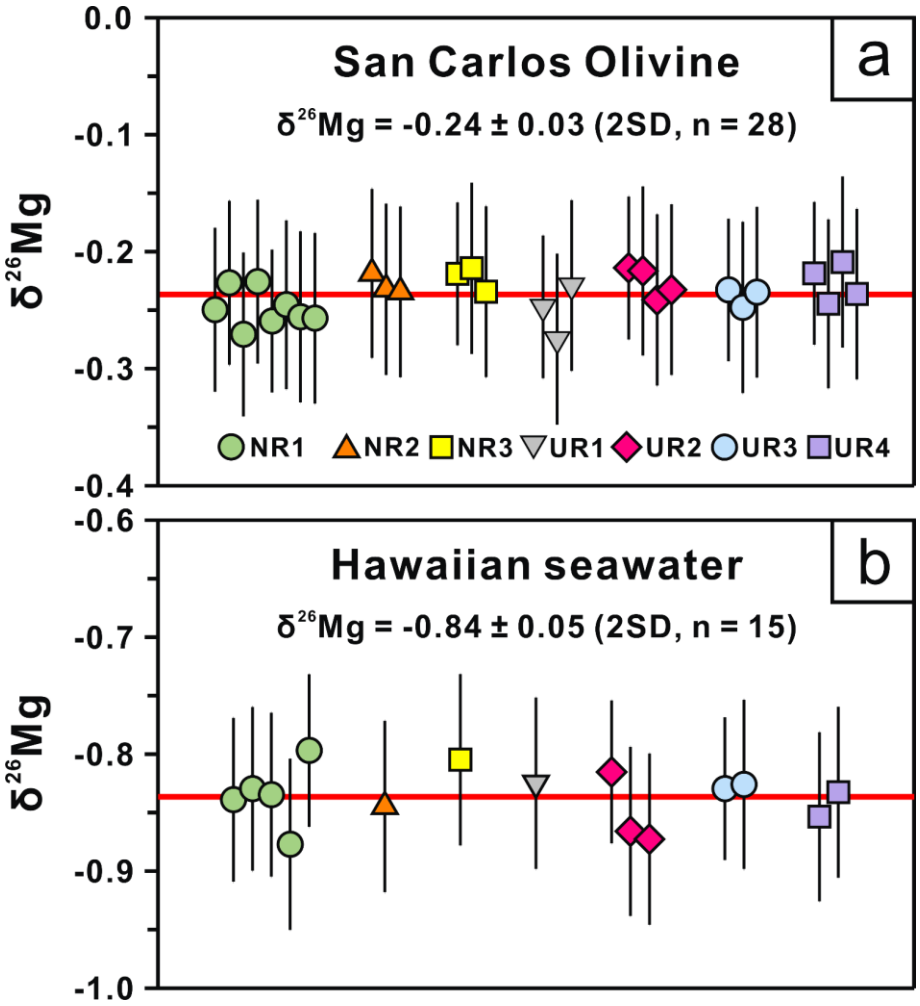

Figure 2-6. Magnesium isotopic compositions of (a) lherzolitic San Carlos olivine and (b) Hawaiian seawater processed through column chemistry using different types of resins. The resin codes are described in Table 2-4. The red horizontal line in each panel represent the average δ^{26}Mg value of all the measured data.

Table 2-3. Magnesium isotopic compositions of Hawaiian seawater and lherzolitic San Carlos olivine processed through resins cleaned in different ways.

Samples	δ^{26}Mg (‰)	2SD	δ^{25}Mg (‰)	2SD
Hawaiian Seawater				
SW-NR1	−0.84[a]	0.07	−0.42	0.05
chemistry duplicate	−0.83[a]	0.07	−0.44	0.06
chemistry duplicate	−0.83[a]	0.07	−0.42	0.05
chemistry duplicate	−0.88	0.07	−0.45	0.06
chemistry duplicate	−0.80	0.07	−0.41	0.06
average	***−0.83***	***0.05***	***−0.43***	***0.04***
SW-NR2	−0.84	0.07	−0.43	0.06
SW-NR3	−0.80	0.07	−0.42	0.06
SW-UR1	−0.82	0.07	−0.40	0.06
SW-UR2	−0.82	0.06	−0.41	0.05
repeat	−0.87	0.07	−0.44	0.06
repeat	−0.87	0.07	−0.43	0.06
average	***−0.85***	***0.04***	***−0.42***	***0.03***
SW-UR3	−0.83	0.06	−0.44	0.05
repeat	−0.83	0.07	−0.42	0.06
average	***−0.83***	***0.05***	***−0.43***	***0.04***
SW-UR4	−0.85	0.07	−0.44	0.06
repeat	−0.83	0.07	−0.43	0.06
average	***−0.84***	***0.05***	***−0.43***	***0.04***
Hawaiian Seawater average (n = 12)	**−0.84**	**0.05**	**−0.43**	**0.03**
Lherzolitic San Carlos Ol				
SC-NR1	−0.25[b]	0.07	−0.13	0.05
repeat	−0.23[b]	0.07	−0.12	0.05
repeat	−0.27[b]	0.07	−0.15	0.06
digestion replicate	−0.23[b]	0.07	−0.10	0.05
digestion duplicate	−0.26	0.06	−0.14	0.05
repeat	−0.25	0.07	−0.14	0.06
repeat	−0.26	0.07	−0.12	0.06
chemistry duplicate	−0.26	0.07	−0.14	0.06

average	***−0.25***	***0.03***	***−0.14***	***0.03***
SC-NR2	−0.22	0.07	−0.10	0.06
repeat	−0.23	0.07	−0.10	0.06
chemistry duplicate	−0.23	0.07	−0.10	0.06
average	***−0.23***	***0.04***	***−0.10***	***0.04***
SC-NR3	−0.22	0.06	−0.12	0.05
repeat	−0.21	0.07	−0.12	0.06
chemistry duplicate	−0.23	0.07	−0.14	0.06
average	***−0.22***	***0.04***	***−0.12***	***0.03***
SC-UR1	−0.25	0.06	−0.12	0.05
repeat	−0.27	0.07	−0.13	0.06
chemistry duplicate	−0.23	0.07	−0.12	0.06
average	***−0.25***	***0.04***	***−0.12***	***0.03***
SC-UR2	−0.21	0.06	−0.12	0.05
repeat	−0.22	0.07	−0.12	0.06
repeat	−0.24	0.07	−0.12	0.06
chemistry duplicate	−0.23	0.07	−0.11	0.06
average	***−0.22***	***0.03***	***−0.12***	***0.03***
SC-UR3	−0.23	0.06	−0.11	0.05
repeat	−0.25	0.07	−0.12	0.06
chemistry duplicate	−0.23	0.07	−0.12	0.06
average	***−0.24***	***0.04***	***−0.11***	***0.03***
SC-UR4	−0.22	0.06	−0.11	0.05
repeat	−0.24	0.07	−0.13	0.06
repeat	−0.21	0.07	−0.11	0.06
chemistry duplicate	−0.24	0.07	−0.12	0.06
average	***−0.23***	***0.03***	***−0.12***	***0.03***
Lherzolitic San Carlos Ol average (n = 24)	**−0.24**	**0.03**	**−0.12**	**0.02**

a: data from Table 2-1.

b: data from Table 2-2.

Digestion replicate indicates full chemical replicates, starting with sample dissolution through chemical separation and instrumental analysis.

Table 2-4. Resin codes and associated Mg blank values.

Resin type	Mg blank (ng)	Cleaning procedure
New resin (NR)		
NR1	3.6	New resin, 3 passes of double-distilled 6 N HCl, 1 pass of double-distilled 1 N HNO_3
NR2	3.4	New resin, 3 passes of single-distilled 6 N HCl, 2 passes of double-distilled 1 N HNO_3
NR3	3.7	New resin, 3 passes of single-distilled 6 N HCl, 1 pass of double-distilled 1 N HNO_3
Used resin (RR)		
UR1	3.7	Used resin, 3 passes of double-distilled 6 N HCl, 2 passes of double-distilled 1 N HNO_3
UR2	5.8	Used resin, 3 passes of double-distilled 6 N HCl, 1 pass of double-distilled 1 N HNO_3
UR3	4.2	Used resin, 3 passes of single-distilled 6 N HCl, 2 passes of double-distilled 1 N HNO_3
UR4	3.8	Used resin, 3 passes of single-distilled 6 N HCl, 1 pass of double-distilled 1 N HNO_3

values from −0.25‰ to −0.22‰, similar to the values of the other two batches of lherzolitic San Carlos olivine, while the Hawaiian seawater gave δ^{26}Mg values from −0.85‰ to −0.80‰ with an average of −0.84 ± 0.05‰ (n = 15), comparable with the recommended value of −0.843 ± 0.057‰ (Teng et al., 2015) (Fig. 2-6). In addition, purified Mg solutions collected from all types of resins had similar levels of Mg blanks (typically < 5 ng) that are negligible compared with the amounts of loaded Mg (≥10 μg) (Table 2-4). These results suggest that the Bio-Rad AG50W-X8 resin can be re-used for Mg separation and that single-distilled HCl can be used directly for resin cleaning without further purification. Therefore, previous differing measurements on San Carlos olivine must have been caused by other factors during chemical separation or instrumental analysis.

3.5. Previous inter-laboratory discrepancies on San Carlos olivine: sample heterogeneity vs. analytical artifacts

Among all the studies where San Carlos olivine was analyzed, Wiechert and Halliday (2007) and Chakrabarti and Jacobsen (2010) reported δ^{26}Mg values significantly different from those of other studies (Figs. 2-1b and 2-4a). However, the clinopyroxene–olivine and orthopyroxene–olivine pairs were in isotope equilibrium in both studies (Fig. 2-4b). In comparison, although the δ^{26}Mg data for San Carlos olivine and orthopyroxene reported by Young et al. (2009) fall within the mantle range, their clinopyroxene separates yielded much higher δ^{26}Mg values (Fig. 2-4a). These clinopyroxene separates had ~0.40‰ higher values than coexisting olivine grains, resulting in the only disequilibrium clinopyroxene–olivine pairs reported for San Carlos peridotites so far (Fig. 2-4b).

Young et al. (2009) ruled out the presence of spinel inclusions as the cause of these

isotopically heavy clinopyroxene grains as this would require an unrealistically high (~50%) contribution of Mg from spinel impurities. However, the calculated whole-rock $\delta^{26}Mg$ values agreed better with the measured values when using the clinopyroxene $\delta^{26}Mg$ values calculated from $\Delta^{26}Mg_{Cpx\text{-}Ol}$ than when using the measured clinopyroxene $\delta^{26}Mg$ values. Therefore, these abnormally high $\delta^{26}Mg$ values of clinopyroxene might be erroneous, as was pointed out by the authors. On the other hand, the low $\delta^{26}Mg$ value of −0.58‰ for San Carlos olivine reported by Pearson et al. (2006) may be related to analytical issues of the laser ablation (LA)-MC-ICP-MS method, such as the matrix effect associated with laser ablation (Norman et al., 2006a). The over 4‰ Mg isotopic variation in olivine grains from different peridotite xenoliths reported in their study has not been found in other LA-MC-ICP-MS studies (Norman et al., 2006, a,b; Xie et al., 2011) or solution aspiration MC-ICP-MS studies (Handler et al., 2009; Yang et al., 2009; Liu et al., 2011; Pogge von Strandmann et al., 2011; Xiao et al., 2013; Wang et al., 2016). As a result, previous inter-laboratory disparities are more likely to reflect systematic analytical artifacts in different laboratories, rather than Mg isotopic heterogeneity within the San Carlos olivine.

A variety of factors can result in analytical artifacts that are several times greater than the typically quoted precision (≤0.1‰ for $\delta^{26}Mg$ values). Among them, the levels of matrix removal and Mg recovery are of primary importance. The presence of matrix elements (e.g., Al, Fe, Ti, Mn, Ca, Na, K, Ni), even in trace amount for certain elements, has been shown to cause severe drift in Mg isotopic measurement (Galy et al., 2001; Huang et al., 2009; Wombacher et al., 2009; Teng et al., 2010a; An et al., 2014; Teng and Yang, 2014). For example, a Ca/Mg ratio of ~0.05 can cause a nearly +0.60‰ shift in $\delta^{26}Mg$ values (Galy et al., 2001; Wombacher et al., 2009) due to spectral interference of doubly

charged ^{48}Ca on ^{24}Mg (Teng and Yang, 2014). This may explain the anomalously high $\delta^{26}Mg$ values obtained by Young et al. (2009) as clinopyroxene hosts a considerable amount of CaO (~20 wt.%) compared with olivine and orthopyroxene (<1 wt.%). Consequently, only their clinopyroxene data are off the mantle range while olivine and orthopyroxene still have mantle-like $\delta^{26}Mg$ values (Fig. 4a). Significant Mg isotope fractionation can also occur during column chemistry since heavy Mg isotopes are preferentially released during cation-exchange chromatography (Chang et al., 2003; Teng et al., 2007). As a result, low Mg yield or shifting of the Mg peak due to sample overloading may cause laboratory-induced Mg isotope fractionation (Huang et al., 2009). During instrumental analysis, mismatch of Mg concentration and acid molarity between sample and standard may also lead to erroneous results (Huang et al., 2009; Teng and Yang, 2014). In addition, the $\delta^{26}Mg$ values of the bracketing standard solutions have been observed to drift to lower values during long-term storage; therefore, failing to use fresh bracketing standard solutions may cause sample $\delta^{26}Mg$ values to drift higher (Huang et al., 2009). In summary, previous inter-laboratory differences are probably due to diverse analytical issues unique to different laboratories instead of a single universal issue shared by all these laboratories. Although the definitive causes of previous inconsistent measurements on San Carlos olivine remain unclear, the majority of the data suggests that San Carlos olivine is homogeneous and is thus an acceptable Mg isotopic standard.

4. Conclusions

(1) The new data show Mg isotopic homogeneity and equilibrium between coexisting olivine, clinopyroxene, and orthopyroxene in a San Carlos harzburgite.

(2) Olivine grains from the San Carlos lherzolite have identical δ^{26}Mg values to those from the harzburgite, suggesting inter-xenolith Mg isotopic homogeneity regardless of the fertility of the host peridotites.

(3) This work, together with previous studies, indicates that Mg isotopes are homogeneously distributed in the San Carlos olivine. San Carlos olivine is thus a suitable standard for Mg isotopic analysis.

(4) Neither acid purity nor re-using the cation-exchange resin causes resolvable shift in Mg isotopic data. Therefore, previous inter-laboratory discrepancies are probably the result of analytical artifacts during chemical separation or instrumental analysis.

Acknowledgements. We would like to thank Elizabeth Anthony and Barbara Dutrow for providing the San Carlos peridotite xenoliths; Debra A. Wallace for her assistance with sample dissolution; and Yan Xiao, Ben-Xun Su and Shui-Jiong Wang for their help with mineral separation. The manuscript has greatly benefited from comments from Kwan-Nang Pang, Corliss Kin I Sio and an anonymous reviewer. This work was financially supported by the National Science Foundation (EAR-1340160 to F.-Z. Teng) and the University of Washington Mary Gates Research Scholarship (to M. Harrington).

Chapter 3. Metasomatism-induced mantle magnesium isotopic heterogeneity: Evidence from pyroxenites

This chapter is published as:

Hu, Y., Teng, F.-Z., Zhang, H.-F., Xiao, Y. and Su, B.-X. (2016) Matasomatism-induced mantle magnesium isotopic heterogeneity: Evidence from pyroxenites. Geochimica et Cosmochimica Acta, 185, 88-111.

Abstract

High-precision Mg isotopic measurements on diverse mantle pyroxenite xenoliths collected from Hannuoba, North China Craton, revealed multi-stage interactions between the lithospheric mantle and melts of different origins. The garnet-bearing pyroxenites yield variable δ^{26}Mg values from −0.48‰ to −0.10‰, consistent with their origin as reaction products between mantle peridotites and melts from subducted oceanic slab with highly heterogeneous δ^{26}Mg. Most of their constituent olivine, clinopyroxene, and orthopyroxene have indistinguishable δ^{26}Mg ratios around the normal mantle range (−0.25 ± 0.07‰, Teng et al., 2010a). The lack of fractionation among these three mineral phases agrees with their similar bonding environments for Mg (6-fold), and hence indicates a general isotopic equilibrium among them. By contrast, garnet has variably lighter δ^{26}Mg values (−0.75‰ to −0.37‰, n = 15), consistent with its higher coordination number for Mg (8-fold), and thus weaker Mg-O bonds. The magnitude of fractionation between garnet and olivine/pyroxene, however, is not correlated with equilibrium temperature, and therefore reflects disequilibrium Mg isotope partitioning. Considering the metasomatic origin of

these garnets, the disequilibrium isotopic fractionation is most likely the result of rapid and incomplete metasomatic reaction during which garnets were formed at the expense of isotopically heavier co-existing minerals, particularly spinels. The two garnet-free clinopyroxenites, which display highly enriched light rare earth element (LREE) patterns and very low Ti/Eu ratios, are characterized by extremely light δ^{26}Mg (as low as −1.51‰). Their formation possibly indicates an episode of carbonatite infiltration. In comparison, the three Cr websterites and one Al websterite, as well as an orthopyroxenite, all have mantle-like wholerock and mineral δ^{26}Mg ratios, with equilibrated clinopyroxene–orthopyroxene pairs. Their presence thus implies different episodes of asthenosphere-derived silicate melt injection into the mantle. Collectively, these observations suggest that mantle metasomatism plays an important role in producing inter-mineral Mg isotopic disequilibrium and local Mg isotopic variation in the lithospheric mantle. Therefore, Mg isotopes can be used to trace metasomatic activities in the mantle.

1. Introduction

Magnesium (Mg) is a major rock-forming element with three stable isotopes (mass 24, 25, and 26). The fractionation of Mg isotopes during partial melting and magma differentiation is limited in the mantle ($\leq$ 0.07‰ for δ^{26}Mg, Teng et al., 2007, 2010a). By contrast, over 7‰ fractionation in δ^{26}Mg has been found at Earth's surface through continental weathering and carbonate precipitation (Wombacher et al., 2011; Liu et al., 2014). The highly variable δ^{26}Mg values found in crustal materials compared with the uniform δ^{26}Mg ratios characterizing mantle-related rocks and minerals thus highlights the potential of using Mg isotopes to trace crustal recycling (e.g., Yang et al., 2012).

A well-constrained mantle δ^{26}Mg value is a prerequisite for resolving crustal signal unambiguously from that of the mantle. Previous analyses on lherzolite-harzburgite-dunite series peridotites worldwide yielded largely consistent δ^{26}Mg values, and hence suggest a homogeneous mantle (δ^{26}Mg = −0.25 ± 0.07‰, Handler et al., 2009; Yang et al., 2009; Bourdon et al., 2010; Teng et al., 2010a; Huang et al., 2011; Liu et al., 2011). However, more recent studies on strongly metasomatized peridotites, particularly wehrlites, found δ^{26}Mg values deviated from the mantle range (Yang et al., 2009; Pogge von Strandmann et al., 2011; Xiao et al., 2013) with evidence for disequilibrium intermineral fractionation (Young et al., 2009; Xiao et al., 2013). Meanwhile, continental basalts are also frequently found to be distinctively depleted in heavy Mg isotopes (Yang et al., 2012; Huang et al., 2015) when compared to the homogeneous oceanic basalts with mantle-like δ^{26}Mg (Bourdon et al., 2010; Teng et al., 2010a). With the general recognition of a compositionally heterogeneous mantle where magmatic refertilization is widespread (Kelemen et al., 1998), it thus needs further investigation on the scale, distribution, and extent of Mg isotopic heterogeneity caused by open-system isotopic exchanges between mantle rocks and migrating metasomatic melts.

Pyroxenites that form veins cross-cutting the mantle are more direct samples than metasomatized peridotites for this purpose as their occurrence marks zones of higher melt/rock ratios in the mantle (Garrido and Bodinier, 1999). They have been variously interpreted as high-pressure cumulates from migrating asthenosphere-derived magmas (Frey, 1980; Irving, 1980), reaction products of metasomatic melts with mantle peridotite wall rocks (Garrido and Bodinier, 1999; Liu et al., 2005), in-situ melts of the host peridotites (Chen et al., 2001), or remnants of subducted oceanic crust (Alle`gre and

Turcotte, 1986) (see Downes, 2007 for a review). Due to their more fusible nature than the ambient peridotites (Anderson, 2005), pyroxenites have been regarded as an important lithologic heterogeneity in the mantle, and are often invoked to explain the chemical and isotopic variations observed in oceanic and continental basalts (e.g., Sobolev et al., 2005, 2007). Yet, whether their presence will also cause Mg isotopic heterogeneity in the mantle and related volcanic rocks is still unknown, due to the lack of Mg isotopic data on mantle pyroxenites.

Here, we present the first systematic Mg isotopic analyses on a variety of mantle pyroxenite xenoliths, along with major and trace element data for the whole rocks and constituent minerals. The xenoliths were collected from the Hannuoba basaltic plateau (27-14 Ma, Zhu, 1998) distributed along the north margin of the North China Craton (NCC), where the entire section of the ancient lithospheric mantle has been modified by intense and multi-stage melt-rock interactions (Tang et al., 2008). These xenoliths were taken as physical evidence for different episodes of melt injection events (Chen et al., 2001; Xu, 2002; Fan et al., 2005; Liu et al., 2005, 2010c). Therefore, they are ideal samples for studying the influence of mantle metasomatism on generating Mg isotopic variation in the mantle. The variable Mg isotopic composition of the pyroxenites and their disequilibrium inter-mineral fractionations indicate a heterogeneous distribution of Mg isotopes in the mantle induced by mantle metasomatism.

2. Sample petrology

Twenty-five pyroxenite xenoliths and two lherzolite xenoliths were selected for Mg isotopic measurements to cover the wide range of texture and modal/compositional

mineralogy of a larger sample collection. They are generally very large and fresh (Fig. 3-1A), and can be broadly divided into garnet-bearing and garnet-free groups. The garnet-bearing group contains two lherzolites, 15 websterites and three clinopyroxenites, in order of increasingly darker appearance. Some garnet pyroxenites form veins infiltrating the host spinel lherzolites, while other discrete samples (without peridotite hosts) with a similar mineralogy could be fragments from wider garnet pyroxenite veins. These xenoliths consist mainly of olivine, garnet, clinopyroxene, and orthopyroxene, with accessory spinel (Fig. 3-1B; Table S1). The most prominent petrographic features of these xenoliths are the secondary nature of the constituent garnet and its close association with spinel. Garnets commonly form rims on spinels, giving rise to the typical spinel-cored garnets (Fig. 3-1C). The observation that garnet progressively replaces spinel suggests that garnet was formed at a later stage, at the expense of spinel (Fig. 3-1D–G). Notably, the relic spinel cores display embayed and amoeboidal grain boundaries (Fig. 3-1C), suggesting that garnets have grown in the presence of melts (Keshav et al., 2007). Garnets also formed from the triple-junctions of co-existing minerals and gradually occupy their grain boundaries, as well as engulf adjacent olivine or pyroxene grains (Fig. 3-1H–J), until growing into noticeably large grains that are much coarser than other co-existing mineral phases and garnets commonly seen in garnet peridotites (Fig. 3-1G). Moreover, different garnet grains are often connected to each other, forming veins in the olivine-pyroxene matrix, and showing elongation along the vein direction (Fig. 3-1A).

While garnet is usually in reacting relationship to olivine and pyroxene, olivine and pyroxene grains frequently show triple-junction contact, implying textural equilibrium (Fig.

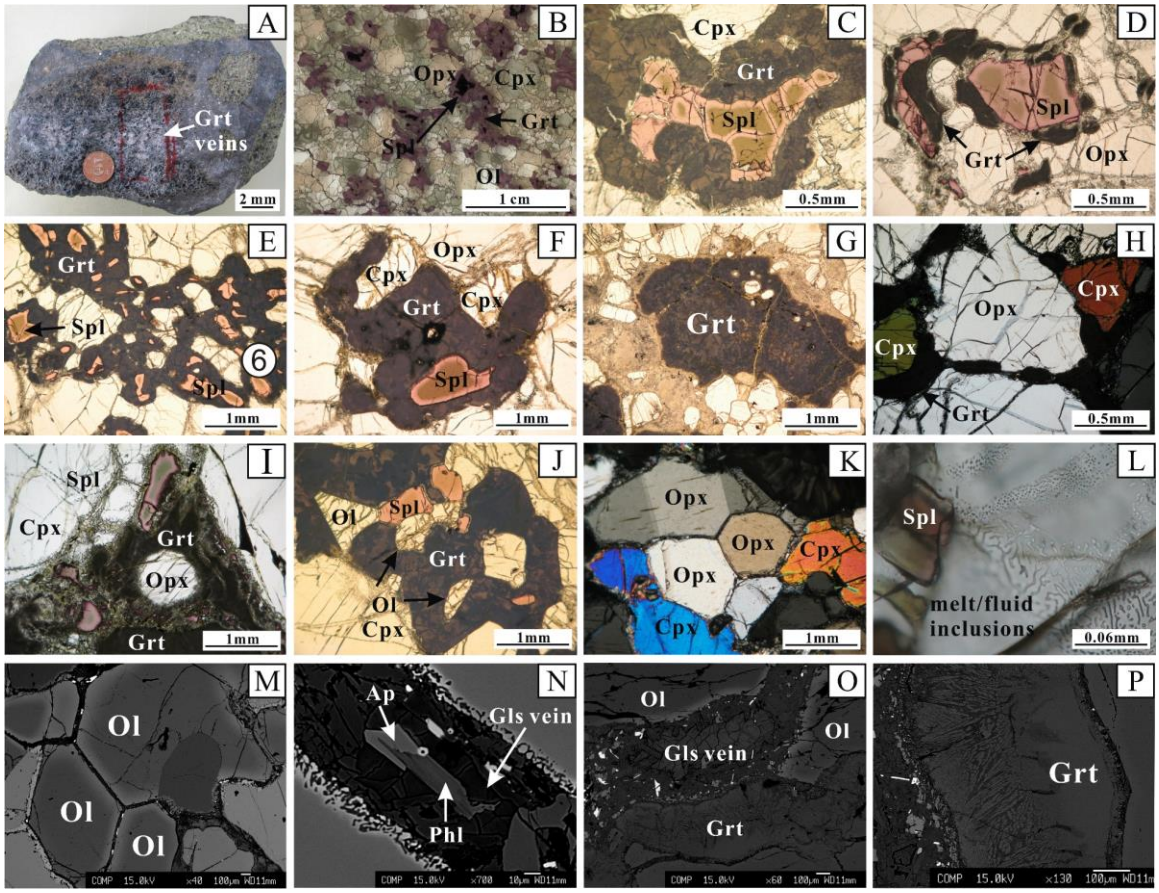

Figure 3-1. Petrological and petrographic characteristics of Hannuoba garnet-bearing xenoliths. (A) A hand specimen of garnet websterite with garnet-rich veins. (B) A scanned thin section image of a garnet websterite showing the typical mineral assemblage of Ol–Cpx–Opx–Grt–Spl. (C) A photomicrograph of a typical spinel-cored garnet. (D)–(G) Photomicrographs showing progressive replacement of spinel by garnet. (H)–(J) Photomicrographs showing garnet engulfs and consumes pyroxene and olivine grains. (K) A photomicrograph showing the triple junction and kink bands in Opx. (L) A photomicrograph showing the fluid/melt inclusions in pyroxene. (M) A back-scattered electron (BSE) image showing texturally equilibrated but compositionally zoned olivine grains. (N) A BSE image showing the rare metasomatic Ap and Phl in a glass vein. (O) A BSE image showing a glass vein in the xenolith, with chemically zoned olivine. (P) A close-up of (O) to show the intergrowth texture of kelyphitic garnet. All the garnets in our sample collection have been decomposed to kelyphites. Ol = olivine; Cpx = clinopyroxene; Opx = orthopyroxene; Grt = garnet; Spl = spinel; Ap = apatite; Phl = phlogopite; Gls = glass.

3-1K and M). Olivines are typically subhedral granular or elongated under deformation. Some olivine grains also occur as anhedral relic phase in garnets or as elongated crystals that gradually taper out between garnets and pyroxenes, suggesting their possible role as a reactant in the garnet-forming reaction. Pyroxenes are generally the dominant phase and occur as large tabular or polygonal grains (Fig. 3-1H and K). Both olivine and orthopyroxene are often strained and exhibit multiple kink bands (Fig. 3-1K). Undulatory extinction is occasionally observed in orthopyroxene as well. These deformation features are consistent with plastic deformation at high temperature and suggestive of a non-cumulative origin for these xenoliths (Ionov et al., 2005). Trapped melt/fluid inclusions are commonly found in pyroxenes (Fig. 3-1L) and some clinopyroxene grains have sieved rims with irregular glass films. In addition to these common mineral phases, glass veins with sparse and tiny metasomatic phlogopite and apatite are observed (Fig. 3-1N).

The garnet-free group includes three green Cr websterites (ranging from clinopyroxene-rich to orthopyroxene-rich in composition), one dark Al websterite, two grayish green Cr clinopyroxenites, and one dark brown orthopyroxenite. Following the classification proposed by Wilshire and Shervais (1975), the Cr websterites are characterized by the presence of emerald green Cr-diopside, while diopsides in the Al websterite are more enriched in Al. The two types of pyroxenes have a similar grain size in two of the Cr websterites while clinopyroxene is much smaller and less abundant in the orthopyroxene-rich Cr websterite and in the orthopyroxenite.

In addition to these xenoliths, two Hannuoba basalts were also analyzed to help identify the presence of subducted crustal material in the Hannuoba mantle, as eastern China basalts that carrying a light $\delta^{26}Mg$ signal were generally thought to have had their

mantle source been modified by carbonatitic melts released from subducted oceanic crust (Yang et al., 2012; Huang et al., 2015). On the other hand, although metamorphosed oceanic crust (i.e., eclogites) have shown highly heterogeneous, and generally light, Mg isotopic composition (Wang et al., 2012), it still needs to be tested to what extent carbonatite metasomatism can shift the Mg isotopic composition of mantle rocks, as previous measurements on carbonate-metasomatized peridotites did not show noticeable deviation from mantle values (Handler et al., 2009; Teng et al., 2010a). Due to the lack of strongly carbonatite-metasomatized sample in our sample collection from Hannuoba, a carbonatite-metasomatized garnet lherzolite from western Qinling, China, was analyzed. It has carbonatite-like trace element patterns and Sr-Pb isotopic composition, and displays positive Sr and Ba anomalies, attesting to the influence of carbonatite metasomatism, while their high Nb and Ta concentrations suggest the influence of subducted components (Su et al., 2012b).

3. Methods for Mg isotopic analysis

Chemical separation of Mg and subsequent isotopic analysis were performed at the University of Arkansas, Fayetteville, following the method developed in Teng et al. (2007). All chemical procedures were performed in a metal-free clean laboratory. Pre-cleaned Savillex Teflon screw-top beakers were used exclusively during chemical separation and instrumental analysis.

The whole-rock powders used for major and trace elemental analyses were used here for Mg isotopic measurements. In addition, optically clean mineral fragments were handpicked under a binocular microscope to >99% purity and triple cleaned with Milli-Q

water in an ultra-sonic bath (≥ 10 min per wash). The mineral and whole-rock samples were attacked sequentially with Optima-grade concentrated HF–HNO_3, HNO_3–HCl, and HNO_3, following the method detailed in Yang et al. (2009). An ultrasonic bath was used to accelerate dissolution by disrupting sample size and hence increasing the solid-acid interface. All samples were finally taken up in 1 N HNO_3 and loaded onto pre-cleaned Bio-Rad cation-exchange resin (AG50W-X8, 200-400 mesh). Matrix elements were eluted away in the first 16 mL of 1 N HNO_3, and Mg was collected in the following 19 mL of the same acid. This purification procedure was repeated twice to ensure maximum elimination of the matrix. The total procedural blank was <10 ng, representing <0.1% of Mg loaded onto the columns (Teng et al., 2010a).

Magnesium isotopic ratios were measured on a Nu Plasma MC-ICPMS. Sample solutions were introduced into the ion source with ‘‘wet” plasma condition, which has been demonstrated to be more resistant to matrix effects and concentration mismatch than the ‘‘dry” plasma introduction for Mg isotopic analysis (Teng and Yang, 2014). Matching in acid molarity and Mg concentration among all analyzed solutions are crucial for accurate Mg isotopic analyses (Teng and Yang, 2014). Therefore, all the sample and standard solutions were prepared at the day of measurement using the same batch of 3% Optima-grade HNO_3. Also, the standard solutions were prepared in the same number, container type, and liquid volume to those of sample solutions, to minimize the effect of evaporation during a batch run. The intensity matching between samples and standards were kept within 95% to avoid instrumental bias in Mg isotopic measurement (Teng and Yang, 2014). At a typical Mg concentration of 300 ppb, ^{24}Mg background is negligible ($<10^{-4}$ V) compared to sample signals (3-4 V). The instrumental fractionation was corrected by sample-standard

bracketing technique assuming a linear mass fractionation drift during a batch run. All Mg isotope data are reported in delta (d) notation on DSM-3 scale (Galy et al., 2003). The δ^{X}Mg values reported represent parts per thousand (‰) deviations of a ratio relative to the average of the two standard ratios measured before and after:

$$\delta^{x}\text{Mg (‰)} = \left\{ \frac{\left({}^{x}\text{Mg}/{}^{24}\text{Mg} \right)_{\text{sample}}}{\left({}^{x}\text{Mg}/{}^{24}\text{Mg} \right)_{\text{DSM3}}} - 1 \right\} \times 1000$$

where X refers to mass 25 or 26.

The accuracy of Mg isotopic analysis was assessed in two ways. First, five international rock standards (DTS-1, PCC-1, BHVO, MAG-1, and Murchison meteorite) were processed through the same procedure as all the unknown samples. They yielded δ^{26}Mg values comparable to previously published data (Table 3-1), and thus provide warranty for our entire analytical procedure, including sample digestion, chemical separation, and mass spectrometry. Then, two in-house standards (e.g., Kilbourne Hole olivine and Hawaiian seawater) were processed through column chemistry and analyzed along with unknown samples during each batch run. The results of these in-house standards also agree with literature values (Table 3-1).

The analytical reproducibility is also critical, particularly in that some data obtained in this study deviate significantly from previously published values for the same type of minerals or rocks, and there is no literature reference for mantle pyroxenites and pyroxenitic garnets. Analytical results from repeat analyses of the same sample, from dissolution or column chromatography to isotopic measurement, were reproduced within ±0.05‰ (2SD) for δ^{26}Mg (Table 3-2). Therefore, the reproducibility during the analytical period of this study is consistent with the conservative long-term (four-year) external

Table 3-1. Magnesium isotopic compositions (‰) of standards analyzed during the course of this study, and comparison with literature data

Standard	Description	n	δ^{26}Mg	2SD	δ^{25}Mg	2SD
Hawaii Seawater (in-house)	HI		−0.92	0.07	−0.48	0.05
			−0.84	0.07	−0.45	0.05
			−0.89	0.07	−0.48	0.06
			−0.79	0.06	−0.40	0.06
			−0.82	0.06	−0.41	0.05
			−0.83	0.06	−0.43	0.05
			−0.83	0.06	−0.40	0.04
			−0.85	0.07	−0.44	0.07
			−0.83	0.08	−0.42	0.07
			−0.87	0.07	−0.44	0.07
			−0.82	0.07	−0.44	0.05
			−0.84	0.07	−0.44	0.05
			−0.84	0.06	−0.43	0.06
Average	**This study**	**13**	**−0.84**	**0.07**	**−0.43**	**0.05**
	Ling et al. (2011)	90	−0.83	0.09	−0.43	0.06
	Higgins & Schrag (2010)	20	−0.79	0.18	-	-
	Foster et al. (2010)	26	−0.82	0.06	−0.43	0.04
	Hippler et al. (2009)	10	−0.80	0.05	−0.42	0.02
	Bolou-Bi et al. (2012)	14	−0.89	0.10	−0.47	0.08
KH Olivine (in-house)	Kilbourne Hole, NM		−0.25	0.08	−0.13	0.06
			−0.26	0.06	−0.13	0.04
			−0.26	0.05	−0.17	0.05
			−0.25	0.06	−0.11	0.05
			−0.23	0.07	−0.15	0.05
			−0.27	0.06	−0.15	0.06
			−0.28	0.06	−0.14	0.06
			−0.25	0.08	−0.09	0.07
			−0.25	0.05	−0.10	0.04
			−0.25	0.05	−0.13	0.04
			−0.29	0.07	−0.12	0.06
			−0.29	0.06	−0.14	0.05

Standard	Description	n	δ^{26}Mg	2SD	δ^{25}Mg	2SD
KH Olivine (in-house)	Kilbourne Hole, NM		−0.29	0.07	−0.18	0.06
			−0.30	0.08	−0.15	0.07
			−0.29	0.07	−0.13	0.05
			−0.22	0.07	−0.13	0.04
Average	**This study**	**16**	**−0.27**	**0.05**	**−0.14**	**0.05**
	Teng et al. (2010)	16	−0.27	0.07	−0.14	0.04
	Teng et al. (2007)	24	−0.31	0.09	−0.14	0.08
DTS-1 (USGS)	Dunite, Twin Sisters mountain, WA		−0.31	0.08	−0.14	0.07
			−0.30	0.06	−0.15	0.06
Average	**This study**	**2**	**−0.30**	**0.05**	**−0.14**	**0.04**
Recommended			***−0.30***	***0.03***	***−0.13***	***0.03***
PCC-1 (USGS)	Peridotite, Cazadero, CA		−0.20	0.07	−0.10	0.05
Recommended			***−0.23***	***0.04***	***−0.10***	***0.03***
BHVO (USGS)	Basalt, Hawaiian Volcanic Observatory		−0.22	0.06	−0.14	0.05
			−0.20	0.07	−0.08	0.03
Average	**This study**	**2**	**−0.21**	**0.05**	**−0.10**	**0.38**
Recommended			***−0.21***	***0.04***	***−0.12***	***0.03***
W-1 (USGS)	Diabase, Centreville, VA		−0.15	0.06	−0.08	0.05
Recommended			***−0.16***	***0.03***	***−0.08***	***0.02***
MAG-1 (USGS)	Marine mud, Gulf of Maine		−0.24	0.06	−0.07	0.06
Recommended			***−0.25***	***0.05***	***−0.11***	***0.04***
Murchison chondrite	Carbonaceous (CM2), VIC, Australia		−0.29	0.06	−0.14	0.06
			−0.28	0.07	−0.15	0.05
Average	**This study**	**2**	**−0.29**	**0.04**	**−0.15**	**0.04**
	Pogge von Strandmann et al. (2011)	1	−0.23	0.02	−0.13	0.01
	Teng et al. (2010)	4	−0.31	0.07	−0.17	0.03
	Teng et al. (2007)	4	−0.41	0.05	−0.21	0.05
	Yang et al. (2009)	4	−0.31	0.06	−0.17	0.06
	Wiechert & Halliday (2007)	13	−0.26	0.25	−0.14	0.14
	Wombacher et al. (2009)	17	−0.26	0.09	−0.13	0.07
	Bourdon et al. (2010)	2	−0.19	0.08	−0.11	0.02

n indicates number of analyses. Recommended values are from Teng et al. (2015).

Table 3-2. Reproducibility check of Mg isotopic measurements (‰) relative to standard DSM3

Sample	Ol				Sample	Cpx			
	δ^{26}Mg	2SD	δ^{25}Mg	2SD		δ^{26}Mg	2SD	δ^{25}Mg	2SD
D 01	0.06	0.06	0.04	0.04	D 06	0.02	0.05	−0.01	0.04
D 01 rc	0.04	0.07	0.02	0.07	D 06 rc	0.00	0.07	0.00	0.06
Average	**0.05**	**0.05**	**0.03**	**0.03**	**Average**	**0.02**	**0.04**	**−0.01**	**0.03**
D 06	−0.03	0.08	−0.02	0.06	D 07	−0.12	0.05	−0.07	0.04
D 06 rd	0.01	0.06	0.01	0.04	D 07 rc	−0.09	0.07	−0.06	0.06
Average	**0.00**	**0.05**	**0.00**	**0.03**	**Average**	**−0.11**	**0.04**	**−0.06**	**0.03**
D 09	−0.01	0.07	0.00	0.05	D 09	−0.11	0.05	−0.06	0.04
D 09 rd	0.01	0.06	0.04	0.04	D 09 rd	−0.12	0.07	−0.08	0.06
Average	**0.00**	**0.05**	**0.03**	**0.03**	**Average**	**−0.11**	**0.04**	**−0.07**	**0.03**
D 22	−0.29	0.07	−0.14	0.07	D 7S	−0.45	0.05	−0.20	0.04
D 22 rr	−0.28	0.06	−0.13	0.06	D 7S rc	−0.47	0.07	−0.24	0.06
D 22 rc	−0.26	0.07	−0.14	0.03	**Average**	**−0.46**	**0.04**	**−0.21**	**0.03**
Average	**−0.28**	**0.04**	**−0.13**	**0.03**	D 2S	−0.11	0.07	−0.08	0.06
D 7S	−0.39	0.06	−0.19	0.04	D 2S rr	−0.11	0.06	−0.05	0.06
D 7S rc	−0.41	0.07	−0.23	0.07	D 2S rc1	−0.14	0.06	−0.07	0.06
Average	**−0.40**	**0.05**	**−0.20**	**0.03**	D 2S rc2	−0.11	0.07	−0.04	0.03
D 2S	−0.12	0.07	−0.08	0.05	**Average**	**−0.12**	**0.03**	**−0.05**	**0.02**
D 2S rc	−0.16	0.07	−0.09	0.07					
Average	**−0.14**	**0.05**	**−0.08**	**0.04**					

Sample	Grt				Sample	Opx			
	δ^{26}Mg	2SD	δ^{25}Mg	2SD		δ^{26}Mg	2SD	δ^{25}Mg	2SD
D 6S	−0.53	0.05	−0.23	0.05	D 06	−0.02	0.06	0.01	0.05
D 6S rr	−0.53	0.07	−0.28	0.03	D 06 rc	0.01	0.07	0.00	0.06
D 6S rc	−0.49	0.07	−0.27	0.03	**Average**	**−0.01**	**0.05**	**0.00**	**0.04**
Average	**−0.52**	**0.03**	**−0.27**	**0.02**	D 07	−0.09	0.06	−0.04	0.05
D 01	−0.74	0.07	−0.38	0.05	D 07 rc	−0.10	0.07	−0.04	0.05
D 01 rr	−0.76	0.08	−0.40	0.06	**Average**	**−0.10**	**0.05**	**−0.04**	**0.03**
Average	**−0.75**	**0.05**	**−0.39**	**0.04**	D 09	0.00	0.06	0.04	0.04
D 06	−0.39	0.08	−0.18	0.07	D 09 rd	0.00	0.07	0.00	0.05
D 06 rr	−0.38	0.06	−0.19	0.06	**Average**	**0.00**	**0.04**	**0.02**	**0.03**
D 06 rc1	−0.36	0.06	−0.20	0.05	D 7S	−0.37	0.06	−0.17	0.05
D 06 rc1rr	−0.34	0.06	−0.18	0.06	D 7S rc	−0.38	0.07	−0.19	0.05
D 06 rc2	−0.37	0.06	−0.20	0.06	**Average**	**−0.37**	**0.05**	**−0.18**	**0.03**
Average	**−0.37**	**0.03**	**−0.19**	**0.03**					
D 07	−0.47	0.05	−0.27	0.05					
D 07 rc	−0.51	0.06	−0.25	0.05					
Average	**−0.48**	**0.04**	**−0.26**	**0.04**					
D 4S	−0.48	0.08	−0.22	0.07					
D 4S rc	−0.50	0.07	−0.26	0.07					
D 4S rcrr	−0.45	0.07	−0.23	0.05					
Average	**−0.47**	**0.04**	**−0.23**	**0.04**					
D 3S	−0.72	0.06	−0.37	0.06					
D 3S rc1	−0.75	0.07	−0.37	0.07					
D 3S rc1rr	−0.72	0.07	−0.38	0.05					
D 3S rc2	−0.75	0.07	−0.40	0.03					
Average	**−0.73**	**0.03**	**−0.39**	**0.02**					

Sample	Whole rock			
	δ^{26}Mg	2SD	δ^{25}Mg	2SD
D 06	−0.10	0.07	−0.05	0.05
D 06 rc	−0.10	0.07	−0.05	0.05
Average	**−0.10**	**0.05**	**−0.05**	**0.03**
D 3S	−0.48	0.07	−0.24	0.07
D 3S rr	−0.50	0.06	−0.26	0.06
D 3S rc1	−0.48	0.06	−0.23	0.06
D 3S rc2	−0.48	0.07	−0.27	0.03
Average	**−0.48**	**0.03**	**−0.25**	**0.02**

rr = repeat instrumental analysis on the same Mg-cut solutions;
rc = repeat column chemistry from another aliquot of dissolved sample solutions;
rd = full chemical replicates, including sample dissolution, column chemistry and instrumental analysis.
The weighted averages are calculated based on inverse-variance weighted model using Isoplot 3.75-4.15.

precision for Mg isotopic data reported from this laboratory (< ±0.07‰ for δ^{26}Mg, Teng et al., 2015).

4. Results

4.1. Whole-rock major and trace element compositions

Major and trace element data for the bulk Hannuoba xenoliths are reported in Tables 3-S2 and 3-S3, respectively. Their average mineral compositions are presented in Tables 3-S4-S8. The temperature and pressure estimates based on different geothermobarometers are provided in Table 3-3. Relevant analytical methods are provided in the Supplementary Materials.

The Hannuoba pyroxenites and garnet-bearing lherzolites display much wider compositional variations compared with spinel-facies peridotites and wehrlites (Fig. 3-2), reflecting their more varied mineralogy (Fig. 3-2C). While they are more enriched in fusible components than peridotites by having higher Al_2O_3 (5.41–14.4 wt.%) and CaO (1.35–21.6 wt.%) (Fig. 3-2A and B), their Mg# and Ni contents are much higher than those of basalts (Fig. 3-2D). In particular, the garnet-bearing group extends from that close to the peridotite field to Si- and Al-rich field approaching the Jiaohe pyroxenites (Fig. 3-2C), which were interpreted as remnants of subducted oceanic crust (Yu et al., 2010). The two Hannuoba basalts analyzed here fall within the range of published basalt data (Fig. 3-2). One of them belongs to the tholeiitic group while the other with slightly higher alkali content and lower SiO_2 belongs to the alkali group based on the TAS diagram (Total Alkalis vs. SiO_2, Le Bas et al., 1986, not shown).

Most of the xenoliths have higher rare earth element (REE) contents than the spinel

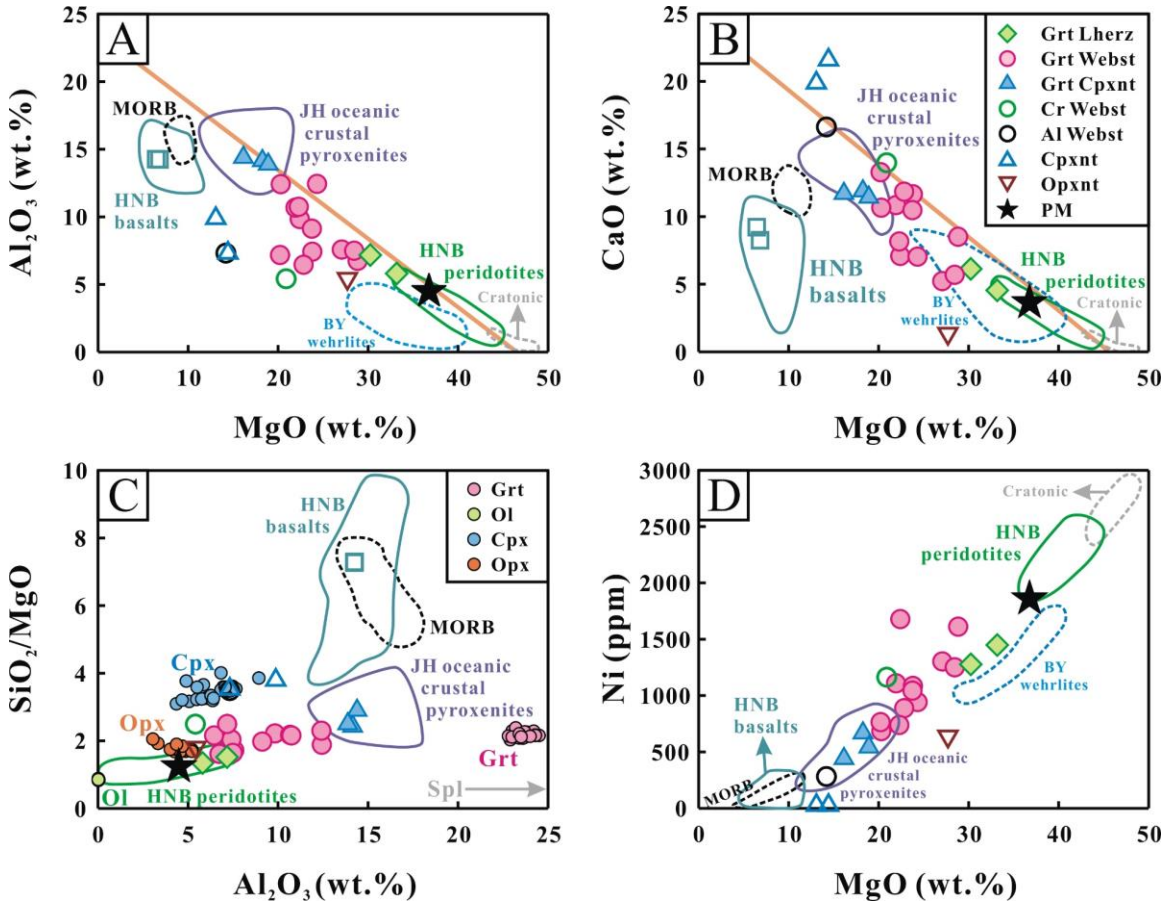

Figure 3-2. Major (A–C) and trace (D) element variations of Hannuoba (HNB) mantle xenoliths studied here in relation to their MgO (wt.%). Data for Hannuoba peridotites (Song and Frey, 1989; Chen et al., 2001; Rudnick et al., 2004; Fan et al., 2005; Choi et al., 2008) and Beiyan (BY) wehrlites (Xiao and Zhang, 2011; Xiao et al., 2013) are plotted for comparison. The star denotes the composition of primitive mantle from McDonough and Sun (1995). The gray dash lines represent the compositional fields of typical cratonic peridotites defined by Tanzanian xenoliths (Lee and Rudnick, 1999). The orange solid lines represent extension between the residual Hannuoba peridotites and calculated equilibrium melts taken from Xu (2002). The data for Jiaohe (JH) oceanic crustal pyroxenites field are from Yu et al. (2010). The data for Hannuoba basalts are from Zhi et al. (1990), Basu et al. (1991), Fan and Hooper (1991), Liu et al. (1994), Qian et al. (2015) and this study (open square). The fields of mid-ocean ridge basalt (MORB) in (A) and (B) are from Downes (2007) with data from Melson et al. (1976), Schilling et al. (1983), Korenaga and Kelemen (2000), in (C) is from Bodinier and Godard (2014) with data from the PetDB database, and in (D) is from Yu et al. (2010) with data from Jacob (2004). Major element data are from Table 3-S2. Mineral compositional data for Ol, Cpx, Opx, Grt in (C) are from Tables 3-S4–S8. Lherz = lherzolite, Webst = websterite, Cpxnt = clinopyroxenite, Opxnt = orthopyroxenite.

peridotite residuals reported in the literature, except the orthopyroxenite that falls within the spinel peridotite field (Fig. 3-3A and C). The REE patterns of garnet-bearing lherzolites and pyroxenites are characterized by flat heavy REE and variable light REE (LREE), ranging from LREE-enriched to LREE-depleted to others having flat patterns. The two garnet-bearing lherzolites and a Cr websterite display U-shaped REE patterns (Fig. 3-3A and C) that are also typical for spinel lherzolites (e.g. Rudnick et al., 2004), which is generally interpreted as the result of re-introduction of highly incompatible elements by metasomatic melts after partial melting (Coltorti, 2008). These garnet-bearing xenoliths are also distinctive in their enrichment in fluid-mobile large ion lithophile element (LILE) with significant peaks at Pb (0.2–0.9 ppm) and Sr (41–368 ppm) in the primitive mantle-normalized trace element diagrams, while no obvious Eu anomaly is presented (Fig. 3-3B and D). The two garnet-free Cr clinopyroxenites contain the highest ΣREE (65.2 and 105 ppm) among all the samples and show convex-upwards REE patterns (Fig. 3-3C), which is commonly observed for cumulative pyroxenites (Frey and Prinz, 1978). The Al websterite exhibits a similar REE pattern with the apex shifts from Ce to Nd (Fig. 3-3C).

4.2. Mineral chemistry

Except spinel, all the other constituent minerals exhibit a compositional affinity to non-cratonic peridotites, and are significantly different from those of pyroxenite cumulates worldwide (Fig. 3-4A and B). In addition, only olivine in the garnet-bearing xenoliths displays clear compositional zoning (Fig. 3-1M), with a Mg-rich core (Mg# = 86.3–91.0) and a Fe-rich rim (Mg# = 82.1–90.8). Up to 500 μm wide zoning has been observed in BSE images, and the intra-grain differences in Mg# can be as large as 6.5, attesting to the

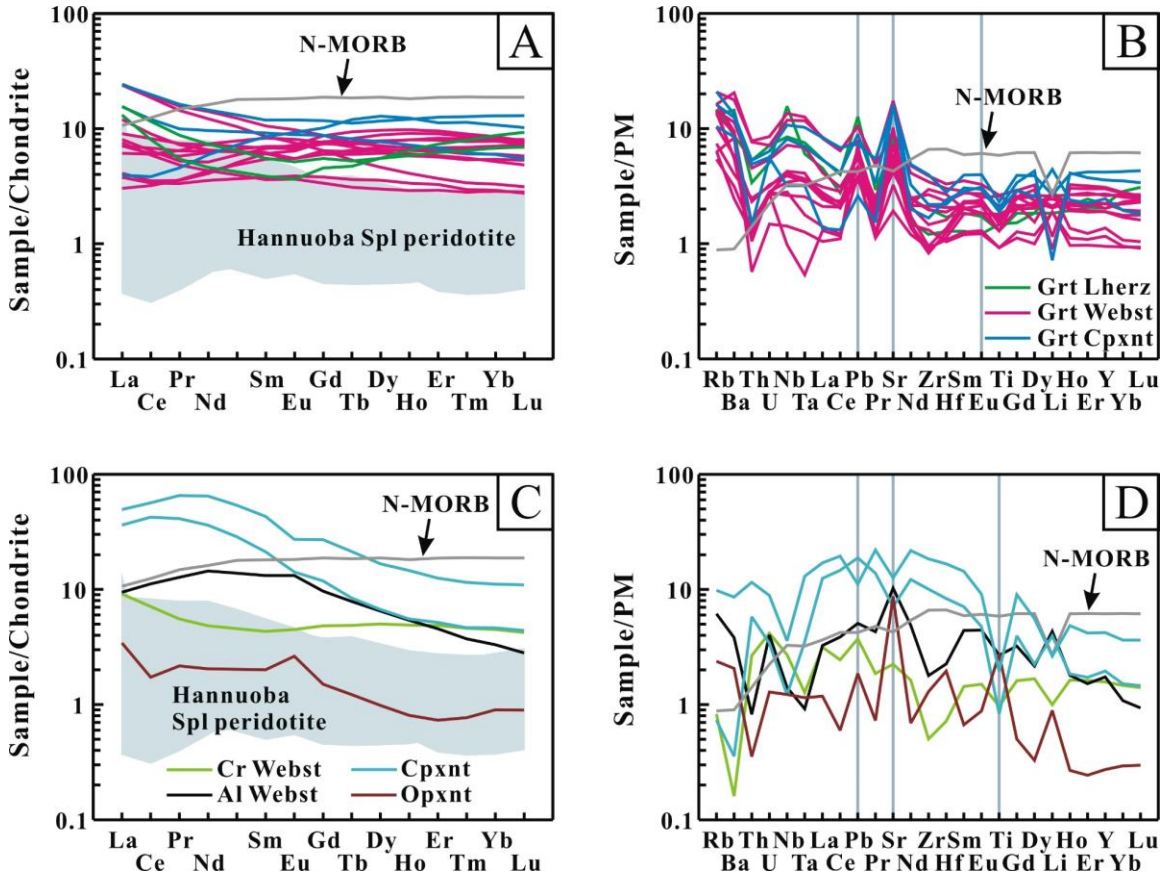

Figure 3-3. Trace element features for Hannuoba mantle xenoliths. (A) and (C) are chondrite-normalized REE patterns for garnet-bearing and garnet-free xenoliths, respectively; (B) and (D) are primitive mantle-normalized trace element patterns for garnet-bearing and garnet-free xenoliths, respectively. Chondrite values are from Anders and Grevesse (1989); primitive mantle and N-MORB values are from McDonough and Sun (1995). Light blue fields represent data of Hannuoba spinel peridotites from Rudnick et al. (2004) and Song and Frey (1989). Trace element data are from Table 3-S3.

major element disequilibrium within individual grains.

All the garnets in samples studied here were replaced by kelyphites consisting of fine-grain intergrowths of spinel and plagioclase (Liu et al., 2005), although fresh relic garnets have rarely been reported (Chen et al., 2001; Liu et al., 2005). These kelyphites still possess an almost identical bulk chemical composition to garnets, with only few analyses yielding higher contents of Na_2O, suggesting alkali ingress from metasomatic melts (Liu et al., 2010c). Garnets are rich in pyrope end-member ($Pyr_{69.0–74.9}$, $Alm_{11.8–18.7}$, $Gro_{10.1–16.8}$), consistent with their relatively high Mg# (78.8–85.8) and mantle origin. Their CaO and Cr_2O_3 contents fall within the websteritic field (Sobolev et al., 1973) (Fig. 3-4C).

Pyroxenes show limited compositional variation in the Wo–En–Fs quadrilateral (Fig. 3-5). Clinopyroxenes have an average composition of $Wo_{45.6}En_{48.9}Fs_{5.52}$, and concentrate on the boundary between diopside and augite while orthopyroxenes range in composition from enstatite to bronzite ($En_{85.6}$ to $En_{90.2}$). In contrast to the Cr-rich spinels commonly found in mantle xenoliths, spinels from the xenoliths analyzed here are Cr-poor and Al-rich, with moderate Mg# (70.8–80.3). Their Cr# values (1.46–15.6) are close to the low Cr# end of non-cratonic peridotitic spinels and spinels found in the reaction zone between a lherzolite and its host basalt, suggesting late-stage modification (Zhang et al., 2007a) (Fig. 3-4D).

Garnet-free pyroxenites consist mainly of pyroxene with minor spinel. Clinopyroxenes are all diopside with slightly different compositions (Fig. 3-5). Those from the Cr websterites are Cr-rich ($Wo_{45.0–49.1}En_{42.6–49.8}Fs_{5.16–9.12}$, with Cr_2O_3 up to 1.1 wt.%), while those from the Al websterite are more Al-, Fe-, and Na-rich ($Wo_{48.0}En_{41.2}Fs_{10.8}$), and those from the clinopyroxenites are Ca-rich ($Wo_{50.7}En_{43.0}Fs_{6.3}$). Orthopyroxenes range from

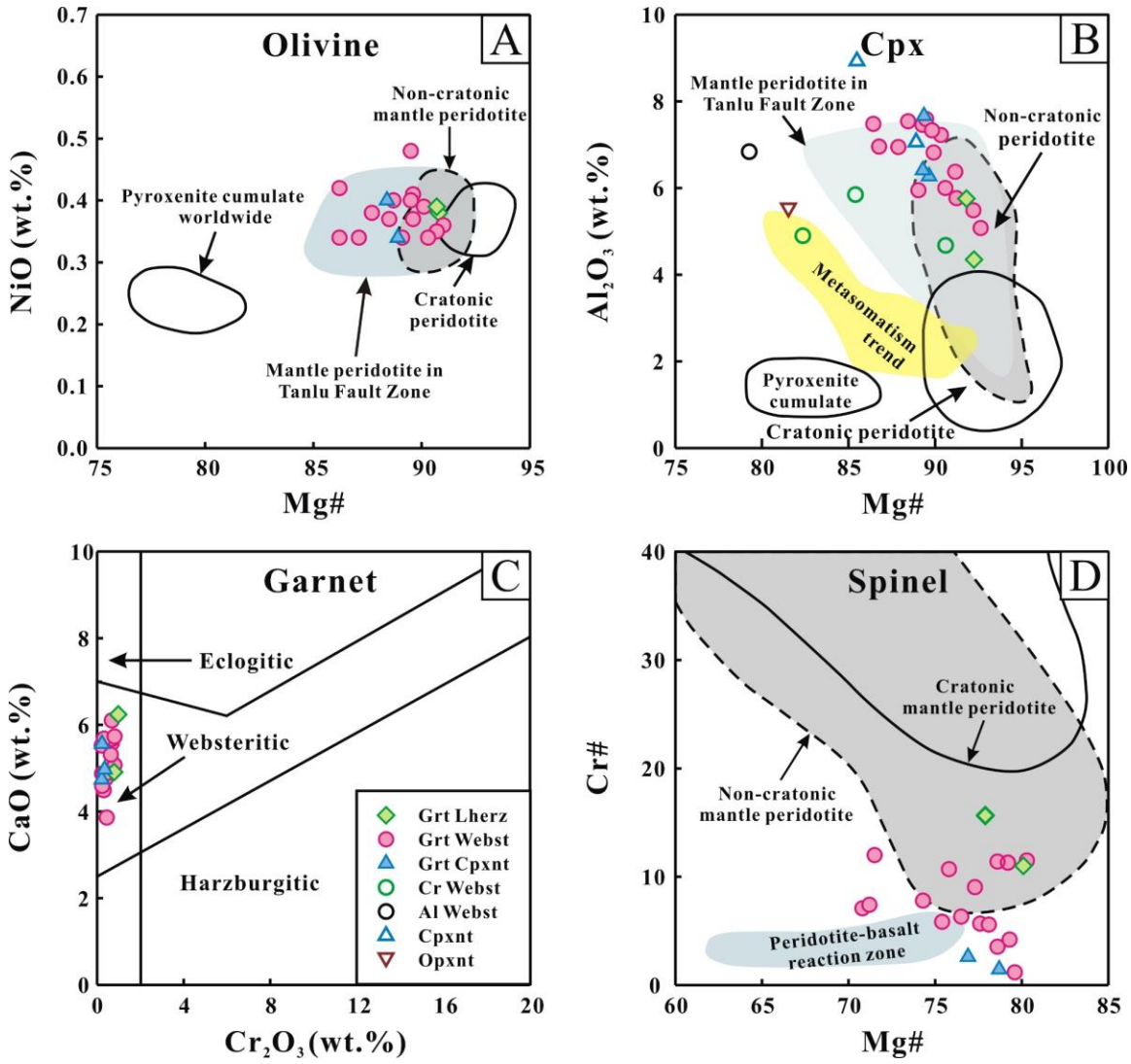

Figure 3-4. Mineral chemical composition plots for Hannuoba mantle xenoliths. (A) Mg# vs. NiO (wt.%) in olivine. (B) Mg# vs. Al_2O_3 (wt.%) in clinopyroxene. (C) Cr_2O_3 (wt.%) vs. CaO (wt.%) in garnet. (D) Mg# vs. Cr# in spinel. In (A), (B) and (D), fields of cratonic and non-cratonic mantle peridotites, and pyroxenite cumulates worldwide are from Walter (2003). Data for mantle peridotitic xenoliths from the Tanlu Fault Zone regions are from Fan et al. (2000), Gao and Zhang (1994), Rudnick et al. (2004), Wang et al. (1987), Xu et al. (1998), Yan et al. (2003), Zhang et al. (2007b), and Zheng et al. (1998). Metasomatism trend in (B) is from Su et al. (2014). In (C), fields for eclogitic, websteritic, and harzburgitic garnets are from Sobolev et al. (1973). In (D), data for spinels from the peridotite-basalt reaction zone are from Zhang et al. (2007a). (A), (B) and (D) are modified from Zhang et al. (2007a). Mineral chemical data are from Tables 3-S4–S8.

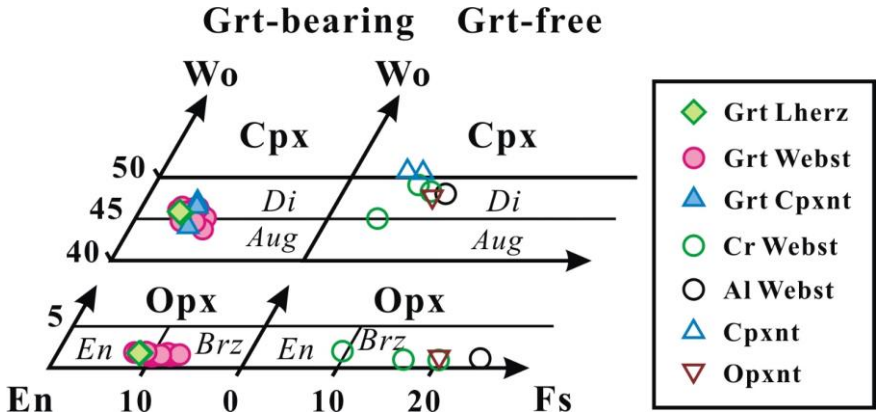

Figure 3-5. Wo–En–Fs classification quadrilateral of pyroxenes from Hannuoba mantle xenoliths.

enstatite to bronzite, with those from the Cr websterites being more Mg-rich (Fs = 9.48–20.1) and those from the Al websterite being more Fe-rich (Fs = 24.3). In addition, clinopyroxenes from the clinopyroxene-rich Cr websterites fall within the peridotite compositional field, whereas those from the Al websterite, the orthopyroxenite, and the orthopyroxene-rich Cr websterite fall along the metasomatic trend defined by Iran pyroxenites that were formed via interaction between lithospheric mantle and slab melts (Fig. 3-4B) (Su et al., 2014). Spinels from the Cr websterites have higher Cr# (26.8 and 10.3) and Mg# (72 and 59.6) than those from the Al websterites (Cr# = 1.02, Mg# = 56.4).

4.3. Temperature and pressure estimates

Equilibrium partitioning of Mg–Fe among clinopyroxene, orthopyroxene and olivine, as indicated by the 1:1 linear correlations between the Mg# of these three minerals (Fig. 3-6A and B) (Keshav and Sen, 2004), and their generally straight and smooth grain boundaries, permits temperature estimates for the Hannuoba xenoliths. Temperatures estimated from five different thermometers agree within 50°C (Table 3-3). This consistency in turn reflects equilibrium distribution of relevant elements among the co-existing minerals. The calculated temperatures and pressures for most garnet-bearing xenoliths fall within the ranges of 900–1040°C, and 1.5–2.0 GPa, respectively (Table 3-3), consistent with previous estimates (Chen et al., 2001; Xu, 2002; Liu et al., 2003, 2005, 2010c; Fan et al., 2005) and overlap with the range for Hannuoba spinel peridotites (839–1072°C, Chen et al., 2001; Rudnick et al., 2004), while are higher than the Hannuoba garnet-bearing mafic granulites (768–835°C, Liu et al., 2010b). Garnet-free pyroxenites generally yield lower equilibrium temperatures (844–868°C), except the most Cr-rich websterite that has an

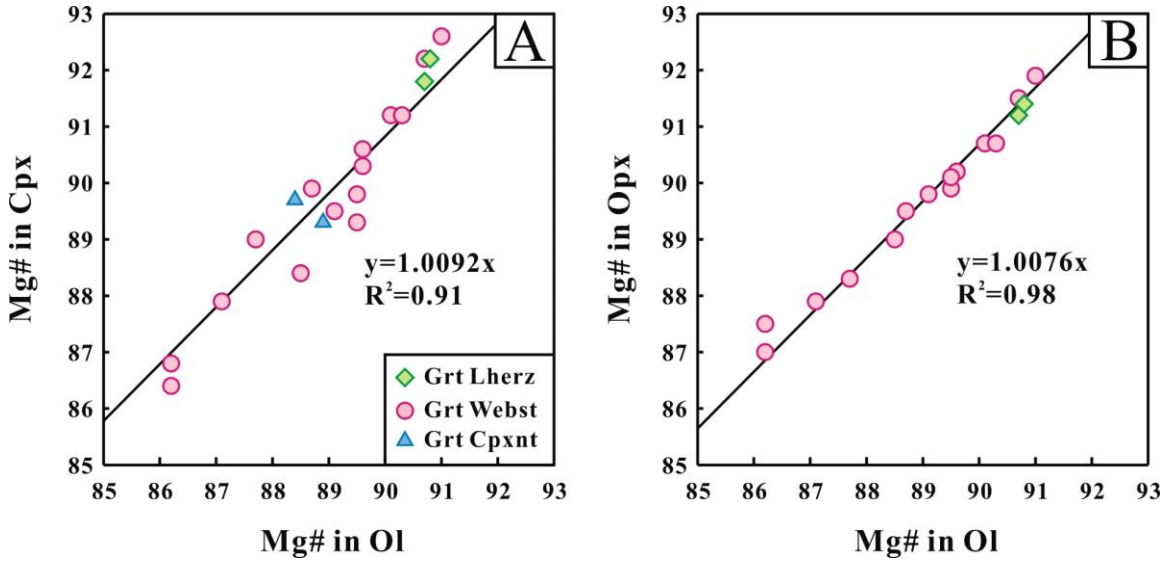

Figure 3-6. Mg# correlations between co-existing (A) Cpx–Ol and (B) Opx–Ol. Mg# = 100 × molar Mg/(Mg + Fe). The best-fit lines are obtained by setting the intercepts to zero. Data are from Table 3-S6–S8.

Table 3-3. Temperature (ºC) and pressure (GPa) estimates for Hannuoba garnet-bearing xenoliths

Sample	*T (W)*	T (B&K1)	T (B&K2)	T (L&D)	T (N&T)	Mg isotope thermometry			P (N&G)	P (B&K1)	P (B&K2)	P (H&G)
	Cpx-Opx	Ca in Opx	Opx-Grt-Cpx	CaO in Opx	Cpx	Ol-Grt	Cpx-Grt	Opx-Grt	Opx-Grt	Ca in Opx	Opx-Grt-Cpx	Grt-Opx
D 02 L	***1028***	1057	1052	1071	1019	1622	1795	1625	1.87	2.06	1.79	1.66
D 6S L	***1020***	1057	1019	1069	1023	1376	1597	1472	1.87	2.02	1.43	1.63
D 01 W	***974***	997	1022	1028	944	776	1113	1170	1.60	1.86	1.73	1.45
D 04 W	***1032***	1061	1036	1077	1020	1404	1421	1381	1.86	1.99	1.69	1.64
D 06 W	***973***	1010	1033	1039	946	1264	1375	1396	1.56	1.84	1.64	1.40
D 07 W	***991***	990	1039	1033	946	1436	1397	1334	1.57	1.63	1.69	1.39
D 09 W	***975***	985	1011	1027	943	804	1006	879	1.55	1.61	1.64	1.42
D 12 W	***1021***	1063	1028	1072	1010				1.90	2.14	1.78	1.68
D 22 W	***991***	1060	1002	1066	978				1.77	2.19	1.54	1.53
D 4S W	***989***	1028	1011	1056	969	1631	1904	1896	1.66	1.77	1.27	1.43
D 5S W	***985***	997	1065	1030	948	1551	1599	1601	1.60	1.75	1.91	1.48
D 7S W	***951***	959	1007	1016	882	2000	2817	2003	1.42	1.38	1.35	1.24
J 13 W	***997***	1024	1080	1046	978	1202	1355	1365	1.66	1.96	1.87	1.50
J 15 W	***970***	997	1033	1032	915	1184			1.54	1.73	1.62	1.40
D802 W	***997***	1030	1030	1049	974				1.74	1.93	1.71	1.55
J 805 W	***975***	996	1044	1037	934				1.48	1.62	1.55	1.32
J 613 W	***1040***	1059	1084	1083	1021				1.74	1.80	1.70	1.51
J 07 C					1029	1294	1297	1357				
D 2S C					895	1199	1300					
D 3S C					877	1039	1130					

Italics indicate values used for Fig. 3-10.

T (W): Cpx-Opx thermometer of Wells (1977).

T (B&K1) and P (B&K1): Ca in Opx thermobarometer of Brey and Köhler (1990).

T (B&K2) and P (B&K2): Cpx-Opx thermobarometer of Brey and Köhler (1990).

T (L&D): Wo in Opx thermometer of Lindsley and Dixon (1976).

T (N&T): Single Cpx thermobarometer of Nimis and Taylor (2000).

P (N&G): Grt-Opx geobarometer of Nickel and Green (1985), using the temperature calculated by thermometer of Wells (1977).

P (H&G): Grt-Opx geobarometer of Harley and Green (1985), using the temperature calculated by thermometer of Wells (1977).

Mg isotope thermometry using parameters provided in Huang et al. (2013).

equilibrium temperature (1039°C) similar to the peridotites. These estimates also agree with the estimates reported by Xu (2002) and Chen et al. (2001).

4.4. Magnesium isotopic compositions

Magnesium isotopic compositions of the garnet-bearing xenoliths are reported in Table 3-4 for both whole rocks and mineral separates. Calculated inter-mineral fractionations are given in Table 3-5 along with mineral equilibration temperature derived from Wells (1977) geothermometer, as this thermometer is commonly used for pyroxenites (e.g., Ying et al., 2013; Su et al., 2014) and yields temperature estimates that are in good agreement with other calibrations. Magnesium isotopic compositions of the garnet-free xenolith group and the two Hannuoba basalts, as well as the carbonatite-metasomatized garnet peridotite from Qinling are presented in Table 3-6, along with their inter-mineral fractionation magnitude and equilibrium temperatures, if applicable. All our samples (including reference materials) fall on a mass-dependent isotope fractionation line, with $\delta^{25}Mg$ being 0.516 times $\delta^{26}Mg$ ($R^2 = 0.99$); therefore, only $\delta^{26}Mg$ values are used in the following and discussion sections.

4.4.1. Whole-rocks

The xenoliths and basalts analyzed in this study have shown a more scattered isotopic distribution than the normally homogeneous mantle peridotites and oceanic basalts, with most of the samples shifting to the lighter-than-mantle side (Fig. 3-7A). The two Hannuoba garnet-bearing lherzolites and the one from western Qinling have similar $\delta^{26}Mg$ values of −0.33‰ to −0.39‰, slightly lighter than the three literature data (−0.21‰ to

Table 3-4. Magnesium isotopic compositions (‰) relative to standard DSM3 of mineral separates and whole rock powders from Hannuoba mantle xenoliths

Sample	Ol (n = 20)				Grt (n = 15)				Cpx (n = 19)				Opx (n = 15)				Whole rock (n = 17)			
	δ^{26}Mg	2SD	δ^{25}Mg	2SD	δ^{26}Mg	2SD	δ^{25}Mg	2SD	δ^{26}Mg	2SD	δ^{25}Mg	2SD	δ^{26}Mg	2SD	δ^{25}Mg	2SD	δ^{26}Mg	2SD	δ^{25}Mg	2SD
D 02 L	−0.30	0.07	−0.15	0.05	−0.53	0.07	−0.26	0.06	−0.29	0.05	−0.17	0.04	−0.26	0.06	−0.14	0.05	−0.36	0.06	−0.18	0.06
D 6S L	−0.21	0.06	−0.16	0.04	**−0.52**	**0.03**	**−0.27**	**0.02**	−0.22	0.05	−0.13	0.04	−0.19	0.06	−0.10	0.05	−0.33	0.07	−0.17	0.07
D 01 W	**0.05**	**0.05**	**0.03**	**0.03**	**−0.75**	**0.05**	**−0.39**	**0.04**	−0.20	0.05	−0.11	0.04	−0.27	0.06	−0.12	0.04	−0.32	0.07	−0.12	0.05
D 04 W	−0.33	0.07	−0.16	0.05	−0.63	0.07	−0.31	0.06	−0.27	0.05	−0.15	0.04	−0.27	0.06	−0.14	0.05	−0.43	0.07	−0.21	0.05
D 06 W	**0.00**	**0.05**	**0.00**	**0.03**	**−0.37**	**0.03**	**−0.19**	**0.03**	**0.02**	**0.04**	**−0.01**	**0.03**	**−0.01**	**0.05**	**0.00**	**0.04**	**−0.10**	**0.05**	**−0.05**	**0.03**
D 07 W	−0.19	0.07	−0.08	0.05	**−0.48**	**0.04**	**−0.26**	**0.04**	**−0.11**	**0.04**	**−0.06**	**0.03**	**−0.10**	**0.05**	**−0.04**	**0.03**	−0.24	0.07	−0.15	0.05
D 09 W	**0.00**	**0.05**	**0.03**	**0.03**	−0.76	0.05	−0.39	0.05	**−0.11**	**0.04**	**−0.07**	**0.03**	**0.00**	**0.04**	**0.02**	**0.03**	−0.20	0.07	−0.09	0.07
D 12 W	−0.28	0.07	−0.14	0.05					−0.27	0.07	−0.12	0.06	−0.26	0.07	−0.12	0.05	−0.34	0.06	−0.18	0.06
D 22 W	**−0.28**	**0.04**	**−0.13**	**0.03**					−0.25	0.06	−0.15	0.05	−0.28	0.06	−0.17	0.04	−0.26	0.07	−0.11	0.07
D 4S W	−0.24	0.06	−0.12	0.04	**−0.47**	**0.04**	**−0.23**	**0.04**	−0.25	0.05	−0.14	0.04	−0.26	0.06	−0.13	0.05	−0.27	0.07	−0.12	0.07
D 5S W	−0.23	0.06	−0.11	0.04	−0.48	0.05	−0.24	0.05	−0.18	0.07	−0.11	0.06	−0.20	0.06	−0.12	0.04	−0.26	0.07	−0.10	0.07
D 7S W	**−0.40**	**0.05**	**−0.20**	**0.03**	−0.56	0.05	−0.28	0.04	**−0.46**	**0.04**	**−0.21**	**0.03**	**−0.37**	**0.05**	**−0.18**	**0.03**	−0.35	0.07	−0.18	0.05
J 13 W	−0.18	0.06	−0.12	0.04	−0.58	0.05	−0.29	0.05	−0.18	0.05	−0.06	0.04	−0.21	0.06	−0.10	0.05	−0.21	0.07	−0.09	0.07
J 15 W	−0.29	0.05	−0.15	0.04	−0.70	0.05	−0.33	0.05									−0.36	0.07	−0.19	0.05
D802 W	−0.27	0.06	−0.12	0.05					−0.24	0.07	−0.12	0.06								
J 805 W	−0.31	0.06	−0.15	0.05					−0.23	0.07	−0.10	0.06	−0.26	0.06	−0.13	0.05				
J 613 W	−0.33	0.07	−0.19	0.05					−0.31	0.07	−0.16	0.05								
J 07 C	−0.26	0.07	−0.12	0.05	−0.61	0.05	−0.30	0.05	−0.19	0.07	−0.09	0.06	−0.24	0.06	−0.13	0.04	−0.34	0.06	−0.22	0.06
D 2S C	**−0.14**	**0.05**	**−0.08**	**0.04**	−0.54	0.07	−0.30	0.06	**−0.12**	**0.03**	**−0.05**	**0.02**					−0.18	0.07	−0.12	0.07
D 3S C	−0.23	0.06	−0.12	0.04	**−0.73**	**0.03**	**−0.39**	**0.02**	−0.20	0.05	−0.09	0.04					**−0.48**	**0.03**	**−0.25**	**0.02**
Average	**−0.22**	**0.24**	**−0.11**	**0.13**	**−0.58**	**0.23**	**−0.29**	**0.12**	**−0.21**	**0.20**	**−0.11**	**0.10**	**−0.21**	**0.21**	**−0.11**	**0.12**	**−0.30**	**0.19**	**−0.15**	**0.11**

L = Lherzolite; W = Websterite; C = Clinopyroxenite; n indicates sample numbers for each mineral phase.
2SD = 2 times the standard deviation of the population of n repeated measurements of the standards during an analytical session. For samples that have been analyzed more than once, the weighted averages (in bold) are reported. Detailed measurement data are reported in Table 3-2. Average values in the last line are arithmetic mean values.

Table 3-5. Inter-mineral Mg isotope fractionations in Hannuoba garnet-bearing xenoliths

Sample	Temp. (°C)	$\Delta^{26}Mg_{Ol\text{-}Grt}$ (n = 15)	2SD	$\Delta^{26}Mg_{Cpx\text{-}Grt}$ (n = 14)	2SD	$\Delta^{26}Mg_{Opx\text{-}Grt}$ (n = 12)	2SD	$\Delta^{26}Mg_{Cpx\text{-}Ol}$ (n = 19)	2SD	$\Delta^{26}Mg_{Opx\text{-}Ol}$ (n = 15)	2SD	$\Delta^{26}Mg_{Cpx\text{-}Opx}$ (n = 15)	2SD
D 02 L	1028	0.24	0.10	0.24	0.09	0.28	0.10	0.01	0.08	0.04	0.09	−0.03	0.08
D 6S L	1020	0.31	0.07	0.30	0.06	0.33	0.07	−0.02	0.08	0.01	0.09	-0.03	0.08
D 01 W	974	0.80	0.07	0.55	0.07	0.48	0.08	−0.25	0.07	−0.32	0.08	0.07	0.08
D 04 W	1032	0.30	0.10	0.36	0.09	0.37	0.10	0.06	0.08	0.06	0.09	0.00	0.08
D 06 W	973	0.36	0.06	0.38	0.05	0.36	0.06	0.02	0.07	0.00	0.07	0.03	0.06
D 07 W	991	0.29	0.08	0.38	0.06	0.39	0.06	0.08	0.08	0.09	0.08	−0.01	0.06
D 09 W	975	0.76	0.07	0.65	0.07	0.76	0.07	−0.11	0.06	0.00	0.07	−0.11	0.06
D 12 W	1021							0.01	0.10	0.02	0.10	−0.01	0.10
D 22 W	991							0.03	0.07	−0.01	0.07	0.04	0.08
D 4S W	989	0.24	0.08	0.22	0.06	0.21	0.07	−0.02	0.08	−0.02	0.09	0.01	0.08
D 5S W	985	0.26	0.08	0.30	0.09	0.28	0.08	0.04	0.09	0.03	0.09	0.01	0.09
D 7S W	951	0.16	0.07	0.11	0.06	0.19	0.06	−0.06	0.06	0.03	0.07	−0.08	0.06
J 13 W	997	0.40	0.08	0.39	0.07	0.37	0.08	0.00	0.08	−0.02	0.09	0.02	0.08
J 15 W	970	0.41	0.07										
D802 W	997							0.03	0.09				
J 805 W	975							0.07	0.09	0.04	0.09	0.03	0.09
J 613 W	1040							0.02	0.10				
J 07 C	1029	0.35	0.09	0.42	0.09	0.38	0.08	0.08	0.10	0.03	0.09	0.05	0.09
D 2S C	895	0.40	0.09	0.42	0.08			0.03	0.06				
D 3S C	877	0.50	0.07	0.53	0.06			0.03	0.08				
Average		**0.39**	**0.36**	**0.38**	**0.28**	**0.37**	**0.29**	**0.00**	**0.15**	**0.00**	**0.19**	**0.00**	**0.10**

Temp. = Temperature

Table 3-6. Magnesium isotopic compositions (‰) of mineral separates and whole rock powders from Hannuoba garnet-free pyroxenite xenoliths, basalts, and a Qinling garnet peridotite xenolith

Sample	Rock type	Cpx				Opx				Whole rock				T	$\Delta^{26}Mg_{Cpx-Opx}$	2SD
		$\delta^{26}Mg$	2SD	$\delta^{25}Mg$	2SD	$\delta^{26}Mg$	2SD	$\delta^{25}Mg$	2SD	$\delta^{26}Mg$	2SD	$\delta^{25}Mg$	2SD			
D 11	Cr Webst	−0.33	0.06	−0.11	0.05	−0.28	0.06	−0.16	0.05	−0.32	0.06	−0.16	0.06	1039	−0.04	0.09
D 17	Cr Webst	−0.25	0.06	−0.11	0.05	−0.23	0.06	−0.13	0.04					844	−0.02	0.08
D 18	Cr Webst	−0.24	0.07	−0.13	0.06	−0.28	0.06	−0.15	0.05					849	0.04	0.09
D 19	Al Webst	−0.29	0.07	−0.12	0.06	−0.21	0.06	−0.11	0.04	−0.26	0.06	−0.13	0.06	868	−0.08	0.09
D 23	Cpxnt	−1.34	0.06	−0.69	0.05					−1.26	0.06	−0.67	0.06			
J 53	Cpxnt	−1.47	0.07	−0.76	0.06					−1.51	0.07	−0.80	0.05			
J 53rr	Cpxnt	−1.38	0.07	−0.68	0.05					−1.40	0.06	−0.77	0.06			
J 53rr2	Cpxnt	−1.39	0.07	−0.73	0.05											
J 52	Opxnt					−0.21	0.07	−0.12	0.05	−0.17	0.06	−0.09	0.06	873		
DA 0605	Alkali Basalt									−0.50	0.08	−0.28	0.07			
DA 0605rr	Alkali Basalt									−0.51	0.07	−0.26	0.05			
DA 0608	Tholeiitic Basalt									−0.35	0.06	−0.18	0.05			
QL 08-1	Grt Peridotite									−0.39	0.08	−0.21	0.07			

Webst = websterite; Cpxnt = Clinopyroxenite; Opxnt = Orthopyroxenite; Grt = garnet.

−0.23‰, Teng et al., 2010a; Pogge von Strandmann et al., 2011). The δ^{26}Mg values of 12 garnet websterites range from −0.43‰ to −0.10‰ and those of the three garnet clinopyroxenites vary from −0.48‰ to −0.18‰.

In contrast to the large variation displayed by the garnet-bearing xenoliths, both the Cr and Al websterites, and the orthopyroxenite have mantle-like δ^{26}Mg values (−0.17‰ to −0.32‰). The two garnet-free clinopyroxenites yield δ^{26}Mg values of −1.39‰ and −1.51‰, which are the lightest δ^{26}Mg values find in this study and reported in the literature for mantle rocks. The two Hannuoba basalts yield δ^{26}Mg of −0.35‰ and −0.51‰, falling into the range reported for the nearby Taihang basalts (−0.30‰ to −0.54‰, Yang et al., 2012).

4.4.2. Mineral separates (olivine, clinopyroxene, orthopyroxene, and garnet)

The 69 mineral separates in the garnet-bearing xenoliths span a total δ^{26}Mg range of 0.80‰, from −0.75‰ in garnet to +0.05‰ in olivine. Among all the mineral phases, garnet shows the widest variation, from −0.37‰ to −0.75‰, and is systematically lighter than co-existing olivine and pyroxene, both of which have δ^{26}Mg values concentrated in the mantle range (Fig. 3-7B). The δ^{26}Mg values of olivine vary from −0.40‰ to +0.05‰, while those of clinopyroxene and orthopyroxene exhibit a similar range of −0.46‰ to +0.02‰ and −0.37‰ to 0‰, respectively, comparable to published data (Handler et al., 2009; Yang et al., 2009; Young et al., 2009; Huang et al., 2011; Liu et al., 2011; Xiao et al., 2013). The average mineral δ^{26}Mg values based on all analyses is −0.22 ± 0.24‰ (n = 20, 2SD) for olivine, −0.21 ± 0.20‰ (n = 19, 2SD) for clinopyroxene, and −0.21± 0.21‰ (n = 15, 2SD) for orthopyroxene.

The four clinopyroxene and orthopyroxene pairs from the garnet-free websterites and the orthopyroxene from the orthopyroxenite have mantle-like δ^{26}Mg values, with δ^{26}Mg varying from −0.24‰ to −0.33‰ in clinopyroxene and −0.21‰ to −0.28‰ in orthopyroxene. Clinopyroxenes from the two clinopyroxenites (−1.37‰ and −1.47‰) are much lighter than the normal mantle clinopyroxene range, whereas are consistent with their extremely light whole-rock δ^{26}Mg values (Fig. 3-7).

5. Discussion

Our data show that the pyroxenite xenoliths have variable Mg isotopic compositions, which might be genetically linked to different episodes of melt activity in the Hannuoba lithospheric mantle. The broad zircon age spectrum and large elemental and isotopic variation in Sr–Nd–Pb–Li–Fe for peridotitic and pyroxenitic xenoliths revealed that the mantle beneath this region has been subjected to multistage modification by both crustal- and mantle-derived melts (Song and Frey, 1989; Tatsumoto et al., 1992; Liu et al., 2004, 2005, 2010c; Rudnick et al., 2004; Tang et al., 2007; Choi et al., 2008; Zhang, 2009; Zheng et al., 2009; Zhao et al., 2010). In this section, we first explore the genetic connection between the Mg isotopic composition of each pyroxenite group and their corresponding origins. Then, we evaluate whether inter-mineral Mg isotope partitioning within each xenolith group has reached equilibrium or not by comparison with theoretical calculations and empirical data. When disequilibrium inter-mineral fractionations are observed, their possible driving forces are examined. Finally, we discuss the implications of δ^{26}Mg variation in mantle pyroxenites on mantle Mg isotopic heterogeneity.

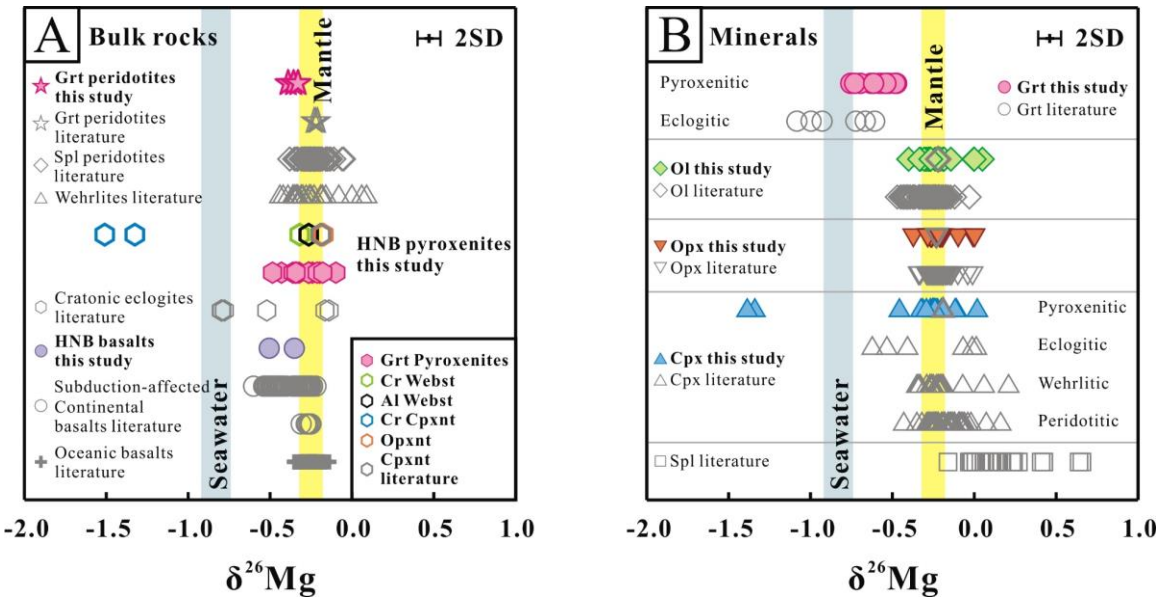

Figure 3-7. Compilation of δ^{26}Mg (‰) for (A) mantle-related rocks and (B) mineral separates. Mantle range is defined as $\delta^{26}Mg = -0.25 \pm 0.07$‰ (Teng et al., 2010a). Global seawater range is defined as $\delta^{26}Mg = -0.83 \pm 0.09$‰ (Ling et al., 2011). Data for Hannuoba mantle xenoliths are from Tables 3-4 and 3-6. Literature data are shown as gray open symbols while colorful symbols are data from this study. Data sources: Spl: Young et al. (2009), Liu et al. (2011), Xiao et al. (2013); Ol, Cpx and Opx: Young et al. (2009), Handler et al. (2009), Yang et al. (2009), Liu et al. (2011), Huang et al. (2011), Xiao et al. (2013); Cratonic eclogite, eclogitic Cpx and Grt: Wang et al. (2012); Pyroxenite: Liu et al. (2011); Oceanic basalts: Bourdon et al. (2010), Teng et al. (2010); Continental basalts: Yang et al. (2012), Huang et al. (2015); Peridotites: Young et al. (2009), Yang et al. (2009), Bourdon et al. (2010), Teng et al. (2010), Huang et al. (2011), Liu et al. (2011), Pogge von Strandmann et al. (2011), Xiao et al. (2013); Wehrlites: Yang et al. (2009), Teng et al. (2010a), Pogge von Strandmann et al. (2011), Xiao et al. (2013).

5.1.Garnet-bearing lherzolites and pyroxenites

5.1.1. Origin of garnet-bearing xenoliths

The occurrence of garnet pyroxenite veins infiltrating the host peridotites establishes their formation at mantle depths, which is consistent with the temperatures and pressure estimates of ~1000°C and 1.5–2.0 Ga based on their mineral compositions. The bulk rocks do not share a common composition with MORB (Fig. 3-2) and lack the positive Eu anomalies (Fig. 3-3A) that are typical for oceanic gabbros (e.g., Stracke et al., 2003). These characteristics rule out their origin as recycled oceanic lithosphere. Their major element compositions also plot off the extension trends between the Hannuoba peridotites and calculated equilibrium melts (Fig. 3-2A and B), and their δ^{26}Mg range is much wider than that of the normal mantle, arguing against their origin as in situ melting products of the host peridotites, as suggested by Chen et al. (2001). Their major constituent minerals show a strong mantle-affinity while are significantly different from those in pyroxenite cumulates worldwide (Fig. 3-4A and B). The lack of convex-upward REE patterns that are typical for cumulative pyroxenites (Frey and Prinz, 1978) and the presence of deformation features are also inconsistent with a cumulate origin (Ionov et al., 2005).

Liu et al. (2005) alternatively proposed a replacive origin for these garnet-bearing pyroxenites. In their model, peridotites were converted to garnet pyroxenites by reaction with melts from ancient subducted oceanic slab, which resulted in formation of pyroxene and garnet at the expense of olivine (Yaxley and Green, 1998; Rapp et al., 1999). This metasomatic origin explains the decoupled major-trace elemental features which show that while the whole rocks are enriched in highly incompatible elements (e.g., Rb, Ba Sr and Pb) (Fig. 3-3B) with some showing relatively high $^{87}Sr/^{86}Sr$ for their ε_{Nd} (Xu, 2002), their

major mineral phases still preserve peridotite affinities (Fig. 3-4A and B). Later experimental studies (Wang et al., 2010; Zhang et al., 2012) have successfully reproduced similar garnet pyroxenites by reacting a Hannuoba spinel lherzolite with a quartz eclogite from central China. Subsequent finding of 315 Ma igneous zircons together with the record of coeval subduction-related magmatism (Zhang et al., 2009) provided further support to this explanation.

5.1.2. Whole-rock Mg isotopic variation

Building on previous discussions, the new Mg isotopic data obtained here further substantiate the replacive origin for these garnet-bearing xenoliths and the critical role of recycled oceanic crust in forming them. In view that the majority of olivine and pyroxene still preserve their mantle-like δ^{26}Mg, the formation of secondary isotopically light garnet thus requires addition of light Mg into the bulk rocks from an external source. The isotopically light alkali basalts that host the xenoliths might be a possible candidate. However, lighter Mg isotopes diffuse faster than their heavy counterparts and they preferentially diffuse toward the hot end along a thermal gradient (Richter et al., 2009 and references therein). Therefore, diffusion of Mg from the xenoliths into their host magmas during magma ascent will result in depletion of light isotopes in these xenoliths, which is opposite to our observation here. In addition, given a typical ascent rate for xenolith-bearing alkali basalts of about 0.1–10 m/s (Spera, 1984), and an entrained depth of approximately 60 km for the xenoliths in this study, the magma should have reached the surface in hours or days. Likewise, basaltic flows commonly cool on the order of weeks (Flynn et al., 1994). The rapid eruption and cooling of alkali basalts thus precludes

extensive interaction between the xenoliths and the host magma. Therefore, the garnets and their host xenoliths must have acquired their Mg isotopic characteristics before entrainment by the host magma.

The isotopically light Hannuoba alkali basalts may alternatively imply the presence of subducted slab in their mantle source, which is a common explanation for the isotopically light basalts found on eastern China (Fig. 3-7B) (e.g. Yang et al., 2012; Huang et al., 2015). This argument is mainly based on the finding of cratonic eclogites that are generally depleted in heavy Mg isotopes (Wang et al., 2012), which were taken as evidence for incorporation of sedimentary carbonates during low-temperature alterationof oceanic crust. The light Mg in carbonates can be incorporated into silicates by metamorphic de-carbonation or fluid-mediated isotopic exchange (Wang et al., 2014a). The major element compositions of these garnet-bearing xenoliths lie on the binary mixing trends between mantle peridotites and recycled oceanic crustal pyroxenites (Fig. 3-2). Their Mg isotopic compositions can also be explained by the triangle defined by mixing between oceanic crust, as represented by the cratonic eclogites (Wang et al., 2012) and NCC peridotites (Teng et al., 2010a) (Fig. 3-8). The presence of altered subducted slab and sediments in the mantle beneath the Hannuoba region may also contribute to the low δ^7Li signature that characterizes Hannuoba peridotites (Tang et al., 2007), and the formation of Al-rich sapphirine in Hannuoba mantle clinopyroxenites (Su et al., 2012a).

5.1.3. Inter-mineral Mg isotope fractionation

Mantle minerals are generally found to be in isotopic equilibrium since high temperature promotes isotope diffusion (Urey, 1947). To reach equilibrium, heavy isotopes

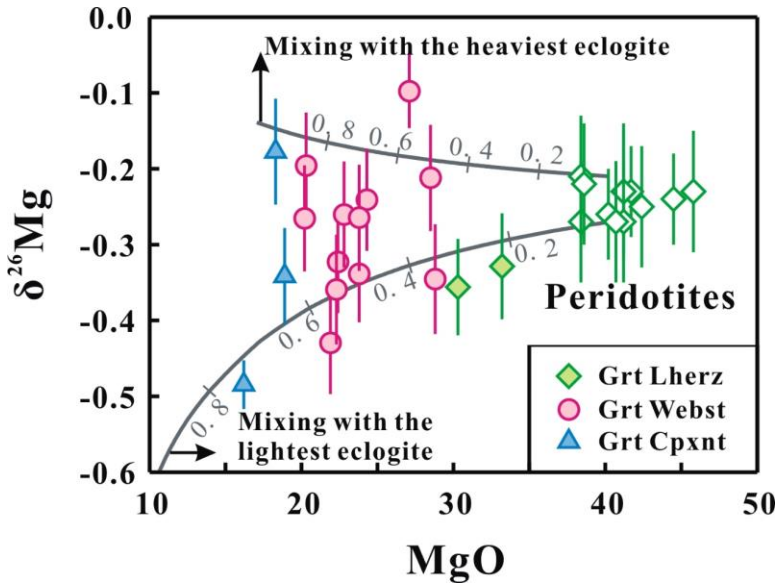

Figure 3-8. δ^{26}Mg (‰) of the Hannuoba garnet-bearing xenoliths in relation to their MgO (wt.%). The two gray lines represent mixing lines between peridotites from the North China Craton (Teng et al., 2010a) and cratonic eclogites from South African (Wang et al., 2012). End-member compositions: the lightest eclogites has a δ^{26}Mg value of −0.798‰and MgO content of 7.37 wt.%., while the heaviest eclogite has a δ^{26}Mg value of −0.139‰ and MgO content of 17.05 wt.%. The δ^{26}Mg values for NCC peridotites range from −0.27‰ to −0.21‰.

are preferentially concentrated in minerals with stronger chemical bonds due to their higher vibrational frequency and therefore greater energy reduction upon isotope exchange (Bigeleisen, 1965). Since Mg only occurs with one oxidation state (+2) in common minerals, the key factor determining Mg–O bond strength is the coordination number of Mg in different minerals. Within a mineral class (e.g., silicates, carbonates, oxides), mineral with higher coordination sites for Mg^{2+} allows a larger Mg^{2+} effective ionic radii, therefore longer and weaker Mg–O bond, which favors lighter Mg isotopes (see Young et al., 2015 for a thorough discussion).

Each Mg^{2+} is bonded to six neighboring oxygen anions in the predominant upper mantle minerals (olivine, clinopyroxene, and orthopyroxene) with a similar bond strength. Therefore, only limited fractionation occurs between them, which is thought to result from the subordinate, but stronger, Mg–^{III}O bonds in pyroxene than the Mg–^{IV}O bonds in olivine (Young et al., 2009, 2015; Liu et al., 2010a, 2011). The Mg isotope fractionation between most co-existing pyroxene and olivine in this study is barely analytically resolvable, with $\Delta^{26}Mg_{Cpx-Ol} = \delta^{26}Mg_{Cpx} - \delta^{26}Mg_{Ol} = -0.06‰$ to $+0.08‰$ (n = 17), $\Delta^{26}Mg_{Opx-Ol} = \delta^{26}Mg_{Opx} - \delta^{26}Mg_{Ol} = -0.02‰$ to $+0.09‰$ (n = 14), and $\Delta^{26}Mg_{Cpx-Opx} = \delta^{26}Mg_{Cpx} - \delta^{26}Mg_{Opx} = -0.08‰$ to $+0.05‰$ (n = 14). The magnitude of this fractionation agrees with published Mg isotope data on equilibrated peridotitic pyroxene and olivine (Handler et al., 2009; Yang et al., 2009; Chakrabarti and Jacobsen, 2010; Huang et al., 2011; Liu et al., 2011; Pogge von Strandmann et al., 2011; Xiao et al., 2013), and falls within the ranges of density functional perturbation theory (DFPT) calculation (Schauble, 2011; Huang et al., 2013), as well as the ranges defined by empirical measurements (Liu et al., 2011) (Fig. 3-9A and B). Therefore, these observations suggest a broad equilibrium Mg isotope fractionation between pyroxene

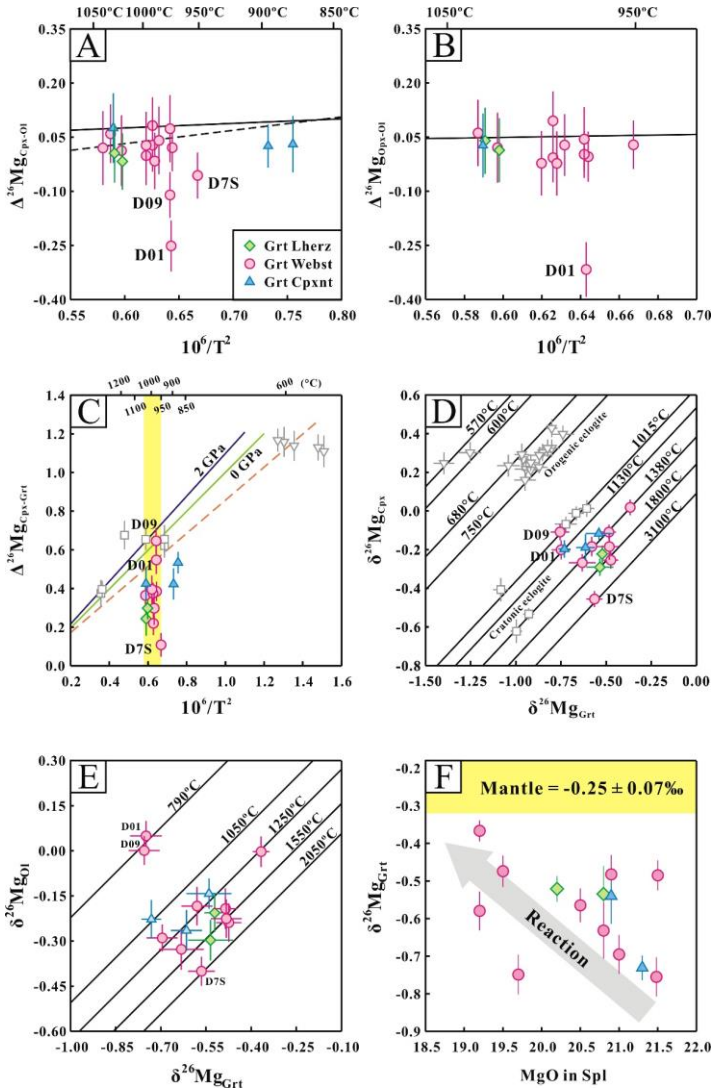

Figure 3-9. Inter-mineral Mg isotope fractionation. (A) and (B): Correlations of inter-mineral fractionation between Cpx–Ol and Opx–Ol with $10^6/T^2$ (T in K). $\Delta^{26}Mg_{X-Y} = \delta^{26}Mg_X - \delta^{26}Mg_Y$, where X and Y represent different mineral phases. The theoretically calculated lines of Schauble (2011) [black solid lines], and Cpx–Ol equilibrium fractionation line established by natural samples (Liu et al., 2011) [dashed line] are plotted for comparison. Data are from Table 3-4. (C) Variation of $\Delta^{26}Mg_{Cpx-Grt}$ with $10^6/T^2$ (T in K) based on DFPT calculation in Huang et al. (2013). Theoretical equilibrium fractionation lines between co-existing garnet and clinopyroxene at 0 GPa (green solid line) and 2 GPa (blue solid line), and that established by empirical measurements on equilibrated eclogitic Grt–Cpx pairs (orange dash line) are shown for reference. (D) and (E) Correlation of $\delta^{26}Mg_{Grt}$ vs. $\delta^{26}Mg_{Cpx}$ and $\delta^{26}Mg_{Ol}$ at different equilibrium temperatures. The calculated equilibrium Mg isotope fractionation lines are from Huang et al. (2013) by assuming the equilibrium pressure of 1.5 GPa throughout. Data for cratonic eclogites (Wang et al., 2012) and orogenic eclogites (Li et al., 2011; Wang et al., 2014b) are shown for comparison, with estimated peak metamorphic pressure of 5 and 3 GPa, respectively. (F) Negative correlation between $\delta^{26}Mg$ of Grt (‰) and MgO content of Spl (wt.%). Data are from Tables 3-4 and 3-5.

and olivine in these samples.

Compared to the 6-fold coordinated Mg in olivine and pyroxene, Mg is 8-fold coordinated in garnet and 4-fold coordinated in spinel, respectively. Therefore, garnets are enriched in light Mg isotopes while spinels have a greater affinity for heavy Mg isotopes. In addition, cation substitution has been suggested to exert a secondary control on the Mg isotopic composition of spinel (Liu et al., 2011; Schauble, 2011; Xiao et al., 2013), as it has both tetrahedral and octahedral sites available for Mg, with $[YO_6]$ octahedrons sharing edge with each other. By contrast, Mg isotopic composition of garnet should be much less sensitive to cation substation since its $[YO_6]$ octahedrons are well separated from each other by $[SiO_4]^{4-}$ (Huang et al., 2013).

The isotopically lighter garnets found in the present study are thus consistent with expectations from DFPT calculations (Huang et al., 2013) and measurements on equilibrated eclogitic garnet and pyroxene (Li et al., 2011; Wang et al., 2012, 2014b). Nonetheless, these garnets appear to be out of Mg isotopic equilibrium with co-existing olivines and pyroxenes, as most of the observed fractionation factors are smaller than the expected values at equilibrium (Fig. 3-9C). Based on the calculated clinopyroxene–orthopyroxene mineral equilibrium temperature of ~1000°C, the empirical equilibrium fractionation line would predict a clinopyroxene-garnet fractionation of −0.52‰ (Li et al., 2011; Wang et al., 2012), while seven out of the 14 clinopyroxene-garnet pairs only have fractionation between 0.36 and 0.42‰. If these values are taken as equilibrium fractionations, they would then require the equilibrium temperatures to be higher than 1380°C (Fig. 3-9D and E). Such high temperatures seem implausible for the Hannuoba locality, as both peridotites and pyroxenites have equilibrium temperatures around 1000°C.

Additionally, over a limited temperature range, the fractionation between garnet and olivine/pyroxene is highly variable, opposed to relatively constant fractionation as would be expected for isotopic equilibrium (Fig. 3-9C). Therefore, we interpret that these garnets have not yet reached isotopic equilibrium with the co-existing olivine and pyroxene.

5.1.4. Mechanism of disequilibrium garnet–olivine/pyroxene fractionation

The deviation of garnet–olivine/pyroxene fractionation from the equilibrium values implies superimposition of kinetic processes on temperature-dependent Mg isotope partitioning among these minerals. Since garnet accounts for a smaller modal abundance than the predominant olivine and pyroxene, both of which have mantle-like δ^{26}Mg and high Mg concentration, the kinetic effects should be more obviously seen in garnets. Considering that δ^{26}Mg in olivine and pyroxene are relatively invariant around the normal mantle values, the reduced $\Delta^{26}Mg_{Grt–Ol/Cpx/Opx}$ fractionations are therefore mainly caused by variably higher-than equilibrium δ^{26}Mg in garnets. While there is no published δ^{26}Mg value on peridotitic garnet for comparison, the Mg isotopic composition of garnets in the Hannuoba lherzolites and pyroxenites are much heavier than garnets from cratonic eclogites formed at similar temperatures (−0.61‰ to −0.72‰in Wang et al., 2012). For example, garnet as heavy as −0.37‰ (δ^{26}Mg) has been found in this study.

Based on discussion in previous sections, the most relevant process accounting for the disequilibrium inter-mineral fractionation is incomplete melt–rock interaction that produced these garnets. The highly variable grain size (even within one hand specimen) and modal abundance of garnet, together with their anhedral shape, are significantly different from the relatively euhedral garnets commonly found in garnet peridotites and

eclogites. Petrographic observations of garnet replacing spinel (Fig. 3-1C–G) also suggest a clear metasomatic origin for the garnets, instead of being the primary refractory phase in depleted peridotites. Therefore, the later-formed garnets could partly inherit the heavy Mg isotopic composition from their embedded isotopically heavy spinel, olivine, or pyroxene grains, and therefore shifted their δ^{26}Mg signals in the heavier direction. For example, using the $\Delta^{26}Mg_{Spl–Ol}$ vs. temperature calibration of Liu et al. (2011), spinel equilibrated with the co-existing olivine in these garnet pyroxenites should be as heavy as +0.11‰. The broad negative correlation between MgO content in spinel and δ^{26}Mg of garnet supports this explanation (Fig. 3-10F). With progressive Mg loss from spinel to the surrounding garnet, garnet exhibits an increasingly heavier δ^{26}Mg. Deviation from this trend may suggest additional Mg input to garnet from olivine or pyroxene (Fig. 3-1H–J). Similar incomplete isotopic exchange processes during melt–rock interaction have also been invoked for the inter-mineral Mg–Fe–Li isotope disequilibrium found in peridotites from this craton (Tang et al., 2007, 2011; Yang et al., 2009; Zhang et al., 2010; Zhao et al., 2010; Xiao et al., 2013).

Among the generally equilibrated olivine-pyroxene mineral pairs, samples D 01, D 09 and D 7S seem to have an anomalous, larger fractionation, suggesting additional influence of small-scale diffusional processes associated with the different Mg diffusivity in these minerals. Sample D 7S has the lightest olivine (−0.40‰), clinopyroxene (−0.46‰), and orthopyroxene (−0.37‰), reflecting isotopic exchange with the inferred isotopically light metasomatic melt, and the consequent reduced fractionation of garnet relative to these minerals (e.g., $\Delta^{26}Mg_{Cpx–Grt}$ = 0.11‰). On the other hand, sample D 01 and D 09 document the largest garnet-olivine/pyroxene fractionations in this study (e.g., $\Delta^{26}Mg_{Ol–Grt}$ = −0.80‰), and their clinopyroxene–garnet fractionations are consistent with equilibrium

fractionation values. Therefore, the anomalously heavy δ^{26}Mg in olivines (δ^{26}Mg = +0.05‰ and 0.00‰) may result from diffusional loss of light Mg isotopes to garnet during re-equilibration with isotopically light garnet (δ^{26}Mg = −0.75‰ and −0.76‰). This explanation is consistent with the faster diffusion of Mg in olivine than in pyroxene (Chakraborty, 2010; Cherniak and Dimanov, 2010).

The Mg isotopic disequilibrium in the garnet-bearing pyroxenites suggests that the melt–rock interaction that gave rise to these xenoliths probably occurred shortly before their entrainment into the host basalts, especially considering the rapid diffusion rate at mantle temperatures. For example, the self-diffusion coefficient of Mg in garnet (~1.6×10^{-15} cm^2/s at 1000°C, Ganguly, 2010) predicts that Mg isotopic disequilibrium may persist for ~1.25 Ma over 2.5 mm in width. Further constraints on the timing of metasomatism may be provided by the olivine Mg–Fe zoning present in some samples. Taking the self-diffusion coefficient of Mg in olivine (~3.2×10^{-15} cm^2/s at 1000°C, Chakraborty, 2010), the widest observed elemental zoning (~500 μm) would be obliterated after 25 kyr. Therefore, these samples have probably been entrained by host magma and transported to the surface not long after the garnets started to form, and thus there was not sufficient time for the metasomatic garnets to reach isotopic equilibrium with the primary olivines and pyroxenes.

5.2. Garnet-free websterites and orthopyroxenite

Both Cr and Al pyroxenites are commonly found in alkali basalts along with peridotites at Hannuoba and worldwide, either as composite xenoliths along with wall rock peridotites or as discrete xenoliths. They are generally interpreted as crystallization

products of high-pressure basaltic melts passing through the lithospheric mantle (Frey and Prinz, 1978; Irving, 1980; Xu, 2002). The Cr and Al websterites, as well as the orthopyroxenite analyzed here have mantle-like δ^{26}Mg for both whole rocks (−0.17‰ to −0.32‰) and minerals (−0.21‰to −0.33‰). In comparison, Hannuoba alkali basalts have lighter δ^{26}Mg values, and are markedly different in Sr–Nd–Pb isotopic composition from the pyroxenites (Xu, 2002; Choi et al., 2008). Therefore, these xenoliths are not co-genetic with their host basalts.

Lithium isotopic characteristics of the Hannuoba peridotites suggested modification of the lithospheric mantle by asthenospheric melts (Tang et al., 2007), which should have δ^{26}Mg values identical to mantle peridotites, as sampled by global oceanic basalts (Teng et al., 2010a). Therefore, the Cr and Al websterites and the orthopyroxenite analyzed here may represent different episodes of silicate melt injection from the asthenosphere. Xu (2002) further suggested the involvement of recycled continental crust in their parental magmas based on Sr–Nd isotopic evidence. However, limited contributions from continental crust are difficult to manifest themselves in Mg isotopic compositions of these pyroxenites since crustal materials from continents have much lower Mg concentration than the mantle and major Mg-bearing minerals in crustal rocks, including biotite, hornblende and pyroxene, have a broadly mantle-like δ^{26}Mg (Liu et al., 2010a).

5.3. Garnet-free clinopyroxenites

The two garnet-free clinopyroxenites analyzed here yield consistent light δ^{26}Mg values for both whole rocks and clinopyroxene fragments, which are also the lightest values

reported for mantle rocks so far. These extremely light Mg isotopic compositions imply that their origin may be closely related to migration of carbonatitic melts in the mantle, which are considered to be a major source of light Mg isotopes (Young and Galy, 2004). The two clinopyroxenites show the strongest enrichment in LREE among all the pyroxenites studied here (Fig. 3-3C), with $La/Yb_{(N)}$ of 16.4 and 17.1. Their elevated Zr/Hf ratios (40.0 and 43.6) than the primitive mantle (36.2) (Fig. 3-3D) also suggest influence from carbonatites, which typically have high Zr/Hf ratios (Rudnick et al., 1993). More importantly, their low Ti/Eu ratios (Fig. 3-10) are consistent with their origin from carbonatites (Rudnick et al., 1993; Coltorti et al., 1999). Clinopyroxenes with similar composition have also been found in a few Hannuoba peridotite xenoliths (Yu et al., 2006).

The presence of 48–64 Ma igneous zircons with pronounced enrichments in REE, U, and Th in garnet pyroxenites (Liu et al., 2010c) and the discovery of carbonatite veins cutting through host peridotites in the Hannuoba locality (Fan et al., 2010; Liu et al., 2010c) also support carbonatitic melt activity. Using the average Ti/Eu ratio of carbonatite reported in Fan et al. (2010), the Mg isotopic composition of these clinopyroxenites can be explained by binary mixing between mantle peridotites and recycled carbonates with $\delta^{26}Mg$ values of −3.00‰ to −5.00‰ (Fig. 3-11), which is the typical $\delta^{26}Mg$ range of carbonate minerals (Young and Galy, 2004; Saenger and Wang, 2014). In addition, the estimated compositions of hypothetical melts in equilibrium with the two garnet-free clinopyroxenite xenoliths are similar to those of carbonatites from the North China Craton (Ying et al., 2004). Therefore, we interpret these clinopyroxenites to be formed by de-carbonation of migrating carbonatite melts, during which the isotopically light Mg together with Ca from the carbonates will be incorporated into clinopyroxene with the release of

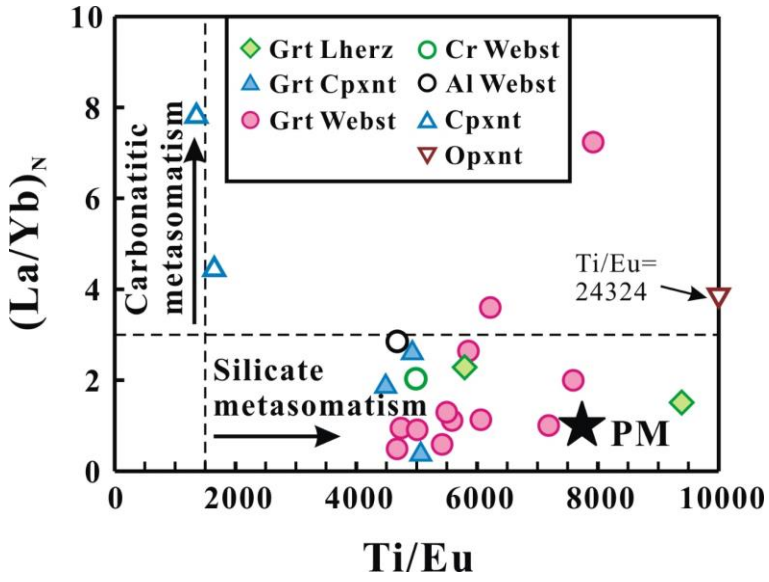

Figure 3-10. Ti/Eu vs. $(La/Yb)_N$ plot for distinguishing between carbonatite metasomatism and silicate metasomatism (Coltorti et al., 1999).

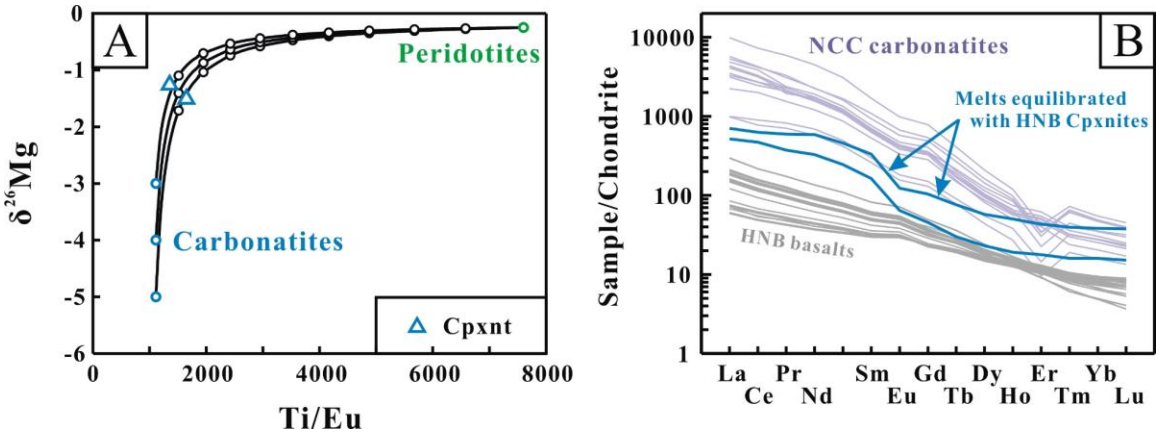

Figure 3-11. Trace element and Mg isotopic compositions of the two Hannuoba clinopyroxenites suggest involvement of carbonatites in their genesis. (A) δ^{26}Mg (‰) versus Ti/Eu ratio for the two Hannuoba garnet-free clinopyroxenites can be modeled by binary mixing between peridotites from the North China Craton (Teng et al., 2010a) and carbonatites that have δ^{26}Mg of −3.00‰ to −5.00‰. Ti/Eu ratios of the carbonatites are based on the average composition of Hannuoba carbonatites reported by Fan et al. (2010). Error bars for δ^{26}Mg are smaller than the sample symbols. (B) Calculated equilibrated melts with these clinopyroxenites by using the Cpx-carbonatite partition coefficients provided in Adam and Green (2001). Compositions of carbonatites from the North China Craton (NCC) (Ying et al., 2004) and Hannuoba (HNB) basalts (Qian et al., 2015) are shown for comparison.

CO_2 (Yaxley et al., 1991; Knoche et al., 1999).

The carbonatitic melts gave rise to these light clinopyroxenites are more likely sourced from recycled carbonates instead of the asthenosphere, as experimental study of Macris et al. (2013) has shown no analytically resolvable fractionation between magnesite and olivine at >800°C, while the fractionation increases significantly at lower temperature (e.g., 0.44‰ at 600°C). This is consistent with the extremely light δ^{26}Mg values found in sedimentary carbonates (e.g., Higgins and Schrag, 2010). Considering the geographical contiguity of the Hannuoba basaltic plateau to the Taihang mountains and the similarity between the δ^{26}Mg feature of the Hannuoba basalts to that of the Taihang basalts, it is reasonable to infer that the Hannuoba lithospheric mantle has likely been affected by the same carbonatitic metasomatic event. Moreover, the isotopically light (δ^{26}Mg = −0.39‰) garnet lherzolite from western Qinling, which has subjected to strong carbonatite metasomatism, further confirms that the δ^{26}Mg value of mantle xenoliths can be lowered by reaction with carbonatitic melts.

5.4. Implications on mantle δ^{26}Mg heterogeneity

Previous Mg isotopic measurements on global peridotite xenoliths and oceanic basalts have suggested a homogeneous mantle with respect to Mg isotope distribution (Teng et al., 2010a). However, there is now accumulating evidence for the existence of local mantle domains with variable δ^{26}Mg values that are thought to be the result of interaction of normal δ^{26}Mg mantle with migrating mantle melts/fluids (Yang et al., 2012; Xiao et al., 2013; Huang et al., 2015). For example, the formation of different types of Hannuoba mantle pyroxenites have been related to injections of melts with diverse

compositions into the subcontinental lithospheric mantle (SCLM), which register these pyroxenites with different δ^{26}Mg characteristics. Likewise, basalts erupted on continents have frequently been found to be isotopically light (Yang et al., 2012; Huang et al., 2015; and this study), in contrast to the homogeneous oceanic basalts (Teng et al., 2010a). Since partial melting and subsequent magma differentiation do not fractionate Mg isotopes (Teng et al., 2007, 2010), the distinct δ^{26}Mg signals carried by these continental basalts should mainly reflect their source heterogeneity. Soughing out the cause of these mantle anomalies is thus critical for us to better understand the overall Mg isotopic composition of the bulk silicate Earth.

The main feature distinguishes basalts generated at continental settings from those at oceanic setting is the existence of a thick layer of SCLM on top of the asthenosphere, which continuously digesting deep fluids/melts rising upward, replenishing the SCLM with elements that were depleted due to earlier melting events. As a result, the SCLM becomes a compositionally and lithologically heterogeneous reservoir (e.g., Brooks et al., 1976; Foley, 2008), contributing to continental magmatism by itself or together with contributions from asthenospheric melts (e.g. McDonough, 1990 and references therein).

Recycled oceanic crusts have been considered as a primary contributor to mantle chemical and isotopic anomalies as they can presumably carry the surface fractionation signals imparted by seafloor alteration into the deep mantle (Yang et al., 2012). The recycled carbonated oceanic crust (−0.80‰ to −0.14‰, Wang et al., 2012) and the overlying sediments (−5.31‰ to −1.09‰, Young and Galy, 2004; Tipper et al., 2006a,b; Brenot et al., 2008; Pogge von Strandmann, 2008; Hippler et al., 2009; Higgins and Schrag, 2010) will thus become an anomalous Mg isotopic reservoir in the mantle. When partial

melting occurs, their heterogeneous Mg isotopic features may propagate into the ambient mantle via a variety of metasomatic melts (e.g., carbonatite, carbonated silicate, and silicate melts), which percolate and infiltrate the mantle wall-rock. The reaction products, as represented by the diverse pyroxenites studied here, do exhibit a larger variation in δ^{26}Mg than peridotites, with δ^{26}Mg values as low as −1.51‰ having been found. Due to their relatively lower solidus temperatures, pyroxenites will melt preferentially with a higher melt-producing efficiency relative to the ambient peridotites. Therefore, when contributed to continental magmatism, these heterogeneous pyroxenites will further modify the Mg isotopic composition of mantle-derived volcanic rocks.

Subducted slabs have also been suggested in the source region of oceanic island basalts (OIB). The absence of isotopically distinct OIB (Teng et al., 2010a) may partially due to the relatively cold and conductive nature of the SCLM, which keeps the isotopically distinct domains lasting longer than those in the warmer sub-oceanic mantle, where largescale convection and continuous melting at the mid-ocean ridge tend to eliminate all heterogeneities. In contrast, the long-term stability of the SCLM makes it an increasingly heterogeneous reservoir through time. During eruption gaps of continental magmatism, the SCLM can receive frequent melt modification and consequently give rise to new anomalous δ^{26}Mg domains. In addition, oceanic–continental subduction is a more frequent phenomenon than oceanic–oceanic subduction. Therefore, there might be more relic slabs sitting beneath the continents. Frequent subduction from circum plates around continents also makes the SCLM a relatively closed system, preventing the isotopically heterogeneous domains from incorporating into the global mantle convection.

6. Conclusions

This study presents the first systematic dataset for high-precision Mg isotopic analyses on mantle pyroxenites, coupled with their whole rock and mineral chemical compositions. It highlights the potential of using Mg isotopes along with the traditional Sr–Nd–Pb isotopic systematics to trace melt activities in the mantle and the origin of different types of mantle pyroxenites. The following conclusions can be drawn:

(1) The garnet-bearing lherzolites and pyroxenites, which represent reaction products between peridotites and slab-derived melts, have variable δ^{26}Mg ranging from −0.48‰ to −0.10‰ (n = 17). There is a broad isotopic equilibrium among co-existing olivine, clinopyroxene, and orthopyroxene. However, garnet that is formed in a reacting relationship with spinel, olivine, and pyroxene has not yet reached Mg isotopic equilibrium with these minerals. Contributions of heavy Mg isotopes from the enclosed minerals, particularly spinel, drove the δ^{26}Mg of garnet to variably heavier values of −0.76‰ to −0.37‰ (n = 15).

(2) Both garnet-free websterites and the orthopyroxenite have δ^{26}Mg values (−0.17‰ to −0.32‰) comparable to that of the mantle range (−0.25 ± 0.07‰, Teng et al., 2010a). They may thus represent different episodes of asthenospheric melts injection into the subcontinental lithospheric mantle.

(3) The extremely light δ^{26}Mg values exhibited by the two garnet-free clinopyroxenites (−1.39‰ and −1.51‰) imply an episode of carbonatitic melt activity. The carbonatitic melts are likely to have been involved in the mantle source of Hannuoba alkali basalt, which also exhibits a light Mg isotopic composition.

7. Appendix A. Supplementary data

Supplementary data associated with this article can be found, in the online version, at http://dx.doi.org/10.1016/ j.gca.2015.11.001.

Acknowledgements. We would like to thank Kang-Jun Huang, Xiao-Ming Liu, and Juan Zhang for analytical and laboratory assistance. We are also grateful to Aaron Brewer, Anthony J. Irving, Scott Kuehner, Yang Sun and Shui-Jiong Wang for stimulating discussions. The manuscript has been greatly benefited from comments by C. A. Macris and two anonymous reviewers; editorial handling by Shichun Huang is also much appreciated. This research has been financially supported by National Science Foundation grants of China (Grants 91214293 and 91014007 to H.-F. Zhang), National Science Foundation of America (EAR-0838227, EAR-1056713 and EAR-1340160 to F.-Z. Teng), and 2014 graduate student research grant from the Geological Society of America (to Y. Hu).

Chapter 4. Magnesium isotopic composition of subducting marine sediments

This chapter is published as:

Hu, Y., Teng, F.-Z., Plank, T. and Huang, K.-J. (2017) Magnesium isotopic composition of subducting marine sediments, Chemical Geology, 466, 15-31.

Abstract

Subducted sediments have been suggested to be a possible cause for local Mg isotopic variation in the overall homogeneous mantle based on anomalous Mg isotopic compositions detected in some mantle-derived rocks. Here we examine the Mg isotopic systematics of 77 bulk marine sediment samples from ten DSDP and ODP drill sites adjacent to the world's major subduction zones to assess their potential to cause mantle heterogeneity. In contrast to the limited mantle range ($\delta^{26}Mg = -0.25 \pm 0.07‰$), $\delta^{26}Mg$ of these sediments varies widely from −1.34‰to +0.46‰, which is similar to values measured in continental sediments and appears to be linked to sediment lithology. Calcareous oozes are generally isotopically lighter than seawater; however, the presence of detrital impurities can shift their $\delta^{26}Mg$ to higher values. In comparison to calcareous oozes, Mg-rich aluminosilicate sediments typically have higher $\delta^{26}Mg$ values, although they may be either isotopically heavier or lighter than the mantle. Detrital sediments are the dominant sediment type and display large variation (−0.90‰ to +0.18‰) that reflects provenance heterogeneity and textural/mineralogical sorting. Sediments derived from juvenile terranes have $\delta^{26}Mg$ similar to mantle values while those derived from mature,

and thus more strongly weathered sources, often have higher δ^{26}Mg values. On the other hand, turbidites may have lower δ^{26}Mg values if containing isotopically light dolomite and/or garnet. In addition, clay-size fractions in turbidites commonly have higher δ^{26}Mg than the associated sands. Hydrogenetic clays have a relatively high and uniform δ26Mg value of +0.02 ± 0.14‰ (2SD, n= 14), suggesting preferential uptake of heavy Mg isotopes during authigenic clay formation while hydrothermal clays have highly variable δ^{26}Mg values (−0.57‰ to +0.46‰) that likely reflect variable exchange with seawater/hydrothermal fluids. Overall, considerable variations exist in both regional Mg mass flux and the weighted δ^{26}Mg average of sedimentary sections subducting at different trenches. The flux-weighted δ^{26}Mg of −0.336‰ is estimated for Global Subducting Sediments (GLOSS-II), which is isotopically lighter than the mantle average because of the presence of thick turbidite sequences with relatively low δ^{26}Mg values and local carbonate enrichment in a few trenches near the equator. Therefore, it appears that subducting marine sediments are a source of heterogeneous δ^{26}Mg values in the mantle, and they may be manifested locally in volcanic rocks that form in regions having a high flux of sediment melts to the mantle.

1. Introduction

Subduction of oceanic crust with its overlying sediments has long been considered an essential mechanism of elemental cycling from Earth's surface to its interior, thereby producing chemical and isotopic heterogeneity in mantle rocks and mantle-derived magmas (e.g., Armstrong, 1968; Hofmann, 2014 and references therein). Recently, this process has also been called upon to explain local Mg isotopic variations in the mantle (e.g.,

Yang et al., 2012; Xiao et al., 2013; Hu et al., 2016a; Li et al., 2017). The majority of mantle peridotites and oceanic basalts have similar Mg isotopic compositions ($\delta^{26}Mg = -0.25 \pm 0.07‰$, 2SD, Teng et al., 2010a), suggesting homogeneous distribution of Mg isotopes in the mantle. Nevertheless, some mantle xenoliths (e.g., wehrlite, pyroxenite and eclogite) and mantle-derived lava possess $\delta^{26}Mg$ values that lie outside the well-defined mantle range, and could reflect a contribution from recycled crustal Mg (Wang et al., 2012, 2015a, 2016; Yang et al., 2012; Xiao et al., 2013; Huang et al., 2015; Liu et al., 2015; Hu et al., 2016a; Tian et al., 2016; Teng et al., 2016; Li et al., 2017).

Despite this indirect evidence, Mg isotopic compositions of subducting input from the down-going oceanic slab and overlying marine sediments are not well constrained as yet. Recent studies on altered oceanic basalts, altered ultramafic rocks, and abyssal peridotites suggest the subducting slab has heterogeneous Mg isotopic compositions (Huang, 2013; Beinlich et al., 2014; Liu et al., 2017). Magnesium isotopic composition of marine sediments, on the other hand, is still largely unknown. The few available studies mainly focused on marine carbonates, which generally take up light Mg from the solutions (Galy et al., 2002; Higgins and Schrag, 2010; Teng, 2017 and references therein). However, marine carbonates only account for approximately 7% of the present-day Global Subducting Sediments (GLOSS) and are dominantly calcareous in composition (Plank and Langmuir, 1998). The low abundance and low Mg concentration of the calcium carbonates limit their impacts on the overall Mg isotopic composition of GLOSS. Instead, aluminosilicate and biosiliceous marine sediments make up the bulk of GLOSS and dominate its Mg budget (Plank and Langmuir, 1998). Their Mg isotopes, however, have been much less studied. As yet, the only measured siliciclastic subducting sediments were

recovered from the Deep Sea Drilling Project (DSDP) sites 543 and 144 near the Antilles margin, and from the Ocean Drilling Program (ODP) site 1230 near the Peru trench (Mavromatis et al., 2014; Teng et al., 2016). Their δ^{26}Mg range (−0.76‰ to +0.52‰) covers half the variation found in siliciclastic sediments on land (−1.64‰ to +1.82‰, Huang et al., 2013; Liu et al., 2014). Furthermore, the δ^{26}Mg values of these sediments are on average higher than those of typical igneous rocks (Li et al., 2010; Liu et al., 2010; Teng et al., 2010a). This enrichment of ^{26}Mg in siliciclastic sediments is consistent with the general trend of Mg isotope fractionation during continental weathering, with light Mg isotopes being preferentially released to the rivers (average δ^{26}Mg = −1.09‰, Tipper et al., 2006a) and oceans (average δ^{26}Mg = −0.83 ± 0.09‰, 2SD, Foster et al., 2010; Ling et al., 2011), leaving an isotopically heavy residue (e.g., Tipper et al., 2006b; Teng et al., 2010b; Wimpenny et al., 2010; Liu et al., 2014). However, the partition mechanisms of Mg isotopes in marine environment, particularly during sediment-seawater/marine life interaction, are still not well understood and require a more detailed study on different types of marine sediments.

Here, to evaluate Mg isotopic variation in subducting sediments on a global scale, we select ten contrasting drill sites adjacent to major active subduction zones and measure the Mg isotopic composition of a total of 77 marine sediment core samples from these sites. They are representative of the global range of sediment age, composition, lithological type, and sedimentary flux at different subduction systems, and link to the work of Plank and Langmuir (1998), Vervoort et al. (2011) and Plank (2014). This study provides the first systematic investigation of Mg isotopic variation in subducting sediments worldwide. Together with the data reported for Antilles sediments in Teng et al. (2016), these data are

used to evaluate the global sedimentary Mg input to subduction zones and to assess their role in intra-plate magmatism and in generating mantle heterogeneity.

2. Samples

Sediments analyzed in this study include those subducting at the following convergent margins in the Pacific, Atlantic and Indian Oceans: DSDP sites 174 (Cascadia), 178 (Alaska), 211 (Java-Sumatra), 291 (Philippines), 294/295 (Ryukyu), 321 (Peru), 595/596 (Tonga), 495 and ODP sites 844B (Central America) and 701 (South Sandwich) (Fig. 4-1). Detailed site descriptions are available in Plank and Langmuir (1998), Vervoort et al. (2011) and Plank (2014). These sediments display wide variations in their major, trace, and Nd-Hf-Pb-Li isotopic compositions (Plank and Langmuir, 1998; Chan et al., 2006; Prytulak et al., 2006; Vervoort et al., 2011; Plank, 2014), with the new estimate of the GLOSS (GLOSS-II, Plank, 2014) falling within the middle of the range (Fig. 4-2).

The first-order control for major element variation in these sediments is dilution of detrital clay by biogenic silica and calcium carbonate (Fig. 4-2A and B). Magnesium in marine sediments is mainly partitioned among three components: 1) detrital phases derived from either primary mafic minerals/oxides or weathering products; 2) authigenic (in situ) clays; and 3) biogenic and abiogenic carbonates. Among them, the detrital component contributes the most important Mg input to subducting sediments due to their predominance in GLOSSII, leading to a positive correlation between MgO and Al_2O_3 (Fig. 4-2C).

The detritus-dominated sediments mainly include turbidites and terrigenous clays. The turbidites likely inherit $\delta^{26}Mg$ signatures from their protoliths due to proximity to the

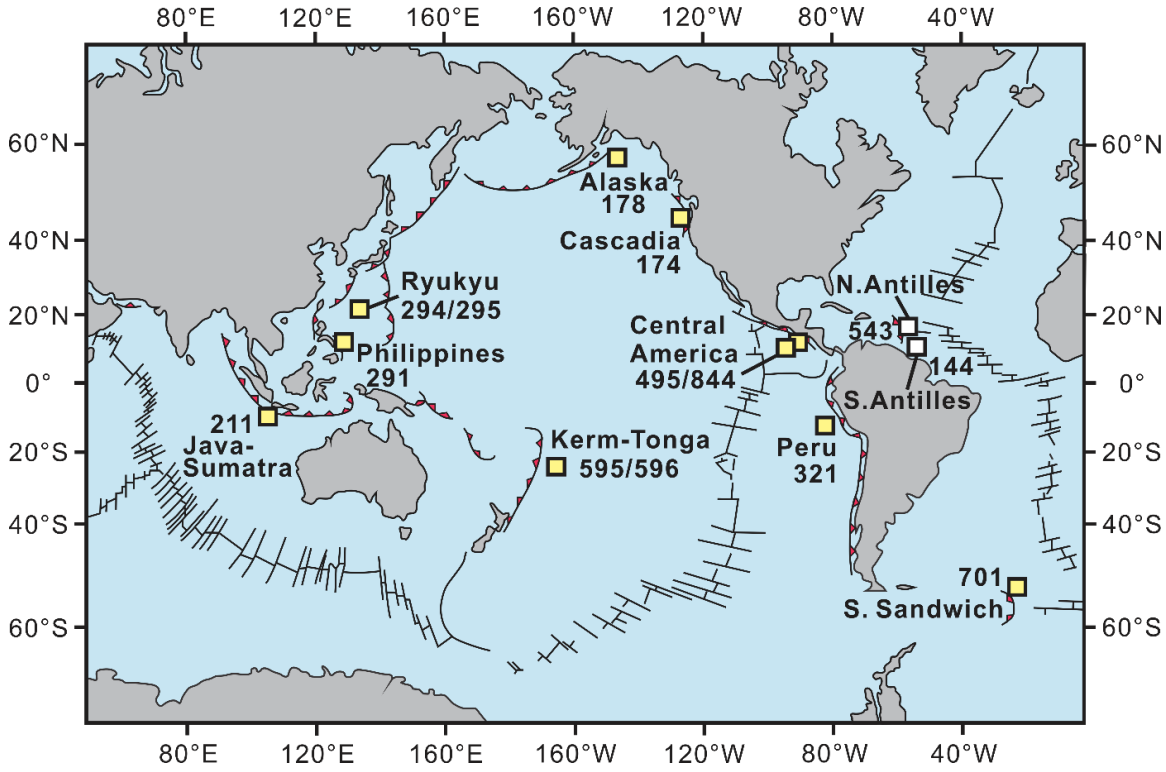

Figure 4-1. Geographic map showing the sample locations of the ten drill sites analyzed in this study (yellow square) and the other two sites analyzed in previous work (white square, Teng et al., 2016). After Plank (2014).

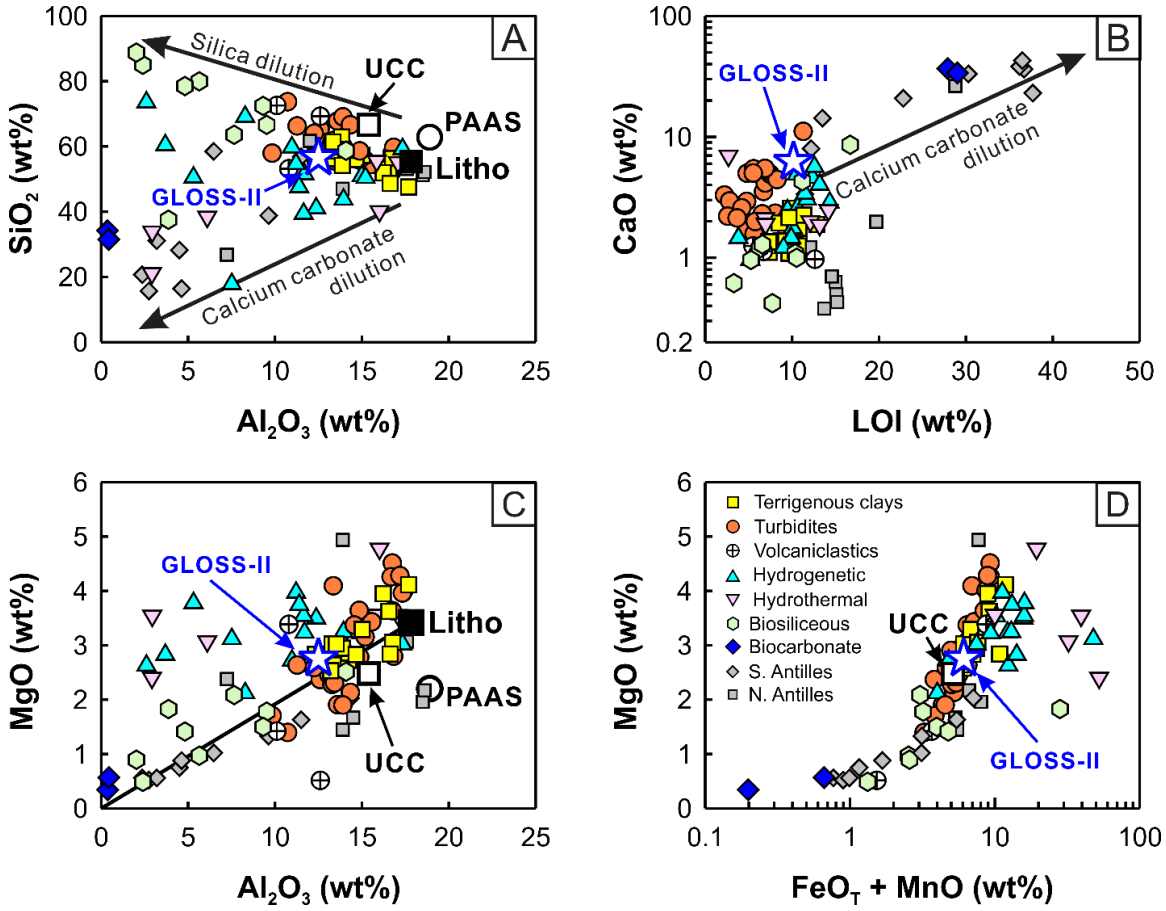

Figure 4-2. Major element variability of subducting sediments investigated in this study. (A) Variations of SiO_2 with Al_2O_3 indicate dilution trends of a clay-rich component by biogenic silica and calcium carbonate, respectively. (B) Positive correlation between CaO and loss on ignition (LOI) reflects the effect of carbonate dilution. (C) Detrital sedimentsand most siliceous oozes have MgO/Al_2O_3 ratios similar to that of the average lithogenous clay ("Litho", Riley and Chester, 1971) while hydrogenetic sediments commonly have elevated MgO/Al_2O_3 ratios. (D) Enrichment of Fe and Mn in hydrothermal (Fe-rich) and hydrogenetic sediments. FeO_T means that total Fe is expressed as FeO. Also shown for comparison are the average compositions of upper continental crust (UCC, Rudnick and Gao, 2014), Post-Archean Australian Shale (PAAS, Taylor and McLennan, 1985), and global subducting sediments (GLOSS-II, Plank, 2014). Element concentration data for this and following figures are from Vervoort et al. (2011) and Carpentier et al. (2009).

continents and rapid deposition. Particularly, the turbidite sequences from DSDP 174 (Cascadia), 178 (Alaska), and 211 (Sumatra-Java) are selected due to their high contributions to the global flux of sediments approaching subduction zones (von Huene and Scholl, 1991). Sediments from ODP 701 (South Sandwich), DSDP 495 (Central America) and DSDP 321 (Peru) contain abundant eolian input derived from the continents. They are classified as terrigenous clays after Vervoort et al. (2011), where "terrigenous" distinguishes pelagic sediments rich in land-derived detritus from those dominated by authigenic phases. Although both are sourced from continents, terrigenous clays may carry a different $\delta^{26}Mg$ signature from turbidites due to concentration of fine-grained clay minerals and depletion of primary minerals.

Sediments from sites approaching the Philippines (DSDP 291), Ryukyu (DSDP 294/295) and Tonga (DSDP 595/596) trenches are dominated by abyssal pelagic clays of brown or black colour. Authigenic phases of hydrogenetic or hydrothermal origin may be an important contributor of Mg to these sediments due to limited detrital input and slow deposition, consistent with the elevated MgO/Al_2O_3 ratios in most of the samples (Fig. 4-2C). Furthermore, these sediments are generally rich in Mn and Fe compared to detrital clays, indicating scavenging of dissolved metal from seawater and subsequent formation of Fe-Mn oxyhydroxides (Fig. 4-2D). The prevalence of authigenic phases in these sediments may hence give them a distinctive $\delta^{26}Mg$ fingerprint.

Sediments along the equatorial Pacific and in the polar oceans often contain abundant biogenic phases. The major sediment-forming biogenic components include calcareous oozes (> 30% skeletal carbonates) and siliceous oozes (> 30% skeletal opals). Biosiliceous oozes in this study have SiO_2 varying mostly between 60 wt% and 80 wt%

except an FeO-rich (28 wt%), SiO_2-poor (38 wt%) radiolarian ooze from DSDP 291 (Philippines). The Mg content in these siliceous oozes may reflect impurities of detrital clays or volcanic ashes, as their MgO/Al_2O_3 ratios generally fall on the dilution trends of turbidites and terrigenous clays. A few samples have slightly higher MgO/Al_2O_3 ratios and higher FeO content (Fig. 4-2C and D), suggesting uptake of Mg by biogenic silica and formation of authigenic aluminosilicate minerals (e.g., Donnelly and Merrill, 1977; Cole and Shaw, 1983). In comparison, calcareous oozes are mainly calcium carbonate in nature, with limited Mg present as a substitute for Ca. Therefore, their Mg isotopic compositions could also be variably affected by more Mg-rich clay impurities.

3. Analytical methods

Chemical separation and isotopic analysis were performed at the Isotope Laboratories of both University of Washington, Seattle, and University of Arkansas, Fayetteville, following previously described techniques (Teng et al., 2007, 2010a; Li et al., 2010). Sample powders containing approximately 50 μg Mg were dissolved in clean Savillex screw-top beakers in a mixture of Optima-grade concentrated HF-HNO_3-HCl at 120 °C.

Up to three stages of cation-exchange chromatographic columns were used in this study to separate Mg from the matrix elements. First, the majority of Ca was removed using Bio-Rad Poly-prep 10 mL columns containing ~1 mL highly cross-linked Bio-Rad AG50W-X 12 resin in 12 N HCl (Ling et al., 2013a). This step was repeated for samples with high Ca/Mg ratios (> 50). The solutions collected from the Ca removal column were dried down and converted to 1 N HNO_3 media, then passed through borosilicate glass

columns packed with Bio-Rad AG50W-X 8 resin. This step was repeated for all samples to ensure complete removal of major matrix elements (e.g., Na, K, Al and Fe). Finally, Mn-rich samples (Mn/Mg > 0.1) were passed through an additional Mn removal column using Bio-Rad AG50W-X8 resin in 0.5 N HCl-95% acetone (Schiller et al., 2010). After this step, sample solutions were evaporated to dryness and converted to nitrate form for instrumental analysis.

Magnesium isotope ratios were measured on three different instruments, including a Nu Plasma HR MC-ICP-MS at the University of Arkansas, Fayetteville, and both a Nu Plasma HR MC-ICP-MS and a Nu Plasma II MC-ICP-MS at the University of Washington, Seattle. Purified samples were diluted to 300 to 500 μg/kg Mg concentration in 3% HNO_3 (Optima-grade) and introduced into the plasma source under wet plasma conditions using a MicroMist low-flow nebulizer in conjunction with a low-volume Cinnabar spray chamber. Magnesium isotopic data are measured using standard-sample bracketing method (Teng and Yang, 2014) and are reported as relative deviations from the DSM-3 standard (Galy et al., 2003) in δ notation according to the following formula:

$$\delta^{x}\mathrm{Mg}\ (‰)=\left\{\frac{\left(^{x}\mathrm{Mg}/^{24}\mathrm{Mg}\right)_{\mathrm{sample}}}{\left(^{x}\mathrm{Mg}/^{24}\mathrm{Mg}\right)_{\mathrm{DSM3}}}-1\right\}\times 1000,$$

where X= 25 or 26. The associated error is 2SD, which represents two times the standard deviation of multiple analyses of bracketing standards during an analytical session (Teng et al., 2015).

To evaluate the accuracy of the full chemical procedure, two shale standards (SCo-1 and SGR-1) from the United States Geological Survey (USGS) and a basalt standard (JB-1) from the Geological Society of Japan (GSJ) were processed along with sediment samples.

The silty marine shale SCo-1 and the carbonate-rich shale from the Green River Formation SGR-1 yield average δ^{26}Mg values of −0.86 ± 0.06‰ (n = 2) and −0.98 ± 0.06‰ (n = 5), respectively, while the basalt JB-1 gives an average δ^{26}Mg value of −0.25 ± 0.03‰ (n = 5). These values are consistent with the recommended values of −0.89 ± 0.08‰, −1.00 ± 0.08‰, and −0.28 ± 0.10‰, respectively (Table A1) (Teng et al., 2015; Teng, 2017). The accuracy of column chemistry and the external reproducibility are further examined by processing and analyzing two in-house standards (San Carlos olivine and Hawaiian seawater) with each batch of column chemistry and instrumental analysis. The lherzolitic San Carlos olivine yields an average δ^{26}Mg value of −0.25 ± 0.04‰ (n = 28), comparable to literature average of −0.24 ± 0.03‰ (Hu et al., 2016b); the Hawaiian seawater yields an average δ^{26}Mg value of −0.84 ± 0.05‰ (n = 20), identical to the recommended value of −0.84 ± 0.06‰ (Teng et al., 2015). The results from repeat, duplicate, and replicate analyses agree within 0.05‰ for both δ^{26}Mg and δ^{25}Mg (Table 4-A1 and Table 4-1), even though some of the samples were processed in two different laboratories and measured on three different instruments. Therefore, the overall analytical uncertainty over the course of this study is compatible with the long-term external precision of this laboratory, i.e., better than 0.07‰ for δ^{26}Mg and 0.05‰ for δ^{25}Mg (Teng et al., 2015).

4. Results

Magnesium isotopic compositions of marine sediments are reported in Table 4-1 and are plotted in Fig. 4-3. The linear regression between δ^{26}Mg and δ^{25}Mg values of all samples and standards analyzed in this study yields a slope of 0.515 (R^2 = 0.997). Hence only δ^{26}Mg values are presented and discussed hereafter.

Table 4-1. Magnesium isotopic compositions of marine sediments from various DSDP and ODP sites outboard of subduction zones

Sample	Unit	Depth (m)	Litho	Age (Ma)	δ^{26}Mg (‰)	2 SD	δ^{25}Mg (‰)	2 SD	Description
DSDP Site 174 – Cascadia									
174A-1-1-62-67*	1	0.62	TB	0.00	−0.20	0.06	−0.12	0.06	silty clay
174A-2-6-47-53	1	45.47	TB	0.20	−0.33	0.07	−0.15	0.05	clay
Repeat					−0.37	0.07	−0.19	0.03	
Duplicate					−0.39	0.07	−0.21	0.05	
repeat					−0.39	0.07	−0.21	0.05	
average					***−0.38***	***0.04***	***−0.20***	***0.02***	
174A-8-3-93-98*	1	98.43	TB	0.44	−0.40	0.06	−0.21	0.06	clay
repeat					−0.41	0.07	−0.22	0.03	
duplicate					−0.43	0.07	−0.21	0.05	
repeat					−0.41	0.07	−0.20	0.03	
average					***−0.41***	***0.03***	***−0.21***	***0.02***	
174A-8-6-57-62*	1	102.57	TB	0.46	−0.49	0.06	−0.24	0.06	sandy
174A-19-2-107-113*	1	201.57	TB	0.90	−0.50	0.06	−0.23	0.06	sand
duplicate					−0.49	0.07	−0.24	0.05	
average					***−0.49***	***0.05***	***−0.24***	***0.04***	
174A-19-4-32-36*	1	203.82	TB	0.91	−0.41	0.06	−0.19	0.06	silty
174A-27-2-125-130*	1	277.75	TB	1.24	−0.49	0.06	−0.22	0.06	silty clay
duplicate					−0.50	0.07	−0.26	0.05	
average					***−0.49***	***0.05***	***−0.24***	***0.04***	
174A-33-2-106-111	2	344.06	TB	1.54	−0.40	0.06	−0.20	0.06	silty clay
174A-33-2-132-137	2	344.32	TB	1.54	−0.57	0.06	−0.28	0.06	sand
duplicate					−0.58	0.07	−0.29	0.05	
average					***−0.57***	***0.05***	***−0.29***	***0.04***	
174A-37-2-123-127*	2	505.73	TB	2.15	−0.44	0.06	−0.20	0.06	clay
duplicate					−0.40	0.07	−0.21	0.05	
repeat					−0.44	0.07	−0.22	0.03	
average					***−0.43***	***0.04***	***−0.22***	***0.02***	
174A-37-2-134-137*	2	505.84	TB	2.15	−0.53	0.06	−0.23	0.06	sand
duplicate					−0.54	0.07	−0.25	0.05	
average					***−0.54***	***0.05***	***−0.24***	***0.04***	
174A-39-2-22-24*	2	751.72	TB	7.94	−0.21	0.06	−0.11	0.06	clayst
174A-39-2-145-150*	2	752.95	TB	8.00	−0.28	0.07	−0.13	0.07	sandst
repeat*					−0.30	0.06	−0.15	0.06	
repeat					−0.30	0.06	−0.15	0.04	
duplicate*					−0.33	0.06	−0.17	0.07	

repeat*					−0.29	0.06	−0.12	0.06	
repeat					−0.31	0.06	−0.16	0.04	
average					***−0.30***	***0.02***	***−0.15***	***0.02***	
178-1-88-94*	1	0.88	TB	0.00	−0.20	0.06	−0.11	0.07	dark green-green silty
repeat*					−0.20	0.07	−0.10	0.06	
replicate**					−0.22	0.08	−0.11	0.05	
average					***−0.21***	***0.04***	***−0.11***	***0.03***	
178-12-2-112-117*	1	98.62	TB	0.94	−0.25	0.07	−0.14	0.07	dark green-green silty
replicate**					−0.25	0.08	−0.14	0.05	
average					***−0.25***	***0.05***	***−0.14***	***0.04***	
178-24-3-87-92*	1	207.87	TB	2.00	−0.18	0.07	−0.08	0.06	green silty clay
replicate**					−0.19	0.08	−0.07	0.05	
average					***−0.19***	***0.05***	***−0.08***	***0.04***	
178-29-5-129-134*	1	256.29	TB	2.23	−0.12	0.06	−0.08	0.07	green silty clay
replicate**					−0.13	0.09	−0.06	0.07	
average					***−0.12***	***0.05***	***−0.07***	***0.05***	
178-39-5-109-110**	2	398.59	VC		−0.14	0.09	−0.08	0.07	ash
178-47-1-127-130*	2	506.77	TB	3.30	−0.19	0.07	−0.06	0.07	turb top clay
repeat*					−0.15	0.07	−0.07	0.06	
repeat*					−0.18	0.07	−0.08	0.05	
duplicate					−0.19	0.06	−0.09	0.04	
replicate**					−0.19	0.09	−0.09	0.07	
average					***−0.18***	***0.03***	***−0.08***	***0.02***	
178-47-1-141-145*	2	506.91	TB	3.30	−0.18	0.07	−0.09	0.06	Turb bottom sand
duplicate					−0.18	0.07	−0.09	0.05	
replicate**					−0.19	0.09	−0.09	0.07	
average					***−0.18***	***0.04***	***−0.09***	***0.03***	
178-49-1-66-71*	2	591.66	TB	4.09	−0.06	0.09	−0.03	0.06	turb top clay
repeat*					−0.06	0.07	−0.02	0.07	
average					***−0.06***	***0.06***	***−0.03***	***0.04***	
178-49-1-85-90*	2	591.85	TB	4.10	−0.16	0.06	−0.09	0.07	turb bottom sand
repeat					−0.17	0.07	−0.08	0.05	
repeat					−0.15	0.07	−0.08	0.06	
duplicate					−0.16	0.07	−0.08	0.06	
average					***−0.16***	***0.03***	***−0.08***	***0.03***	
178-52-2-127-131*	2	688.77	TB	5.00	−0.24	0.06	−0.09	0.06	diatom clay
repeat*					−0.23	0.07	−0.09	0.06	
repeat					−0.23	0.06	−0.10	0.04	
duplicate					−0.21	0.06	−0.11	0.04	

replicate**					−0.20	0.09	−0.09	0.07	
average					***−0.22***	***0.03***	***−0.10***	***0.02***	
178-54-4-109-113*	3	747.59	HT		−0.06	0.09	−0.02	0.06	brown clay
178-57-1-136-140*	3	769.36	HT	45.00	0.44	0.09	0.23	0.06	brown clay
repeat*					0.47	0.06	0.22	0.06	
duplicate					0.45	0.06	0.23	0.04	
replicate**					0.46	0.09	0.23	0.07	
average					***0.46***	***0.04***	***0.23***	***0.03***	
211-1-2-36-41*	1	1.86	TB	0.50	−0.48	0.10	−0.27	0.07	ash-rich diatom ooze
duplicate					−0.48	0.05	−0.25	0.05	
average					***−0.48***	***0.05***	***−0.26***	***0.04***	
211-1-3-126-127*	1	4.26	VC	0.41	−0.37	0.10	−0.20	0.07	ash layer
duplicate					−0.34	0.05	−0.17	0.05	
average					***−0.35***	***0.05***	***−0.18***	***0.04***	
211-2-4-11-16	1	13.61	TB	2.00	−0.30	0.05	−0.14	0.05	clay-rich diatom ooze
211-5-2-36-40	2	134.86	TB	3.28	−0.06	0.05	−0.02	0.06	rad-rich clay
repeat					−0.04	0.07	−0.03	0.04	
repeat					−0.03	0.06	−0.02	0.05	
average					***−0.05***	***0.03***	***−0.02***	***0.03***	
211-6-4-50-55*	2	185.59	TB	3.82	−0.43	0.10	−0.22	0.07	silty clay
duplicate					−0.42	0.05	−0.22	0.05	
average					***−0.42***	***0.05***	***−0.22***	***0.04***	
211-6-4-60-63*	2	185.69	TB	3.82	−0.36	0.10	−0.18	0.07	silty sand
repeat					−0.37	0.05	−0.18	0.05	
average					***−0.37***	***0.05***	***−0.18***	***0.04***	
211-7-1-131-136*	3	229.31	TB	4.28	−0.91	0.07	−0.45	0.07	silty sand
repeat*					−0.90	0.06	−0.44	0.06	
duplicate					−0.91	0.05	−0.47	0.05	
average					***−0.90***	***0.03***	***−0.45***	***0.03***	
211-9-1-109-115*	3	295.59	TB	4.98	−0.32	0.06	−0.17	0.06	silty clay
701A-1H-4-145-150*	1A	5.9	TC	0.20	−0.20	0.07	−0.11	0.06	diatom ooze+ash
701B-1H-5-145-150*	1A	77.4	TC	3.88	−0.12	0.07	−0.08	0.06	diatom ooze+ash
701B-9H-5-46-50*	1B	150	TC	4.77	−0.38	0.07	−0.20	0.06	diatom ooze+ash
701C-27X-2-140-150*	2A	246.7	TC	11.40	0.09	0.07	0.05	0.06	mud+diatom
701C-31X-2-140-150*	2A	284.7	TC	18.80	−0.03	0.07	−0.03	0.06	silic clay
701C-42X-1-140-150*	2A	387.7	TC	32.00	0.18	0.07	0.11	0.06	clay
duplicate					0.18	0.07	0.10	0.06	
average					***0.18***	***0.05***	***0.11***	***0.04***	

321-1-53-58*	1	0.53	TC	0.5	−0.32	0.06	−0.16	0.06	siliceous detrital clay
321-3-6-24-30*	1	19.08	TC	1.9	−0.30	0.06	−0.14	0.06	siliceous detrital clay
321-4-2-34-40*	1	22.34	TC	2.2	−0.26	0.06	−0.14	0.06	siliceous detrital clay
321-5-4-27-33*	2	34.77	TC	4.7	−0.24	0.06	−0.13	0.06	volcanic glass clay
321-5-4-145-150*	2	35.95	VC	5.1	−0.38	0.06	−0.20	0.07	ash
duplicate					−0.35	0.07	−0.18	0.06	
average					***−0.36***	***0.05***	***−0.19***	***0.04***	
321-6-4-33-39*	2	44.33	TC	8.1	−0.22	0.07	−0.09	0.07	volcanic-glass rich clay
repeat*					−0.22	0.07	−0.10	0.06	
average					***−0.22***	***0.05***	***−0.10***	***0.05***	
321-7-1-93-97*	3	49.93	HD	10.1	−0.12	0.07	−0.03	0.07	brown zeolite clay
duplicate					−0.11	0.07	−0.06	0.05	
average					***−0.11***	***0.05***	***−0.05***	***0.04***	
495-3-1-25-31*	1	19.25	TC	0.5	−0.27	0.07	−0.14	0.06	hemipelagic mud
495-4-5-20-26*	1	34.14	TC	1.1	−0.13	0.07	−0.08	0.06	biogenic silty mud
495-13-3-31-37*	1	117.31	HD	4.4	0.00	0.07	−0.02	0.06	diatomaceous mud
495-16-7-30-35*	1	150.78	HD	8.5	−0.04	0.06	−0.02	0.06	siliceous mud
844B-4H-4-56-57*	IB	28.6	TC	2.8	−0.20	0.10	−0.10	0.07	rad diatom clay (grey)
repeat					−0.21	0.07	−0.11	0.05	
average					***−0.21***	***0.06***	***−0.11***	***0.04***	
844B-6H-6-102-104*	IB	51.03	TC	7.7	−0.21	0.07	−0.11	0.06	rad nanno ooze (grey)
repeat*					−0.23	0.10	−0.10	0.07	
repeat					−0.22	0.07	−0.11	0.05	
average					***−0.22***	***0.05***	***−0.11***	***0.04***	
844B-21X-6-100-102	IIB	193.5	BC	14.3	−1.34	0.05	−0.70	0.05	nanno ooze (light grey)
repeat					−1.33	0.07	−0.68	0.05	
average					***−1.34***	***0.04***	***−0.69***	***0.03***	
844B-30X-6-145-150*	IIB	280.6	BC	17.0	−0.53	0.10	−0.25	0.07	nanno ooze (light grey)
repeat					−0.54	0.07	−0.28	0.05	
repeat					−0.56	0.05	−0.28	0.05	
average					***−0.55***	***0.04***	***−0.27***	***0.03***	
DSDP Site 291 - Philippines									
291-1-1-130-135*	1	1.3	TC	0.4	−0.16	0.07	−0.08	0.07	silty yellow clay
duplicate					−0.14	0.07	−0.05	0.06	
average					***−0.15***	***0.05***	***−0.06***	***0.04***	
291-2-1-133-139*	1	61.33	TC	20.4	0.03	0.07	0.01	0.07	brown silty clay
291-3-1-126-132*	3	80.26	HD	26.8	−0.04	0.07	−0.02	0.07	yellow rad ooze

291-4-1-88-94*	4	98.88	HD	33.0	0.12	0.07	0.07	0.07	brown nanno-rad silty
291-4-2-132-137*	4	100.82	HD	33.6	0.00	0.07	0.00	0.07	brown rad zeolite clay
repeat*					0.01	0.07	0.01	0.05	
average					***0.01***	***0.05***	***0.01***	***0.04***	
291-4-4-62-67*	4	103.12	HD	34.4	0.07	0.07	0.04	0.07	brown Fe-zeolite clay
repeat					0.05	0.06	0.03	0.04	
duplicate					0.07	0.06	0.03	0.04	
average					***0.06***	***0.04***	***0.03***	***0.03***	
DSDP Site 294/5 - Ryukyu									
294-1-3-56-61*	1	3.56	TC	2.0	−0.23	0.07	−0.09	0.07	silt-rich clay
duplicate					−0.22	0.07	−0.12	0.06	
average					***−0.23***	***0.05***	***−0.11***	***0.04***	
294-4-1-110-115*	1	94.1	HD	53.5	0.07	0.07	0.05	0.07	brown clay
repeat					0.06	0.07	0.04	0.05	
repeat					0.06	0.07	0.05	0.06	
duplicate					0.07	0.07	0.04	0.05	
average					***0.07***	***0.04***	***0.04***	***0.03***	
294-4-4-45-50	2	97.95	HT	55.0	−0.58	0.06	−0.30	0.04	brown-black clay
repeat					−0.54	0.07	−0.28	0.05	
average					***−0.57***	***0.04***	***−0.29***	***0.03***	
294-6-1-118-123*	2	106.68	HT	55.0	−0.15	0.07	−0.06	0.07	pebbly black Fe clay
duplicate					−0.18	0.05	−0.09	0.05	
average					***−0.17***	***0.04***	***−0.08***	***0.04***	
295-2-1-34-39*	2	120.34	HD	51.6	0.10	0.07	0.06	0.07	dark brown clay
repeat*					0.09	0.07	0.04	0.06	
average					***0.10***	***0.05***	***0.05***	***0.05***	
295-2-6-84-89*	2	128.34	HT	55.0	−0.48	0.06	−0.25	0.06	black-brown clay
duplicate					−0.47	0.07	−0.25	0.05	
repeat					−0.49	0.07	−0.24	0.03	
average					***−0.48***	***0.04***	***−0.25***	***0.02***	
295-3-2-30-35*	2	140.8	HT	55.0	−0.50	0.06	−0.24	0.06	black clay
DSDP Site 595/6 - Tonga									
596-1-1-105-108*	1	1.05	TC	1.05	−0.18	0.06	−0.11	0.07	yellow brown clay
repeat*					−0.14	0.07	−0.06	0.06	
duplicate*					−0.14	0.10	−0.05	0.07	
repeat					−0.18	0.05	−0.10	0.05	
average					***−0.17***	***0.03***	***−0.08***	***0.03***	
596-1-cc	1	5.50	TC	18.48	−0.12	0.07	−0.07	0.03	medium brown clay

duplicate					−0.12	0.07	−0.05	0.05	
average					***−0.12***	***0.05***	***−0.06***	***0.03***	
595A-2-3-57-60*	1	6.37	HD	21.12	0.01	0.07	0.01	0.07	brown black clay
repeat					0.02	0.06	0.00	0.04	
duplicate					−0.01	0.05	0.01	0.05	
average					***0.01***	***0.03***	***0.00***	***0.03***	
595A-2-cc	2	12.20	HD	47.22	−0.18	0.06	−0.09	0.04	dark brwn Mn nodule
repeat					−0.15	0.07	−0.09	0.06	
average					***−0.17***	***0.05***	***−0.09***	***0.03***	
596-2-6-70-72*	2	13.70	HD	54.55	0.02	0.09	0.01	0.06	very dark brown clay
596-3-1-115-117*	2	16.25	HD	67	−0.04	0.09	−0.02	0.06	dark brown clay
repeat*					−0.05	0.07	−0.02	0.06	
average					***−0.05***	***0.06***	***−0.02***	***0.04***	
596-3-5-100-102*	2	22.10	HD	69.36	0.11	0.09	0.06	0.06	dark brown clay
596-5-2-114-116*	3	36.94	HD	75.34	0.07	0.06	0.05	0.06	dark brown clay/chert
duplicate					0.06	0.06	0.02	0.04	
average					***0.06***	***0.04***	***0.03***	***0.03***	
595A-5-cc*	3	38.00	HD	75.77	0.22	0.09	0.11	0.06	yellow brown
repeat*					0.21	0.07	0.10	0.06	
repeat					0.21	0.07	0.11	0.06	
duplicate					0.22	0.07	0.11	0.05	
average					***0.21***	***0.04***	***0.11***	***0.03***	
595A-8-5-100-103*	3	57.60	HD	83.67	0.09	0.09	0.05	0.06	yellow chert
repeat*					0.11	0.06	0.06	0.06	
average					***0.10***	***0.05***	***0.05***	***0.04***	

Note: repeat = repeat instrumental analysis on the same Mg-cut solution. Duplicate means repeat column chemistry and instrumental analysis. Replicate means re-dissolution, column chemistry and instrumental analysis.

* denotes samples analyzed on a MC-ICPMS at the University of Washington (Seattle).

** denotes samples analyzed on a MC-ICPMS at the University of Arkansas (Fayetteville).

Samples without the star specification were analyzed on a Nu II MC-ICPMS at the University of Washington (Seattle).

Lithological code: TB = turbidite; TC = terrigenous clay; HD = hydrogenetic; HT = hydrothermal; BC = biogenic carbonate.

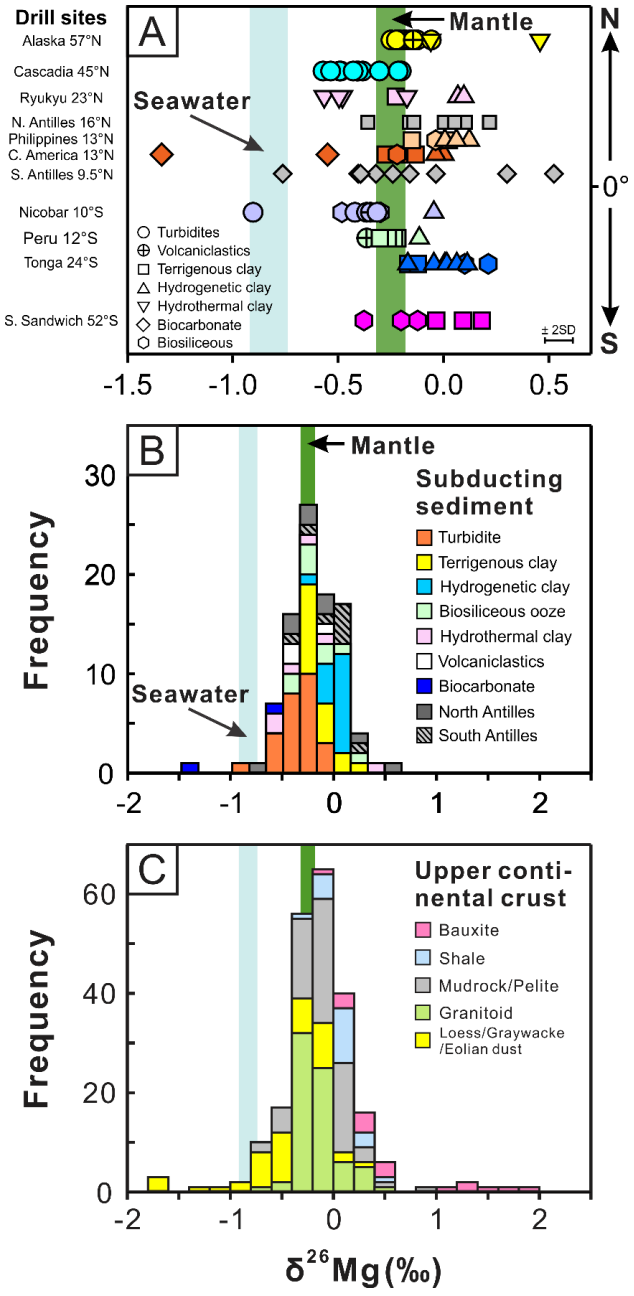

Figure 4-3. Magnesium isotopic compositions of subducting marine sediments. (A) δ^{26}Mg variation as a function of drill site latitude. Symbols with the same colors represent samples from the same drill sites. (B) Histogram of δ^{26}Mg in subducting sediments shows a similar distribution frequency to that of (C) upper continental rocks and sediments. Data sources: marine sediments: this study and Teng et al. (2016) for Antilles sediments; upper crustal rocks and sediments: Shen et al. (2009); Li et al. (2010, 2014); Liu et al. (2010); Telus et al. (2012); Huang et al. (2013); Ling et al. (2013b); Liu et al. (2014); Wimpenny et al. (2014b) and Wang et al. (2015a, 2015b). δ^{26}Mg ranges of seawater (Ling et al., 2011) and mantle (Teng et al., 2010a) are plotted as references.

The $\delta^{26}Mg$ values of the 77 studied bulk sediments span a wide range comparing to global seawater and the mantle, varying from −1.34‰to +0.46‰ (Fig. 4-3A and B). Among the ten drill sites located between 60°N and 60°S, those close to the equator display the greatest variability, as would be expected from the higher levels of biogenic inputs. In general, terrigenous clays and hydrogenetic clays occupy the high-$\delta^{26}Mg$ end while calcareous oozes reside at the low-$\delta^{26}Mg$ end. Turbidites and hydrothermal clays have a wide spread of $\delta^{26}Mg$, with values both higher and lower than the mantle range. Overall, the $\delta^{26}Mg$ variation covers a similar spectrum to that reported for rocks and sediments on continents (Fig. 4-3B and C). There is no uniform down-core variation with respect to either MgO or $\delta^{26}Mg$ except that the terrigenous clays from DSDP 321 (Peru) display a monotonic increase in $\delta^{26}Mg$ with both depth and age.

Detailed results for the subducting marine sediments are reported below as three broad lithological groups: (1) detrital sediments (turbidites, terrigenous clays, and associated volcanic ashes); (2) hydrogenetic and hydrothermal clays; and (3) biogenic siliceous and calcareous oozes.

4.1. Detrital sediments

4.1.1. Turbidites

Turbidites are represented by sand-silt-clay sequences that are deposited relatively rapidly and typically close to land. The three turbidite sections from Cascadia (DSDP 174), Alaska (DSDP 178) and Nicobar Fan (DSDP 211) have $\delta^{26}Mg$ values comparable to, but less variable than, the turbidites-dominated mudrocks from the British Caledonides ($\delta^{26}Mg$ = −0.24 ± 0.43‰, 2SD, Wang et al., 2015b) and suspended load/bedload sediments from

rivers that drain dominantly silicate catchments ($\delta^{26}Mg = -0.29 \pm 0.59‰$, 2SD, Pogge von Strandmann et al., 2008; Wimpenny et al., 2011). Furthermore, the three sections show minor, yet distinguishable, Mg isotopic characteristics (Fig. 4-3A). DSDP sites 174 and 178 are both located within the Northeast Pacific Turbidite Province (Horn et al., 1970), and sediments from these sites contain primarily of detrital mica, with minor amounts of montmorillonite, amphibole, chlorite, and dolomite (Zemmels and Cook, 1973). Site 174, located in the Astoria Submarine Fan, contains abundant landderived detritus. Based on their Nd-Hf-Pb isotopes, the majority of the turbidites are sourced from Precambrian terranes that are over 1000 km away inland with only the top layer of sediments being supplied by the Columbia River Basalt (Prytulak et al., 2006). The shallowest sample of the Cascadia turbidites has a $\delta^{26}Mg$ value (−0.20‰) that is comparable to the Columbia River Basalts (−0.33‰ to −0.15‰, Liu et al., 2014), but is distinguishably heavier than the deeper samples. This shift in sediment $\delta^{26}Mg$ is consistent with the change in sediment provenance. The rest of the section can be further divided into two units separated by a seismic discontinuity while they share a similar range in Hf-Nd-Pb isotopes (Prytulak et al., 2006). Similarly, the $\delta^{26}Mg$ values range from −0.49‰ to −0.38‰ for Unit 1 and from −0.57‰ to −0.40‰ for Unit 2. In addition, the claystone and sandstone at the bottom of the section have higher $\delta^{26}Mg$ values (−0.21‰ and −0.30‰) than the unconsolidated sediments.

Site 178, located in the Gulf of Alaska, is characterized by highly uniform petrologic and climatologic conditions on the continent and a strong nepheloid layer (Ewing et al., 1970). Sediments there are rich in mica and chlorite, and contain appreciable ice-rafted erratics (Zemmels and Cook, 1973), reflecting the dominance of physical

weathering and low intensity of chemical weathering at high latitude regions (Griffin et al., 1968). They display a more restricted δ^{26}Mg range of−0.25‰to −0.12‰, apart from a slightly heavier clay (δ^{26}Mg = −0.06‰). These values are similar to those of fresh oceanic basalts (−0.26 ± 0.07‰, Teng et al., 2010a) and glacial flour from the Canadian shield (−0.165‰ to −0.106‰, Tipper et al., 2012).

Site 211 is located in the eastern equatorial Indian Ocean. The turbidites supplied by the Ganges-Brahmaputra River contain abundant illite, with lesser amounts of smectite, chlorite and kaolinite in the < 2 μm fractions. Mica with small amounts of amphibole are the dominant Mg-bearing minerals in the coarser fractions (Venkatarathnam, 1974). With the exception of an isotopically light carbonate-rich silty sand (δ^{26}Mg =−0.90‰), the three other silty clay/sand samples have similar δ^{26}Mg values (−0.42‰ to −0.32‰). The silicic volcanic ash sample derived from the Indonesian Island arc contains abundant smectite and has a similar δ^{26}Mg value of −0.35‰.

4.1.2. Terrigenous clays

This group consists mainly of land-derived detritus transported by eolian processes. Consequently, sediments from this group are dominated by fine-grained clay minerals. Sediments from DSDP site 321 and ODP site 701 are representative samples of this group. Site 321 is located on the eastern edge of the Nazca Plate where the Peru-Chile trench effectively traps windborne volcanic and terrigenous sediments from the Andes (Quilty et al., 1976). Clay sediments from the top two units have a fairly uniform chemical composition, with high contents of volcanic glass and ash. The Mg-bearing minerals presented include kaolinite, chlorite and mica (illite), as well as montmorillonite that is

closely associated with volcanic glass (Zemmels and Cook, 1976). These clays and a single ash sample have similar δ^{26}Mg values (−0.36‰ to −0.22‰) that fall within the range of typical igneous rocks (Li et al., 2010; Liu et al., 2010; Teng et al., 2010a). The three terrigenous clays from central America (DSDP site 495 and ODP site 844) have δ^{26}Mg values (−0.27‰ to −0.13‰) that mainly reflect Mg hosted in the volcanic glass and smectite (Latouche and Maillet, 1982). In contrast to the largely mantle-like δ^{26}Mg values of clays from the Peru and Central America trenches, those from ODP site 701, which is located on the western flank of the Mid-Atlantic Ridge, have generally higher δ^{26}Mg values (−0.03‰ to +0.18‰). Similarly high δ^{26}Mg values have been reported for terrigenous clays from DSDP site 543 (North Antilles, Teng et al., 2016). In addition to those clay-dominated sites, sediment sections cored at DSDP sites 291, 294/295, and 595/596, which consist primarily of hydrogenetic clays (see next section), also contain a thin layer of terrigenous clays on top, with δ^{26}Mg values varying from −0.23‰ to +0.03‰.

4.2. Hydrogenetic and hydrothermal clays

Hydrogenetic sediments are collected mainly from DSDP sites 291, 294/295, and 595/596, which are cored on the outer swell of the Philippine trench, in the northeastern West Philippine Basin, and in the south central/west Pacific, respectively. Hydrogenetic clays from sites 291 and 294/295 display a significantly negative Ce anomaly that is indicative of seawater derivation (Piper, 1974). Their Mg is mainly hosted in montmorillonite with minor mica and clinoptilolite (Cook et al., 1975). In comparison, the extremely low sedimentation rate at sites 595/596 leads to the deposition of metalliferous clays rich in hydrogenetic amorphous oxides (up to 90%), Fe-Mn micronodules, and fish

teeth. The 14 hydrogenous clays from various sites have relatively uninform δ^{26}Mg values with an average of +0.02 ± 0.14‰, except for a single Mn nodule from site 595 that has a slightly lower δ^{26}Mg value of −0.17‰.

Sediment sections from sites 294/295 (Ryukyu) also contain a lower unit that is enriched in hydrothermal clays. This unit is composed of iron oxides (goethite and hematite), zeolite, and manganese micronodules, in addition to the clay fraction that is dominated by montmorillonite (Cook et al., 1975). These FeO-rich (up to 42 wt%) hydrothermal clays generally have low δ^{26}Mg values (−0.57‰ to −0.48‰) except for a pebbly black clay, which has the lowest FeO concentration (17 wt%) and a δ^{26}Mg value (−0.17‰) similar to detrital clays. In comparison, the two basal brown clays from Alaskan turbidites are isotopically heavy, with δ^{26}Mg values of −0.06‰ and +0.46‰. These two Alaskan clays are dominated by montmorillonite and kaolinite in composition, and have much lower FeO contents (8–9 wt%) (Zemmels and Cook, 1973).

4.3. Biogenic sediments

Biogenic sediments in this study mainly include radiolarian/diatom oozes and calcareous oozes, which are commonly abundant at sites in the equatorial region. For example, ODP site 844B is located within the eastward-flowing North Equatorial Countercurrent and close to the Costa Rica Dome. The two nanno oozes from the lower unit are characterized by low δ^{26}Mg values (−0.55‰ and −1.34‰), similar to those of the siliceous chalk oozes from DSDP site 144 (Teng et al., 2016). The five diatomaceous oozes from ODP site 701 (South Sandwich) and DSDP site 211 (Nicobar Fan), and a single radiolarian nanno ooze from ODP site 844B have been mixed with varying proportions of

volcanic ash, clay and mud. These samples thus display a positive correlation between δ^{26}Mg and MgO contents and have δ^{26}Mg values (−0.48‰ to −0.12‰) that are comparable to the detrital clays (Fig. 4-4). By contrast, an FeO-rich (28 wt%) yellow radiolarian ooze from DSDP site 291 yields a δ^{26}Mg value (−0.04‰) that is similar to those of the hydrogenetic clays. The zeolitic radiolarian-bearing chert and porcellanite from DSDP site 595 (Tonga) have δ^{26}Mg values of +0.10‰ and +0.21‰, respectively, slightly higher than those of the hydrogenetic sediments from the same site.

5. Discussion

The Mg isotopic composition of subducting marine sediments investigated here ranges from −1.34‰ to +0.46‰, the variation of which mirrors that of rocks and sediments from the upper continental crust (Fig. 4-3). This similarity is consistent with the dominance of land-derived detrital components in the subducting marine sediments. In this section, we first explore the mechanisms of Mg isotope fractionation in different types of marine sediments. Then, we calculate the sedimentary Mg input to global subduction zones. Finally, we discuss the impact of crustal recycling on arc magmatism and mantle Mg isotopic heterogeneity.

5.1. Mechanisms of Mg isotope fractionation in marine sediments

The overall distribution of Mg and its isotopes in marine sediments are primarily controlled by (1) the relative proportions of different phases with distinct Mg isotopic signatures; and (2) the processes by which Mg is transported into the ocean and incorporated into the sediments. In detail, different mechanisms are responsible for Mg

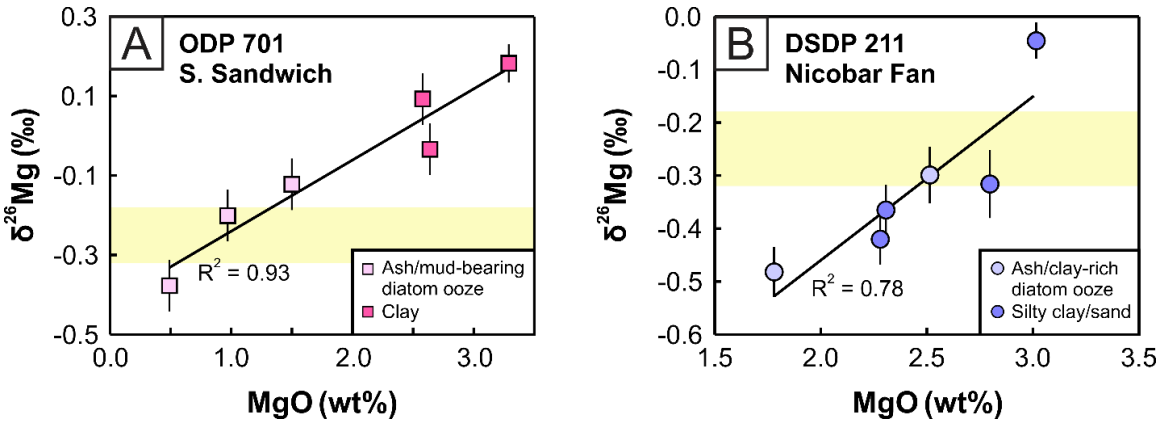

Figure 4-4. Positive correlations of δ^{26}Mg with MgO in sediments from (A) ODP 701 (South Sandwich) and (B) DSDP 211 (Nicobar Fan) indicate a mixing trend between Mg-depleted siliceous oozes and Mg-rich detrital clays. The yellow bar in this and following figures represent the mantle range (δ^{26}Mg = −0.25 ± 0.07‰, Teng et al., 2010a).

isotope fractionation in different types of samples. The isotopically light calcareous oozes are consistent with the preferential uptake of light Mg isotopes from seawater during precipitation of carbonates. Meanwhile, the δ^{26}Mg values of calcareous and siliceous oozes may be biased by the presence of various proportions of detrital components. Detrital sediments (i.e., turbidites and terrigenous clays) display a mineralogy and size dependence on δ^{26}Mg. Fractionation in hydrogenetic clays may be related to clay authigenesis, while variation in hydrothermal clays is presumably associated with exchange with seawater/hydrothermal fluids. These factors are considered in the following sections, in turn.

5.1.1. Mineralogical control on marine sediment δ^{26}Mg values

The subducting marine sediments studied here, to a first order, can be viewed as mixtures between silicates and carbonates, which differ significantly in their Mg isotopic compositions (Teng, 2017). Carbonates are enriched in light Mg isotopes (Saenger and Wang, 2014), whereas clay minerals and soils formed as weathering residue are generally more enriched in heavy Mg isotopes compared to the unweathered parent rocks (Teng et al., 2010b; Huang et al., 2012; Liu et al., 2014). Nonetheless, both silicate- and carbonate-rich sediment groups display large variations in δ^{26}Mg (see Saenger and Wang, 2014; Teng, 2017 for recent reviews).

Sediment mineralogy (carbonate vs. clay) can be estimated by Rb/Sr and CaO/TiO_2 ratios, as Rb and Ti are mainly retained in detrital phases, whereas Ca and Sr are much more enriched in carbonates (Fig. 4-5A). The broad inverse relationship between δ^{26}Mg value and CaO/TiO_2 ratio in both marine and continental sediments is consistent with the

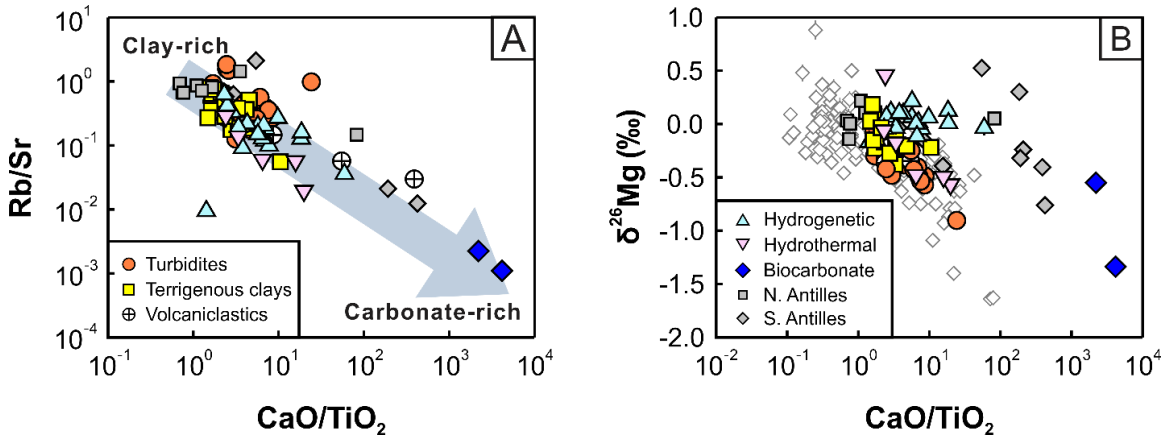

Figure 4-5. Mineralogical control on Mg isotopic composition of marine sediments. (A) Negative correlation between Rb/Sr and CaO/TiO_2 ratios suggests that clay and carbonate are the two major mineral constituents of these sediments. (B) Negative relationship between $\delta^{26}Mg$ values and CaO/TiO_2 ratios indicates an increasingly light Mg isotopic composition of the sediments with increasing amounts of carbonate present in the sediments. The open diamond symbols in Fig. 4-5 B represent literature data of various upper crust rocks and sediments (see Fig. 4-3 caption for source information).

mineralogy as a first order control, with the calcareous oozes being the low-δ^{26}Mg endmember (−0.55‰ and −1.34‰) among the measured sediments (Fig. 4-5B). Their bulk δ^{26}Mg values are similar to those of the carbonate-rich (CaO > 20 wt%) sediments from DSDP site 144 reported by Teng et al. (2016), whereas are considerably higher than the leached fractions of calcareous sediments from the Atlantic (−1.78 ± 1.29‰, n= 13) and Pacific oceans (−2.43 ± 1.63‰, n = 9) (Rose-Koga and Albarède, 2010). This shift in δ^{26}Mg toward higher values may reflect the presence of clay impurities, as supported by the positive correlations between their δ^{26}Mg values and Cs and Rb contents, which have a strong affinity for clay minerals (Fig. 4-6) (Sawhiney, 1972).

Clay minerals are the dominant constituent of lithogenous component in marine sediments and they display a wide range in δ^{26}Mg both within and between different clay mineral groups (e.g., >2‰ variability, Wimpenny et al., 2014a). This variation in δ^{26}Mg is proportional to the Mg in structural versus exchangeable sites, with the former favoring heavy Mg isotopes and the latter preferentially taking up light Mg isotopes from fluids (Wimpenny et al., 2014a). In addition to various clay minerals, turbidites could preserve significant amount of primary mafic silicates, which generally have a mantle-like δ^{26}Mg value except for isotopically light garnets (Li et al., 2011; Wang et al., 2012). Therefore, mixing of different types of silicate phases and Mg isotopic heterogeneity in clay minerals can lead to large Mg isotopic variation in silicate-rich sediments.

5.1.2. Detrital sediments: source signature and sorting effects

Magnesium in detrital sediments is mainly derived from the continents, and their δ^{26}Mg values are affected principally by source composition, weathering, and sorting

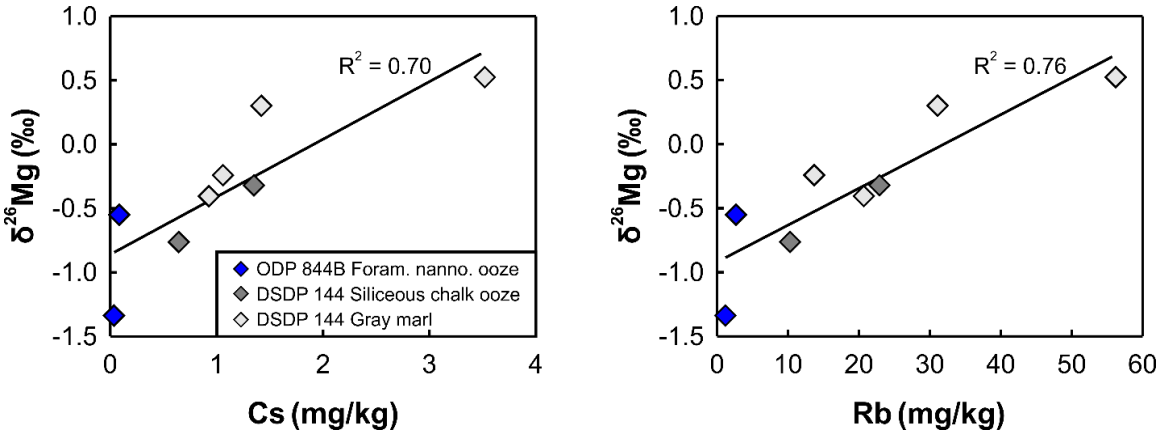

Figure 4-6. Positive correlations between δ^{26}Mg values and Cs, Rb contents in carbonate-rich sediments , which indicate the influence of clay impurities on the bulk δ^{26}Mg values of these sediments.

history.

5.1.2.1. Source signature: provenance heterogeneity

The provenance of the studied sediments is diverse as indicated by their wide variation in Nd-Pb-Hf-Li isotopes (Plank and Langmuir, 1998; Bouman et al., 2004; Chan et al., 2006; Prytulak et al., 2006; Carpentier et al., 2008, 2009; Vervoort et al., 2011; Tang et al., 2014). Since different types of protoliths are likely to carry a distinguishable Mg isotopic fingerprint, δ^{26}Mg variation in detrital sediments may partly reflect their source heterogeneity. For example, while most granites have a mantle-like δ^{26}Mg (Li et al., 2010; Liu et al., 2010), those incorporated weathered crustal components have been found to be more enriched in heavy Mg isotopes (Shen et al., 2009; Li et al., 2010). On the contrary, some continental granites and basalts are isotopically lighter relative to the mantle (as light as −0.47‰), which may reflect metasomatism of their mantle sources by low-δ^{26}Mg carbonates (Yang et al., 2012; Huang et al., 2015; Liu et al., 2015; Ke et al., 2016; Tian et al., 2016; Wang et al., 2016). Metasomatism by carbonate-rich fluids has also been proposed to account for some low-δ^{26}Mg granulites (Yang et al., 2016). As for sedimentary protoliths, some siliciclastic rocks (e.g., mudrocks and shales) can be isotopically light if containing appreciable amounts of carbonates (Wang et al., 2015b; Teng, 2017). Otherwise, they are similar to the mantle (e.g., greywacke and tillite, Li et al., 2010), or more often shifting toward high-δ^{26}Mg end (Li et al., 2010; Ma et al., 2015).

The negative La/Sm vs. $\varepsilon_{Nd(i)}$ correlation in these sediments indicates a mixed source between mature (evolved) upper crustal materials and more juvenile crustal materials (recent mantle derivatives) and seawater, where a higher La/Sm ratio and a more

negative $\varepsilon_{Hf(i)}$ value indicate derivation from a continental source (Fig. 4-7A). The terrigenous clays from Peru and Central America, and turbidites from Alaska have $\varepsilon_{Nd(i)}$ values close to zero and relatively low La/Sm ratios. These sediments received significant detrital contributions from volcanic arcs or juvenile terranes, which are expected to have δ^{26}Mg values similar to the oceanic basalts. Their relatively homogeneous and mantle-like δ^{26}Mg values are consistent with this expectation (Fig. 4-7B).

On the other hand, samples with lower $\varepsilon_{Nd(i)}$ values and higher La/Sm ratios, which indicate an increased input from more mature continental sources, display a large dispersion in δ^{26}Mg (Fig. 4-7B), consistent with the prolonged intra-crustal processes (e.g., melting, weathering, and sedimentation) underwent by these sources. Sediments from Cascadia (DSDP 174), Nicobar Fan (DSDP 211) and Antilles margins (DSDP 144 and 543) have the most enriched radiogenic Nd-Hf-Pb isotopes. Among them, the Cascadia turbidites have a distinguishably light Mg isotopic composition. Their Pb isotopes suggest predominant derivation from a distal Proterozoic source from North America mixed with a proximal primitive source like the Columbia River Basalts (Prytulak et al., 2006). The δ^{26}Mg values in Cascadia turbidites are positively correlated with $\varepsilon_{Nd(i)}$ values (Fig. 4-7B) and negatively correlated with $^{207}Pb/^{204}Pb$ and La/Sm ratios (Fig. 4-8A and B). These correlations suggest that the basaltic source has a mantle-like δ^{26}Mg signature while the more evolved source has a low δ^{26}Mg signature. The latter can be attributed to the presence of isotopically light carbonate, particularly Mg-rich dolomite (Zemmels and Cook, 1973), and garnet (Prytulak et al., 2006) in these sediments.

Sediments from the Antilles margins, on the contrary, are characterized by heavy Mg isotopic compositions (Teng et al., 2016). These sediments have Nd-Hf-Pb-Li isotopes

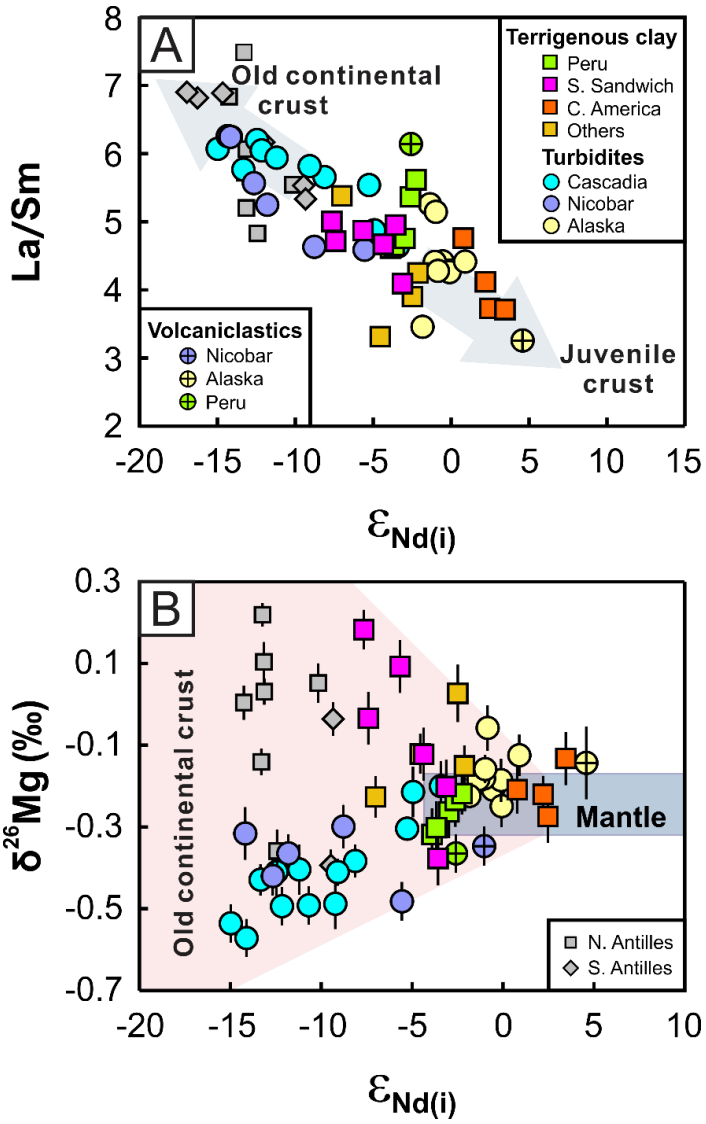

Figure 4-7. δ^{26}Mg variation in subducting sediments with relation to their contrasting provenance compositions. (A) The negative correlation between La/Sm and $\varepsilon_{Nd(i)}$ in detrital sediments indicates their source compositions ranging from old continental crust to juvenile crust. (B) δ^{26}Mg variation in detrital sediments as a function $\varepsilon_{Nd(i)}$. Neodymium isotopic data are from Carpentier et al. (2008) and Vervoort et al. (2011).

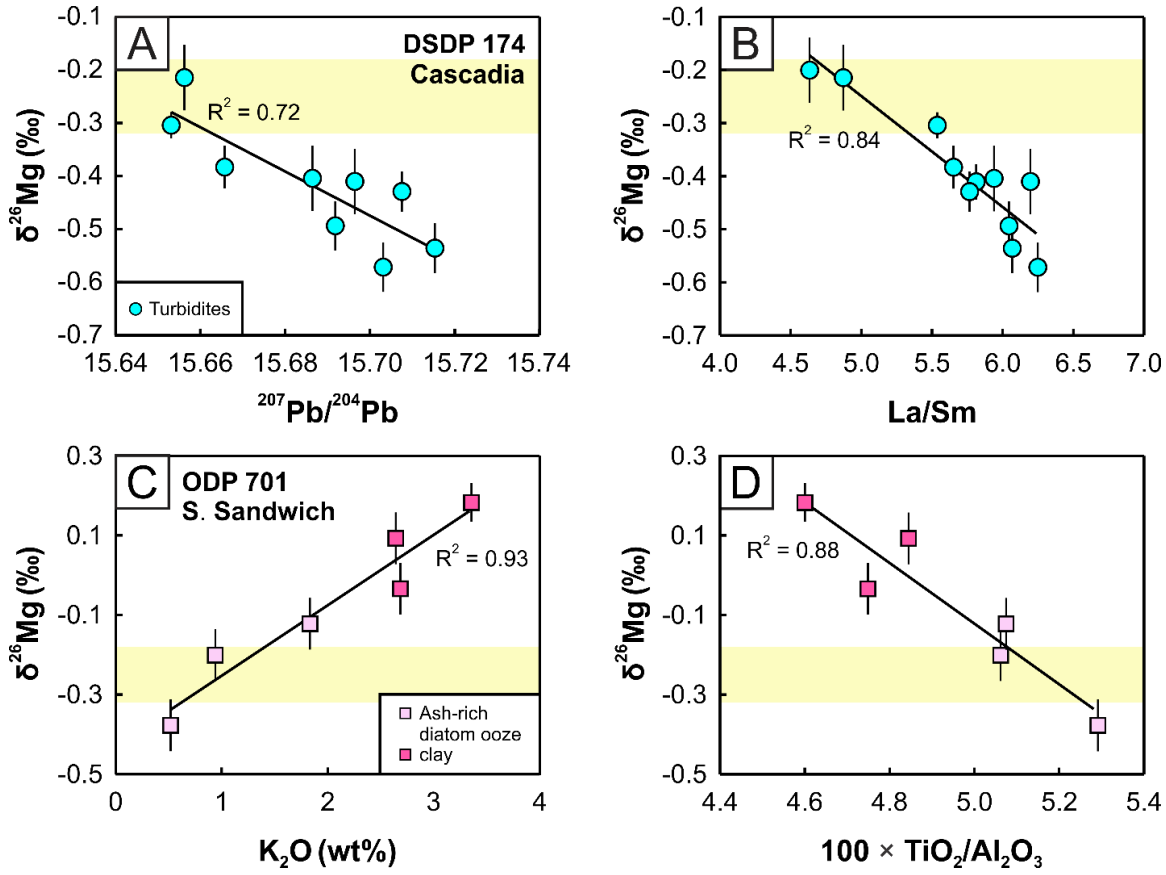

Figure 4-8. The effect of source rock heterogeneity on Mg isotopic composition of subducting sediments. (A) and (B) Correlations between $\delta^{26}Mg$, $^{207}Pb/^{204}Pb$, and La/Sm in Cascadia turbidites suggest isotopic mixing between an evolved continental source with a low $\delta^{26}Mg$ signature and a primitive source with mantle-like $\delta^{26}Mg$. Pb isotopic data are from Prytulak et al. (2006). (C) and (D) Correlations between $\delta^{26}Mg$, K_2O and TiO_2/Al_2O_3 in South Sandwich terrigenous sediments indicate source mixing between a weathered, high-$\delta^{26}Mg$ continental source and a juvenile volcanic source with mantle-like $\delta^{26}Mg$.

that indicate derivation from a highly weathered, and hence high-$\delta^{26}Mg$, low-$\delta^{7}Li$, old continental source on the South American craton (Westbrook et al., 1984; White et al., 1985). In comparison, sediments from ODP site 701 (South Sandwich) have intermediate $\varepsilon_{Nd(i)}$ values and La/Sm ratios. Their $\delta^{26}Mg$ values are positively correlated with MgO and K_2O concentrations (Fig. 4-4A and Fig. 4-8C) and negatively correlated with $\varepsilon_{Nd(i)}$ and TiO_2/Al_2O_3 (Fig. 4-7B and Fig. 4-8D). These correlations suggest a binary mixing between volcanic ash and K-rich terrigenous clay, likely illite, which is the dominant type of clay minerals in marine sediments from the Atlantic Ocean (Riley and Chester, 1971). Specifically, the three ash/mud-bearing siliceous oozes have less negative ƐNd(i) values and mantle-like $\delta^{26}Mg$ values (−0.38‰ to −0.12‰), consistent with their volcanogenic origin, whereas the three terrigenous clay samples have lower $\varepsilon_{Nd(i)}$ values and higher $\delta^{26}Mg$ values (−0.03‰ to +0.18‰). The highest $\delta^{26}Mg$ value is identical to an illite clay sample measured by Wimpenny et al. (2014a).

5.1.2.2. Source signature: intensity of chemical weathering

Chemical weathering exerts a strong control on the geochemistry and mineralogy of siliciclastic sediments (e.g. Nesbitt and Young, 1982; McLennan et al., 1993). Magnesium isotopes are also significantly fractionated during this process, with preferential loss of light isotopes to fluids and accumulation of heavy ones in the weathered residue (see Teng, 2017 for a recent review). Notably, the highest $\delta^{26}Mg$ values reported so far (up to +1.8‰) were found in bauxites that formed via extreme weathering of basalts with great Mg depletion (MgO = 0.12 to 0.25 wt%) (Liu et al., 2014).

The degree of chemical weathering underwent by sediment source rocks can be

quantified by a number of chemical indices. The chemical index of alteration (CIA; Nesbitt and Young, 1982) and chemical index of weathering (CIW; Harnois, 1988) have been used widely to monitor the decomposition of feldspar, which is the most abundant rock-forming mineral group in the upper continental crust. These two indices are calculated in a similar way except that CIW excludes K_2O in the equation due to its inconsistent geochemical behaviors during weathering (being leached or accumulated). Unweathered rocks typically have CIA values around 50 or less if they contain abundant amphibole (CIA = 10–30) or clinopyroxene (CIA = 0–20). On the contrary, CIA values for secondary minerals are much higher, approximately 70 to 85 for smectites and illites, and close to 100 for kaolin-group minerals (Nesbitt and Young, 1982). The marine sediments investigated here have CIA values ranging between 40 and 64, indicating that their sources were subjected to low to moderate degrees of chemical weathering compared to shales (average CIA = 70–75, Taylor and McLennan, 1985). Both the calculated CIA and CIW values form a broad positive correlation with $\delta^{26}Mg$ in detrital sediments, consistent with the general trend of preferential retention of heavy Mg isotopes during chemical weathering (Fig. 4-9A and B). Scatter in the data may be caused by compositional differences in sediment protoliths, Mg isotopic heterogeneity in clay minerals, and different degrees of sorting underwent by the sediments (see next section). The rough negative correlation between $\delta^{7}Li$ and $\delta^{26}Mg$, particularly in the carbonate-rich sediments from DSDP 144 (South Antilles) (Fig. 4-9C), lends further support to the role of chemical weathering, which leads to preferential leaching of heavy Li isotopes; thus Li and Mg isotopes fractionate in the opposite direction (see Tomascak et al., 2016; Penniston-Dorland et al., 2017 for recent reviews). In addition to $\delta^{7}Li$, Li concentration in sediments is also an effective weathering index due to its strong

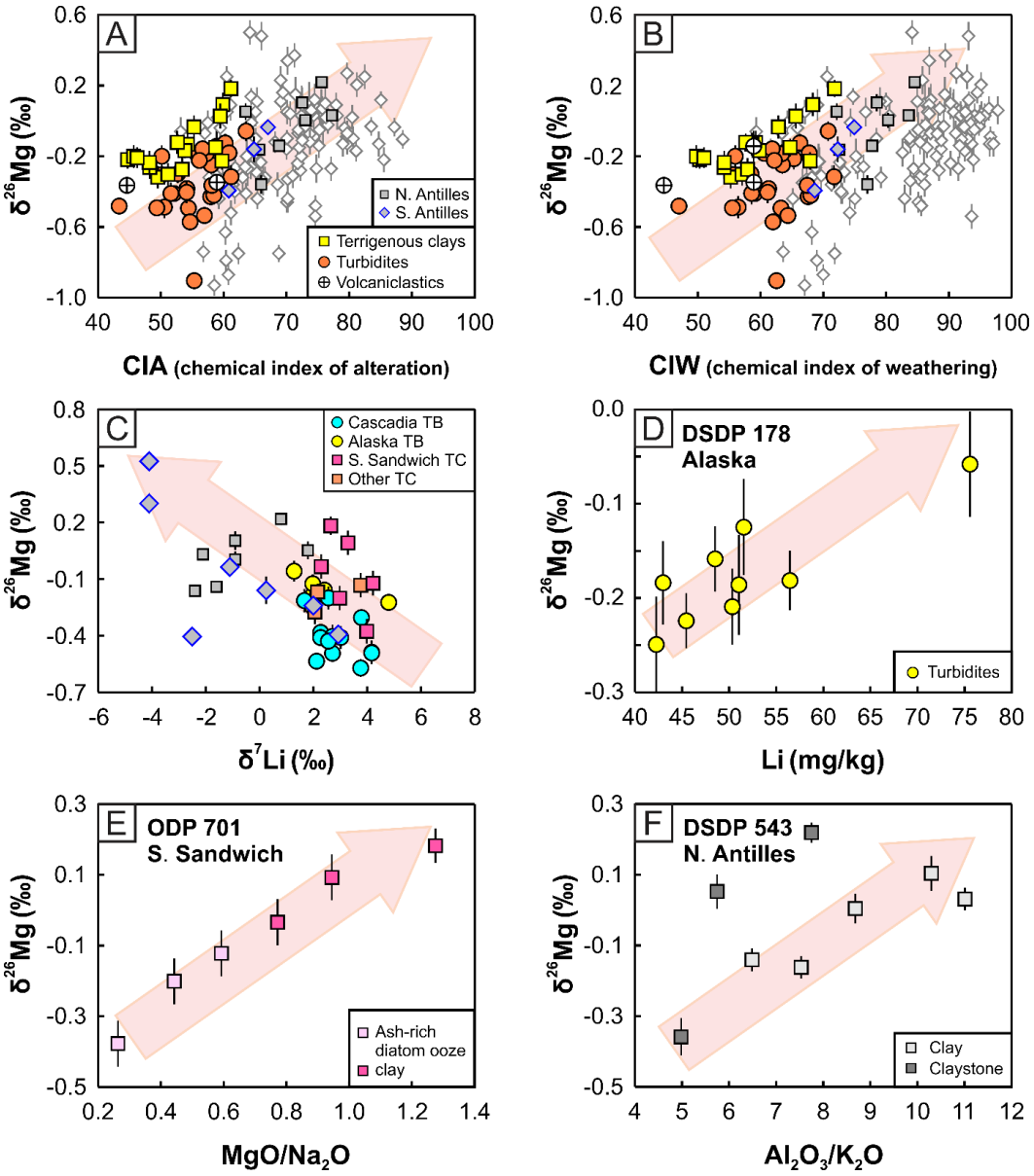

Figure 4-9. δ^{26}Mg variation in detrital sediments during progressive chemical weathering. Chemical Index of Alteration (CIA) values in (A) were calculated using the formula CIA= 100 ×molar Al2O_3/(Al_2O_3 +CaO* +Na_2O +K_2O) after Nesbitt and Young (1982). Chemical Index of Weathering (CIW) values in (B) were calculated using a similar formula without K_2O (Harnois, 1988). CaO* in both CIA and CIW takes into account only CaO content in the silicate fraction of the sediments. The open diamond symbols represent literature data of various upper crust rocks and sediments (see Fig. 4-3 caption for source information). Li isotopic data in (C) are from Bouman et al. (2004), Chan et al. (2006) and Tang et al. (2014). When no direct measurements are available, δ^7Li values were taken as those of sediments with similar lithology from the same or nearby sites.

affinity to clay minerals (Qiu et al., 2009). The trend of increasing $\delta^{26}Mg$ value with increasing Li content in Alaskan turbidites thus reflects a weathering effect (Fig. 4-9D). Intensity of chemical weathering can also be evaluated by using element pairs with different lability to weathering, such as MgO/Na_2O and Al_2O_3/K_2O ratios, in which cases Mg and Al are less mobile compared to Na and K, respectively (e.g. Schneider et al., 1997). These weathering-induced $\delta^{26}Mg$ variation patterns have been observed in detrital sediments from ODP 701 (South Sandwich) and DSDP 543 (North Antilles) (Fig. 4-9E and F).

5.1.2.3. Sediment transport: grain-size sorting

Grain-size sorting. Grain-size sorting along with sediment transport leads to systematic fractionation of sediment mineralogy and chemical composition between fine-grained and associated coarse-grained fractions. Magnesium isotopes are likely to be fractionated during this process as a result of changes in the relative proportions of mineral phases carrying distinct Mg isotopic signatures. For example, some loess sediments have their δ26Mg values vary inversely with their grain sizes (Huang et al., 2013). This trend is consistent with the observation that sedimentary rocks dominated by fine-grained clay minerals, such as shale and pelite, comprise the high-$\delta^{26}Mg$ endmember on continents (e.g. Li et al., 2010; Ma et al., 2015), as opposed to the coarser loess sediments that can host appreciable carbonates and are therefore depleted in heavy Mg isotopes (Huang et al., 2013; Wimpenny et al., 2014b). The TiO_2/Zr ratio is a sensitive index for the degree of sediment sorting since the coarse-grained fraction of the sediments tends to concentrate heavy minerals (e.g. zircon, hence Zr) together with quartz, whereas TiO_2 tends to follow Al_2O_3

and therefore is preferentially retained in the fine-grained weathering products (Garcia et al., 1994). TiO_2/Zr ratios correlate positively with sediment $\delta^{26}Mg$ values in detrital sediments, particularly in turbidites (Fig. 4-10A and B), consistent with the trend of concentration of fine-grained, isotopically heavy clay minerals with increasing degree of sediment sorting. The effect of zircon sorting has also been well documented to cause the negative deviation of ε_{Hf} in zircon-bearing detrital sediments from the Terrestrial Array (Patchett et al., 1984; Carpentier et al., 2009; Vervoort et al., 2011). Along with zircon, detrital carbonate and other heavy minerals, such as garnet, are preferentially concentrated in the coarser sandier fractions. This may explain the positive correlation between $\delta^{26}Mg$ and $\varepsilon_{Hf(i)}$ values in the Cascadia turbidites, with the sand-rich fractions containing more abundant low-$\delta^{26}Mg$ carbonate/garnet and low-$\varepsilon_{Hf(i)}$ old zircon (Fig. 4-10C).

5.1.3. Non-detrital sediments

5.1.3.1. Hydrogenetic clays and Mn nodule

Hydrogenetic sediments are enriched in authigenic components formed by direct precipitation from seawater or submarine alteration of pre-existing materials. The hydrogenetic sediments analyzed in this study commonly display higher MgO/Al_2O_3 ratios than detrital sediments (Fig. 4-2C), suggesting in-situ formation of magnesian clays with uptake of Mg from seawater. They have a relatively homogenous and high $\delta^{26}Mg$ value of $+0.02 \pm 0.14‰$ (n = 14). This is consistent with results from modeling of sediment pore water, which suggest that the formation of authigenic clays preferentially remove heavy Mg from the fluid phase into their structure, with a fractionation factor of 0‰ to +1.25‰ (Higgins and Schrag, 2010). Likewise, brucite synthesis experiments found that the

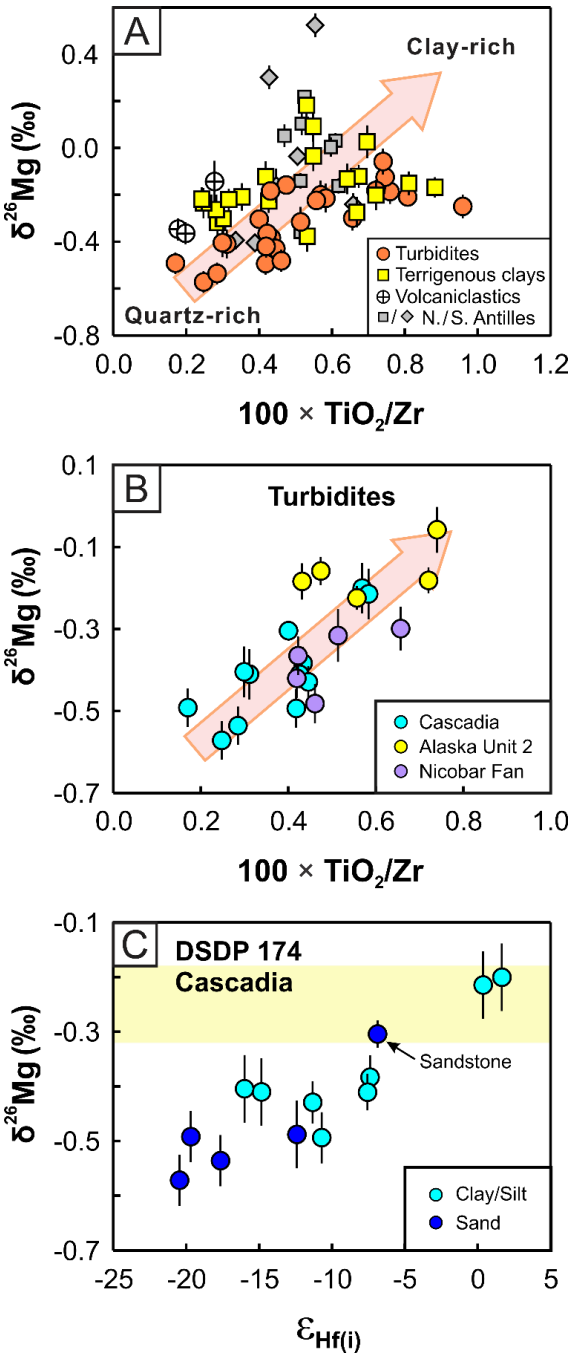

Figure 4-10. δ^{26}Mg variation related to grain-size sorting during sediment transport. (A) TiO_2/Zr ratio is a sensitive index for sediment sorting and measures the proportion of fine-grained clays relative to coarse-grained quartz (and zircon). (B) The effect of sorting is particularly prominent in turbidites. (C) As a result of sorting, low-$\varepsilon_{Hf(i)}$ zircon and low-δ^{26}Mg carbonate/garnet were concentrated in the coarser sand fractions, leading to the positive correlation between δ^{26}Mg and $\varepsilon_{Hf(i)}$ in Cascadia turbidites. Hafnium isotopic data for these sediments are from Vervoort et al. (2011).

precipitated brucite is isotopically heavier than the solution (Wimpenny et al., 2014a). The hydrogenetic sediments from Tonga (DSDP sites 595/596) also have elevated Li concentrations and Li isotopic compositions relative to the upper continental crust, which were attributed to adsorption of isotopically heavy seawater-derived Li (Chan et al., 2006). Therefore, Mg and Li isotopes fractionate by different mechanisms during the formation of hydrogenetic sediments, with heavy Mg isotopes being incorporated into clay structure while heavy Li isotopes being adsorbed to clays and hydroxyoxides, resulting in a positive correlation between δ^{26}Mg and δ^{7}Li in Tonga sediments (Fig. 4-11), as opposed to the general negative correlation in detrital sediments produced by chemical weathering (Fig. 4-9C).

In addition, the porcellanite and chert samples from Tonga have δ^{26}Mg values similar to the hydrogenetic clays from the same site but are isotopically heavier than siliceous oozes from other drill sites. Their elevated δ^{26}Mg values may as well reflect formation of isotopically heavy authigenic clays during diagenetic recrystallization of amorphous opal.

Hydrogenetic sediments also differ significantly from detrital sediments in that they have higher Fe and Mn concentrations due to the abundance of ferro-manganese oxides (Fig. 4-2D). The single Mn nodule sample analyzed here belongs to the hydrogenetic vernadite class due to its high Co concentration (3120 mg/kg, Chan et al., 2006), in contrast with the diagenetic Mn nodules that are dominated by the todorokite class with no or low Co content (Halbach et al., 1981; Uspenskaya et al., 1987). The δ^{26}Mg value of this sample (−0.17‰) falls at the high-δ^{26}Mg end of the wide range reported for global Mn nodules (−2.94‰ to +0.69‰), indicating insignificant early diagenesis, which drives δ^{26}Mg in Mn

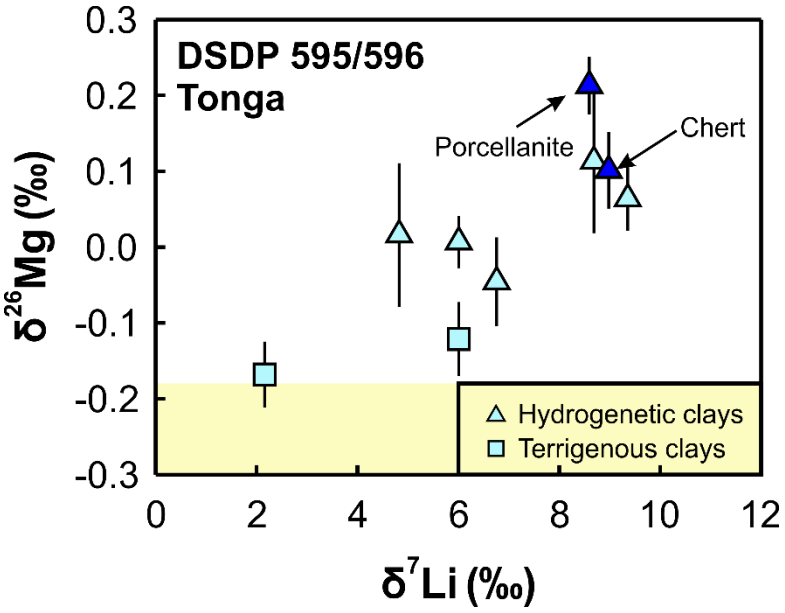

Figure 4-11. $\delta^{26}Mg$ variation in Tonga hydrogenetic sediments reflects the preferential uptake of heavy Mg isotopes during authigenic mineral formation. $\delta^{7}Li$ data are from Chan et al. (2006).

nodules to lighter values (Rose-Koga and Albarède, 2010).

5.1.3.2. Hydrothermal clays

Hydrothermal clays typically occur in the basal layer of sediment columns immediately above the basement rocks. They consist primarily of authigenic Fe-Mn precipitates from spreading ridge hydrothermal fluids admixed with rock detritus (Fig. 4-12A). They display large variation in δ^{26}Mg value, which shows a negative correlation with FeO/Al_2O_3 ratio (Fig. 4-12B). In detail, the two brown clay samples from DSDP site 178 (Alaska) have a chemical composition similar to that of the average terrigenous matter ("TM"). Their Mg budgets are dominated by montmorillonite with minor mica and chlorite (Zemmels and Cook, 1973), and they have high δ^{26}Mg values (−0.06‰ and +0.46‰) that are commonly seen in clay minerals. By contrast, the four hydrothermal black/brown clay samples from DSDP sites 294/295 (Ryukyu) have much higher Fe and Mn concentrations and lower Al concentrations that plotted close to the composition of the East Pacific Rise metalliferous deposit ("EPR"). These hydrothermal clays contain abundant hematite and lesser amount of montmorillonite (Cook et al., 1975). The relatively low δ^{26}Mg values of −0.48‰ to −0.57‰ in these hydrothermal clays might reflect Mg exchange between clays and ^{26}Mg-depleted seawater, or formation of secondary Mg-bearing minerals that have a preference for light Mg isotopes at hydrothermal temperatures (Pogge von Strandmann et al., 2008). The single pebbly black hydrothermal clay has a much higher Al content than the other three hydrothermal clays from Ryukyu (16 wt% vs. 3–6 wt%). Its higher δ^{26}Mg value of −0.17‰ may reflect dominance of terrigenous detritus. Therefore, a mixed contribution of Mg from the continental detritus and seawater/ hydrothermal fluids may

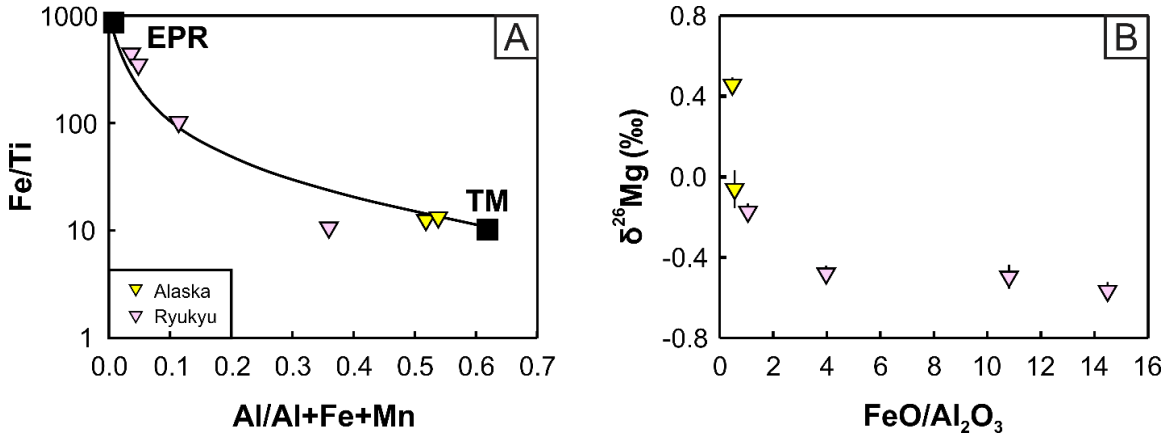

Figure 4-12. $\delta^{26}Mg$ variation related to hydrothermal sediments. "TM" and "EPR" represent the average compositions of terrigenous materials and of East Pacific Rise deposits, respectively, from Böstrom et al. (1976).

produce the Mg isotopic variation seen in these hydrothermal sediments.

5.2. Sedimentary Mg input to global subduction zones

To evaluate the variation in Mg flux and isotopic signature of sediment sections delivered to modern subduction zones on a global basis, we calculated the mass-weighted average δ^{26}Mg value and total Mg flux for all sediment columns that have been included in the calculation of GLOSS-II, which account for ~86% of the global flux (Plank, 2014). The comprehensive datasets of subducting marine sediments over worldwide trench systems provided in Plank (2014) serve as a basis for estimating the global subducting sedimentary Mg input. Similar to the elemental flux calculation in Plank and Langmuir (1998), the sedimentary Mg flux per unit arc length (F) is calculated using the following equation:

$$F = C\ (1- w)\ t\ \rho\ R,$$

where C, w, t, ρ and R represent depth-integrated concentration, water content, thickness, density, and convergence rate, respectively. The average δ^{26}Mg value for each trench considered is calculated based on averaged data for individual lithologic units (see Appendix B for calculation details). Calculation results are summarized in Table 4-2 and Fig. 4-13. For more than half of the trenches, no Mg isotopic analysis is available and their δ^{26}Mg values are estimated from the correlation with CaO/TiO_2 ratios (Fig. 4-B1) or taken as the averages of compositionally similar sediment endmembers. Despite the potential uncertainties in these estimates, they provide a preliminary quantification of the δ^{26}Mg values for a variety of sedimentary columns that are being delivered to the trenches.

The calculated sedimentary Mg fluxes differ by two orders of magnitude among

Table 4-2. Calculated Mg fluxes and bulk δ^{26}Mg values of global subducting sedimentary columns

Trench	Subd. rate (cm/yr)	Thickness (m)	Density (g/cc)	Water (%)	Trench (km)	Sediment (%)	Average Mg (wt%)	Mg mass (%)	Mg Flux per (g/yr/cm)	Total Mg (kg/yr)	Average (‰)
N.Zealand	2.7	1600	2.00	30.00	600	2.7%	3.16	5.1%	1910	1.15E+08	−0.28
Kermadec	6.5	200	1.40	58.00	1400	0.8%	1.14	0.5%	87	1.22E+07	−0.24
Tonga	16	70	1.31	62.57	1350	0.5%	1.62	0.5%	89	1.21E+07	0.02
Vanuatu	8.1	650	1.60	38.35	1800	6.9%	1.67	6.9%	867	1.56E+08	−0.29
E.Sunda	7	500	1.71	34.89	1000	2.9%	1.48	2.6%	577	5.77E+07	−0.09
Java	6.5	300	1.65	40.30	2010	2.9%	1.64	2.8%	316	6.35E+07	−0.08
Sumatra	4.7	1400	1.95	24.49	1000	7.1%	1.50	6.4%	1450	1.45E+08	−0.32
Andaman	3	3500	2.05	20.17	1500	19.0%	1.46	16.7%	2504	3.76E+08	−0.36
Makran	3.5	4200	2.05	20.17	950	16.8%	2.11	21.4%	5057	4.80E+08	−0.51
Philippines	6.7	120	1.31	62.57	1550	0.5%	1.86	0.5%	74	1.14E+07	−0.01
Ryuku	7.1	160	1.40	58.00	1350	0.7%	1.83	0.7%	122	1.65E+07	−0.14
Nankai	3	350	2.20	20.00	800	1.1%	1.34	0.9%	248	1.98E+07	−0.44
Marianas	4	476	1.86	23.00	1400	2.8%	2.16	3.7%	590	8.26E+07	−0.21
Izu-Bonin	4.1	408	1.74	31.57	1050	1.5%	0.98	0.9%	196	2.05E+07	−0.18
Japan	8.2	285	1.58	42.68	800	1.2%	1.13	0.8%	238	1.90E+07	−0.16
Kurile	7.8	345	1.64	38.80	1650	3.3%	0.93	1.8%	251	4.15E+07	−0.13
Kamchatka	7.5	435	1.70	35.15	550	1.5%	0.80	0.7%	286	1.57E+07	−0.16
Aleutians	6	350	1.64	41.54	1900	2.8%	1.63	2.8%	329	6.24E+07	−0.26
Alaska	5.3	780	1.80	32.40	800	3.0%	1.96	3.5%	985	7.88E+07	−0.15
Cascadia	3.5	900	1.88	30.00	1300	4.0%	1.53	3.7%	634	8.24E+07	−0.42
Mexico	5.2	170	1.37	59.01	1450	0.5%	1.73	0.6%	86	1.24E+07	−0.24
CentAm	7	425	1.62	48.69	1450	2.7%	0.92	1.5%	227	3.30E+07	−0.61
Colombia	5.9	290	1.44	53.04	1050	0.9%	0.95	0.5%	109	1.15E+07	−0.43
Peru	7.6	125	1.47	50.00	1500	0.8%	1.11	0.5%	77	1.16E+07	−0.50
Chile-35°	7.2	1000	1.88	30.00	495	3.5%	1.83	3.8%	1738	8.60E+07	−0.32
Chile-40°	7.5	1200	1.88	30.00	550	4.8%	1.84	5.3%	2176	1.20E+08	−0.34
Chile-45°	7.5	1500	1.88	30.00	275	3.0%	1.88	3.4%	2780	7.64E+07	−0.38
Sandwich	6.2	200	1.49	50.00	800	0.5%	1.35	0.4%	125	1.00E+07	0.00
N.Antilles	1.8	235	1.66	37.30	400	0.1%	1.42	0.1%	63	2.51E+06	−0.06
S. Antilles	1.8	1750	1.88	30.00	400	1.2%	1.15	0.8%	477	1.91E+07	−0.07
GLOSS-II							**1.658**			**2.25E+09**	**-0.336**

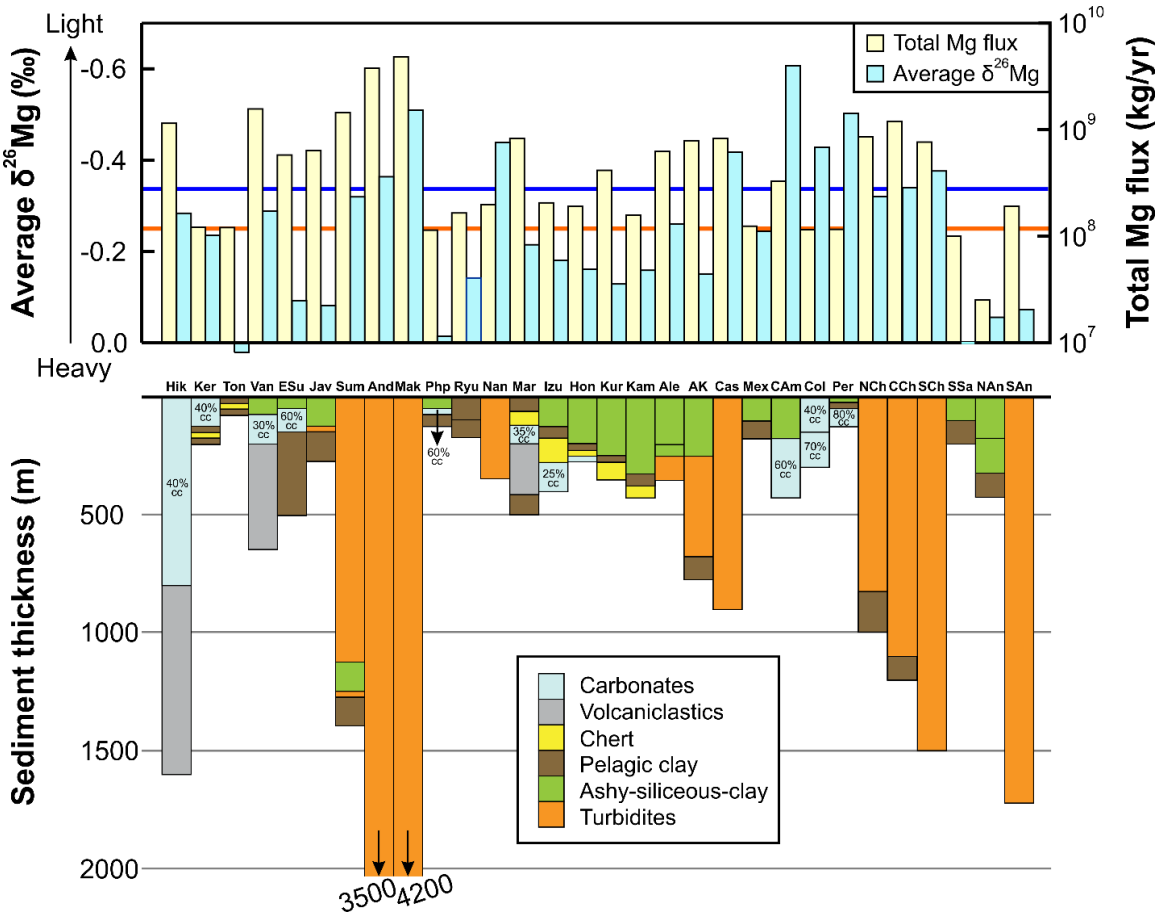

Figure 4-13. Variations of Mg mass fluxes and estimated average δ^{26}Mg values for sedimentary sections subducting at major subduction zones. Sediment sections displayed in the lower panel of the figure are after Plank (2014). The blue horizontal line represents the average δ^{26}Mg value for GLOSS-II (this study) and the red horizontal line represents the mantle average from Teng et al. (2010a). Note that δ^{26}Mg axis is in reverse order and higher blue bars are more negative and therefore isotopically lighter; all values are negative except for one.

the arcs investigated here (Fig. 4-13), ranging from 2.5 × 10^7 kg/yr at the North Antilles margin to 4.8 × 10^9 kg/yr at the Makran trench. The variation is mainly a function of sediment type and section thickness. Generally, Mg fluxes are the highest in trenches fed by thick turbidites. For example, turbidites subducting at Andaman and Makran account for almost 40% of the Mg budget of GLOSS-II. In addition, trenches that contain a thick volcaniclastic section, such as New Zealand and Vanuatu trenches, could contribute significant amount of Mg (~12%) due to high Mg concentration in volcaniclastic sediments. On the other hand, biogenic-dominated trenches, such as South Sandwich, Peru and Colombia, are usually at the low-Mg flux end (≤0.5%) due to low Mg concentration in carbonate and opaline silica and their commonly thin sediment thickness. Convergence rates are generally similar among different trench systems hence they play a secondary role in determining the sediment flux, except for a few cases where they are considerably different. For example, although the sediment section at Tonga is only 70 m thick, its fast subduction rate of 16 cm/year results in a similar Mg flux (1.2× 10^8 kg/yr) to that of the South Antilles (1.9 ×10^8 kg/yr), where the sediment column is 1750 km thick but subducts at a much slower rate of 1.8 cm/year (Table 4-2).

Similar to the large range in regional Mg fluxes, estimated average sedimentary δ^{26}Mg values for different trenches also display a significant arc-to-arc variation from −0.61‰ to +0.02‰, reflecting different dominant lithology among global sediments (Fig. 4-13). Sediment sections rich in clay-size detritus derived from mature and highly weathered continental sources acquire an accompanying heavy Mg isotopic signature (e.g., Antilles and South Sandwich), in comparison with less-differentiated volcaniclastic-dominated or glacially transported sediments that preserve mantle-like δ^{26}Mg signatures

(e.g., Peru and Alaska). Grain-size sorting also fractionates Mg isotopes within turbidites. Those sequences enriched in coarse-size detritus could possibly host higher amounts of low-δ^{26}Mg carbonate and/or garnet, leading to a lighter Mg isotopic signature. Enrichment in hydrogenetic phases leads to heavier Mg isotopic compositions in some sediment sections (e.g., Philippines and Tonga) as a result of preferential uptake of heavy Mg isotopes during authigenic clay formation. On the contrary, a few sites near the equatorial regions, such as Central America, Peru and Colombia, contain a high fraction of biogenic carbonate, which drives their bulk δ^{26}Mg to variably lighter values. The global variation in sedimentary δ^{26}Mg input to active subduction zones falls within the range found in continental sediments, while the flux-weighted δ^{26}Mg average for GLOSS-II (−0.336‰) is slightly lower than both the average upper continental crust (−0.22‰, Li et al., 2010) and normal upper mantle (−0.25 ± 0.07‰, Teng et al., 2010a).

The relatively lower δ^{26}Mg of GLOSS-II is consistent with the fact that GLOSS-II, as well as its Mg content, is heavily weighted by a few isotopically light turbidites sequences and volcaniclastic sections (Fig. 4-13, Table 4-2). The thick turbidite sequences subducting at Sumatra, Andaman, Makran, Cascadia and Chile margins together account for > 60% of the total Mg flux of the GLOSS-II, and they have variably low δ^{26}Mg averages (−0.51‰ to −0.32‰, Table 4-2). Among them, the lowest average δ^{26}Mg value occur at the thickest Makran section (4200 m, Plank, 2014) that contributes to > 20% of the Mg flux of the GLOSS-II. Likewise, the thick MgO-rich volcaniclastics sections at New Zealand-Hikurangi trough and Vanuatu trench result in high average MgO values in the incoming sediment columns (e.g., up to 5.24 wt% in the former, Plank, 2014). Meanwhile, the thick carbonate units above the volcaniclastics layers drive the bulk δ^{26}Mg values (~

−0.30‰) to slightly lower than the mantle average. Furthermore, local enrichment of carbonate in some sediment sections that close to the equator, such as sediments from Central America and Colombia-Ecuador trenches, may also contribute to the overall lower δ^{26}Mg average for the GLOSSII. In addition, marine sediments generally underwent lower degree of chemical weathering and hence are less enriched in heavy Mg isotopes compared with widespread highly weathered shales on continents.

5.3. Implications for arc magmatism and mantle Mg isotopic heterogeneity

Subducted sediments were considered to be one of the key components in producing the enriched mantle endmembers (e.g. Hofmann, 2014). Non-mantle δ^{26}Mg values found in some mantle derivatives have also been tentatively ascribed to contributions from subducted slabs (Yang et al., 2012; Wang et al., 2012, 2015a, 2016; Xiao et al., 2013; Huang et al., 2015, Liu et al., 2015; Hu et al., 2016a; Tian et al., 2016; Teng et al., 2016; Li et al., 2017). Our study provides the direct evidence that Mg isotopic compositions of subducting marine sediments are indeed highly heterogeneous (Fig. 4-13). More importantly, trenches with high sedimentary Mg fluxes have average δ^{26}Mg values different from the mantle, suggesting they may exert a significant impact on mantle Mg isotopic heterogeneity. Furthermore, recent studies have revealed that altered oceanic crust and abyssal peridotites also have heterogeneous Mg isotopic compositions (Huang, 2013; Liu et al., 2017). Since metamorphic dehydration does not fractionate Mg isotopes (Li et al., 2011, 2014; Teng et al., 2013; Wang et al., 2014a, 2015b, 2015c), the subducting slab as a whole can carry significant amount of distinct Mg isotopes into the mantle.

Different slab components, however, are expected to release Mg at different depths

and by different mechanisms, hence they may contribute differently to arc magmatism and mantle Mg isotopic heterogeneity. Marine sediments may undergo partial melting during subduction because the primary hydrous phase in sediments breaks down above the fluid-saturated solidus (Johnson and Plank, 1999). However, dehydration is more likely to occur than melting for basaltic crust at the thermal structure of most modern subduction zones, and these fluids further promote sediment melting. In addition, the slab-mantle interface is a sedimentary-mafic/ultramafic mixing zone (Bebout, 2007),

6. Conclusions

Marine sediments from ten drill sites in front of the world's major subduction zones display large variation in their Mg isotopic compositions, which mainly reflects differences in sediment mineralogy, provenance composition, and sedimentary processes. The following conclusions can be drawn:

(1) The bulk marine sediments have highly heterogeneous δ^{26}Mg values (−1.34‰ to +0.46‰), the variation of which largely mirrors that found in rocks and sediments on continents.

(2) Sediment mineralogy plays an important role on the Mg isotopic distribution among different sediment types. Carbonate-rich sediments favor light Mg isotopes, while clay-rich sediments are generally more enriched in heavy Mg isotopes.

(3) Chemical weathering and sediment textural/mineralogical sorting can potentially alter the relative proportions of fine-grained clay to coarse-grained sand and, therefore, drive the δ^{26}Mg of clay-rich marine sediments to heavier values, while the presence of detrital carbonate and/or garnet in the coarser fraction drives turbidites to variably

lower δ^{26}Mg values.

(4) Hydrogenetic clays have a relatively uniform and, on average, heavy Mg isotopic composition, consistent with preferential uptake of heavy isotopes by authigenic clays. In comparison, hydrothermal clays have highly variable δ^{26}Mg values, which may result from variable mixing between detrital phases and hydrothermal fluids or seawater.

(5) The Mg mass flux and isotopic composition of subducting sediment sections vary substantially from arc to arc. Recycling of these isotopically heterogeneous marine sediments, together with altered oceanic crust and abyssal peridotites, into the mantle may lead to local mantle domains with distinct Mg isotopic compositions and generate heterogeneous volcanic rocks.

7. Appendix A. Supplementary data

Supplementary data to this article can be found online at http://dx.doi.org/10.1016/j.chemgeo.2017.06.010.

Acknowledgements. We would like to thank the Deep Sea Drilling Program and Ocean Drilling Program for providing the core samples for this study. Brian Atwater, Charlotte Schreiber, Ronald Sletten, Scott Kuehner and Melissa Harrington are thanked for stimulating discussions. Constructive comments of Ming Tang and an anonymous reviewer, and efficient editorial handling by Michael E. Böttcher are gratefully acknowledged. This work was financially supported by the National Science Foundation (EAR-1340160 to F.-Z. Teng), National Natural Science Foundation of China (41602343 to K.-J. Huang), 2015

graduate student research grant from the Geological Society of America (to Y. Hu), and George Edward Goodspeed Geology Scholarship from the Earth and Space Sciences Department of the University of Washington (to Y. Hu).

Chapter 5. Magnesium cycling at subduction zones constrained by Mg isotopic composition of sub-arc mantle beneath southern Kamchatka

This chapter is in preparation for publication as:

Hu, Y., Teng, F.-Z. and Dmitri A. Ionov (in prep) Magnesium cycling at subduction zones constrained by Mg isotopic composition of sub-arc mantle beneath southern Kamchatka.

Abstract

Subduction of the oceanic slab may add to mantle components with stable isotopic signatures fractionated at low-temperatures. The highly variable Mg isotopic compositions of the subducted oceanic slab input and arc lava output imply that components with atypical Mg isotopic compositions are present in the mantle wedge. Magnesium isotopic data on samples from the sub-arc mantle are still limited, however. To characterize the Mg isotopic composition of a typical supra-subduction zone mantle domain, 23 large and fresh spinel harzburgite xenoliths from the Avacha volcano in Kamchatka, Russia, were analyzed. These harzburgites were formed by ~30% melt extraction at fluid fluxing conditions, followed by subduction-derived small-scale fluid metasomatism. They are similar in modal and chemical composition to forearc harzburgites and harzburgite xenoliths from the western Pacific. The δ^{26}Mg values of the Avacha xenoliths display limited variation from −0.30‰ to −0.21‰, overlapping the mantle average at −0.25 ± 0.07‰. The overall mantle-like and uniform δ^{26}Mg range of the Avacha sub-arc peridotites may be due to their high MgO contents (≥44 wt%) and low fluid/rock mass ratios during flux melting and metasomatism. Clinopyroxene, a rare late-stage mineral (−0.24 ± 0.10‰, 2SD, n = 5),

appears to be in Mg isotopic equilibrium with olivine (−0.26 ± 0.04‰, 2SD, n = 17) and orthopyroxene (−0.23 ± 0.04‰, 2SD, n = 17). Collectively, this study finds that melting residues in the mantle wedge in the western Pacific, where dehydration of slab crust serves as the major water supplier for melting and metasomatism, likely have a mantle-like δ^{26}Mg. Fluids released from oceanic crust at pressures of ~2 to 3 GPa are well buffered during their migration in the mantle wedge due to their low Mg concentrations. Large-scale dehydration of isotopically distinct materials at higher pressures may be required to produce isotopically diverse arc lavas.

1. Introduction

Slab-mantle interaction at subduction zones is central to global element cycling, arc magmatism, and seismic activities, which ultimately contribute to the formation of the continental crust and physicochemical evolution of the mantle. The Mg isotope system has recently been suggested as a potential tracer of crustal recycling due to its solubility in fluids, the lack of measurable Mg isotope fractionation during metamorphic dehydration (e.g., Teng et al., 2013; Li et al., 2014; Wang et al., 2014), and the large isotopic contrast between typical mantle rocks and surface materials (Teng, 2017 and references therein). Magnesium is overwhelmingly enriched in the mantle relative to the crust, and has shown a uniform isotope ratio (δ^{26}Mg) in the majority of peridotites and oceanic basalts (Teng et al., 2010a). By contrast, low-temperature continental chemical weathering and seafloor alteration fractionate Mg isotopes significantly, leading to a highly heterogeneous subducting slab that contains marine sediments, altered oceanic crust, and altered abyssal peridotite (Wimpenny et al., 2012; Beinlich et al., 2014; Teng et al., 2016; Hu et al., 2017;

Liu et al., 2017; Huang et al., 2018). Therefore, contributions of recycled crustal materials to sub-arc mantle could potentially be seen in δ^{26}Mg values of arc lavas that deviate from the normal mantle range. Studies of arc lavas from Lesser Antilles and Philippines have found δ^{26}Mg values higher than the normal mantle, which are attributed to hydration and modification of the mantle wedge by fluids released from subducting slabs, in particularly abyssal peridotites (Teng et al., 2016; Li et al., 2017).

The highly variable Mg isotopic compositions of the subducting slab input and arc lava output suggest that slab-derived Mg isotopic signatures could be detected in the mantle wedge, which serves as the primary sink for various slab-released fluids/melts and is the main source of arc magmas. Compared to arc lavas that commonly undergo magmatic differentiation and crustal assimilation during their ascent through the overlying crust, arc peridotite xenoliths are fragments of mantle lithosphere above the subducted slab accidentally entrained in arc magmas and brought to the surface by explosive eruptions. They are thus direct samples of materials processed in the mantle wedge that may provide insights into the melting and slab-mantle interaction processes that are independent of, but complementary to, observations from arc lavas. However, Mg isotopic data on arc peridotite xenoliths remain sparse due to the scarcity of representative samples, making the sub-arc mantle one of the most important, but least documented, mantle reservoirs.

The Kamchatka peninsula in far eastern Russia (Fig. 5-1) hosts one of the few arcs where mantle xenoliths are available. The most common xenoliths near the arc front are refractory spinel harzburgites interpreted as residues of flux melting in sub-arc mantle variably affected by slab-related fluids and/or melts during or after their incorporation in the mantle lithosphere (Halama et al., 2009; Ionov, 2010, 2011; Bénard and Ionov, 2012;

Hopp and Ionov, 2011; Ionov et al., 2011, 2013; Bénard et al., 2013, 2016, 2017). Much work on Kamchatka xenoliths (including those inland from the arc) examined microstructural deformation, volatile and fluid-mobile elements, and Sr-Os-Pb-$^{4}He/^{3}He$ isotopes, along with the formation of late-stage minerals, glass inclusions and a variety of pyroxene-rich veins (Soustelle et al., 2010; Kepezhinskas et al., 1995, 1996, 1997, 2002; Kepezhinskas and Defant, 1996; Arai et al., 2003; Widom et al., 2003; Saha et al., 2005; Ishimaru et al, 2006, 2007, 2009; Bryant et al., 2007; Arai and Ishimaru, 2008; Ishimaru and Arai, 2008a,b,c, 2011). Partial melting of sub-arc mantle beneath Kamchatka generated a wide variety of lavas that display elemental and isotopic enrichments (H-O-Sr-Nd-Pb-Hf and U series) (Hochstaedter et al., 1994; Kersting and Arculus, 1995; Kepezhinskas et al., 1996, 1997; Turner et al., 1998; Pineau et al., 1999; Dorendorf et al., 2000; Churikova et al., 2001, 2007; Ishikawa et al., 2001; Yogodzinski et al., 2001; Dosseto et al., 2003; Duggen et al., 2007; Portnyagin et al., 2007; Auer et al., 2009; Dosseto and Turner, 2014; Kayzar et al., 2014).

To further constrain the Mg isotope systematics in subduction zones, we analyze a suite of 23 spinel harzburgite xenoliths from the Avacha volcano in southern Kamchatka arc. These samples are uncommonly large, fresh, and texturally equilibrated. Importantly, they do not show evidence for late-stage interaction with host magmas or extensive recrystallization reported for other xenolith suites from Avacha (e.g., Arai et al., 2003; Ishimaru et al., 2007; Ishimaru and Arai, 2008). Therefore, their composition reflects the nature of original sub-arc lithospheric mantle. The Mg isotopic composition of sub-arc mantle peridotites are examined in conjunction with published arc lava $\delta^{26}Mg$ data to explore the relationship between slab dehydration and $\delta^{26}Mg$ variation in the lavas. Our

results demonstrate that the mantle wedge beneath the southern Kamchatka arc, which represents a typical subduction zone in the western Pacific, has largely a uniform and mantle-like Mg isotopic composition despite interaction with slab-derived fluids. Subduction of oceanic crust with its overlying sediments has long been considered an essential mechanism of elemental cycling from Earth's surface to its interior, thereby producing chemical and isotopic heterogeneity in mantle rocks and mantle-derived magmas (e.g., Armstrong, 1968; Hofmann, 2014 and references therein). Recently, this process has also been called upon to explain local Mg isotopic variations in the mantle (e.g., Yang et al., 2012; Xiao et al., 2013; Hu et al., 2016a; Li et al., 2017). The majority of mantle peridotites and oceanic basalts have similar Mg isotopic compositions (δ^{26}Mg = −0.25 ± 0.07‰, 2SD, Teng et al., 2010a), suggesting homogeneous distribution of Mg isotopes in the mantle. Nevertheless, some mantle xenoliths (e.g., wehrlite, pyroxenite and eclogite) and mantle-derived lava possess δ^{26}Mg values that lie outside the well-defined mantle range, and could reflect a contribution from recycled crustal Mg (Wang et al., 2012, 2015a, 2016; Yang et al., 2012; Xiao et al., 2013; Huang et al., 2015; Liu et al., 2015; Hu et al., 2016a; Tian et al., 2016; Teng et al., 2016; Li et al., 2017).

2. Geologic setting

The Kamchatka arc lies in the northern part of the c.a. 2000 km-long Kamchatka-Kurile convergent margin formed by subduction of the Mesozoic Pacific plate beneath the Eurasian plate in northwestern Pacific at a rate of 8 cm/yr (Gorbatov et al., 1997) (Fig. 5-1). Orthogonal intersection with the Aleutian transform fault-trench system, where the Pacific plate subducts beneath the North American plate, sets the northern limit of the

Kamchatka arc and divides it into a volcanically inactive north segment and active central and south segments (Hochstaedter et al., 1994; Kepezhinskas et al., 1995). At the north segment, westward subduction of the young (< 25 Ma) and hot oceanic lithosphere formed by short-lived spreading in the Komandorsky basin (Bogdanov, 1988) had produced arc volcanism in the Sredinny Range (SR) until 2 Ma (Firsov, 1987). Closure of the Vetlovka basin and subsequent accretion of the Kronotsky terrane led to formation of the Eastern Volcanic Front (EVF) at the southern segment and the 200 km-wide Central Kamchatka depression (CKD) between the SR and EVF in the central segment.

The Avacha (Avachinsky) stratovolcano (53°15'N, 158°52'E) is located in the middle part of the EVF (Fig. 5-1). It is situated ~ 120 km above the slab surface, where the 70 km-thick Pacific slab is subducting at 55° (Gorbatov et al., 1997). A layer of low P-velocity has been observed at 70 to 130 km and was interpreted to represent the asthenospheric mantle wedge (Nizkous et al., 2006). The Avacha volcano formed in late Pleistocene, producing volcanic ash-fall (or trephra) and pyroclastic flow deposits of calc-alkaline affinity.

3. Samples and evidence for slab - mantle interaction

A unique feature of partial melting in arc settings is the high fluid flux supplied by down-going slab, which facilitates melt extraction, leaving behind highly refractory peridotite residues (Bizimis et al., 2000). The xenoliths analyzed in this study are medium- to coarse-grained spinel harzburgites (Ionov, 2010; Bénard et al., 2017). They are primarily composed of olivine (67-82.5%) and orthopyroxene (Opx, 18-30%) as well as accessory spinel, late-stage interstitial clinopyroxene (Cpx, 1-3%) formed mainly by exsolution from

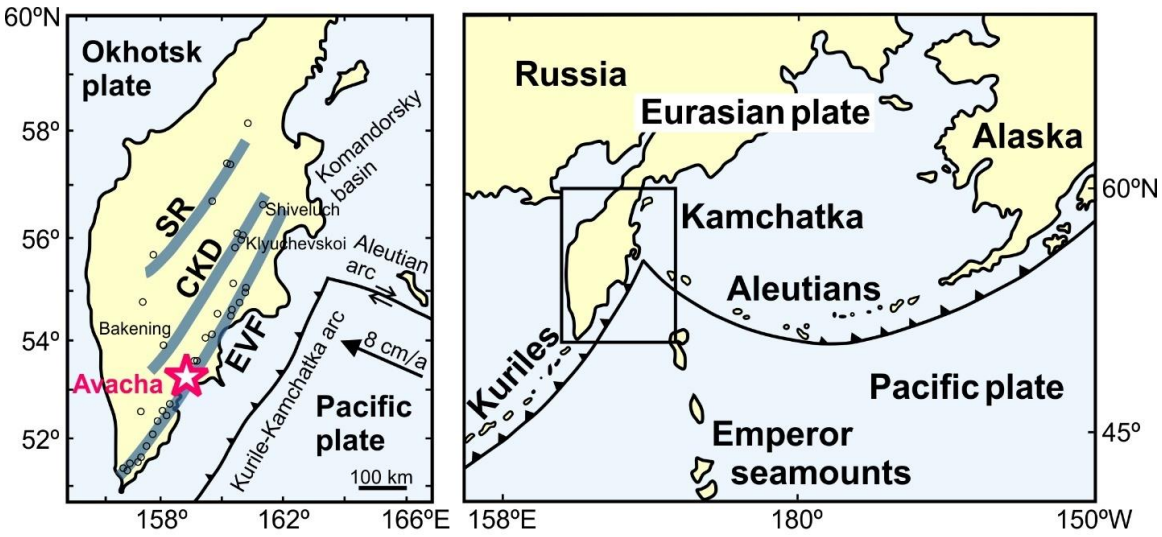

Figure 5-1. Geological map of the Kamchatka peninsula, Russia. The boxed area of Kamchatka is enlarged on the left to show the locations of major Quaternary volcanoes. Modified from Kersting and Arculus (1995) and Ionov (2010). EVF = Eastern Volcanic Front, SR = Sredinny Range, CKD = Central Kamchatka Depression.

high-temperature Opx on cooling, and amphibole (< 1%). These highly refractory (≥ 44 wt.% MgO) peridotites containing no primary Cpx were inferred to have formed by high degree (28-35%) melt extraction at 45 to 65 km depth (Ionov, 2010). Compared to the local Moho depth at ~ 37 km (Levin et al., 2002), these harzburgites represent the shallow lithospheric mantle beneath Avacha affected by fluid metasomatism (Ionov, 2010), veining (Halama, 2009; Bénard et al., 2013, 2016) and high-temperature creep-related deformation (Soustelle et al., 2010).

A distinctive characteristic of the Avacha peridotite suite is the paradoxical enrichment in silica (hosted by opx) despite their highly refractory nature (Fig. 5-2a), which requires an enrichment process in addition to partial melting (Herzberg, 2004). It was initially suggested, based on studies of xenoliths containing fine-grained Opx, that the Avacha peridotites were enriched in Opx after the melting (shortly before their capture by magma) due to reaction of primary olivine with subduction-related fluids (e.g. Ishimaru et al., 2007). By contrast, Ionov (2010) reported silica enrichments in peridotites from this study that contain no fine-grained Opx and argued that the enrichments took place during the melting because of the input of slab-derived components and effects of fluids on modal proportions in the residues. Recently, modeling of mantle melting further suggested that the Avacha peridotites could be residues after extraction of picrites and high Ca-boninites (Bénard and Ionov, 2012, Bénard et al., 2016) from a hybrid source that formed by interaction of refractory mantle with slab-derived components before flux melting (Bénard et al., 2017).

The subduction of old and hence cold Pacific plate (~ 100 Ma) beneath southern Kamchatka implies that slab dehydration beneath the EVF produces hydrous fluids rather

than melts, which is supported by thermal modeling for the Kamchatka arc (Manea and Manea, 2007). This is consistent with the fact that nearly all Avacha harzburgites contain accessory amphibole and show U-shaped trace element patterns with widespread (but low-degree) enrichments in fluid-mobile elements (Rb, Ba, U, Pb, Sr, and B) relative to fluid-immobile, melt-mobile elements (e.g., MREE, Nb, Y) (Ionov, 2010), similar to serpentinized forearc peridotites (Savov et al., 2005) (Fig. 5-2). Locally, at high fluid/rock ratios, the reaction of such fluids with refractory mantle produced small-volume boninitic melts that formed rare, thin veins (Bénard and Ionov, 2013), as well as melt inclusions in spinel (Bénard et al., 2016), in some xenoliths. To sum up, the Avacha xenoliths show ubiquitous, but weak effects of percolation of slab-derived fluids on bulk-rock compositions, in addition, some xenoliths contain veins formed by boninitic melts.

The Sr-Nd-Pb isotopic signatures of the southern Kamchatkan basalts and xenoliths are similar to those in Pacific MORB, suggesting the dominant role of fluids from the altered oceanic crust with limited sediment contribution (< 1%) in the volatile input to the mantle wedge (Kersting and Arculus, 1995; Kepezhinskas et al., 1997; Churikova et al., 2001; Saha et al., 2005; Duggen et al., 2007). This is consistent with the radiogenic Os isotopes of peridotite xenoliths (Widom et al., 2003; Saha et al., 2005) and high-$\delta^{18}O$ signatures from lava-hosted phenocrysts (Dorendorf et al., 2000). In addition, studies of volatiles in melt inclusions from lava-hosted olivine, and B concentration and isotopic signatures of the lavas suggest a possible role of serpentinite dehydration (Ishikawa et al., 2001; Churikova et al., 2007; Portnyagin et al., 2007). Serpentinite dehydration is independently supported also by the observation of a double seismic zone in Kamchatka (Gobatov et al., 1997), which is commonly attributed to breakdown of antigorite (Peacock

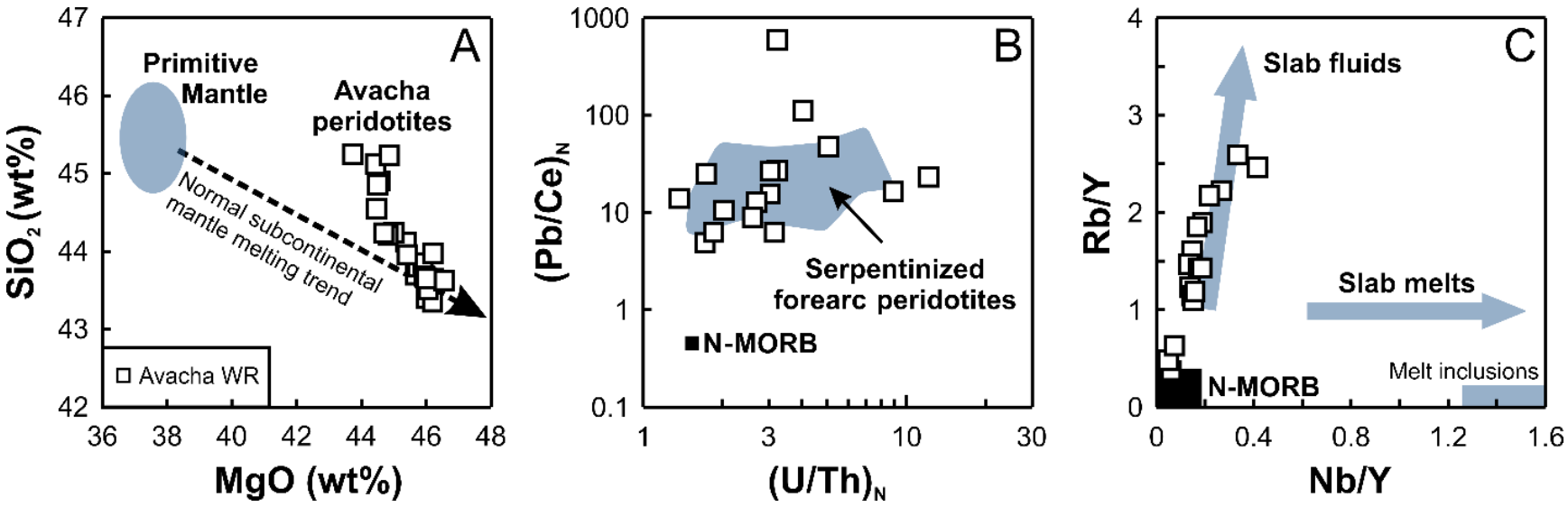

Figure 5-2. Geochemical evidence for subduction-related metasomatism recorded in the Avacha peridotite xenoliths. Major and trace element concentrations are from Ionov (2010). Ce/Pb and U/Th abundances are normalized to primitive mantle of McDonough and Sun (1995). The compositions of serpentinized forearc peridotites (Savov et al., 2005) and N-MORB (Sun and McDonough, 1989) are plotted for comparison. The field of slab melts trapped in the Kamchatka mantle are based on analyses of glass veins and melt inclusions in Kamchatka mantle xenoliths (Kepezhinskas et al., 1996; Kepezhinskas and Defant, 1996).

et al., 2001).

4. Analytical methods

Magnesium isotopic analysis was performed at the Isotope Laboratory of the University of Washington, Seattle. Protocols for sample digestion, chemical separation and instrumental analysis are outlined in Teng et al. (2007, 2010) and are summarized here. The whole-rock powders analyzed here are the same as those used in Ionov (2010) and Bénard et al. (2017). Olivine and pyroxene fragments were hand-picked under a binocular. Whole-rock powders and pre-cleaned mineral fragments were dissolved in a mixture of Optima HF-HNO_3-HCl with no insoluble residue present in the solution. After complete dissolution, sample solutions were evaporated to dryness and then fluxed with 1 N HNO_3 for column chromatography. Magnesium was quantitatively extracted and purified by two passes of the pre-cleaned Bio-Rad cation exchange resin (AG50W-X8 resin, 200-400 mesh) in 1 N HNO_3. Magnesium isotopic ratios were then measured on a Nu Plasma II multi-collector inductively coupled plasma mass spectrometer (MC-ICPMS) using sample-standard bracketing method. Dried Mg cuts were diluted to 300 ppb Mg concentration in 3% Optima HNO_3 shortly before analysis. The sample solutions were introduced under "wet" plasma conditions and were analyzed in low-resolution mode. Sample intensity was adjusted to within 10% of that of the bracketing standard. Magnesium isotopic data are expressed as per mil (‰) deviation relative to the DSM3 standard:

$$\delta^{x}\mathrm{Mg}\ (‰) = \left\{ \frac{\left({}^{x}\mathrm{Mg}/{}^{24}\mathrm{Mg} \right)_{\mathrm{sample}}}{\left({}^{x}\mathrm{Mg}/{}^{24}\mathrm{Mg} \right)_{\mathrm{DSM3}}} - 1 \right\} \times 1000$$

where x = 25 or 26. The associated error of each data is 2SD, which represents two times

the standard deviation of multiple analyses of bracketing standards during an analytical session.

The accuracy of the method was checked by processing and measuring three international rock standards, and two in-house standards (San Carlos olivine and Hawaiian seawater) along with the unknown samples (Table 5-1). The two peridotite standards (PCC-1 and DTS-1) yield average $\delta^{26}Mg$ of −0.25 ± 0.03‰ (n = 4) and −0.31 ± 0.05‰ (n = 2), and the basalt standard (JB-1) has a similar average $\delta^{26}Mg$ of −0.28 ± 0.03‰ (n = 3). The average $\delta^{26}Mg$ for 15 measurements on San Carlos olivine and 7 analyses on Hawaiian seawater are −0.25 ± 0.03‰ and −0.85 ± 0.03‰, respectively. The results of all these standards agree well with recommended values listed in Table 5-1 (Ling et al., 2011; Teng et al., 2015; Hu et al., 2016a).

5. Results

Magnesium isotopic compositions for bulk peridotites are reported in Table 5-2 along with mineral modes, MgO and Al_2O_3 contents, and estimated equilibrium temperatures reported in Ionov (2010) and Bénard et al. (2017). The Mg isotopic compositions of mineral separates are presented in Table 5-3. Table 5-4 reports the degree of inter-mineral Mg isotopic fractionation, calculated as $\Delta^{26}Mg_{X-Y} = \delta^{26}Mg_X - \delta^{26}Mg_Y$, where X and Y refer to two different mineral phases. All measurements during the course of this study fall on a single mass-dependent fractionation line with a slope of 0.51 (R^2 = 0.99) (not shown) and therefore only $\delta^{26}Mg$ values are discussed hereafter.

Table 5-1. Mg isotopic compositions of standards analyzed during the course of this study.

Standard	δ^{26}Mg	2SD	δ^{25}Mg	2SD	Reference
PCC-1	−0.25	0.05	−0.14	0.04	
Harzburgite (USGS)	−0.25	0.05	−0.11	0.06	
	−0.26	0.07	−0.14	0.06	
	−0.26	0.07	−0.14	0.05	
Average	*−0.25*	*0.03*	*−0.14*	*0.02*	
Recommended	**−0.23**	**0.06**	**−0.10**	**0.01**	Teng (2017)
DTS-1	−0.31	0.07	−0.17	0.06	
Dunite (USGS)	−0.31	0.06	−0.15	0.05	
Average	*−0.31*	*0.05*	*−0.16*	*0.04*	
Recommended	**−0.30**	**0.01**	**−0.13**	**0.01**	Teng (2017)
JB-1	−0.28	0.06	−0.15	0.04	
Basalt (GSJ)	−0.25	0.07	−0.13	0.04	
	−0.29	0.06	−0.16	0.04	Teng (2017)
Average	*−0.28*	*0.03*	*−0.15*	*0.02*	
Recommended	**−0.28**	**0.1**	**−0.15**	**0.04**	
San Carlos olivine	−0.26	0.05	−0.13	0.05	
	−0.23	0.05	−0.12	0.06	
	−0.26	0.05	−0.15	0.04	
	−0.24	0.07	−0.11	0.05	
	−0.26	0.07	−0.13	0.06	
	−0.26	0.06	−0.13	0.04	
	−0.23	0.08	−0.12	0.05	
	−0.22	0.06	−0.12	0.05	
	−0.24	0.07	−0.13	0.03	
	−0.25	0.06	−0.13	0.04	
	−0.26	0.07	−0.13	0.04	
	−0.25	0.07	−0.14	0.04	
	−0.26	0.07	−0.15	0.05	
	−0.22	0.06	−0.12	0.04	
	−0.25	0.06	−0.13	0.04	
Average	*−0.25*	*0.03*	*−0.13*	*0.02*	
Recommended	**−0.24**	**0.03**	**−0.12**	**0.02**	Hu et al. (2016a)
Hawaiian seawater	−0.86	0.07	−0.45	0.06	
	−0.83	0.05	−0.43	0.04	
	−0.83	0.07	−0.42	0.04	
	−0.86	0.05	−0.42	0.05	
	−0.87	0.06	−0.43	0.05	
	−0.85	0.07	−0.45	0.05	
	−0.85	0.07	−0.44	0.06	
Average	*−0.85*	*0.03*	*−0.43*	*0.03*	
Recommended	**−0.84**	**0.06**	**−0.43**	**0.04**	Teng et al. (2015)

Table 5-2. Mg isotopic compositions of bulk Avacha harzburgite xenoliths.

Sample	δ^{26}Mg (‰)	2SD (‰)	δ^{25}Mg (‰)	2SD (‰)	MgO (wt. %)	Mg#	Al_2O_3 (wt. %)	T (Ca-Opx) (°C)	T (Ol-Spl) (°C)
Spl harzburgite									
Av-1	−0.29	0.07	−0.13	0.04	45.67	0.91	0.50	903	950
re-dissolution	−0.29	0.05	−0.15	0.05					
average	*−0.29*	*0.04*	*−0.14*	*0.03*					
Av-2	−0.30	0.07	−0.17	0.04	45.37	0.91	0.55	906	969
Av-3	−0.30	0.07	−0.14	0.04	45.74	0.91	0.41	946	950
Av-4	−0.28	0.07	−0.13	0.03	43.73	0.91	0.75	920	792
duplicate	−0.30	0.07	−0.14	0.04					
re-dissolution	−0.30	0.05	−0.16	0.05					
average	*−0.29*	*0.04*	*−0.14*	*0.02*					
Av-5	−0.26	0.06	−0.13	0.04	44.56	0.91	0.63	900	988
Av-6	−0.27	0.06	−0.15	0.04	45.97	0.91	0.48	993	995
duplicate	−0.27	0.07	−0.14	0.05					
re-dissolution	−0.25	0.05	−0.14	0.05					
average	*−0.26*	*0.04*	*−0.14*	*0.03*					
Av-7	−0.27	0.08	−0.13	0.05	46.02	0.91	0.42	916	907
Av-8	−0.30	0.07	−0.15	0.05	44.50	0.91	0.78	958	976
re-dissolution	−0.29	0.05	−0.14	0.05					
average	*−0.29*	*0.04*	*−0.14*	*0.04*					
Av-9	−0.27	0.05	−0.14	0.05	46.19	0.91	0.50	923	964
duplicate	−0.27	0.07	−0.13	0.04					
average	*−0.27*	*0.04*	*−0.13*	*0.03*					
Av-10	−0.28	0.05	−0.15	0.05	45.00	0.91	0.62	949	989
duplicate	−0.21	0.07	−0.10	0.04					
average	*−0.25*	*0.04*	*−0.12*	*0.03*					
Av-11	−0.30	0.05	−0.15	0.05	46.21	0.91	0.44	930	914
duplicate	−0.30	0.07	−0.16	0.04					
average	*−0.30*	*0.04*	*−0.16*	*0.03*					
Av-12	−0.24	0.05	−0.12	0.05	46.05	0.91	0.62	917	978

duplicate	−0.25	0.07	−0.12	0.04					
average	*−0.24*	*0.04*	*−0.12*	*0.03*					
Av-13	−0.29	0.05	−0.16	0.05	45.90	0.91	0.53	954	997
duplicate	−0.24	0.07	−0.11	0.04					
average	*−0.27*	*0.04*	*−0.13*	*0.03*					
Av-14	−0.27	0.05	−0.14	0.05	44.47	0.91	0.85	915	972
duplicate	−0.28	0.07	−0.12	0.04					
average	*−0.27*	*0.04*	*−0.13*	*0.03*					
Av-15	−0.27	0.05	−0.12	0.05	44.82	0.91	0.63	960	972
duplicate	−0.22	0.07	−0.11	0.04					
average	*−0.25*	*0.04*	*−0.12*	*0.03*					
Av-16	−0.29	0.05	−0.14	0.05	46.20	0.92	0.52	989	993
duplicate	−0.29	0.07	−0.13	0.04					
average	*−0.29*	*0.04*	*−0.13*	*0.03*					
Av-17	−0.27	0.05	−0.13	0.05	46.54	0.91	0.50	895	915
duplicate	−0.23	0.07	−0.12	0.04					
average	*−0.25*	*0.04*	*−0.12*	*0.03*					
Av-33	−0.27	0.07	−0.15	0.04	44.69	0.91	0.66		
Av-40	−0.30	0.07	−0.15	0.04	45.93	0.91	0.52		
Av-41	−0.28	0.06	−0.14	0.05	46.00	0.91	0.62		
duplicate	−0.27	0.05	−0.13	0.04					
average	*−0.28*	*0.04*	*−0.14*	*0.03*					
Av-42	−0.31	0.07	−0.16	0.04	45.42	0.91	0.59		
duplicate	−0.28	0.05	−0.14	0.04					
average	*−0.29*	*0.04*	*−0.15*	*0.03*					
Av-G1	−0.20	0.07	−0.11	0.04	44.44	0.90	0.71		
duplicate	−0.22	0.07	−0.11	0.05					
average	*−0.21*	*0.05*	*−0.11*	*0.03*					
Av-G2	−0.23	0.06	−0.12	0.04	44.86	0.91	0.71		
duplicate	−0.22	0.07	−0.11	0.05					
average	*−0.23*	*0.05*	*−0.12*	*0.03*					

Overall, both the bulk peridotites and their constituent minerals display narrow variations in δ26Mg, which are not correlated with their modal or major element compositions (Fig. 5-3). The δ^{26}Mg values of the 23 Avacha peridotites vary from −0.30‰ to −0.21‰ with an average of −0.27 ± 0.05‰ (2SD). Similarly, olivine separates from the Avacha harzburgites have uniform δ^{26}Mg ranging between −0.30‰ and −0.23‰. Opx and Cpx have slightly higher and more heterogeneous δ^{26}Mg values of −0.27‰ to −0.19‰ and −0.32‰ to −0.20‰, respectively. The average δ^{26}Mg are −0.26 ± 0.04‰ (2SD, n = 15) for olivine, −0.23 ± 0.04‰ (2SD, n = 15) for Opx and −0.24 ± 0.10‰ (2SD, n = 5) for Cpx. The 15 olivine – Opx pairs yield $\Delta^{26}Mg_{Opx\text{-}Ol}$ from +0.01‰ to +0.08‰, with an average of +0.04 ± 0.04‰, while the five olivine – Cpx pairs yield $\Delta^{26}Mg_{Cpx\text{-}Ol}$ from −0.06‰ to +0.08‰, with an average of +0.02 ± 0.11‰ (Fig. 5-4).

6. Discussion

The Avacha tuff-hosted xenoliths analyzed in this study were rapidly carried to surface by volatile-rich andesitic magmas, and cooled down immediately after the explosive eruption. They have not undergone observable post-eruption alteration as indicated by petrographic data as well as mass gain on ignition (proportional to iron contents) and hence lack of hydrous phases, apart from rare accessory amphibole of mantle origin (Ionov, 2010). Therefore, these xenoliths record genuine sub-arc signatures and provide an opportunity to examine the nature and processes of Mg isotope distribution in an active subduction zone setting. Detailed petrographic and geochemical investigation on the Avacha peridotite suite suggested that their modal and chemical compositions mainly reflect melt extraction and moderate subduction-related enrichments (Ionov, 2010). Since

Table 5-3. Mg isotopic compositions of mineral separates

	Olivine (Ol)				Orthopyroxene (Opx)				Clinopyroxene (Cpx)			
Samples	**δ^{26}Mg**	**2SD**	**δ^{25}Mg**	**2SD**	**δ^{26}Mg**	**2SD**	**δ^{25}Mg**	**2SD**	**δ^{26}Mg**	**2SD**	**δ^{25}Mg**	**2SD**
Av-1	−0.27	0.07	−0.13	0.06	−0.18	0.07	−0.10	0.05	−0.24	0.05	−0.11	0.06
duplicate	−0.23	0.06	−0.10	0.05	−0.18	0.06	−0.09	0.04	−0.24	0.07	−0.12	0.04
Fine grain	−0.23	0.06	−0.12	0.52	−0.18	0.05	−0.09	0.04				
duplicate	−0.26	0.06	−0.14	0.04	−0.23	0.07	−0.11	0.06				
average	*−0.25*	*0.03*	*−0.12*	*0.03*	*−0.19*	*0.03*	*−0.10*	*0.02*	*−0.24*	*0.04*	*−0.11*	*0.03*
Av-2	−0.26	0.07	−0.14	0.06	−0.21	0.05	−0.10	0.04				
duplicate					−0.23	0.07	−0.12	0.06				
average					*−0.22*	*0.04*	*−0.11*	*0.03*				
Av-3	−0.26	0.06	−0.13	0.04	−0.24	0.05	−0.12	0.04	−0.32	0.05	−0.16	0.06
duplicate					−0.24	0.07	−0.12	0.06	−0.33	0.06	−0.15	0.04
average					*−0.24*	*0.04*	*−0.12*	*0.03*	*−0.32*	*0.04*	*−0.16*	*0.03*
Av-4	−0.28	0.07	−0.15	0.06	−0.22	0.05	−0.11	0.04				
duplicate	−0.32	0.06	−0.17	0.04	−0.24	0.07	−0.13	0.06				
average	*−0.30*	*0.04*	*−0.16*	*0.04*	*−0.22*	*0.04*	*−0.12*	*0.03*				
Av-7	−0.25	0.06	−0.14	0.05	−0.24	0.05	−0.12	0.04				
duplicate					−0.21	0.07	−0.11	0.06				
average					*−0.23*	*0.04*	*−0.12*	*0.03*				
Av-8	−0.28	0.07	−0.14	0.06	−0.25	0.05	−0.14	0.04				
duplicate	−0.26	0.06	−0.12	0.05	−0.28	0.07	−0.15	0.06				
duplicate	−0.29	0.06	−0.15	0.04								
average	*−0.28*	*0.04*	*−0.14*	*0.03*	*−0.26*	*0.04*	*−0.14*	*0.03*				
Av-9	−0.24	0.06	−0.11	0.05	−0.17	0.06	−0.09	0.04	−0.21	0.05	−0.11	0.06
Fine grain	−0.24	0.07	−0.12	0.06	−0.18	0.05	−0.10	0.04	−0.24	0.07	−0.12	0.04
duplicate	−0.26	0.06	−0.12	0.04	−0.20	0.06	−0.11	0.04				
duplicate					−0.21	0.07	−0.10	0.06				
average	*−0.25*	*0.04*	*−0.12*	*0.03*	*−0.19*	*0.03*	*−0.10*	*0.02*	*−0.22*	*0.04*	*−0.12*	*0.03*
Av-10	−0.22	0.07	−0.11	0.06	−0.22	0.05	−0.11	0.04				

duplicate	−0.25	0.06	−0.13	0.05	−0.22	0.07	−0.10	0.06				
duplicate	−0.24	0.06	−0.12	0.04								
average	*−0.23*	*0.04*	*−0.12*	*0.03*	*−0.22*	*0.04*	*−0.11*	*0.03*				
Av-11	−0.29	0.07	−0.16	0.06	−0.27	0.05	−0.15	0.04				
duplicate	−0.29	0.06	−0.14	0.05	−0.25	0.07	−0.13	0.06				
average	*−0.29*	*0.05*	*−0.14*	*0.04*	*−0.27*	*0.04*	*−0.14*	*0.03*				
Av-12	−0.22	0.07	−0.12	0.06	−0.25	0.05	−0.14	0.04	−0.22	0.07	−0.12	0.04
duplicate	−0.26	0.06	−0.14	0.04	−0.23	0.07	−0.11	0.06	−0.22	0.07	−0.11	0.03
duplicate									−0.24	0.06	−0.12	0.04
Fine grain	−0.29	0.07	−0.14	0.06	−0.22	0.05	−0.11	0.04				
duplicate	−0.29	0.06	−0.14	0.05	−0.25	0.06	−0.13	0.04				
average	*−0.27*	*0.03*	*−0.13*	*0.03*	*−0.24*	*0.03*	*−0.12*	*0.02*	*−0.23*	*0.04*	*−0.11*	*0.02*
Av-13	−0.27	0.07	−0.14	0.06	−0.25	0.05	−0.13	0.04				
duplicate	−0.27	0.06	−0.15	0.04	−0.23	0.07	−0.11	0.06				
average	*−0.27*	*0.04*	*−0.14*	*0.04*	*−0.24*	*0.04*	*−0.12*	*0.03*				
Av-14	−0.25	0.07	−0.13	0.05	−0.23	0.05	−0.10	0.04				
duplicate					−0.23	0.07	−0.13	0.06				
average					*−0.23*	*0.04*	*−0.11*	*0.03*				
Av-15	−0.28	0.07	−0.15	0.05	−0.22	0.05	−0.11	0.04	−0.21	0.07	−0.12	0.04
duplicate	−0.28	0.06	−0.14	0.04	−0.26	0.07	−0.13	0.06	−0.19	0.06	−0.09	0.04
average	*−0.28*	*0.04*	*−0.14*	*0.03*	*−0.23*	*0.04*	*−0.12*	*0.03*	*−0.20*	*0.04*	*−0.11*	*0.03*
Av-16	−0.27	0.06	−0.13	0.05	−0.21	0.05	−0.10	0.04				
duplicate					−0.22	0.07	−0.11	0.06				
average					*−0.21*	*0.04*	*−0.10*	*0.03*				
Av-17	−0.27	0.07	−0.13	0.06	−0.21	0.05	−0.10	0.04				
duplicate	−0.25	0.06	−0.14	0.05	−0.22	0.07	−0.12	0.06				
average	*−0.26*	*0.05*	*−0.14*	*0.04*	*−0.21*	*0.04*	*−0.11*	*0.03*				

Table 5-4. Inter-mineral Mg isotope fractionation

Samples	$\Delta^{26}Mg_{Opx\text{-}Ol}$	2SD	$\Delta^{26}Mg_{Cpx\text{-}Ol}$	2SD
Av-1	0.06	0.04	0.01	0.05
Av-2	0.04	0.08		
Av-3	0.02	0.07	−0.06	0.07
Av-4	0.08	0.06		
Av-7	0.01	0.07		
Av-8	0.02	0.05		
Av-9	0.06	0.05	0.03	0.05
Av-10	0.01	0.05		
Av-11	0.02	0.06		
Av-12	0.03	0.04	0.04	0.05
Av-13	0.03	0.06		
Av-14	0.03	0.08		
Av-15	0.05	0.06	0.08	0.06
Av-16	0.06	0.07		
Av-17	0.05	0.06		

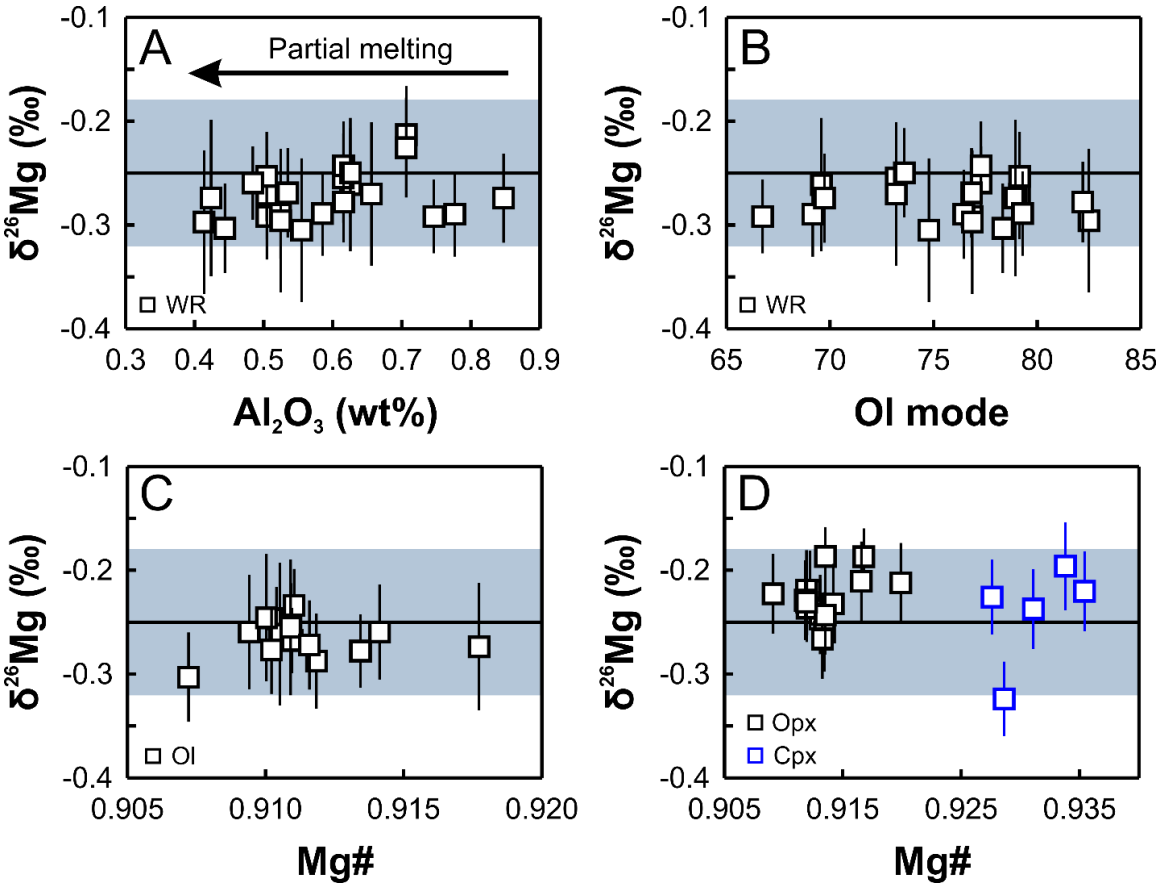

Figure 5-3. δ^{26}Mg in bulk Avacha peridotite xenoliths and their constituent minerals plotted against modal and chemical parameters. The grey band and horizontal solid line in each panel represent normal mantle range and average from Teng et al. (2010). Olivine mode, whole-rock (WR) Al_2O_3 content and Mg# of olivine (Ol), orthopyroxene (Opx) and clinopyroxene (Cpx) are from Ionov (2010).

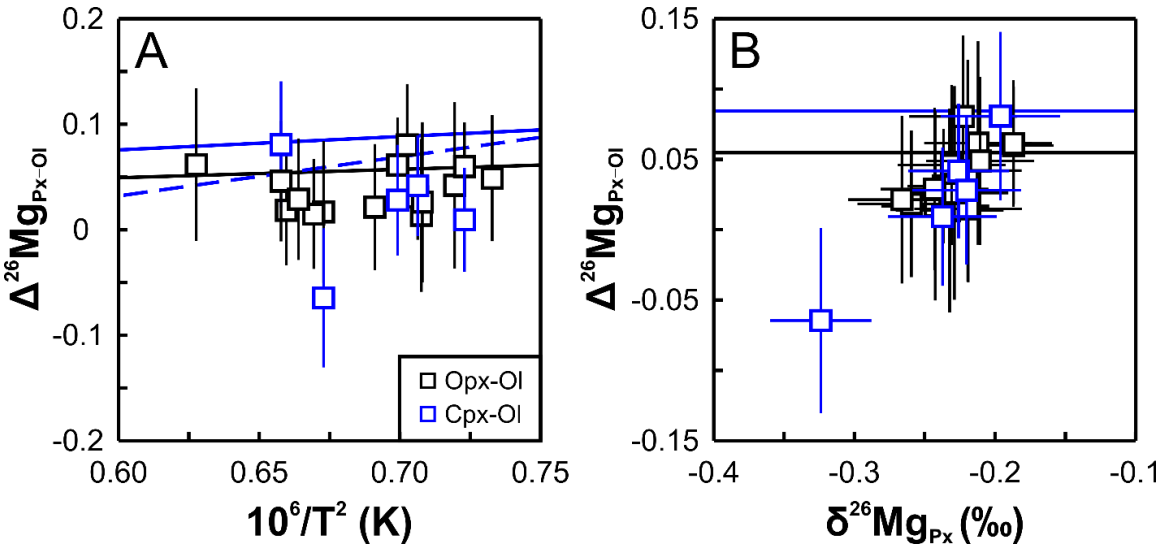

Figure 5-4. Inter-mineral fractionation between pyroxene (Px) and olivine (Ol) in Avacha peridotites. The solid blue and black lines correspond to theoretical equilibrium fractionation lines for Cpx-Ol and Opx-Ol pairs, respectively, at temperature of 950°C using the parameters provided in Schauble (2011). The blue dash line represents Cpx-Ol equilibrium fractionation line based on measurements on natural samples (Liu et al., 2011). The average temperature for Avacha peridotites are from Ionov (2010).

partial melting does not produce measurable Mg isotope fractionation (Teng et al., 2007, 2010a), the discussion below mainly focuses on the effects of fluid-rock interaction on the Mg isotope systematics in subduction zones.

6.1.Magnesium isotopic compositions of slab-derived fluids

The Mg isotopic compositions of the major components of the subducting slabs (marine sediments, altered oceanic crust and mantle) overlap broadly and can be highly varied with δ^{26}Mg values both higher and lower than the normal mantle. Systematic investigation of Mg isotope systematics in global marine sediments revealed an δ^{26}Mg range from −1.34‰ to +0.52‰, with the highly weathered, continental detritus-dominated silicate sediments defining the high-δ^{26}Mg end-member and carbonate-dominated sediments as the low-δ^{26}Mg end-member (Teng et al., 2016; Hu et al., 2017). Analyses on altered Pacific crust drilled outboard of the Mariana trench yielded highly variable, but mostly heavier-than-mantle δ^{26}Mg values (−2.76 to +0.21‰) that are attributed to prolonged low-temperature seawater alteration, leading to a gradual build-up of isotopically heavy secondary saponite (Huang et al., 2018). Likewise, abyssal peridotites that underwent extensive hydrothermal alteration and marine weathering are enriched in heavy Mg isotopes (δ^{26}Mg of −0.25‰ to +0.10‰) due to the preferential loss of light Mg into seawater, while serpentinization process itself is largely isochemical and does not fractionate Mg isotopes (Wimpenny et al., 2012; Beinlich et al., 2014; Liu et al., 2017).

Consistent with these slab inputs, exhumed metamorphic slab equivalents also display very broad Mg isotopic variations. For example, cratonic eclogite xenoliths that are fragments of ancient subducted oceanic crust exhibited a wide range in δ^{26}Mg (−1.60‰ to

+0.17‰, Wang et al., 2012, 2015a). Similarly, ultramafic rocks from the Catalina Schist that are considered to represent fragments of slab-mantle interface have δ^{26}Mg values ranging from −0.50‰ to −0.01‰, with the variation attributed to different modal compositions developed during fluid-peridotite reactions (Li et al., 2016). Furthermore, Mg isotopic exchange between relatively ^{26}Mg-rich silicates and much lighter fluids or melts equilibrated with carbonates may further differentiate the Mg isotopic compositions of silicate minerals (Wang et al., 2014a). Therefore, slab-derived fluids are expected to have variable Mg isotopic compositions.

6.2.Magnesium isotopic compositions in mantle wedge peridotites

Despite various lines of evidence for fluid metasomatism (Fig. 5-2) in the Avacha xenolith suite on one hand, and highly heterogeneous Mg isotopic compositions inferred for dehydration fluids from subducted slabs on the other hand, the peridotite xenoliths analyzed in this study revealed strikingly uniform Mg isotopic compositions that are not correlated with common indices of fluid metasomatism, such as Ba/La and Pb/Ce (Fig. 5-5). The δ^{26}Mg values in all the 23 Avacha peridotites and their constituent minerals fall within the range for normal upper mantle defined by the Mg isotopic composition of global peridotite xenoliths and oceanic basalts (Fig. 5-3). In addition, the bulk δ^{26}Mg values of the Avacha peridotites are identical to those of arc lavas reported for Kamchatka (Li et al., 2017). Similarly, the same Avacha xenoliths display mantle-like δ^{7}Li isotopic signatures (Ionov and Seitz, 2008), which is remarkable considering that lithium is highly fluid-mobile and thus a sensitive tracer for slab-derived fluids (e.g. Zack et al., 2003). Furthermore, the lack of Mg isotope differences between the Avacha peridotites and normal

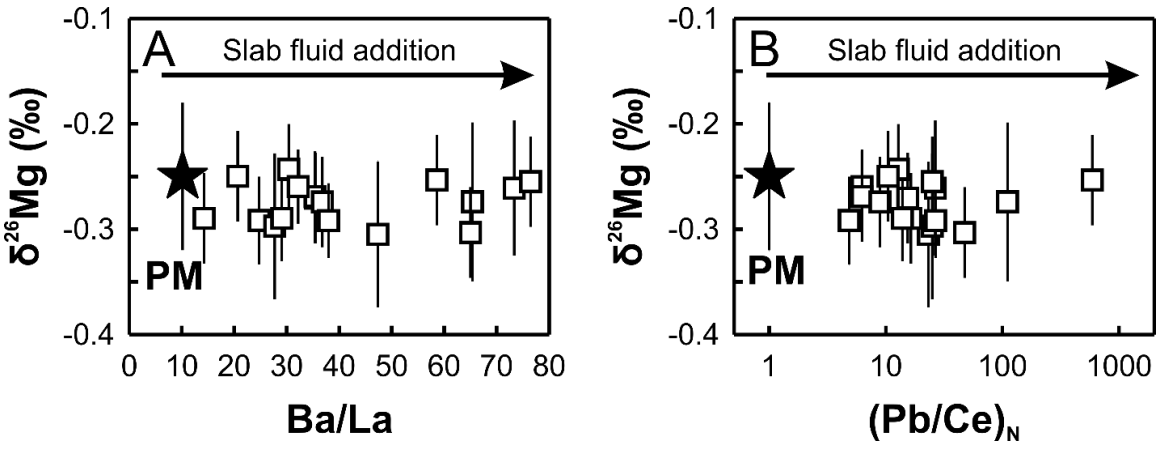

Figure 5-5. Lack of correlation between δ^{26}Mg in Avacha peridotites with common indices for slab fluid-peridotite interaction. PM stands for primitive mantle and its trace element concentrations are from Sun and McDonough (1989). Its δ^{26}Mg is assumed to be identical to the normal mantle average from Teng et al. (2010a).

mantle is consistent with mantle-like Fe isotope signatures in these rocks (Weyer and Ionov, 2007). This could be explained by the high mass ratios of both Mg and Fe in the mantle peridotites relative to metasomatic melts or fluids.

Pogge von Strandmann et al. (2011) obtained slightly different δ^{26}Mg values for six Avacha samples analyzed in this study and for δ^{7}Li data by Ionov and Seitz (2008). They found a negative correlation between δ^{7}Li and δ^{26}Mg, which was attributed to diffusion-driven interaction with slab-derived fluids. In addition, their results for samples Av-1, -4, and -6 (δ^{26}Mg = −0.16‰ to −0.10‰, Pogge von Strandmann et al., 2011) are higher than those we obtained. Since their duplicate analyses on the same samples may differ by 0.07‰, yet the total variation in δ^{26}Mg is within the claimed analytical reproducibility, the apparent δ^{7}Li vs. δ^{26}Mg correlation and higher δ^{26}Mg values might be accidental.

The mantle-like Mg isotopic composition of the Avacha sub-arc peridotite xenoliths is, on the other hand, comparable to published Mg isotopic data on some other rocks of likely mantle wedge origin. For example, the Horoman massif peridotites from Japan are interpreted as samples of ancient mantle wedge above the Hidaka subduction zone. Despite various lines of geochemical evidence and the formation of secondary Opx that suggests infiltration by slab-derived fluids/melts (e.g., Yoshikawa and Nakamura, 2000), the Horoman peridotites yielded mantle-like δ^{26}Mg values (−0.27‰ to −0.19‰, Lai et al., 2015). Su et al. (2015) reported a δ^{26}Mg range from −0.28‰ to −0.14‰ for variably metasomatized Tibetan ophiolitic peridotites and attributed the slightly heavier δ^{26}Mg values in some of their samples to hydrothermal alteration of the oceanic crust (Su et al., 2015). It appears that not only the Avacha xenoliths but also other sub-arc mantle wedge suites show no distinctive Mg isotopic signatures relative to normal upper mantle caused

by subduction-related fluid infiltration.

The uniform Mg isotopic compositions of the bulk Avacha peridotites are further supported by the equilibrium isotope fractionation between coexisting olivine and Opx ($\Delta^{26}Mg_{Opx\text{-}Ol}$ = +0.01‰ to +0.08‰) over the entire temperature range in the Avacha samples in this study (Fig. 5-4A). Unlike Opx, however, Cpx appears to slightly deviate from the equilibrium fractionation line toward lighter values (Fig. 5-4A). Furthermore, the Mg isotope fractionation between Cpx and olivine ($\Delta^{26}Mg_{Cpx\text{-}Ol}$) display a positive correlation with $\delta^{26}Mg_{Cpx}$, implying that the variation of inter-mineral fractionation is mainly caused by the variation in $\delta^{26}Mg_{Cpx}$ (Fig. 5-4B). These observations suggest slight isotope disequilibrium between olivine and Cpx, which is consistent with the late-stage origin of Cpx (Ionov, 2010). Furthermore, the larger (0.2-0.3 mm) Cpx grains in the Avacha peridotites that were handpicked for the analyses appear to be mainly metasomatic (formed by reaction with percolating fluids), by contrast to smaller Cpx grains exsolved from coarse, residual Opx on cooling.

6.3.Behavior of Mg in the mantle wedge-slab system

The data on the Avacha sub-arc mantle peridotites in this study suggest that interaction of the arc mantle with fluids expelled from dehydrated Pacific slab does not affect its Mg isotope composition within the analytical uncertainty (Fig. 5-5). This can be explained by the following reasons. Firstly, Mg behaves conservatively during metamorphic dehydration at relatively shallow depths; therefore, only limited amounts of Mg partition to the fluids (MgO < 0.5 wt%, Manning, 2004 and references therein). This is supported by the consistent Mg isotopic ratios measured in a series of genetically related

prograde metamorphic rocks ranging from greenschist to amphibolite to eclogite in a continental subduction zone (Wang et al., 2014b). Similar conclusion has been reached for metamorphic dehydration of metapelites after as much as 75% loss of the initial volatiles (Li et al., 2014). These studies imply that the majority of slab-hosted Mg will retain in silicates and be carried to the deeper mantle whereas the fluids released beneath the arc volcanic regions must have relatively low Mg contents.

Secondly, although Mg can be transported by fluids, it is a highly compatible element with a strong affinity for Mg-silicates relative to fluids ($D_{Mg}^{rock/fluid}$ of ~ 10 at sub-arc depth, Ayer et al., 1997). Consequently, it would be preferentially incorporated into mantle minerals along fluid pathways. Given that the depth to the slab surface beneath Avacha is approximately 100-120 km (Gorbatov et al., 1997), whereas the peridotite xenoliths originate from the mantle lithosphere above 65 km depth (Ionov, 2010), ambient mantle peridotites may effectively sequester fluid-carried Mg during its ascent, in a process analogous to chromatography (e.g., Ionov et al., 2002). Therefore, probably only limited amounts of slab fluids could make their way to the shallow part of the mantle wedge, from where the xenoliths were entrained by andesitic magmas. This is consistent with the low abundance of hydrous amphibole (< 1 %) and relatively low $(La/Yb)_N$ (< 1) in the bulk peridotite xenoliths (Ionov, 2010).

Thirdly, the Mg isotopic compositions of slab-expelled fluids are expected to be strongly and continuously modified during their migration in the mantle. The equilibrium Mg isotope fractionation between olivine and Opx in the Avacha harzburgites indicates that Mg isotopes reached exchange equilibrium within and between individual samples. This is further supported by the lack of correlation between $\Delta^{26}Mg_{Opx\text{-}Ol}$ with chemical

compositions of Opx and olivine (Fig. 5-3), the lack of Mg concentration zoning in minerals, and the identical Mg isotopic compositions obtained for different batches of dissolution for the same mineral phase from a single xenolith sample (Table 5-3). Therefore, diffusive Mg isotopic equilibration between metasomatic fluids and ambient peridotite is probably a relatively recent and rapid process in the sub-arc mantle. This inference is also supported by the links of amphibole (and other metasomatic phases) disseminated in the peridotites with quenched veins (Bénard and Ionov, 2013). The Mg isotopic composition of percolating fluids and fluid-rich melts can thus be effectively buffered by the mantle wedge as a result of the high Mg content and much larger mass of the mantle wedge compared to the relatively limited amounts of fluids.

The lack of a clear fluid-imparted δ^{26}Mg signature in the Avacha harzburgites does not rule out the possibility that fluid metasomatism may alter the mantle wedge locally where the fluid flux is unusually high. This has been demonstrated by significant Mg isotope fractionation in exhumed metamorphic rocks from subduction channels or fore-arc mélange, where fragments of different lithologies interact with each other (Pogge von Strandmann et al., 2015; Chen et al., 2016; Wang et al., 2017). Figure 5-6 illustrates the expected δ^{26}Mg variations in mantle rocks that exchange Mg isotopes with an isotopically enriched fluid phase at various fluid/rock ratios in an open-system. It shows that fluids derived from oceanic crust are too depleted in MgO to shift the Mg isotopic composition of the mantle because such a shift requires high fluid/rock ratios and large $\Delta^{26}Mg_{rock\text{-}fluid}$. In comparison, fluids derived from serpentinized peridotites are more effective metasomatic agents for Mg. In addition, the efficiency of metasomatism could be further enhanced if the fluids travel through the mantle by channelized flow, in which case they

will react less with surrounding peridotites and therefore preserve their δ^{26}Mg signatures for longer travel distances during fluid ascent.

6.4. Comparison with arc lavas: Implications for Mg cycling in subduction zones and beyond

Compositions of arc lavas provide additional observational constraints on the role of slab input in sub-arc mantle sources. Although Mg isotopic data on arc lavas remain scarce, they have revealed significant among-arc variations. These lavas display dominant contributions from slab-derived fluids except that those from Lesser Antilles also exhibit a strong sediment signal (Fig. 5-7A and B). Arc lavas from the Kamchatka and Costa Rica volcanic fronts display mantle-like Mg isotopic compositions whereas those from Lesser Antilles and Philippines are characterized by variably higher δ^{26}Mg values, which are attributed to dehydration fluids released from altered abyssal peridotites (Teng et al., 2016; Li et al., 2017). There are no apparent correlations between the Mg isotopic compositions of these lavas and their Ba/Th and Dy/Yb ratios (Fig. 5-7C and D), indicating that neither the amount of fluid additions to their mantle sources nor fractional crystallization of garnet from the magmas could be responsible for the variably ^{26}Mg-enriched arc lava compositions.

Thermal structure of a given subduction zone has a profound influence on the dehydration path of a subducting plate and the nature and flux of slab-mantle mass transfer agent (fluid vs. melt), which ultimately affect the compositions of arc magmas. The average δ^{26}Mg values of these arcs show co-variation trends with their subduction parameters, e.g.

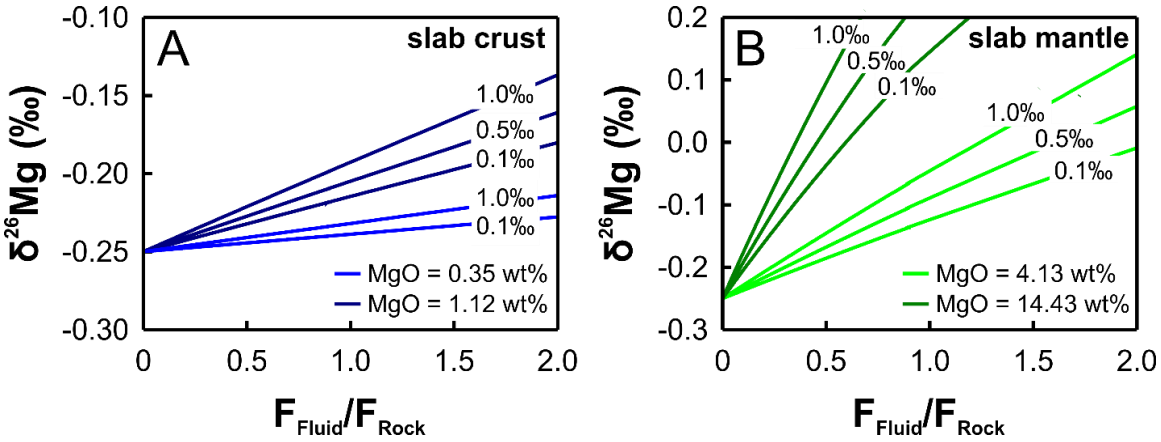

Figure 5-6. Illustration of Mg isotope evolution of mantle peridotites during open-system fluid-peridotite interaction at different fluid/rock ratios and different $\Delta^{26}Mg_{rock\text{-}fluid}$ values. The latter is indicated on each of the solid lines in the figures. The mantle is assumed to have an average MgO content identical to that of Avacha harzburgites (45.4 wt%) with a $\delta^{26}Mg$ of normal mantle average (−0.25‰, Teng et al., 2010a). The MgO concentration ranges of fluids derived from oceanic basalt and peridotite are from Kessel et al. (2005) and Dvir et al. (2011), respectively. These fluids are assumed to have a $\delta^{26}Mg$ of +1.1‰ (Wang et al., 2015b).

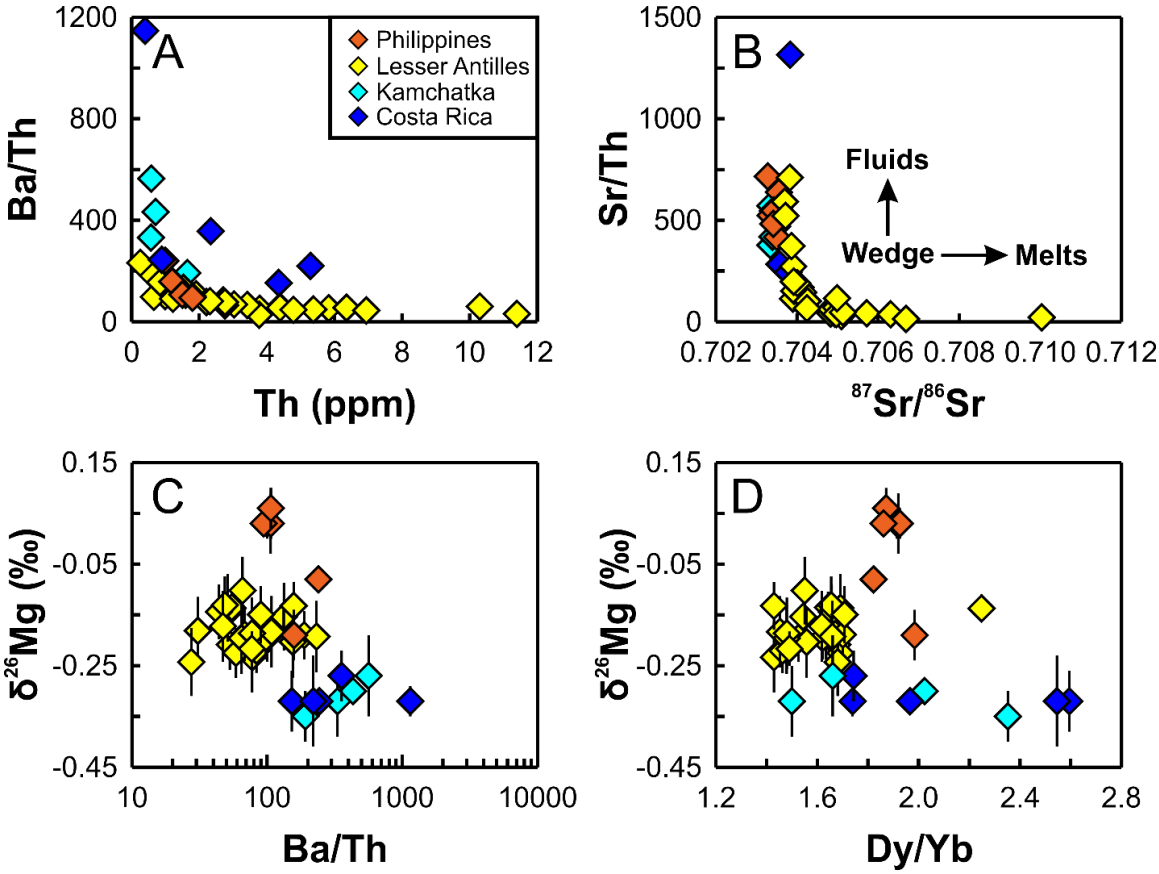

Figure 5-7. Compilations of published arc lava δ^{26}Mg data with their trace element characteristics. (A) and (B) Trace element and isotopic characteristics for the published arc lava data in literature, which indicate a dominant role of slab-derived fluids in Philippines, Kamchatka, and Costa Rica, whereas both slab-fluids and sediments contribute to genesis of Lesser Antilles arc lavas. (C) and (D) Magnesium isotopic compositions of published arc lava data plotted against indices for fluid addition and garnet crystallization. Data are from Teng et al. (2016) and Li et al. (2017).

increasingly higher δ^{26}Mg values with an increase in slab surface temperatures and slab depths (Fig. 5-8). These correlations suggest that the Mg isotopic signatures of the volcanic front lavas may be controlled by specific dehydration reactions that occur at specific P-T conditions in the subduction zone. For lavas that are derived at relatively shallow depths, the primary water suppliers of the oceanic crust are amphibole, chlorite, lawsonite, zoisite, and paragonite (Schmidt and Poli, 2014). These minerals either do not contain much Mg (e.g., lawsonite, zoisite), or likely have Mg isotopic compositions similar to those of mantle olivine and pyroxene due to similar Mg-O bond strength (e.g., amphibole). By contrast, for magmas produced by deeper partial melting, the higher slab temperatures facilitate water liberation from the serpentinized peridotite layer of the oceanic slab or those from above the slab surface. Compared to oceanic crust, serpentinites have much higher water contents and Mg concentrations. More importantly, the relevant phyllosilicates in serpentinized peridotites generally have Mg isotopic compositions that are different from those in the normal mantle. For example, an extremely low δ^{26}Mg value has been reported for brucite (−1.82‰, Wimpenny et al., 2014), whereas variably heavy Mg isotopic compositions have been measured in talc and antigorite (up to +0.30‰, Beinlich et al., 2014), as well as in altered serpentinites (e.g., Wimpenny et al., 2012; Liu et al., 2017).

At typical melting depths beneath the arcs, K-bearing hydrous phases (e.g. phlogopite and phengite) and magnesite, which commonly have heavy (up to +0.59‰, Li et al., 2011; Liu et al., 2011) and light (e.g., −1‰, Beinlich et al., 2014) Mg isotopic compositions, respectively, are still stable and hence capable of carrying their distinctive Mg isotopic signatures further down into the deep mantle. They may later be involved in the formation of isotopically light continental basalts and potassium-rich rocks, such as

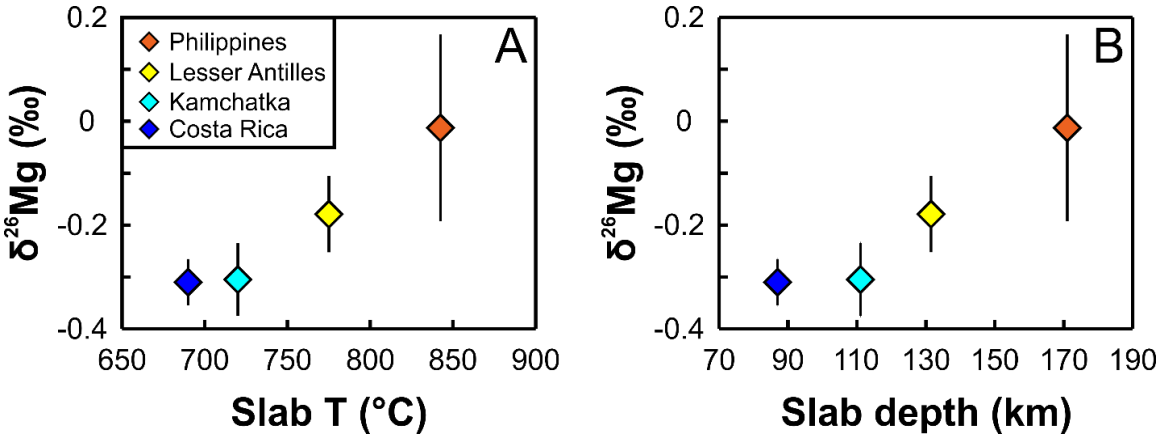

Figure 5-8. The average δ^{26}Mg value for each arc as a function of slab temperature and slab depth. Slab parameters are from Syracuse et al. (2010). Magnesium isotopic data are from Teng et al. (2016) and Li et al. (2017).

those in eastern China (Yang et al., 2012; Huang et al., 2015; Tian et al., 2016; Li et al., 2017; Su et al., 2017; Sun et al., 2017). Alternatively, such melts formed at greater depths could be consumed in the subcontinental lithospheric mantle to generate a diverse range of metasomatic rocks such as wehrlite and pyroxenite that were found to have variable bulk Mg isotopic compositions and disequilibrium inter-mineral Mg isotope fractionations (e.g., Yang et al., 2009; Xiao et al., 2013; Hu et al., 2016b).

7. Conclusions

The heterogeneous Mg isotopic compositions in different components of downgoing slabs, and non-mantle Mg isotopic ratios found in a few studied arc lavas, implicate that the mantle wedge may bear atypical Mg isotopic signatures. Our Mg isotopic data, however, show that there is no significant difference between the normal mantle and the metasomatized sub-arc lithospheric mantle sampled by the Avacha xenoliths from the Kamchatka arc. Therefore, we conclude that a typical mantle wedge where slab input is dominated by addition of fluids from the subducting crust probably has an overwhelmingly mantle-like Mg isotopic composition. This could be due to a combination of chromatographic removal of Mg from slab-derived fluids and diffusive Mg isotopic re-equilibration between migrating fluids and ambient mantle rocks. Arc lavas that display abnormal Mg isotopic compositions may have formed in subduction zones with deeper and hotter slab surface that allows dehydration of serpentinized peridotites to occur.

Acknowledgements. This work was financially supported by the National Science Foundation (EAR-1340160) to F.-Z. Teng) and Harry Wheeler Scholarship to Y. Hu. D.

Ionov acknowledges support from the Chinese Academy of Sciences (CAS) President's International Fellowship Initiative (PIFI) for 2017-18 and from the PNP-INSU program in France. Scott Kuehner, Bruce Nelson and Bernard Evans are thanked for constructive comments and discussions.

Chapter 6. Summary and future work

This dissertation investigates Mg isotope systematics in crustal and mantle materials. I first examine the analytical results of other laboratories compared to ours'. Next, the recycling of crustal materials into the mantle is considered, which is the primary mechanism for transporting fractionated, low-temperature stable isotopic signatures to the mantle. Specifically, I approach this topic by studying the Mg isotopic composition of lithological heterogeneities (i.e., pyroxenites) in the peridotite-dominated mantle, exploring the source materials for metasomatic melts that may lead to anomalous mantle Mg isotopic compositions, and investigating processes that can influence the Mg isotope redistribution. The results from this dissertation contribute to understanding of the Mg isotope behaviors in subduction zone processes and lay the foundation for using Mg isotopes to trace crust-mantle recycling. The main conclusions drawn from this dissertation along with future directions are discussed below:

(1) The first topic (Chapter 2) investigates intra-mineral and inter-mineral Mg isotopic heterogeneity of two peridotite xenoliths from San Carlos, Arizona. Previous measurements of a single or a few olivine samples showed large differences between values obtained by different laboratories in the measured δ^{26}Mg (e.g., Wiechert and Halliday, 2007; Chakrabarti and Jacobsen, 2010). We measured two xenoliths where we separated the mineral grains of olivine, clinopyroxene, and orthopyroxene, and determined that all the minerals have a homogeneous Mg isotope composition. These results indicate that previously documented large inter-laboratory discrepancies are likely not accurate. We find that the San Carlos peridotites have a normal peridotite-like Mg isotopic composition, and may be useful as a standard for comparing

consistency to other laboratories.

(2) Chapter 3 focus on Mg isotope variation in mantle pyroxenites, which represent the local parts of the mantle that have been significantly modified (high melt/rock ratio) by reacting with melts generated from the mantle. Our study finds that reaction of mantle peridotites with metasomatic melts of diverse origins, particularly those linked to subducted oceanic crust and carbonates, can produce local mantle domains with anomalous Mg isotopic compositions; this is opposed to the largely homogeneous Mg isotopic compositions shared by upper mantle peridotites that are not strongly modified. These isotopically-altered mantle domains may subsequently serve as the source region of isotopically distinct continental basalts. Since the anomalously light continental basalts were explained to reflect contributions from carbonatitic melts supplied by subducted oceanic slab (Yang et al., 2012; Huang et al., 2015), future examination on Mg isotopic variation in carbonated peridotites, mantle carbonatites, and Mg isotope fractionation during silicate-carbonate immiscibility are required to further our understanding of carbonate-peridotite interaction in the mantle, which are still rarely studied.

(3) Chapter 4 presents a systematic investigation on Mg isotopic variations in subducting sediments recovered from drill cores conducted by Deep Sea Drilling Project and Ocean Drilling Program in front of 10 active subduction zones. These sediments display diverse lithologies and serve as a substantial Mg input to global subduction zones albeit their Mg isotope systematics are poorly constrained. The 77 bulk sediments measured yield a wide variation in δ^{26}Mg (−1.34‰ to +0.46‰), and together with our study on altered oceanic crust (Huang et al., in revision), they support that subduction

of oceanic slab is an important process introducing the large isotope fractionations produced at the Earth's surface into the deep mantle, generating local mantle heterogeneities. In this respect, future studies on oceanic island basalts with end-member isotopic compositions are needed, in particular for basalts with a HIMU signature (enriched mantle with elevated $\mu = {}^{238}U/{}^{204}Pb$) and with EM II signature (enriched mantle type II with high ${}^{87}Sr/{}^{86}Sr$), which that are believed to have incorporated subducted slab components in their mantle sources.

(4) Chapter 5 presents a Mg isotope investigation on a suite of supra-subduction zone peridotites from Avacha, Russia, which were chosen due to their genuine sub-arc nature and their representative of western Pacific mantle wedge. Results from this study along with published arc lava data (Teng et al., 2016; Li et al., 2017) suggest that fluids released from oceanic crust at pressures of ~2–3 GPa are well buffered during their migration in the mantle wedge due to their low Mg concentrations. Large-scale dehydration of isotopically distinct materials at higher pressures may be required to produce isotopically diverse arc lavas. Therefore, to further constrain the role of subduction of oceanic slab in arc magma genesis, future studies on arc lavas derived from subduction zones with contrasting thermal structures are needed, which permits inter-arc comparison on how dehydration of different hydrous phases at various pressure-temperature conditions affect the Mg isotopic compositions of arc magmas.

(5) In addition to work presented in this dissertation and the proposed future directions, coupling Mg isotope systematics with other non-traditional stable isotopes, such as potassium (K) and boron (B), which behave differently from Mg during geological processes, will give a more complete picture of the working mechanism for subduction

zone recycling in general. Both K and B are highly enriched in the crust relative to the mantle. In addition, the heavier isotopes of both the elements are preferentially enriched in seawater. These heavy isotopic signatures in the seawater could be transferred to the oceanic slab during low-temperature interactions with seawater, which then may be subducted to the mantle and release fluids or melts that inherited these heavy isotopic signatures to the mantle. In this way, K and B isotopes may provide an archive of recent slab addition whereas Mg isotopes preserve a fingerprint of comparatively longer-term modification event and mantle heterogeneity.

References

Adam J. and Green T. (2001) Experimentally determined partition coefficients for minor and trace elements in peridotite minerals and carbonatitic melt, and their relevance to natural carbonatites. *Eur. J. Mineral.* 13, 815–827.

Allègre C. J. and Turcotte D. L. (1986) Implications of a two-component marble-cake mantle. *Nature* 323, 123–127.

An Y.-J., Wu F., Xiang Y.-X., Nan X.-Y., Yu X., Yang J.-H., Yu H.-M., Xie L.-W., and Huang F. (2014) High-precision Mg isotope analyses of low-Mg rocks by MC-ICP-MS. *Chem. Geol.* 390, 9–21.

An Y., Huang J.-X., Griffin, W. L., Liu C., and Huang F. (2017) Isotopic composition of Mg and Fe in garnet peridotites from the Kaapvaal and Siberian cratons. *Geochim. Cosmochim. Acta* 200, 167–185.

Anders E. and Grevesse N. (1989) Abundances of the elements: meteoritic and solar. *Geochim. Cosmochim. Acta* 53, 197–214.

Anderson D. L. (2005) Large igneous provinces, delamination, and fertile mantle. *Elements* 1, 271–275.

Arai S., Ishimaru S., and Okrugin V. M. (2003) Metasomatized harzburgite xenoliths from Avacha volcano as fragments of mantle wedge of the Kamchatka arc: implication for the metasomatic agent. *Island Arc* 12, 233–246.

Arai S. and Ishimaru S. (2008) Insights into petrological characteristics of the lithosphere of mantle wedge beneath arcs through peridotite xenoliths: a review. *J. Petrol.* 49, 665–695.

Armstrong R. (1968) A model for Sr and Pb isotope evolution in a dynamic earth. *Rev. Geophys.* 6, 175–199.

Auer S., Bindeman I., Wallace P., Ponomareva V., and Portnyagin M. (2009) The origin of hydrous, high-$\delta^{18}O$ voluminous volcanism: diverse oxygen isotope values and high magmatic water contents within the volcanic record of Klyuchevskoy volcano, Kamchatka, Russia. *Contrib. Mineral. Petrol.* 157, 209–230.

Ayers J. C., Dittmer S. K., and Layne G. D. (1997) Partitioning of elements between peridotite and H_2O at 2.0–3.0 GPa and 900–1100°C and application to models of subduction zone processes. *Earth Planet. Sci. Lett.* 150, 381–398.

Basu A. R., Junwen W., Wankang H., Guanghong X., and Tatsumoto M. (1991) Major element, REE, and Pb, Nd and Sr isotopic geochemistry of Cenozoic volcanic rocks of eastern China: implications for their origin from suboceanic-type mantle reservoirs. *Earth Planet. Sci. Lett.* 105, 149–169.

Bebout G. E. (2007) Metamorphic chemical geodynamics of subduction zones. *Earth Planet. Sci. Lett.* 260, 373–393.

Beinlich A., Mavromatis V., Austrheim H., and Oelkers E. H. (2014) Inter-mineral Mg isotope fractionation during hydrothermal ultramafic rock alteration—implications for the global Mg-cycle. *Earth Planet. Sci. Lett.* 392, 166–176.

Bénard A. and Ionov D. A. (2012) A new petrogenetic model for low-Ca boninites: Evidence from veined sub-arc xenoliths on melt-mantle interaction and melt fractionation. *Geochem. Geophys. Geosyst.* 13, Q0AF05, doi:10.1029/2012GC004145.

Bénard A. and Ionov D. A. (2013) Melt- and fluid-rock interaction in supra-subduction lithospheric mantle: evidence from andesite-hosted veined peridotitic xenoliths. *J. Petrol.* 54, 2339–2378.

Bénard A., Nebel O., Ionov D. A., Arculus R. J., Shimizu N., and Métrich N. (2016) Primary silica-rich picrite and high-Ca boninite melt inclusions in pyroxenite veins from the Kamchatka sub-arc mantle. *J. Petrol.* 57, 1955–1982.

Bénard A., Arculus R. J., Nebel O., Ionov D. A., and McAlpine S. R. B. (2017) Silica-enriched mantle sources of subalkaline picrite-boninite-andesite island arc magmas. *Geochim. Cosmochim. Acta* 199, 287–303.

Bigeleisen J. (1965) Chemistry of isotopes. *Science* 147, 463–471.

Bizimis, M., Salters, V. J. M., and Bonatti, E. (2000) Trace and REE content of clinopyroxenes from supra-subduction zone peridotites. Implications for melting and enrichment processes in island arcs. *Chem. Geol.* 165, 67–85.

Bodinier J.-L. and Godard M. (2014) Orogenic, ophiolitic, and abyssal peridotites. In *The Mantle and Core*. Treatise on Geochemistry (ed. R. W. Carlson). Elsevier-Pergamon, Oxford, pp. 103–167.

Bogdanov N. A. (1988) Geology of the Komandorsky deep basin. *J. Phys. Earth* 36, 65–71.

Bolou-Bi E. B., Vigier N., Brenot A., and Poszwa A. (2009) Magnesium isotope compositions of natural reference materials. *Geostand. Geoanal. Res.* 33, 95–109.

Boström K., Joensuu O., Valdés S., Charm W., and Glaccum R. (1976) Geochemistry and origin of East Pacific sediments sampled during DSDP Leg 34. doi:10.2973/dsdp.proc.34.149.1976.

Bouman C., Elliott T., and Vroon P. Z. (2004) Lithium inputs to subduction zones. *Chem. Geol.* 212, 59–79.

Bourdon B., Tipper E. T., Fitoussi C., and Stracke A. (2010) Chondritic Mg isotope composition of the Earth. *Geochim. Cosmochim. Acta* 74, 5069–5083.

Bouvier A., Wadhwa M., Simon S. B., and Grossman L. (2013) Magnesium isotopic fractionation in chondrules from the Murchison and Murray CM2 carbonaceous chondrites. *Meteorit. Planet. Sci.* 48, 339–353.

Breeding C. M., Ague J. J., and Brocker M. (2004) Fluid-metasedimentary interactions in subduction zone mélange: Implications for the chemical composition of arc magmas. *Geology* 32, 1041–1044.

Brenot A., Cloquet C., Vigier N., Carignan J., and France-Lanord C. F. (2008) Magnesium isotope systematics of the lithologically varied Moselle river basin, France. *Geochim. Cosmochim. Acta* 72, 5070–5089.

Brey G. P. and Kohler T. (1990) Geothermobarometry in fourphase lherzolites II: new thermobarometers, and practical assessment of existing thermobarometers. *J. Petrol.* 31, 1353–1378.

Brooks C., James D. E., and Hart S. R. (1976) Ancient lithosphere: its role in young continental volcanism. *Science* 193, 1086–1094.

Bryant J. A., Yogodzinski G. M., and Churikova T. G. (2007) Melt-mantle interactions beneath the Kamchatka arc: Evidence from ultramafic xenoliths from Shiveluch volcano. *Geochem. Geophys. Geosyst.* 8, Q04007, doi:10.1029/2006GC001443.

Carpentier M., Chauvel C., and Mattielli N. (2008) Pb-Nd isotopic constraints on sedimentary input into the Lesser Antilles arc system. *Earth Planet. Sci. Lett.* 272, 199–211.

Carpentier M., Chauvel C., Maury R. C., and Mattielli N. (2009) The "zircon effect" as recorded by the chemical and Hf isotopic compositions of Lesser Antilles forearc sediments. *Earth Planet. Sci. Lett.* 287, 86–99.

Chan L.-H., Leeman W. P., and Plank T. (2006) Lithium isotopic composition of marine sediments. *Geochem. Geophys. Geosys.*7, doi: 10.1029/2005GC001202.

Chang V. T.-C., Makishima A., Belshaw N. S., O'Nions R. K. (2003) Purification of Mg from low-Mg biogenic carbonates for isotope ratio determination using multiple collector ICPMS. *J. Anal. At. Spectrom.* 18, 296–301.

Chakrabarti R. and Jacobsen S. B. (2010) The isotopic composition of magnesium in the inner Solar System. *Earth Planet. Sci. Lett.* 293, 349–358.

Chakraborty S. (1997) Rates and mechanisms of Fe–Mg interdiffusion in olivine at 980°-1300 °C. *J. Geophys. Res.* 102, 12317–12331.

Chakraborty S. (2010) Diffusion coefficients in olivine, wadsleyite and ringwoodite. *Rev. Mineral. Geochem.* 72, 603–639.

Chen S., O'Reilly S. Y., Zhou X., Griffin W. L., Zhang G., Sun M., Feng J., and Zhang M. (2001) Thermal and petrological structure of the lithosphere beneath Hannuoba, Sino-Korean Craton, China: evidence from xenoliths. *Lithos* 56, 267–301.

Chen Y.-X., Schertl H. P., Zheng Y.-F., Huang F., Zhou K., and Gong Y.-Z. (2016) Mg-O isotopes trace the origin of Mg-rich fluids in the deeply subdcuted continental crust of Western Alps. *Earth Planet. Sci. Lett.* 456, 157–167.

Cherniak D. J. and Dimanov A. (2010) Diffusion in pyroxene, mica and amphibole. *Rev. Mineral. Geochem.* 72, 641–690.

Choi S. H., Mukasa S. B., Zhou X. H., Xian X. H., and Andronikov A. V. (2008) Mantle dynamics beneath East Asia constrained by Sr, Nd, Pb and Hf isotopic systematics of ultramafic xenoliths and their host basalts from Hannuoba, North China. *Chem. Geol.* 248, 40–61.

Churikova T., Dorendorf F. and Wörner G. (2001) Sources and fluids in the mantle wedge below Kamchatka, evidence from across-arc geochemical variation. *J. Petrol.* 42, 1567–1593.

Churikova T., Wörner G., Mironov N., and Kronz A. (2007) Volatile (S, Cl and F) and fluid mobile trace element compositions in melt inclusions: implications for variable fluid sources across the Kamchatka arc. *Contrib. Mineral. Petrol.* 154, 217–239.

Cole, F. G. and Shaw, H. F. (1983) The nature and origin of authigenic smectites in some Recent marine sediments. *Clay Minerals.* 18, 239–252.

Coltorti M., Bonadiman C., Hinton R. W., Siena F., and Upton B. G. J. (1999) Carbonatite metasomatism of the oceanic upper mantle: evidence from clinopyroxenes and glasses in ultramafic xenoliths of Grande Comore, Indian Ocean. *J. Petrol.* 40, 133–165.

Coltorti M. (2008) Metasomatism in oceanic & continental lithospheric mantle. *Geol. Soc. Spec. Pub.* No. 293 (eds. M. Coltorti and M. Gregoire).

Cook H. E., Zemmels I., and Matti J. C. (1975) X-ray mineralogy data, far western Pacific, Leg 31 Deep Sea Drilling Project. doi: 10.2973/dsdp.proc.31.app.1975.

Donnelly T. W. and Merrill L. (1977) The scavenging of magnesium and other chemical species by biogenic opal in deep-sea sediments. *Chem. Geol.* 19, 167–186.

Downes H. (2007) Origin and significance of spinel and garnet pyroxenites in the shallow lithospheric mantle: ultramafic massifs in orogenic belts in Western Europe and NW Africa. *Lithos* 99, 1–24.

Dorendorf F., Wiechert U., and Wörner G. (2000) Hydrated sub-arc mantle: a source for the Kluchevskoy volcano, Kamchatka/Russia. *Earth Planet. Sci. Lett.* 175, 69–86.

Dosseto A., Bourdon B., Joron J. L., and Dupré B. (2003) U-Th-Pa-Ra study of the Kamchatka arc: New constraints on the genesis of arc lavas. *Geochim. Cosmochim. Acta* 67, 2857–2877.

Dosseto A. and Turner S. (2014) Reappraisal of uranium-series isotope data in Kamchatka lavas: implications for continental arc magma genesis. *Geol. Soc. London, Spec. Publ.* 385, 103–116.

Duggen S., Portnyagin M., Baker J., Ulfbeck D., Hoernle K., Garbe-Schönberg D., and Grassineau N. (2007) Drastic shift in lava geochemistry in the volcanic-front to rear-arc region of the Southern Kamchatkan subduction zone: evidence for the transition from slab surface dehydration to sediment melting. *Geochim. Cosmochim. Acta* 71, 452–480.

Dvir O., Pettke T., Fumagalli P., and Kessel R. (2011) Fluids in the peridotite–water system up to 6 GPa and 800°C: new experimental constrains on dehydration reactions. *Contrib. Mineral. Petrol.* 161, 829–844.

Ewing M. and Connary S. D. (1970) Nepheloid layer in the North Pacific. In Hayes, J.D. (Ed.) 1970. Geological Investigations of the North Pacific. *Geol. Soc. Am. Mem.* 126.

Fan Q. C. and Hooper P. R. (1991) The Cenozoic basaltic rocks of eastern China: petrology and chemical composition. *J. Petrol.* 32, 765–810.

Fan W.-M., Zhang H.-F., Baker J., Jarvis K. E., Mason P. R. D., and Menzies M. A. (2000) On and off the North China Craton: where is the Archaean keel? *J. Petrol.* 41, 933–950.

Fan Q. C., Zhang H. F., Sui J. L., Zhai M. G., Sun Q. and Li N. (2005) Magma underplating and Hannuoba present crust–mantle transitional zone composition: xenolith petrological and geochemical evidence. *Sci. China Ser. D* 48, 1089–1105 (in Chinese with English abstract).

Fan Q. C., Du X. X., Sui J. L., and Zhao Y. W. (2010) Genesis of carbonatite from Hannuoba and Yangyuan. *Acta Petrol. Sin.* 26, 3189–3194 (in Chinese with English abstract).

Firsov L. V. (1987) Geochronology of magmatic rocks from the southwestern part of the Koryak upland (Olyutor Depression). In: Nikolaeva, I. V. (ed.) Regional Geochronology of Siberia and Soviet Far East. Novosibirsk: Nauka, pp. 7–32 (in Russian).

Flynn L. P., Mouginis-Mark J., and Korton K. A. (1994) Distribution of thermal areas on an active lava flow field: landsat observations of Kilauea, Hawaii, July 1991. *Bull. Volcanol.* 56, 284–296.

Foley S. F. (2008) Ancient lithosphere: its role in young continental volcanism. *Nat. Geosci.* 1, 503–510.

Foster G. L., Pogge von Strandmann P. A. E., and Rae J. W. B. (2010) Boron and magnesium isotopic composition of seawater. *Geochem. Geophys. Geosyst.* 11(Q08015). http://dx.doi.org/10.1029/2010GC003201.

Frey F. A. and Prinz M. (1978) Ultramafic inclusions from San Carlos, Arizona: petrologic and geochemical data bearing on their petrogenesis. *Earth Planet. Sci. Lett.* 38, 129–176.

Frey F. A. (1980) The origin of pyroxenites and garnet pyroxenites from Salt Lake Crater, Oahu, Hawaii: trace element evidence. *Am. J. Sci.* 280-A, 427–449.

Galer S. J. G. and O'Nions R. K. (1989) Chemical and isotopic studies of ultramafic inclusions from the San Carlos Volcanic Field, Arizona: A bearing on their petrogenesis. *J. Petrol.* 30, 1033–1064.

Galy A., Belshaw N. S., Halicz L., and O'Nions P. K. (2001) High-precision measurement of magnesium by multiple-collector inductively coupled plasma mass spectrometry. *Inter. J. Mass Spectrom.* 208, 89–98.

Galy A., Bar-Matthews M., Halicz L., O'Nions P. K. (2002) Mg isotopic composition of carbonate: insight from speleothem formation. *Earth Planet. Sci. Lett.* 201, 105–115.

Galy A., Yoffe O., Janney P. E. Williams R. W., Cloquet C., Alard O., Halicz L., Wadhwa M., Hutcheon I. D., Ramon E., and Carignan J. (2003) Magnesium isotope heterogeneity of the isotopic standard SRM980 and new reference materials for magnesium-isotope-ratio measurements. *J. Anal. At. Spectrom.* 18, 1352–1356.

Ganguly J. (2010) Cation diffusion kinetics in aluminosilicate garnets and geological applications. *Rev. Mineral. Geochem.* 72, 559–601.

Gao Z.-Y. and Zhang L.-C. (1994) A study on the genesis of the mantle-derived inclusions and the host rock in Dashan volcanic cone. *J. NW Univ.* 24, 61–65 (in Chinese with English abstract).

Garcia D., Fonteilles M., and Moutte J. (1994) Sedimentary fractionations between Al, Ti, and Zr and the genesis of strongly peraluminous granites. *J. Geol.* 102, 411–422.

Garrido C. J. and Bodinier J.-L. (1999) Diversity of mafic rocks in the Ronda peridotite: evidence for pervasive melt–rock reaction during heating of subcontinental lithosphere by upwelling asthenosphere. *J. Petrol.* 40, 729–754.

Gorbatov A., Kostoglodov V., Suárez G. and Gordeev E. (1997) Seismicity and structure of the Kamchatka subduction zone. *J. Geophys. Res.* 102, 17883–17898.

Grant T., Harlov D., and Rhede D. (2016) Experimental formation of pyroxenite veins by reactions between olivine and Si, Al, Ca, Na and Cl-rich fluids at 800°C and 800 MPa: implications for fluid metasomatism in the mantle wedge. *Am. Mineral.* 101, 808–818.

Griffin J. J., Windom H., and Goldberg E. D. (1968) The distribution of clay minerals in the World Ocean. *Deep-Sea Res.* 15, 433–459.

Halama R., Savov I. P., Rudnick R. L., and McDonough W. F. (2009) Insights into Li and Li isotope cycling and sub-arc metasomatism from veined mantle xenoliths, Kamchatka. *Contrib. Mineral. Petrol.* 158, 197–222.

Halbach P., Scherhag C., Hebisch U., and Marchig, V. (1981) Geochemical and mineralogical control of different genetic types of deep-sea nodules from the Pacific Ocean. *Miner. Deposita* 16, 59–64.

Handler M. R., Baker J. A., Schiller M., Bennett V. C., and Yaxley G. M. (2009) Magnesium stable isotope composition of Earth's upper mantle. *Earth Planet. Sci. Lett.* 282, 306–313.

Harley S. L. and Green D. H. (1982) Garnet–orthopyroxene barometry for granulites and peridotites. *Nature* 300, 697–701.

Harnois L. (1988) The CIW index: A new chemical index of weathering. *Sediment. Geol.* 55, 319–322.

Herzberg C. (2004) Geodynamic information in peridotite petrology. *J. Petrol.* 45, 2507–2530.

Higgins J. A. and Schrag D. P. (2010) Constraining magnesium cycling in marine sediments using magnesium isotopes. *Geochim. Cosmochim. Acta* 74, 5039–5053.

Hippler D., Buhl D., Witbaard R., Richter D. K. and Immenhauser A. (2009) Towards a better understanding of magnesium-isotope ratios from marine skeletal carbonates. *Geochim. Cosmochim. Acta* 73, 6134–6146.

Hochstaedter A. G., Kepezhinskas P. K., Defant M. J., Drummond M. S. and Bellon H. (1994) On the tectonic significance of arc volcanism in northern Kamchatka. *J. Geol.* 102, 639–654.

Hofmann A. W. (2014) Sampling mantle heterogeneity through oceanic basalts: isotope and trace elements. Vol. 3 Treatise on Geochemistry (second ed.) (eds. H. Holland and K. Turekian). Elsevier, Oxford, pp. 67–101.

Hopp J. and Ionov D. A. (2011) Tracing partial melting and subduction-related metasomatism in the Kamchatkan mantle wedge using noble gas compositions. *Earth Planet. Sci. Lett.* 302, 121–131.

Horn D. R., Horn B. M., Delach M. N. (1970) Sedimentary provinces of the North Pacific. In Hayes, J.D. (Ed.). Geological Investigations of the North Pacific. *Geol. Soc. Am. Mem.* 126, 1–22.

Hu Y., Teng F.-Z., Zhang H.-F., Xiao Y., and Su B.-X. (2016a) Metasomatism-induced mantle magnesium isotopic heterogeneity: Evidence from pyroxenites. *Geochim. Cosmochim. Acta* 185, 88–111.

Hu Y., Harrington M. D., Sun Y., Yang Z., Konter J., and Teng F.-Z. (2016b) Magnesium isotopic homogeneity of San Carlos olivine: a potential standard for Mg isotopic analysis by multi-collector inductively coupled plasma mass spectrometry. *Rapid commun. Mass Spectrom.* 30, 2123–2132.

Hu Y., Teng F.-Z., Plank T. and Huang K.-J. (2017) Magnesium isotopic composition of subducting marine sediments. *Chem. Geol.* 466, 15–31.

Huang F., Glessner J., Ianno A., Lundstrom C. C. and Zhang Z.-F. (2009) Magnesium isotopic composition of igneous rock standards measured by MC-ICP-MS. *Chem. Geol.* 268, 15–23.

Huang F., Zhang Z., Lundstrom C. C., and Zhi X. (2011) Iron and magnesium isotopic compositions of peridotite xenoliths from Eastern China. *Geochim. Cosmochim. Acta* 75, 3318–3334.

Huang K.-J., Teng F.-Z., Wei G.-J., Ma J.-L., and Bao Z.-Y. (2012) Adsorption- and desorption-controlled magnesium isotope fractionation during extreme weathering of basalt in Hainan Island, China. *Earth Planet. Sci. Lett.* 359–360, 73–83.

Huang F., Chen L., Wu Z., and Wang W. (2013) First-principles calculations of equilibrium Mg isotope fractionations between garnet, clinopyroxene, orthopyroxene, and olivine: implications for Mg isotope thermometry. *Earth Planet. Sci. Lett.* 367, 61–70.

Huang K.-J. (2013a) The behavior of magnesium isotopes during low-temperature water-rock interactions. PhD dissertation. China University of Geosciences, Wuhan, China.

Huang K.-J., Teng F.-Z., Elsenouy A., Li W.-Y., and Bao Z.-Y. (2013b) Magnesium isotopic variations in loess: Origins and implications. *Earth Planet. Sci. Lett.* 374, 60–70.

Huang K.-J., Teng F.-Z., Plank T., Staudigel H., Hu Y., and Bao Z.-Y. (2018) Magnesium isotopic composition of the altered oceanic crust: Implications for the magnesium geochemical cycle, *Geochim Cosmochim Acta* 238, 357–373.

Huang J., Li S.-G., Xiao Y. L., Ke S., Li W.-Y., and Tian Y. (2015) Origin of low δ^{26}Mg Cenozoic basalts from South China Block and their geodynamic implications. *Geochim. Cosmochim. Acta* 164, 298–317.

Ionov D. A., Chanefo I. and Bodinier J.-L. (2005) Origin of Fe-rich lherzolites and wehrlites from Tok, SE Siberia by reactive melt percolation in refractory mantle peridotites. *Contrib. Mineral. Petrol.* 50, 335–353.

Ionov D. A. and Seitz H. M. (2008) Lithium abundances and isotopic compositions in mantle xenoliths from subduction and intra-plate settings: mantle sources vs. eruption histories. *Earth Planet. Sci. Lett.* 266, 316–331.

Ionov D. A. (2010) Petrology of mantle wedge lithosphere: new data on supra-subduction zone peridotite xenoliths from the andesitic Avacha volcano, Kamchatka. *J. Petrol.* 51, 327–361.

Ionov D. A., Bénard A. and Plechov P. Y. (2011) Melt evolution in subarc mantle: evidence from heating experiments on spinel-hosted melt inclusions in peridotite xenoliths from the andesitic Avacha volcano (Kamchatka, Russia). *Contrib. Mineral. Petrol.* 162, 1159–1174.

Ionov D. A., Bodinier J.-L., Mukasa S. B., and Zanetti A. (2002) Mechanisms and sources of mantle metasomatism: major and trace element compositions of peridotite xenoliths from Spitsbergen in the context of numerical modeling. *J. Petrol.* 43, 2219-2259.

Irving A. J. (1980) Petrology and geochemistry of composite ultramafic xenoliths in alkali basalts and implications for magmatic processes within the mantle. *Am. J. Sci.* 280, 389–426.

Ishikawa T., Tera F. and Nakazawa T. (2001) Boron isotope and trace element systematics of the three volcanic zones in the Kamchatka arc. *Geochim. Cosmochim. Acta* 65, 4523–4537.

Ishimaru S., Arai S., Ishida Y., Shirasaka M., and Okrugin V. M. (2006) Melting and multi-stage metasomatism in the mantle wedge beneath a frontal arc inferred from highly

depleted peridotite xenoliths from the Avacha volcano, southern Kamchatka. *J. Petrol.* 48, 395–433.

Ishimaru S. and Arai S. (2008a) Nickel enrichment in mantle olivine beneath a volcanic front. *Contrib. Mineral. Petrol.* 156,119–131.

Ishimaru S. and Arai S. (2008b) Calcic amphiboles in peridotite xenoliths from Avacha volcano, Kamchatka, and their implications for metasomatic conditions in the mantle wedge. *Geol. Soc. London, Spec. Publ.* 293, 35–55.

Ishimaru S. and Arai S. (2008c) Highly silicic glasses in peridotite xenoliths from Avacha volcano, Kamchatka arc; implications for melting and metasomatism within the sub-arc mantle. *Lithos* 107, 93–106.

Ishimaru S. and Arai S. (2011) Peculiar Mg–Ca–Si metasomatism along a shear zone within the mantle wedge: inference from fine-grained xenoliths from Avacha volcano, Kamchatka. *Contrib. Mineral. Petrol.* 161, 703–720.

Jacob D. (2004) Nature and origin of eclogite xenoliths from kimberlites. *Lithos* 77, 295–316.

Johnson, M. C. and Plank T. (1999) Dehydration and melting experiments constrain the fate of subducted sediments. *Geochem. Geophys. Geosyst.* 1, doi: 10.1029/1999GC000014.

Kayzar T. M., Nelson B. K., Bachmann O., Bauer A. M., and Izbekov P. E. (2014). Deciphering petrogenic processes using Pb isotope ratios from time-series samples at Bezymianny and Klyuchevskoy volcanoes, Central Kamchatka Depression. *Contrib. Mineral. Petrol.* 168, 1067.

Ke S., Teng F.-Z., Li S.-G., Gao T., Liu S.-A., He Y., and Mo X. (2016) Mg, Sr, and O isotope geochemistry of syenites from northwest Xinjiang, China: Tracing carbonate recycling during Tethyan oceanic subduction. *Chem. Geol.* 437, 109–119.

Kelemen P. B., Hart S. R., and Bernstein S. (1998) Silica enrichment in the continental upper mantle via melt/rock reaction. *Earth Planet. Sci. Lett.* 164, 387–406.

Kersting A. B. and Arculus R. J. (1995) Pb isotope composition of Klyuchevskoy volcano, Kamchatka and North Pacific sediments: implications for magma genesis and crustal recycling in the Kamchatkan arc. *Earth Planet. Sci. Lett.* 136, 133–148.

Kepezhinskas P., Defant M. J and Drummond M. S. (1995) Na metasomatism in the island arc mantle by slab melt-peridotite interaction: evidence from mantle xenoliths in the north Kamchatka arc. *J. Petrol.* 36, 1505–1527.

Kepezhinskas P., Defant M. J., and Drummond M. S. (1996) Progressive enrichment of island arc mantle by melt-peridotite interaction inferred from Kamchatka xenoliths. *Geochim. Cosmochim. Acta* 60, 1217–1229.

Kepezhinskas P. and Defant M. J. (1996) Contrasting styles of mantle metasomatism above subduction zones: constraints from ultramafic xenoliths in Kamchatka. *Geophys. Monogr.* AGU 96,307–313.

Kepezhinskas P., McDermott F., Defant M. J., Hochstaedter A., Drummond M. S., Hawkesworth C. J., Koloskov A., Maury R. C., and Bellon H. (1997) Trace element and Sr-Nd-Pb isotopic constraints on a three-component model of Kamchatka arc petrogenesis. *Geochim. Cosmochim. Acta* 61, 577–600.

Kepezhinskas P., Defant M. J., and Widom E. (2002) Abundance and distribution of PGE and Au in the island-arc mantle: implications for sub-arc metasomatism. *Lithos* 60, 113–128.

Keshav S. and Sen G. (2004) The depth of magma fractionation in the oceanic mantle: insights from garnet-bearing xenoliths from Oahu, Hawaii. *Geophys. Res. Lett.* 31, L04611.

Keshav S., Sen G., and Presnall D. C. (2007) Garnet-bearing xenoliths from Salt Lake Crater, Oahu, Hawaii: high-pressure fractional crystallization in the oceanic mantle. *J. Petrol.* 48, 1681–1724.

Kessel R., Ulmer P., Pettke T., Schmidt M. W., and Thompson A. B. (2005) The water-basalt system at 4 to 6 GPa: phase relations and second critical endpoint in a K-free eclogite at 700 to 1400 °C. *Earth Planet. Sci. Lett.* 237, 873–892.

Knoche R., Sweeney R. J., and Luth R. W. (1999) Carbonation and decarbonation of eclogites: the role of garnet. *Contrib. Mineral. Petrol.* 135, 332–339.

Korenaga J. and Kelemen P. B. (2000) Major element heterogeneity in the mantle source of the North Atlantic igneous province. *Earth Planet. Sci. Lett.* 184, 251–268.

Lai Y.-J., Pogge von Strandmann P. A. E., Dohmen R., Takazawa E. and Elliott T. (2015) The influence of melt infiltration on the Li and Mg isotopic composition of the Horoman Peridotite Massif. *Geochim. Cosmochim. Acta* 164, 318–332.

Latouche C. and Maillet N. (1982) X-ray mineralogy studies, Leg 67 (sites 495 – 500): the middle America Trench transect off Guatemala. doi:10.2973/dsdp.proc.67.120.1982.

Le Bas M. J., Lemaitre R. W., Streckeisen A., and Zanettin B. (1986) A chemical classification of volcanic-rocks based on the total alkali silica diagram. *J. Petrol.* 27, 745–750.

Lee C. T. and Rudnick R. L. (1999) Compositionally stratified cratonic lithosphere: petrology and geochemistry of peridotite xenoliths from the Labait volcano, Tanzania. In Proceedings of the 7th International Kimberlite Conference l (eds. J. J. Gurney, J. L. Gurney and M. D. Pascoe). Red Roof Design, Cape Town, pp. 503–521.

Levin V., Park J., Brandon M., Lees J., Peyton V., Gordeev E., and Ozerov A. (2002) Crust and upper mantle of Kamchatka from teleseismic receiver functions. *Tectonophysics* 358, 233–265.

Li S.-G., Yang W., Ke S., Meng X., Tian H., Xu L., He Y., Huang J., Wang X.-C., Xia Q., Sun W., Yang X., Ren Z.-Y., Wei H., and Liu Y. (2017) Deep carbon cycles constrained by a large-scale mantle Mg isotope anomaly in eastern China. *Natl. Sci. Rev.* 4, 111–120.

Li W.-Y., Teng F.-Z., Ke S., Rudnick R. L., Gao S., Wu F.-Y., and Chappell B. W. (2010) Heterogeneous magnesium isotopic composition of the upper continental crust. *Geochim. Cosmochim. Acta* 74, 6867–6884.

Li W.-Y., Teng F.-Z., Xiao Y.-L., and Huang J. (2011) High-temperature inter-mineral magnesium isotope fractionation in eclogite from the Dabie orogen, China. *Earth Planet. Sci. Lett.* 304, 224–230.

Li W.-Y., Teng F.-Z., Wing B. A., and Xiao Y. (2014) Limited magnesium isotope fractionation during metamorphic dehydration in metapelites from the Onawa contact aureole, Maine. *Geochem. Geophys. Geosyst.* 15, 408–415.

Li W.-Y., Xiao Y.-L., and Teng F.-Z. (2016) Metasomatism-induced magnesium isotope fractionation in ultramafic rocks: evidence from the Franciscan Complex, California. American Geophysical Union Fall Meeting, San Francisco.

Lindsley D. H. and Dixon S. A. (1976) Diopside-enstatite equilibria at 850° to 1400°C, 5 to 35 kb. *Am. J. Sci.* 276, 1285–1301.

Ling M.-X., Sedaghatpour F., Teng F.-Z., Hays P. D., Strauss J., and Sun W. (2011) Homogeneous magnesium isotopic composition of seawater: an excellent geostandard for Mg isotope analysis. *Rapid Commun. Mass Spectrom.* 25, 2828–2836.

Ling M.-X., Liu Y.-L., Williams I. S., Teng F.-Z., Yang X.-Y., Ding X., Wei G.-J., Xie L.-H., Deng W.-F., and Sun W.-D. (2013a) Formation of the world's largest REE deposit through protracted fluxing of carbonatite by subduction-derived fluids. *Sci. Rep.* 3. http://dx.doi.org/10.1038/srep01776.

Ling M.-X., Li Y., Ding X., Teng F.-Z., Yang X.-Y., Fan W.-M., Xu Y.-G., and Sun W.D. (2013b) Destruction of the North China Craton induced by ridge subductions. *J. Geol.* 121, 197–213.

Liu C. Q., Masuda A., and Xie G. H. (1994) Major- and trace-element compositions of Cenozoic basalts in eastern China: petrogenesis and mantle source. *Chem. Geol.* 114, 19–42.

Liu D., Zhao Z.-D., Zhu D.-C., Niu Y.-L., Widom E., Teng F.-Z., DePaolo D.-J., Ke S., Xu J.-F., Wang Q., and Mo X.-X. (2015) Identifying mantle carbonatite metasomatism through Os–Sr–Mg isotopes in Tibetan ultrapotassic rocks. *Earth Planet. Sci. Lett.* 430, 458–469.

Liu P.-P., Teng F.-Z., Dick H. J. B., Zhou M.-F., and Chung S.-L. (2017) Magnesium isotopic composition of the oceanic mantle and oceanic Mg cycling. *Geochim. Cosmochim. Acta* 206, 151–165.

Liu Y. S., Gao S., Liu X. M., Chen X. M., Zhang W. L., and Wang X. C. (2003) Thermodynamic evolution of lithosphere of North China Craton: records from lower crust and upper mantle xenoliths from Hannuoba. *Chin. Sci. Bull.* 48, 2371–2377.

Liu Y. S., Yuan H. L., Gao S., Hu Z. C., Wang X., Liu X. M., and Lin W. L. (2004) Zircon U–Pb ages of olivine pyroxenite xenolith from Hannuoba: links between the 97–158 Ma basaltic underplating and granulite-facies metamorphism. *Chin. Sci. Bull.* 49, 1055–1062.

Liu Y. S., Gao S., Lee C. T. A., Hu S. H., Liu X. M., and Yuan H. L. (2005) Melt–peridotite interactions: links between garnet pyroxenite and high-Mg# signature of continental crust. *Earth Planet. Sci. Lett.* 234, 39–57.

Liu S.-A., Teng F.-Z., He Y., Ke S., and Li S.-G. (2010a) Investigation of magnesium isotope fractionation during granite differentiation: implication for Mg isotopic composition of the continental crust. *Earth Planet. Sci. Lett.* 297, 646–654.

Liu X.-M., Teng F.-Z., Rudnick R. L., McDonough W. F., Cummings M. L. (2014) Massive magnesium depletion and isotope fractionation in weathered basalts. *Geochim. Cosmochim. Acta* 135, 336–349.

Liu Y. S., Gao S., Gao C. G., Hu Z. C., and Ling W. L. (2010b) Garnet-rich granulite xenoliths from the Hannuoba basalts, north China: petrogenesis and implications for the Mesozoic crust–mantle interaction. *J. Earth Sci.* 21, 669–691.

Liu Y. S., Gao S., Hu Z., Gao C., Zong K., and Wang D. (2010c) Continental and oceanic crust recycling-induced melt–peridotite interactions in the Trans-North China Orogen: U–Pb dating, Hf isotopes and trace elements in zircons from mantle xenoliths. *J. Petrol.* 51, 537–571.

Liu S.-A., Teng F.-Z., Yang W., and Wu F.-Y. (2011) High-temperature inter-mineral magnesium isotope fractionation in mantle xenoliths from the North China craton. *Earth Planet. Sci. Lett.* 308, 131–140.

Ma L., Teng F.-Z., Jin L.-X., Ke S., Yang W., Gu H.-O., and Brantley S. L. (2015) Magnesium isotope fractionation during shale weathering in the Shale Hills Critical Zone Observatory: Accumulation of light Mg isotopes in soils by clay mineral transformation. *Chem. Geol.* 397, 37–50.

Macris C. A., Young E. D., and Manning C. E. (2013) Experimental determination of equilibrium magnesium isotope fractionation between spinel, forsterite, and magnesite from 600 to 800°C. *Geochim. Cosmochim. Acta* 118, 18–32.

Manea V. C. and Manea M. (2007) Thermal models beneath Kamchatka and the Pacific plate rejuvenation from a mantle plume impact. In: Eichelberger, J., Izbekov, P.,

Ruppert, N., Gordeev, E., Lees, J. (eds) Volcanism and tectonics of the Kamchatka peninsula and adjacent arcs. *Geophys. Monogr.* 172, 77–90.

Manning C. E. (2004) The chemistry of subduction-zone fluids. *Earth Planet. Sci. Lett.* 223, 1–16.

Mavromatis V., Meister P., and Oelkers E. H. (2014) Using stable Mg isotopes to distinguish dolomite formation mechanisms: A case study from the Peru Margin. *Chem. Geol.* 385, 84–91.

McDonough W. F. and Sun S.-S. (1995) The composition of the Earth. *Chem. Geol.* 120, 223–253.

McDonough W. F. (1990) Constraints on the composition of the continental lithospheric mantle. *Earth Planet. Sci.Lett.* 101, 1–18.

McLennan S. M., Hemming S., McDaniel D. K., and Hanson G. N. (1993) Geochemical approaches to sedimentation, provenance, and tectonics. *Geol. Soc. Lond. Spec. Publ.* 284, 21–40.

Melson W. G., Vallier T. L., Wright T. L., Byerly G., and Nelen J. (1976) Chemical diversity of abyssal volcanic glass erupted along the Pacific, Atlantic and Indian Ocean sea-floor spreading centres. In *The Geophysics of the Pacific Ocean Basin and its Margin*. Am Geophys. Union, Washington, DC, pp. 351–368.

Nesbitt H. W. and Young G. M. (1982) Early Proterozoic climates and plate motions inferred from major element chemistry of lutites. *Nature* 299, 715–717.

Nickel K. G. and Green D. H. (1985) Empirical geothermobarometry for garnet peridotites and implications for the nature of the lithosphere, kimberlites and diamonds. *Earth Planet. Sci. Lett.* 73, 158–170.

Nimis P. and Taylor W. R. (2000) Single clinopyroxene thermobarometry for garnet peridotites. Part I. Calibration and testing of a Cr-in-Cpx barometer and an enstatite-in-Cpx thermometer. *Contrib. Mineral. Petrol.* 139, 541–554.

Nizkous I. V., Sanina I. A., Kissling E., and Gontovaya L. I. (2006) Velocity properties of the lithosphere in the ocean-continent transition zone in the Kamchatka region from seismic tomography data. Izvestiya. *Phys. Solid Earth* 42, 286–296.

Norman M. D., McCulloch M. T., O'Neill H. S., and Yaxley G. M. (2006). Magnesium isotopic analysis of olivine by laser-ablation multi-collector ICP-MS: composition dependent matrix effects and a comparison of the Earth and Moon. *J. Anal. At. Spectrom.* 21, 50–54.

Norman M. D., Yaxley G. M., Bennett V. C., and Brandon A. D. (2006) Magnesium isotopic composition of olivine from the Earth, Mars, Moon, and pallasite parent body. *Geophys. Res. Lett.* 33, L15202, DOI: 10.1029/2006GL026446.

O'Reilly S. Y. and Griffin W. L. (2013) Mantle Metasomatism. In: Metasomatism and the Chemical Transformation of Rock. Lecture Notes in Earth System Sciences. Springer, Berlin, Heidelberg.

Patchett J., White W. M., Feldmann H., Kielinczuk S., and Hofmann A. W. (1984) Hafnium/rare earth element fractionation in the sedimentary system and crustal recycling into the Earth's mantle. *Earth Planet. Sci. Lett.* 69, 365–378.

Peacock S. M. (2001) Are the lower planes of double seismic zones caused by serpentine dehydration in subducting oceanic mantle? *Geology* 29, 299–302.

Pearson N. J., Griffin W. L., Alard O., and O'Reilly S. Y. (2006) The isotopic composition of magnesium in mantle olivine: Records of depletion and metasomatism. *Chem. Geol.* 226, 115–133.

Penniston-Dorland S., Liu X.-M., and Rudnick R. L. (2017) Lithium Isotope Geochemistry. *Rev. Mineral. Geochem.* 82, 165–206.

Pineau F., Semet M. P., Grassineau N., Okrugin V. M., and Javoy M. (1999) The genesis of the stable isotope (O, H) record in arc magmas: the Kamtchatka's case. *Chem. Geol.* 153, 93–124.

Piper D. (1974) Rare Earth Elements in the sedimentary cycle: A summary. *Chem. Geol.* 14, 285–304.

Plank T. and Langmuir C. H. (1998) The chemical composition of subducting sediment and its consequences for the crust and mantle. *Chem. Geol.* 145, 325–394.

Plank T. (2014) The chemical composition of subducting sediments. In *The Crust* (ed. R. L. Rudnick), Vol. 4 Treatise on Geochemistry (second ed.) (eds. H. Holland and K. Turekian) Elsevier, Oxford, pp. 607–629.

Pogge von Strandmann P. A. E. (2008) Precise magnesium isotope measurements in core top planktic and benthic foraminifera. *Geochem. Geophys. Geosyst.* 9, Q12015. http://dx.doi.org/10.1029/2008GC002209.

Pogge von Strandmann P. A. E., Elliott T., Marschall H. R., Coath C., Lai Y. J., Jeffcoate A. B., and Ionov D. A. (2011) Variations of Li and Mg isotope ratios in bulk chondrites and mantle xenoliths. *Geochim. Cosmochim. Acta* 75, 5247–5268.

Pogge von Strandmann P. A. E., Dohmen R., Marschall H. R., Schumacher J. C., and Elliott T. (2015) Extreme magnesium isotope fractionation at outcrop scale records the mechanism and rate at which reaction fronts advance. *J. Petrol.* 56, 33–58.

Portnyagin M., Hoernle K., Plechov P., Mironov N., and Khubunaya S. (2007) Constraints on mantle melting and composition and nature of slab components in volcanic arcs from volatiles (H_2O, S, Cl, F) and trace elements in melt inclusions from the Kamchatka Arc. *Earth Planet. Sci. Lett.* 255, 53–69.

Prytulak J., Vervoort J. D., Plank T., Yu C. (2006) Astoria Fan sediments, DSDP site 174, Cascadia Basin: Hf–Nd–Pb constraints on provenance and outburst flooding. *Chem. Geol.* 233, 276–292.

Qian S. P., Ren Z. R., Zhang L., Hong L. B., and Liu J. Q. (2015) Chemical and Pb isotope composition of olivine-hosted melt inclusions from the Hannuoba basalts, North China Craton: implications for petrogenesis and mantle source. *Chem. Geol.* 401, 111–125.

Qiu L., Rudnick R. L., McDonough W. F., and Merriman R. J. (2009) Li and δ^7Li in mudrocks from the British Caledonides: metamorphism and source influences. *Geochim. Cosmochim. Acta* 73, 7325–7340.

Quilty P. G., Sachs H. M., Benson W. E., Vallier T. L., and Blechschmidt G. (1976) Sedimentologic history, Leg 34 Deep Sea Drilling Project. doi: 10.2973/dsdp.proc.34.166.1976.

Rapp R. P., Shimizu N., Norman M. D., and Applegate G. S. (1999) Reaction between slab-derived melts and peridotite in the mantle wedge: experimental constraints at 3.8 GPa. *Chem. Geol.* 160, 335–356.

Richter F. M., Dauphas N., and Teng F.-Z. (2009) Non-traditional fractionation of non-traditional isotopes: evaporation, chemical diffusion and Soret diffusion. *Chem. Geol.* 258, 92–103.

Riley J. P. and Chester R. (1971) Introduction to marine chemistry. Academic Press London and New York.

Rudnick R. L., McDonough F., and Chappell B. W. (1993) Carbonatite metasomatism in the northern Tanzanian mantle: petrographic and geochemical characteristics. *Earth Planet. Sci. Lett.* 114, 463–475.

Rudnick R. L., Gao S., Ling W. L., Liu Y. S., and McDonough W. F. (2004) Petrology and geochemistry of spinel peridotite xenoliths from Hannuoba and Qixia, North China Craton. *Lithos* 77, 609–637.

Rudnick R. L. and Gao S. (2014) Composition of the continental crust. In *The Crust* (ed. R. L. Rudnick), Vol. 4 Treatise on Geochemistry (second ed.) (eds. H. Holland and K. Turekian) Elsevier, Oxford, pp. 1–51.

Rose-Koga E. F. and Albarède F. (2010) A data brief on magnesium isotope compositions of marine calcareous sediments and ferromanganese nodules. *Geochem. Geophys. Geosyst.* 11, doi: 10.1029/2009GC002899.

Saenger C. and Wang Z.-R. (2014) Magnesium isotope fractionation in biogenic and abiogenic carbonates: implications for paleoenvironmental proxies. *Quatern. Sci. Rev.* 90, 1–21.

Savov I. P., Ryan J. G., D'Antonio M., Kelley K., and Mattie P. (2005) Geochemistry of serpentinized peridotites from the Mariana Forearc Conical Seamount, ODP leg

125: implications for the elemental recycling at subduction zones. *Geochem Geophys Geosyst* 6, Q04J15. doi:10.1029/2004GC000777.

Sawhiney B. (1972) Selective sorption and fixation of cations by clay minerals: a review. *Clays Clay Miner.* 20, 93–100.

Schauble E. A. (2011) First-principles estimates of equilibrium magnesium isotope fractionation in silicate, oxide, carbonate and hexaaquamagnesium (2+) crystals. *Geochim. Cosmochim. Acta* 75, 844–869.

Schiller M., Baker J. A., and Bizzarro M. (2010) ^{26}Al–^{26}Mg dating of asteroidal magmatism in the young Solar System. *Geochim. Cosmochim. Acta* 74, 4844–4864.

Schilling J. G., Zajac M., Evans R., Johnston T., White W., Devine J. D., and Kingsley R. (1983) Petrologic and geochemical variations along the Mid-Atlantic Ridge from 27°N to 73°N. *Am. J. Sci.* 283, 510–586.

Schmidt M. W. and Poli S. (2014) Devolatilization during subduction. In: Treatise in Geochemistry, vol. 4, 669–701.

Schneider R. R., Price B., Müller P. J., Kroon D., and Alexander I. (1997) Monsoon related variations in Zaire (Congo) sediment load and influence of fluvial silicate supply on marine productivity in the east equatorial Atlantic during the last 200,000 years. *Paleoceanography* 12, 463–481.

Shen B., Jacobsen B., Lee C.-T.A., Yin Q.-Z., and Morton D. M. (2009) The Mg isotopic systematics of granitoids in continental arcs and implications for the role of chemical weathering in crust formation. *Proc. Natl. Acad. Sci. USA* 106, 20652–20657.

Sio C. K. I., . Dauphas Teng N, F.-Z., Chaussidon M., Helz R. T., and Roskosz M.. (2013) Discerning crystal growth from diffusion profiles in zoned olivine by in-situ Mg-Fe isotopic analyses. *Geochim. Cosmochim. Acta* 123, 302–321.

Sobolev N. V., Lavrent'ev Y. G., Pokhilenko N. P., and Usova L. V. (1973) Chrome-rich garnets from the kimberlites of Yakutia and their parageneses. *Contrib. Mineral. Petrol.* 40, 39–52.

Sobolev A. V., Hofmann A. W., Sobolev S. V., and Nikogosian I. K. (2005) An olivine-free mantle source of Hawaiian shield basalts. *Nature* 434, 590–597.

Sobolev A. V., Hofmann A. W., Kuzmin D. V., Yaxley G. M., Arndt N. T., Chung S. L., Danyushevsky L. V., Elliott T., Frey F. A., and Garcia M. O. (2007) The amount of recycled crust in sources of mantle-derived melts. *Science* 316, 412–417.

Song Y. and Frey F. A. (1989) Geochemistry of peridotite xenoliths in basalt from Hannuoba, eastern China: implications for subcontinental mantle heterogeneity. *Geochim. Cosmochim. Acta* 53, 97–113.

Spera F. J. (1984) Carbon dioxide in petrogenesis III: role of volatiles in the ascent of alkaline magma with special reference to xenolith-bearing mafic lavas. *Contrib. Mineral. Petrol.* 88, 217–232.

Stracke A., Zindler A., Salters V. J. M., McKenzie D., Blichert- Toft J., Albarède F. and Grönvold K. (2003) Theistareykir revisited. *Geochem. Geophys. Geosyst.* 4. http://dx.doi.org/10.1029/2001GC000201.

Su B.-X., Zhang H.-F., Hu Y., Santosh M., Tang Y.-J., and Xiao Y. (2012a) The genesis of mantle-derived sapphirine. *Am. Mineral.* 97, 856–863.

Su B.-X., Zhang H.-F., Ying J.-F., Tang Y.-J., Hu Y., and Santosh M. (2012b) Metasomatized lithospheric mantle beneath the Western Qinling, Central China: insight into carbonatite melts in the mantle. *J. Geol.* 120, 671–681.

Su B.-X., Chung S.-L., Zarrinkoub M. H., Pang K.-N., Chen L., Ji W.-Q., Brewer A., Ying J. F., and Khatib M. M. (2014) Composition and structure of the lithospheric mantle beneath NE Iran: constraints from mantle xenoliths. *Lithos* 202–203, 267–282.

Su B.-X., Teng F.-Z., Hu Y., Shi R.-D., Zhou M.-F., Zhu B., Liu F., Gong X.-H., Huang Q.-S., Xiao Y., Chen C., and He Y.-S. (2015) Iron and magnesium isotope fractionation in oceanic lithosphere and sub-arc mantle: Perspectives from ophiolites. *Earth Planet. Sci. Lett.* 430, 523–532.

Su B.-X., Hu Y., Teng F.-Z., and Xiao Y. (2017) Magnesium isotope constraints on subduction contribution to Mesozoic and Cenozoic East Asian continental basalts. *Chem. Geol.* 466, 116–122.

Sun S.-s. and McDonough W. F. (1989) Chemical and isotopic systematics of oceanic basalts: implications for mantle composition and processes. *Geol. Soc. London Spec. Publ.* 42, 313 –345.

Sun Y., Teng F.-Z., Ying J.-F., Su B.-X., Hu Y., Fan Q.-C., and Zhou X.-H. (2017) Magnesium isotopic evidence for ancient subducted oceanic crust in LOMU-like potassium-rich volcanic rocks. *J. Geophys. Res.* 122, 7562–7572.

Syracuse E. M., van Keken P. E., and Abers G. A. (2010) The global range of subduction zone thermal models. *Phys. Earth Planet. Inter.* 183, 73–90.

Tang M., Rudnick R. L., and Chauvel C. (2014) Sedimentary input to the source of Lesser Antilles lavas: A Li perspective. *Geochim. Cosmochim. Acta* 144, 43–58.

Tang Y.-J., Zhang H.-F., Nakamura E., Moriguti T., Kobayashi K., and Ying J.-F. (2007) Lithium isotopic systematics of peridotite xenoliths from Hannuoba, North China Craton: implications for melt–rock interaction in the considerably thinned lithospheric mantle. *Geochim. Cosmochim. Acta* 71, 4327–4341.

Tang Y.-J., Zhang H.-F., Ying J.-F., Zhang J., and Liu X.-M. (2008) Refertilization of ancient lithospheric mantle beneath the central North China Craton: evidence from petrology and geochemistry of peridotite xenoliths. *Lithos* 101, 435–452.

Tang Y.-J., Zhang H.-F., Nakamura E., and Ying J.-F. (2011) Multistage melt/fluid-peridotite interactions in the refertilized lithospheric mantle beneath the North China Craton: constraints from the Li–Sr–Nd isotopic disequilibrium between minerals of peridotite xenoliths. *Contrib. Mineral. Petrol.* 161, 845–861.

Tatsumoto M., Basu A. R., Huang W. K., Wang J. W., and Xie G. H. (1992) Sr, Nd, and Pb isotopes of ultramafic xenoliths in volcanic-rocks of Eastern China: enriched components EMI and EMII in subcontinental lithosphere. *Earth Planet. Sci. Lett.* 113, 107–128.

Taylor S. R. and McLennan S. M. (1985) The Continental Crust: Its Composition and Evolution. Blackwell, Oxford.

Telus M., Dauphas N., Moynier F., Tissot F. L. H., Teng F.-Z., Nabelek P. I., Craddock P. R., and Groat L. A. (2012) Iron, zinc, magnesium and uranium isotopic fractionation during continental crust differentiation: The tale from migmatites, granitoids, and pegmatites. *Geochim. Cosmochim. Acta* 97, 247–265.

Teng F.-Z. and Yang W. (2014) Comparison of factors affecting the accuracy of high-precision magnesium isotope analysis by multi-collector inductively coupled plasma mass spectrometry. *Rapid Commun. Mass Spectrom.* 28, 19–24.

Teng F.-Z., Wadhwa M., and Helz R. T. (2007) Investigation of magnesium isotope fractionation during basalt differentiation: implications for a chondritic composition of the terrestrial mantle. *Earth Planet. Sci. Lett.* 261, 84–92.

Teng F.-Z., Li W.-Y., Ke S., Marty B., Dauphas N., Huang S. C., Wu F.-Y., and Pourmand A. (2010a) Magnesium isotopic composition of the Earth and chondrites. *Geochim. Cosmochim. Acta* 74, 4150–4166.

Teng F. -Z., Li W.-Y., Rudnick R. L., and Gardner L. R. (2010b) Contrasting lithium and magnesium isotope fractionation during continental weathering. *Earth Planet. Sci. Lett.* 300, 63–71.

Teng F.-Z., Yang W., Rudnick R. L., and Hu Y. (2013) Heterogeneous magnesium isotopic composition of the lower continental crust: A xenolith perspective. *Geochem. Geophys. Geosys.* 5, doi: 10.1002/ggge.20238.

Teng F.-Z., Li W.-Y., Ke S., Yang W., Liu S.-A., Sedaghatpour F., Wang S.-J., Huang K.-J., Hu Y., Ling M.-X., Xiao Y., Liu X.- M., Li X.-W., Gu H.-O., Sio C. K., Wallace D. A., Su B.-X., Zhao L., Chamberlin J., Harrington M., and Brewer A. (2015) Magnesium isotopic compositions of international geostandards. *Geostandard. Geoanal. Res.* 39, 329–339.

Teng F.-Z., Hu Y., and Chauvel C. (2016) Magnesium isotope geochemistry in arc volcanism. *Proc. Natl. Acad. Sci. U.S.A.* 113, 7082–7087.

Teng F.-Z. (2017) Magnesium Isotope Geochemistry. *Rev. Mineral. Geochem.* 82, 219–287.

Tian H.-C., Yang W., Li S.-G. Ke S., and Chu Z.-Y. (2016) Origin of low δ^{26}Mg basalts with EM-I component: Evidence for interaction between enriched lithosphere and carbonated asthenosphere. *Geochim. Cosmochim. Acta* 188, 93–105.

Tipper E. T., Galy A., and Bickle M. J. (2006a) Riverine evidence for a fractionated reservoir of Ca and Mg on the continents: implications for the oceanic Ca cycle. *Earth Planet. Sci. Lett.* 247, 267–279.

Tipper E. T., Galy A., Gaillardet J., Bickle M. J., Elderfield H., and Carder E. A. (2006b) The magnesium isotope budget of the modern ocean: constraints from riverine magnesium isotope ratios. *Earth Planet. Sci. Lett.* 250, 241–253.

Tipper E. T., Lemarchand E., Hindshaw R. S., Reynolds B. C., and Bourdon B. (2012) Seasonal sensitivity of weathering processes: Hints from magnesium isotopes in a glacial stream. *Chem. Geol.* 312–313, 80–92.

Tomascak P. B., Magna T., Dohmen R. (2016) Advances in Lithium Isotope Geochemistry. Springer International Publishing.

Turner S., McDermott F., Hawkesworth C., and Kepezhinskas P. (1998) A U-series study of lavas from Kamchatka and the Aleutians: constraints on source composition and melting processes. *Contrib. Mineral. Petrol.* 133, 217–234.

Urey H. C. (1947) The thermodynamic properties of isotopic substances. *J. Chem. Soc.* (London), 562–581.

Uspenskaya T. Y., Gorshkov A. I., Sivtsov A. V. (1987) Mineralogy and internal structure of Fe-Mn nodules from the Clarion–Clipperton fracture zone, *Int. Geol. Rev.* 29, 363–371.

Vervoort J. D., Plank T., Prytulak J. (2011) The Hf–Nd isotopic composition of marine sediments. *Geochim. Cosmochim. Acta* 75, 5903–5926.

Venkatarathnam K. (1974) Mineralogical data from sites 211, 212, 213, 214, and 215 of the Deep-Sea Drilling Project, Leg 22, and origin of noncarbonate sediments in the equatorial Indian Ocean. doi:10.2973/dsdp.proc.22.123.1974.

von Huene R. and Scholl D. W. (1991) Observations at convergent margins concerning sediment subduction, subduction erosion, and the growth of continental crust. *Rev. Geophys.* 29, 279–316.

Walter M. J. (2003) Melt extraction and compositional variability in mantle lithosphere. In Treatise on Geochemistry-*The mantle and core* (ed. R. W. Carlson). Carnegie Institute of Washington, Washington, DC, pp. 363–394.

Wang F.-Z., Jin L.-Y., and Xu Y.-R. (1987) The study of ultramafic inclusions in Cenozoic basalt in Shandong, Linqu of Shandong. *Earth Sci.* 12, 249–256 (in Chinese with English abstract).

Wang C., Jin Z.-M., Gao S., Zhang J.-F., and Zheng S. (2010) Eclogite-melt/peridotite reaction: experimental constraints on the destruction mechanism of the North China Craton. *Sci. China Earth Sci.* 53, 797–809.

Wang S.-J., Teng F.-Z., Williams H. M., and Li S.-G. (2012) Magnesium isotopic variations in cratonic eclogites: origins and implications. *Earth Planet. Sci. Lett.* 359–360, 219–226.

Wang S.-J., Teng F.-Z., and Li S.-G. (2014a) Tracing carbonate-silicate interaction during subduction using magnesium and oxygen isotopes. *Nat. Commun.* 5. http://dx.doi.org/10.1038/ncomms6328.

Wang S.-J., Teng F.-Z., Li S.-G., and Hong J.-A. (2014b) Magnesium isotopic systematics of mafic rocks during continental subduction. *Geochim. Cosmochim. Acta* 143, 34–48.

Wang S.-J., Teng F.-Z., Rudnick R. L., and Li S.-G. (2015a) Magnesium isotope evidence for a recycled origin of cratonic eclogites. *Geology* 43, 1071–1074.

Wang S.-J., Teng, F.-Z., Rudnick R. L., and Li S.-G. (2015b) The behavior of magnesium isotopes in low-grade metamorphosed mudrocks. *Geochim. Cosmochim. Acta* 165, 435–448.

Wang S.-J., Teng F.-Z., and Bea F. (2015c) Magnesium isotopic systematics of metapelite in the deep crust and implications for granite petrogenesis. *Geochem. Perspect. Lett.* 1, 75–83.

Wang S.-J., Teng F.-Z., and Scott J. (2016) Tracing the origin of continental HIMU-like intraplate volcanism using magnesium isotope systematics. *Geochim. Cosmochim. Acta* 185, 78–87.

Wang S.-J., Teng F.-Z., Li S.-G., Zhang L.-F., Du J.-X., He Y.-S., and Niu Y. (2017) Tracing subduction zone fluid-rock interactions using trace element and Mg-Sr-Nd isotopes. *Lithos* 290-291, 94–103.

Westbrook G. K., Mascle A., and Biju-Duval B, (1984) Geophysics and the structure of Lesser Antilles Forearc. In: Biju-Duval, B., Moore, J.C.J. (Eds.), Initial Reports of the Deep Sea Drilling Program 78A. U.S. Government Printing Office, Washington, pp. 23–28.

Wells P. R. A. (1977) Pyroxene thermometry in simple and complex systems. *Contrib. Mineral. Petrol.* 62, 129–139.

Weyer S. and Ionov D. A. (2007) Partial melting and melt percolation in the mantle: the message from Fe isotopes. *Earth Planet. Sci. Lett.* 259, 119–133.

White W. M., Dupré, B., and Vidal P. (1985) Isotope and trace element geochemistry of sediments from the Barbados Ridge-Demerara Plain region, Atlantic Ocean. *Geochim. Cosmochim. Acta* 49, 1875–1886.

Widom E., Kepezhinskas P., and Defant M. (2003) The nature of metasomatism in the sub-arc mantle wedge: evidence from Re–Os isotopes in Kamchatka peridotite xenoliths. *Chem. Geol.* 196, 283–306.

Wiechert U. and Halliday A. N. (2007) Non-chondritic magnesium and the origins of the inner terrestrial planets. *Earth Planet. Sci. Lett.* 256, 360–371.

Wilshire H. G. and Shervais J. W. (1975) Al-augite and Cr-diopside ultramafic xenoliths in basaltic rocks from western United States. *Phys. Chem. Earth* 9, 257–272.

Wimpenny J., Gíslason S. R., James R. H., Gannoun A., Pogge von Strandmann P. A. E., and Burton K. W. (2010) The behaviour of Li and Mg isotopes during primary phase dissolution and secondary mineral formation in basalt. *Geochim. Cosmochim. Acta* 74, 5259–5279.

Wimpenny J., Burton K. W., James R. H., Gannoun A., Mokadem F., and Gíslason S. R. (2011) The behaviour of magnesium and its isotopes during glacial weathering in an ancient shield terrain in West Greenland. Earth Planet. Sci. Lett. 304, 260–269.

Wimpenny J., Harvey J., and Yin Q. (2012) The effects of serpentinization on Mg isotopes in Mid-Atlantic ridge peridotite. American Geophysical Union Fall Meeting, San Francisco.

Wimpenny J., Colla C. A., Yin Q.-Z., Rustad J. R., and Casey W. H. (2014a) Investigating the behaviour of Mg isotopes during the formation of clay minerals. *Geochim. Cosmochim. Acta* 128, 178–194.

Wimpenny J., Yin Q.-Z., Tollstrup D., Xie L.-W., and Sun J. (2014b) Using Mg isotope ratios to trace Cenozoic weathering changes: A case study from the Chinese Loess Plateau. *Chem. Geol.* 376, 31–43.

Wombacher F., Eisenhauer A., Heuser A., and Weyer S. (2009) Separation of Mg, Ca and Fe from geological reference materials for stable isotope ratio analyses by MC-ICP-MS and double-spike TIMS. *J. Anal. Atom. Spectrom.* 24, 627–636.

Wombacher F., Eisenhauer A., Böhm F., Gussone N., Regenberg M., Dullo W.-C., and Rüggeberg A. (2011) Magnesium stable isotope fractionation in marine biogenic calcite and aragonite. *Geochim. Cosmochim. Acta* 75, 5797–5818.

Woodhead J. D., Greenwood P., Harmon R. S., and Stoffers P. (1993) Oxygen isotope evidence for recycled crust in the source of EM-type ocean island basalts. *Nature* 362, 809–813.

Woodhead J. D., Harmon R. S., and Fraser D. G. (1987) O, S, Sr, and Pb isotope variations in volcanic rocks from the northern Mariana islands; implications for crustal recycling in intra-oceanic arcs. *Earth Planet. Sci. Letters* 83, 39–52.

Xiao Y. and Zhang H.-F. (2011) Effects of melt percolation on platinum group elements and Re-Os systematics of peridotites from the Tan-Lu fault zone, eastern North China Craton. *J. Geol. Soc. Lond.* 168, 1201–1214.

Xiao Y., Teng F.-Z., Zhang H.-F., and Yang W. (2013) Large magnesium isotope fractionation in peridotite xenoliths from eastern North China craton: product of melt–rock interaction. *Geochim. Cosmochim. Acta* 115, 241–261.

Xie L.-W., Yin Q.-Z., Yang J.-H., Wu F.-Y., and Yang Y.-H. (2011). High precision analysis of Mg isotopic composition in olivine by laser ablation MC-ICP-MS. *J. Anal. At. Spectrom.* 26, 1773–1780.

Xu X.-S., O'Reilly S. Y., Griffin W. L., Zhou X.-M., and Huang X.- L. (1998) The nature of the Cenozoic lithosphere at Nüshan, Eastern China. In Mantle Dynamics and Plate Interactions in East Asia (eds. M. F. J. Flower, S. L. Chung, C. H. Lo and T. Y. Lee). American Geophysical Union, pp. 167–196.

Xu Y. G. (2002) Evidence for crustal components in the mantle and constrains on crustal recycling mechanism: pyroxenite xenoliths from Hannuoba, North China. *Chem. Geol.* 182, 301–322.

Yan J., Chen J.-F., Xie Z., and Zhou T.-X. (2003) Mantle derived xenoliths in the late Cretaceous basalts in eastern Shandong: new constraints on the timing of lithospheric thinning in east China. *Chin. Sci. Bull.* 48, 1570–1574 (in Chinese with English abstract).

Yang W., Teng F.-Z., and Zhang H.-F. (2009) Chondritic magnesium isotopic composition of the terrestrial mantle: a case study of peridotite xenoliths from the North China craton. *Earth Planet. Sci. Lett.* 288, 475–482.

Yang W., Teng F.-Z., Zhang H.-F., and Li S.-G. (2012) Magnesium isotopic systematics of continental basalts from the North China craton: implications for tracing subducted carbonate in the mantle. *Chem. Geol.* 328, 185–194.

Yang W., Teng F.-Z., Li W.-Y., Liu S.-A., Ke S., Liu Y.-S., Zhang H.-F., and Gao S. (2016) Magnesium isotopic composition of the deep continental crust. *Am. Mineral.* 101, 243–252

Yaxley G. M. and Green D. H. (1998) Reactions between eclogite and peridotite: mantle refertilisation by subduction of oceanic crust. Schweiz. *Mineral. Petrogr. Mitt.* 78, 243–255.

Yaxley G. M., Crawford A. J., and Green D. H. (1991) Evidence for carbonatite metasomatism in spinel peridotite xenoliths from western Victoria, Australia. *Earth Planet. Sci. Lett.* 107, 305–317.

Ying J.-F., Zhou X.-H., and Zhang H.-F. (2004) Geochemical and isotopic investigation of the Laiwu–Zibo carbonatites from western Shandong Province, China, and implications for their petrogenesis and enriched mantle source. *Lithos* 75, 413–426.

Ying J.-F., Zhang H.-F., Tang Y.-J., Su B.-X., and Zhou X.-H. (2013) Diverse crustal components in pyroxenite xenoliths from Junan, Sulu orogenic belt: implications for lithospheric modification invoked by continental subduction. *Chem. Geol.* 356, 181–192.

Yogodzinski G. M., Lees J. M., Churikova T. G., Dorendorf F., Wöerner G., and Volynets O. N. (2001) Geochemical evidence for the melting of subducting oceanic lithosphere at plate edges. *Nature* 409, 500–504.

Yoshikawa M. and Nakamura E. (2000) Geochemical evolution of the Horoman peridotite complex: implications for melt extraction, metasomatism, and compositional layering in the mantle. *J. Geophys. Res.* 105, 2879–2901.

Young E. D. and Galy A. (2004) The isotope geochemistry and cosmochemistry of magnesium. In Geochemistry of Nontraditional Stable Isotopes. Rev. Mineral. Geochem. (eds. C. M. Hohnson, B.L. Beard and F. Albarede). pp. 197–230.

Young E. D., Tonui E., Manning C. E., Schauble E., and Macris C. A. (2009) Spinel-olivine magnesium isotope thermometry in the mantle and implications for the Mg isotopic composition of Earth. *Earth Planet. Sci. Lett.* 288, 524–533.

Young E. D., Manning C. E., Schauble E. A., Shahar A., Macris C. A., Lazar C., and Jordan M. (2015) High-temperature equilibrium isotope fractionation of non-traditional stable isotopes: experiments, theory, and applications. *Chem. Geol.* 395, 176–195.

Yu C.-M., Zheng J.-P., and Griffin W. L. (2006) Petrography and geochemistry of peridotite xenoliths from Hannuoba and significance for lithospheric mantle evolution. *J. China Univ. Geosci.* 17, 25–33 (in Chinese with English abstract).

Yu S.-Y., Xu Y.-G., Ma J.-L., Zheng Y.-F., Kuang Y.-S., Hong L.-B., Ge W.-C., and Tong L.-X. (2010) Remnants of oceanic lower crust in the subcontinental lithospheric mantle: trace element and Sr–Nd–O isotope evidence from aluminous garnet pyroxenite xenoliths from Jiaohe, Northeast China. *Earth Planet. Sci. Lett.* 297, 413–422.

Zack T., Tomascak P. B., Rudnick R. L., Dalpé C., and McDonough W. F. (2003) Extremely light Li in orogenic eclogites: the role of isotope fractionation during dehydration in subducted oceanic crust. *Earth Planet. Sci. Lett.* 208, 279–290.

Zemmels I. and Cook H. E. (1973) X-Ray mineralogy of sediments from the Northeast Pacific and Gulf of Alaska – Leg 18 Deep Sea Drilling Project. doi:10.2973/dsdp.proc.18.app4.1973.

Zemmels I. and Cook H. E. (1976) X-Ray mineralogy from the Nazca Plate – Leg 34 Deep Sea Drilling Project. doi:10.2973/dsdp.proc.34.151.1976.

Zhang H.-F., Nakamura E., Kobayashi K., Zhang J., Ying J.-F., Tang Y.-J., and Niu L.-F. (2007a) Transformation of subcontinental lithospheric mantle through deformation-enhanced peridotite-melt reaction: evidence from a highly fertile mantle xenolith from the North China craton. *Int. Geol. Rev.* 49, 658–679.

Zhang H.-F., Ying J.-F., Shimoda G., Kita N. T., Morishita Y., Shao J.-A., and Tang Y.-J. (2007b) Importance of melt circulation and crust–mantle interaction in the lithospheric evolution beneath the North China Craton: evidence from Mesozoic basalt-borne clinopyroxene xenocrysts and pyroxenite xenoliths. *Lithos* 96, 67–89.

Zhang S.-H., Zhao Y., Song B., Hu J.-M., Liu S.-W., Yang Y.-H., Chen F.-K., Liu X.-M., and Liu J. (2009) Contrasting Late Carboniferous and Late Permian-Middle Triassic intrusive suites from the northern margin of the North China craton: geochronology, petrogenesis, and tectonic implications. *Geol. Soc. Am. Bull.* 121, 181–200.

Zhang H.-F., Deloule E., Tang Y.-J., and Ying J.-F. (2010) Melt/rock interaction in remains of refertilized Archean lithospheric mantle in Jiaodong Peninsula, North China Craton: Li isotopic evidence. *Contrib. Mineral. Petrol.* 160, 261–277.

Zhang J.-F., Wang C., and Wang Y. F. (2012) Experimental constraints on the destruction mechanism of the North China Craton. *Lithos* 149, 91–99.

Zhang H.-F. (2009) Peridotite–melt interaction: a key point for the destruction of cratonic lithospheric mantle. *Chin. Sci. Bull.* 54, 3417–3437.

Zhao X.-M., Zhang H.-F., Zhu X.-K., Tang S., and Tang Y. (2010) Iron isotope variations in spinel peridotite xenoliths from North China Craton: implications for mantle metasomatism. *Contrib. Mineral. Petrol.* 160, 1–14.

Zheng J. P., O'Reilly S. Y., Griffin W. L., Lu F.-X., and Zhang M. (1998) Nature and evolution of Cenozoic lithospheric mantle beneath Shandong peninsula, Sino-Korean Craton, eastern China. *Int. Geol. Rev.* 40, 471–499.

Zheng J. P., Griffin W. L., Qi L., O'Reilly S. Y., Sun M., Zheng S., Pearson N., Gao J. F., Yu C. M., Su Y. P., Tang H. Y., Liu Q. S., and Wu X. L. (2009) Age and composition of granulite and pyroxenite xenoliths in Hannuoba basalts reflect Paleogene underplating beneath the North China Craton. *Chem. Geol.* 264, 266–280.

Zhi X.-C., Song Y., Frey F. A., Feng J.-L., and Zhai M.-Z. (1990) Geochemistry of Hannuoba basalts, eastern China: constraints on the origin of continental alkali and tholeiitic basalt. *Chem. Geol.* 88, 1–33.

Zhu B. Q. (1998) Theory and Applications of Isotope Systematics in Geosciences: Evolution of Continental Crust and Mantle in China (in Chinese). Science Press, Beijing.

Zindler A. and Hart S. (1986) Chemical geodynamics. *Annu. Rev. Earth Planet. Sci.* 14, 494–571.